Andrés Kecskeméthy
Francisco Geu Flores
Eliodoro Carrera
Dante A. Elias   *Editors*

Interdisciplinary Applications of Kinematics

Proceedings of the Third International Conference (IAK)

Springer

Mechanisms and Machine Science

Volume 71

This book series establishes a well-defined forum for monographs, edited Books, and proceedings on mechanical engineering with particular emphasis on MMS (Mechanism and Machine Science). The final goal is the publication of research that shows the development of mechanical engineering and particularly MMS in all technical aspects, even in very recent assessments. Published works share an approach by which technical details and formulation are discussed, and discuss modern formalisms with the aim to circulate research and technical achievements for use in professional, research, academic, and teaching activities. This technical approach is an essential characteristic of the series. By discussing technical details and formulations in terms of modern formalisms, the possibility is created not only to show technical developments but also to explain achievements for technical teaching and research activity today and for the future. The book series is intended to collect technical views on developments of the broad field of MMS in a unique frame that can be seen in its totality as an Encyclopaedia of MMS but with the additional purpose of archiving and teaching MMS achievements. Therefore, the book series will be of use not only for researchers and teachers in Mechanical Engineering but also for professionals and students for their formation and future work.

The series is promoted under the auspices of International Federation for the Promotion of Mechanism and Machine Science (IFToMM).

Prospective authors and editors can contact Mr. Pierpaolo Riva (publishing editor, Springer) at: pierpaolo.riva@springer.com

Indexed by SCOPUS and Google Scholar.

More information about this series at http://www.springer.com/series/8779

Andrés Kecskeméthy · Francisco Geu Flores ·
Eliodoro Carrera · Dante A. Elias
Editors

Interdisciplinary Applications of Kinematics

Proceedings of the Third International
Conference (IAK)

Springer

Editors
Andrés Kecskeméthy
Department of Mechanical Engineering
University of Duisburg-Essen
Duisburg, Germany

Francisco Geu Flores
Chair of Mechanics and Robotics
University of Duisburg-Essen
Duisburg, Nordrhein-Westfalen, Germany

Eliodoro Carrera
Faculty of Engineering
University of Piura
Piura, Peru

Dante A. Elias
Department of Engineering
Pontifical Catholic University of Peru
Lima, Peru

Organization Committee

Chair

Andrés Kecskeméthy (Germany)

Co-Chair

Francisco Geu Flores (Germany)
Eliodoro Carrera (Peru)
Dante A. Elias (Peru)

International Scientific Committee

J. Ambrosio (Portugal)
J. Angeles (Canada)
M. Ceccarelli (Italy)
B. Corves (Germany)
J. Cuadrado (Spain)
H. Ding (China-Beijing)
S. Dubowsky (USA)
M. Dutra (Brasil)
P. Flores (Portugal)
J. Herder (The Netherlands)
T. Huang (China-Beijing)
M. Husty (Austria)
K. Kazerounian (USA)
W. Kowalczyk (Germany)

J. Lenarcic (Slovenia)
H. Liu (China-Beijing)
C. Lopez-Cajún (Mexico)
J.-P. Merlet (France)
M. Morlock (Germany)
A. Müller (Austria)
V. Parenti-Castelli (Italy)
A. Pott (Germany)
D. Pisla (Romania)
B. Roth (USA)
B. Siciliano (Italy)
P. Wenger (France)
C. Woernle (Germany)

Local Organizing Committee

Rocio Callupe (PUCP)
Elizabeth Villota (PUCP)
Miguel Castro Sánchez (UDEP)
Daniel Marcelo Aldana (UDEP)
Jorge Rodríguez (Chair IFToMM Peru)

Patronage

International Federation for the Promotion of Mechanism and Machine Science
University of Duisburg-Essen
Pontificia Universidad Católica del Perú
Universidad de Piura, Campus Lima

Preface

The present proceedings collect 25 papers that were selected after peer review for the Third Conference on Interdisciplinary Applications in Kinematics, held in Lima, Peru, during March 5–7, 2018.

The objective of the conference was to bring together researchers from different fields, where kinematics plays a key role. This includes not only theoretical fields where kinematics is traditionally established, but in particular applications in which kinematics might contribute new perspectives for practical applications. Examples are the areas of biomechanics, industrial machinery, molecular kinematics, railway vehicles and many others.

The participation of 34 researchers and 12 students from 7 countries shows the strong interest these topics find in the scientific community. Moreover, the site of the conference in Peru not only proved to be very successful, but also helped to foster the international scientific cooperation in this region, which has outstanding potentials.

Duisburg, Germany   Andrés Kecskeméthy
Duisburg, Germany   Francisco Geu Flores
Piura, Peru   Eliodoro Carrera
Lima, Peru   Dante A. Elias

Contents

Chapter 1
Optimal Lap Time for a Race Car: A Planar Multibody Dynamics Approach

Jorge Ambrósio and Luís Marques

Abstract   The optimal lap time for a race vehicle in a race track represents the minimum possible time for a vehicle to negotiate a complete round about the racetrack. In this work, a 2D multibody dynamic analysis program is developed to allow modelling and simulating the vehicle and racetrack scenario by implementing all the necessary kinematic constraints, which includes a steering constraint for a 4-wheel vehicle with a front steering axle and the necessary force elements including traction and braking and tyre-road contact. A trajectory optimization, on a given track with a prescribed geometry, which is obtained by a mix of the shortest and the least curvature paths with a speed profile optimized within limits for the longitudinal and lateral vehicle accelerations. A controller is developed to enforce that the vehicle follows the optimal path and the speed profile. This controller uses a preview distance, which allows for the vehicle to find its way even when it starts or goes off-track. The controller and the dynamic analysis program are demonstrated in a scenario in which the behavior of a race car in a realistic racetrack is analyzed.

1.1   Introduction

The optimal time lap problem has great interest, not only in racing but also in the design of different transportation activities. Knowing what a vehicle is capable of, at its maximum level of performance, allows to understand the behavior of the vehicle negotiating any racetrack, even before it is built. The search for the minimal time for a trajectory in a closed or open loop track has been addressed in particular as a problem in motorsports. Braghin et al. [6], Bertolazi et al. [4, 5], Lot and Bianco [12] or Sharp [18] propose different solution methods for both automotive and motorcycle racing while Otto and Seifried [15] address the problem in the context of crane trajectories.

J. Ambrósio (✉) · L. Marques
IDMEC, Instituto Superior Técnico, University of Lisbon, Av. Rovisco Pais 1, 1049 Lisbon, Portugal
e-mail: jorge.ambrosio@tecnico.ulisboa.pt

L. Marques
e-mail: luis.marques@tecnico.ulisboa.pt

Another part of the problem is to ensure the ability for the vehicle to follow the optimal trajectory. This issue has been addressed by Sharp [17], introducing the concept of previewing in the path following control, or by Thommyppillai et al. [19, 20], with enhancements of the optimal control.

The first step in the work presented here consists in developing a 2D multibody dynamics analysis program able to handle simple models of automobiles, by allowing using a limited number of bodies with revolute joints between the wheels and chassis. A steering constraint for the front wheels of the vehicle is developed and a tyre model, based on the Pacejka magic formula [16], is implemented to compute the lateral and longitudinal forces acting on each wheel of the vehicle. In the second step, a controller is developed using a Linear Quadratic Regulator based on the work of Antos and Ambrósio [2], which is supported in a simplified vehicle to follow a pre-determined trajectory. The vehicle is acted upon, exclusively, by the steering angle and by wheel torques. A preview distance for the control is implemented in this work in order not only to stabilize its action even when the car is off-track but also to better represent the realistic driver attitude. Furthermore, the controller is upgraded with the ability to follow a determined speed profile by acting on the traction and braking of the wheels.

Apart from the controlling methodology, an optimization of the trajectory and speed profile is carried based on the work by Cardamone et al. [7] and Braghin et al. [6]. A mixed shortest path and least curvature approach is used to find the optimal path while the speed profile is computed by using upper and lower bounds of the lateral and longitudinal accelerations that can be developed by the tires due to the tyre contact forces.

1.2   Multibody Dynamics Equations of Motion

A multibody system is, generally, composed by several types of rigid and flexible, bodies, connected by mechanical joints and acted upon by passive or active force elements. Let the planar multibody system of a vehicle be depicted in Fig. 1.1. The rear wheels are fixed to the chassis, making a single rigid body, while the front wheels are independent bodies pinned to the main chassis via revolute joints. The position and orientations of the n_b bodies of a multibody system are denoted by $\mathbf{q} = [\mathbf{q}_1^T \ldots \mathbf{q}_{n_b}^T]^T$ being the position $\mathbf{r}_i$ and orientation θ_i of each individual body i in vector $\mathbf{q}_i = [\mathbf{r}_i^T \ \theta_i]^T$. The equations of motion for a multibody system are [14]

$$\begin{bmatrix} \mathbf{M} & \mathbf{\Phi}_{\mathbf{q}}^T \\ \mathbf{\Phi}_{\mathbf{q}} & \mathbf{0} \end{bmatrix} \begin{bmatrix} \ddot{\mathbf{q}} \\ -\boldsymbol{\lambda} \end{bmatrix} = \begin{bmatrix} \mathbf{g} \\ \boldsymbol{\gamma} \end{bmatrix} \qquad (1.1)$$

where $\mathbf{\Phi}_{\mathbf{q}}$ is the Jacobian matrix of the kinematic constraints, $\mathbf{M}$ is the system mass matrix, $\boldsymbol{\lambda}$ is the vector of unknown Lagrange multipliers, $\ddot{\mathbf{q}}$ is the acceleration vector, $\mathbf{g}$
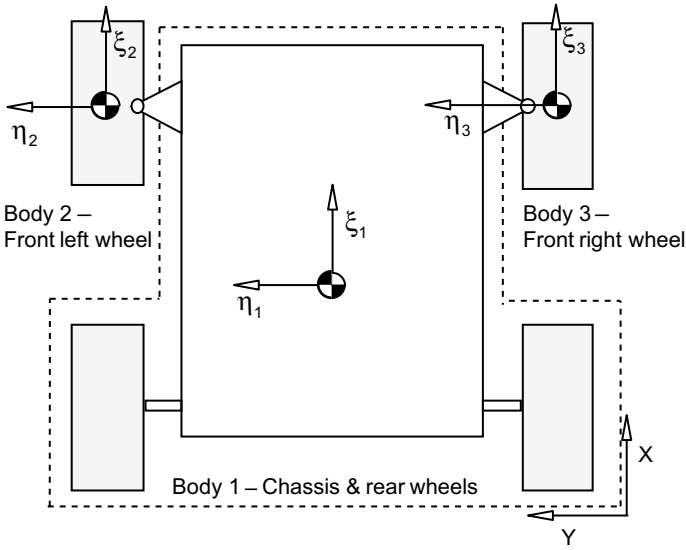
Fig. 1.1 Planar multibody model of the road vehicle

the vector of applied forces and $\boldsymbol{\gamma}$ the vector with the right-hand-side of the kinematic acceleration equations.

1.2.1 Kinematic Constraints

For the vehicle multibody model considered in this work the kinematic constraints are associated to the revolute joints between the front wheels and the chassis, corresponding to the knuckle to wheel connection, and to the front wheel steering. The formulation of the revolute joint constraints are straightforward, as described in Nikravesh [14]. The steering constraints are of fundamental importance for the vehicle dynamics being presented hereafter.

The steering constraint is aimed to control the steering angle between each front wheel and the chassis. With reference to Fig. 1.2, the steering kinematic constraint equation for each wheel is written as

$$^{(str,1)}\boldsymbol{\Phi} = (\theta_w - \theta_c) - \delta_{str} = 0 \tag{1.2}$$

where θ_w is the angular position of the wheel k, θ_c is the angular position of the chassis and δ_{str} is the desired steering angle, as shown in Fig. 1.2.

When an automobile is negotiating a corner at a slow speed, there is a relation between the inner and outer wheel angles, the Ackerman geometry, as the arc of circle
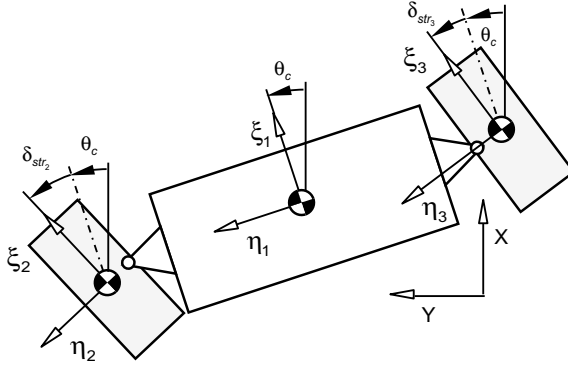
Fig. 1.2 Steering of the front wheels
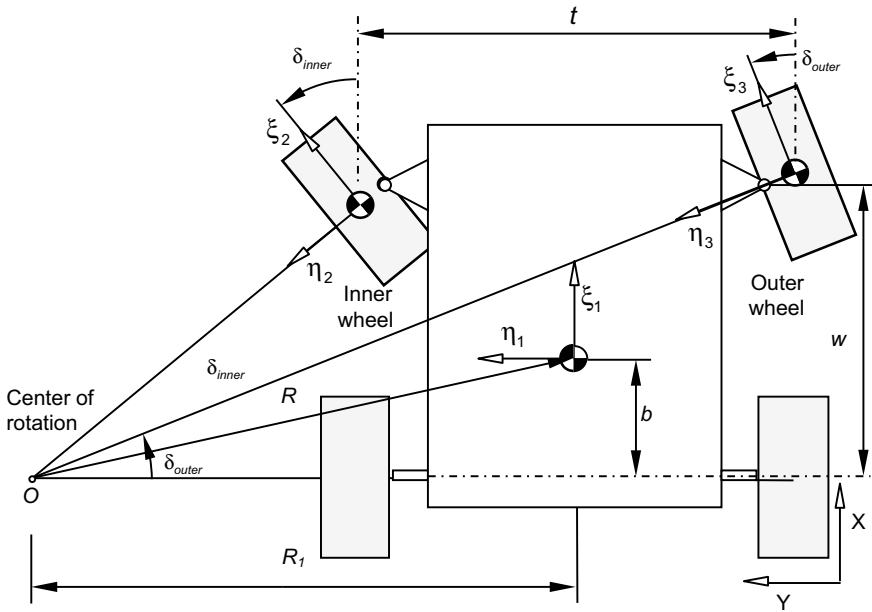
Fig. 1.3 Steering of a vehicle according to the Ackermann geometry

travelled by each wheel implies a different steering angle for each wheel in order to have to turn slip-free [11]. With reference to Fig. 1.3, the Ackerman condition is [9]:

$$\delta_{inner} = \arctan \frac{w}{R_1 - t/2}; \quad \delta_{outer} = \arctan \frac{w}{R_1 + t/2} \tag{1.3}$$

where w is the vehicle wheelbase, t is the vehicle track, δ_{inner} and δ_{outer} are the angle of the inner and outer wheels, respectively, and R_1 is the distance between the turning center and the point of the rear axle at the vehicle half-track width.

The steering angle of the vehicle is mapped into the inner and outer steering angles according to Eq. (1.3). Without lack of generality, let the left wheel steering angle, included in the steering constraint expressed by Eq. (1.2), be the output of the steering control described in this work. Depending on if, the left wheel is the inner or the outer wheel in the curve, the steering angle of the right wheel is depicted by using Eq. (1.3) to obtain the steering angle compatible with the Ackermann steering geometry.

Note that real vehicles do not necessarily fulfil the conditions of the Ackermann geometry, and race cars much less. During steering the normal forces in the outside wheel are higher, or much higher, than those on the inside wheel. An oversteering bias of the outside wheel is used to overcome the limitations of the steering ability of the interior wheel, which in some extreme maneuvers becomes unloaded. The model used here is planar and the variation on the normal wheel load not represented. Therefore, the considerations on the application of the Ackerman geometry have no consequences.

1.2.2 Tire Forces on the Wheels

The automotive tires are the only means to transfer forces between the vehicle and the road [9]. The tyre is a complex composite structure made up of several rubber layers and reinforcement with steel chords, whose contact mechanics can be represented by a large number of models [8, 10, 16]. In a spatial configuration the tyre kinematics is related to the contact forces, shown in Fig. 1.4a, using modelling constitutive laws that include the tyre and road material and geometric properties.

The vehicle model considered in this work is planar and several simplifying assumptions are used for the kinematics of the tyre shown in Fig. 1.4b: (1) the camber angle is null; (2) The vertical dynamics of the tyre is neglected, being the normal load assumed constant; (3) The out-of-plane velocity components are neglected.

The tyre longitudinal and lateral forces and self-aligning moment as function of the slip angle α and slip ratio s, which re given by [10]

$$\alpha = \arctan\left(\dot{r}_\xi / \dot{r}_\eta\right); \quad s = \left(R_{eff}\,\omega_w - \dot{r}_\xi\right) / \max\left(\left|\dot{r}_\xi\right|, \left|R_{eff}\,\omega_w\right|\right) \qquad (1.4)$$

where $\dot{r}_\xi$ and $\dot{r}_\eta$ are the components of the wheel velocity vector $\dot{\mathbf{r}}$ expressed in the wheel coordinate system, R_{eff} is the tyre radius and ω_w the wheel spinning velocity, to be discussed in Sect. 1.2.3. The force components and self-aligning moment of the wheel are given by Pacejka Magic Formula, written for pure slip conditions as [16]

(a)
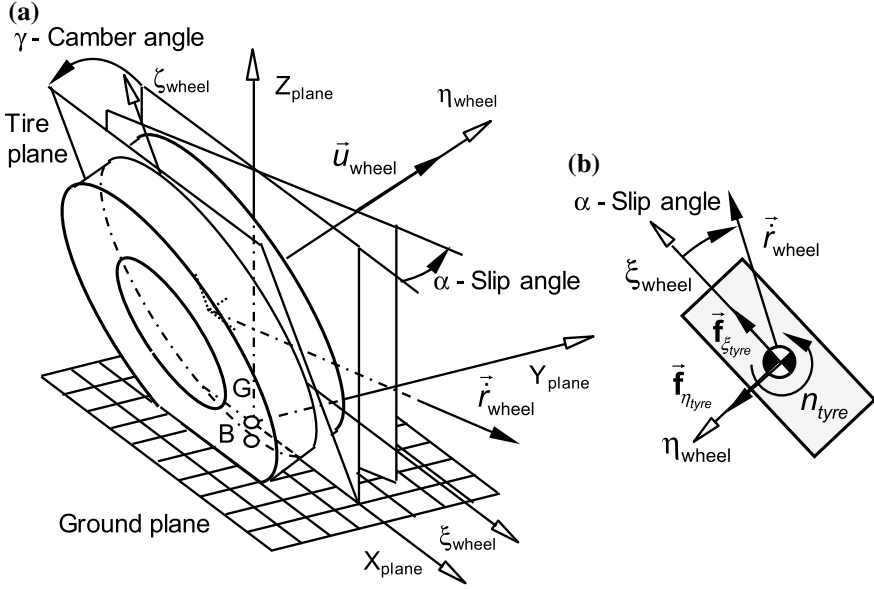
Fig. 1.4 **a** Spatial tyre coordinate system and velocity vectors; **b** Planar tyre coordinate system, velocity vector and road interaction forces

$$f_{\xi_p} = D_x \sin\{C_x \arctan[B_x s_x - E_x(B_x s_x - \arctan(B_x s_x))]\} + S_{Vx} \qquad (1.5)$$

$$f_{\eta_p} = D_y \sin\{C_y \arctan[B_y \alpha_y - E_y(B_y \alpha_y - \arctan(B_y \alpha_y))]\} + S_{Vy} \qquad (1.6)$$

$$n_p = -t_p f_{\eta_p} + D_r \cos[C_r \arctan(B_r \alpha_r)] \qquad (1.7)$$

in which B is the stiffness factor, C the shape factor, D the peak value, E the curve factor, S_H the horizontal shift and S_V the vertical shift. Other quantities in Eqs. (1.5–1.7) are $s_x = s + S_{Hx}$, $\alpha_y = \alpha + S_{Hy}$, $\alpha_t = \tan\alpha + S_{Ht}$, $\alpha_r = \tan\alpha + S_{Hf}$ and $t_p = D_t \cos\{C_t \arctan[B_t \alpha_t - E_t(B_t \alpha_t - \arctan(B_t \alpha_t))]\} \cos\alpha$. In all quantities the subscript p means pure slip conditions. When combined slip exists, i.e., when both the slip angle and the slip ratio are not null, the tyre forces are

$$f_\xi = G_{x\alpha} f_{\xi_p} \qquad (1.8)$$

$$f_\eta = G_{ys} f_{\eta_p} + S_{Vys} \qquad (1.9)$$

$$n = D_r \cos(C_r \arctan\alpha_{r,eq}) - t(f_\eta - S_{Vys}) + C_s f_\xi \qquad (1.10)$$

Fig. 1.5 Wheel rotation with the identification of applied forces and angular velocity
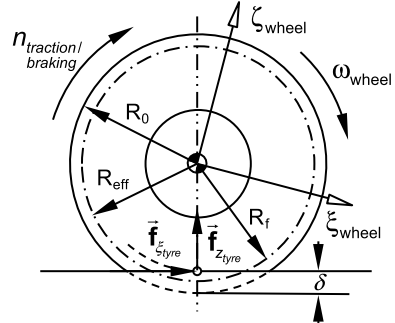
with $\alpha_{r,eq} = B_r \sqrt{\alpha_r^2 + \left(K_x \big/ K_y\right)^2 s^2} \mathrm{sgn}\alpha_r$, $\alpha_{t,eq} = B_t \sqrt{\alpha_t^2 + \left(K_x \big/ K_y\right)^2 s^2} . \mathrm{sgn}\alpha_t$ and $t = D_t \cos\{C_t \arctan[\alpha_{t,eq} - E_t(\alpha_{t,eq} - \arctan\alpha_{t,eq})]\} \cos\alpha$. Note that the complete Pacejka Magic Formula also includes shape parameters, not considered here, to adjust the tyre constitutive model to specific operational conditions [16].

1.2.3 Wheels Angular Equations of Motion

One of the particular aspects of tyre/road interaction force modelling is the need to evaluate the slip ratio that involves the wheel spinning dynamics, which occurs out of the *XY* plane in which the complete vehicle dynamics takes place. The approach followed here is to consider that the wheel spin takes place in the wheel local $\xi\zeta$ plane, as shown in Fig. 1.5, being completely decoupled from the vehicle planar dynamics.

Each wheel of the vehicle has a traction or braking moment, $n_{traction/braking}$, and the tyre longitudinal force, f_ξ, applied, being its angular equation of motion given as

$$I_{wheel} \, \dot{\omega}_{wheel} = n_{\substack{traction/ \\ braking}} - f_{\xi_{tyre}} R_{eff} \qquad (1.11)$$

in which I_{wheel} is the wheel moment of inertia about the direction η and $\dot{\omega}_{wheel}$ is the wheel spinning acceleration. The normal wheel/road contact force, f_{ztyre}, is assumed to be a fourth of the vehicle weight, depending on the rear-front weight distribution of the vehicle, and constant throughout the planar vehicle dynamic analysis.

The wheel radius effective radius, R_{eff}, has a precise definition in contact tyre mechanics that involves the tyre radial stiffness definition and the tyre undeformed radius. In what follows, the tyre effective radius is approximated by the tyre undeformed radius, thus neglecting the vertical tyre deformation.
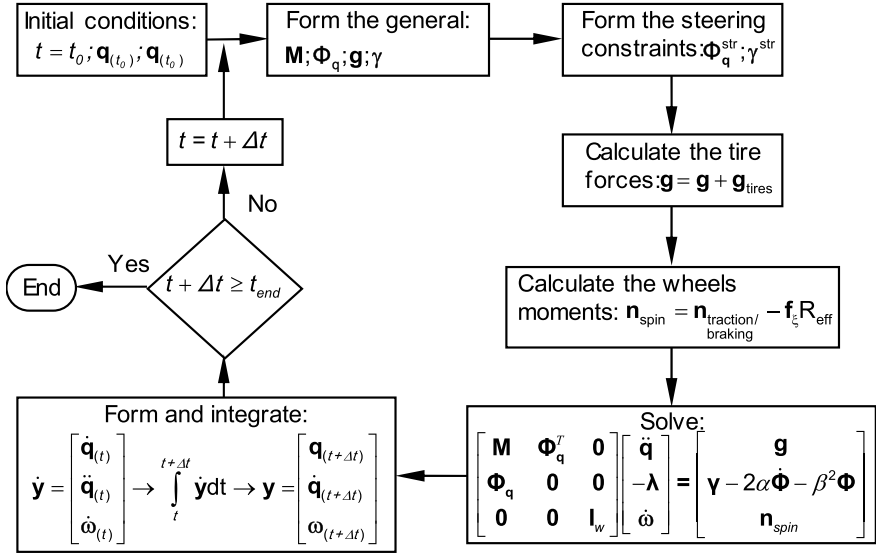
Fig. 1.6 Flowchart for the numerical solution of the multibody system and vehicle wheels angular equations of motion

1.2.4 Numerical Solution of the Equations of Motion

The equations of motion of the multibody system, given by Eq. (1.1), and of the vehicle wheels, each one written as Eq. (1.11), have to be solved and integrated in time. This numerical process is prone to the accumulation of numerical errors in the positions and velocities because the position and velocity constraint equations are not explicitly used. The Baumgarte constraint violation method is used to maintain the constraint violations under workable limits [3]. The complete flowchart for the solution of the system equations of motion and time integration of the accelerations and velocities is depicted in Fig. 1.6.

The steering angle, required for updating the steering constraints, and the traction/braking moments, required for the evaluation of the wheels moments, may be prescribed functions of time or, as in this work, the output of a controller designed to steer the vehicle in a prescribed trajectory.

1.3 Vehicle Planar Model

The Lancia Stratos is an Italian sports car from the 1970's which served as the base vehicle for the successful Lancia that competed and won races in the world rally championship. The Lancia Stratos is a rear wheel driving vehicle, which means

Fig. 1.7 General dimensions of the road vehicle (in mm)
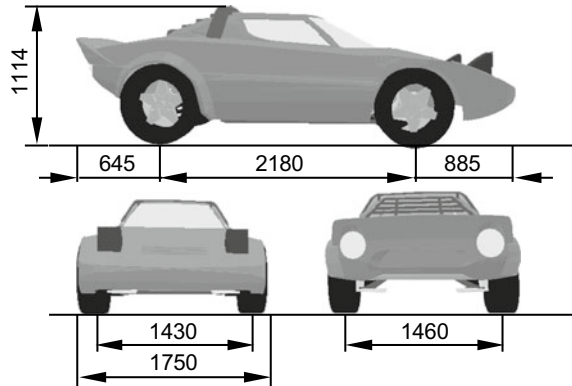
Table 1.1 Inertia and initial kinematic data for the road vehicle planar model

Body	Description	Mass (Kg)/Inertia (Kg/m^2)	Initial position x(m)/y(m)/θ(º)
1	Chassis and rear wheels	783/750	0.000/0.000/0.000
2	Front-left wheel	29/10	1.250/0.715/0.000
3	Front-right wheel	29/10	1.250/−0.715/0.000

Table 1.2 Kinematic joints types and geometric data

Joint	Description	Body i	Body j	$(\xi/\eta)^{P_i}$	$(\xi/\eta)^{P_j}$
1	Revolute	1	2	1.250/0.700	0.000/−0.015
2	Revolute	1	3	1.250/−0.700	0.000/0.015
3	Steering	2	1		
4	Steering	3	1		

that only the rear wheels can produce traction, and is a front wheel steering car. Furthermore, it has front double A-Arm suspension and rear McPherson suspension. The vehicles main dimensions are described in Fig. 1.7, being the most important for the purpose of this work the wheelbase, with 2.180 m, the front track, with 1.430 m, and the rear track, with 1.460 m.

The simplified multibody system for the Lancia Stratos used in the 2D dynamics analysis program is adapted from its spatial counterpart described by Ambrosio and Gonçalves [1]. The multibody system, composed by 3 bodies, is shown in Fig. 1.1 and the inertia and geometric data and kinematic joints data shown in Tables 1.1 and 1.2. The Pacejka Magic Formula model for the tires requires that the parameters used in Eqs. (1.5–1.10) are obtained using the formulation shown in Appendix 1.1. The tires used are the Hoosier 13 × 8 slick racing tyre, with the data presented in Appendix 1.2.

(a)
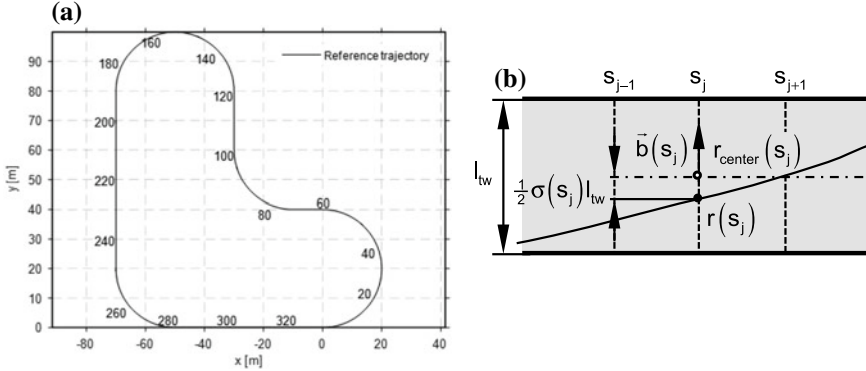
Fig. 1.8 Example of a track geometry: **a** Centerline trajectory with arc-length denoted; **b** Discretized track model with variation of control point inside boundary

1.4 Vehicle Prescribed Trajectory

The required vehicle trajectory, deemed as track reference, is described as a collection of line segments, which may be either linear or curve. This path, is defined by a collection of n_p points on the path centerline as function of a parameter s given by.

$$(x_{tj}, y_{tj}) = (x(s_j), y(s_j)), \quad j = 1, \ldots, n_p \tag{1.12}$$

where the parameter s_j is the total arc length from the origin of the path up to point P_j. In order to have a continuous description of the track reference, the n_p points are interpolated by using a cubic spline, denoted as $({}^{sp}x(s), {}^{sp}y(s))$, as that illustrated in Fig. 1.8a. The track reference angle for any given point is:

$$\varepsilon_t(s) = \arctan\left(\frac{\delta^{sp}y(s)}{\delta s}, \frac{\delta^{sp}x(s)}{\delta s}\right) \tag{1.13}$$

The curvature of the track reference, at a given point, is provided by the relation

$$k(s) = \frac{1}{R(s)} = \frac{{}^{sp}x'(s){}^{sp}y''(s) - {}^{sp}y'(s){}^{sp}x'(s)}{\sqrt{{}^{sp}x'(s)^2 + {}^{sp}y'(s)^2}} \tag{1.14}$$

where ${}^{sp}y'(s)$ and ${}^{sp}y''(s)$ are the first and second parametric derivatives of the parametric curve with respect to parameter s.

With the track centerline and the track width l_w, any vehicle trajectory is acceptable, provided that it stays inside the track. Referring to Fig. 1.8b any acceptable vehicle trajectory is defined by nodal control points, whose location is written as

$$\mathbf{r}(s_j) = \mathbf{r}_{center}(s_j) + \tfrac{1}{2}l_{tw}\sigma(s_j)\mathbf{b}(s_j), \quad j = 1, \ldots, n_p \tag{1.15}$$
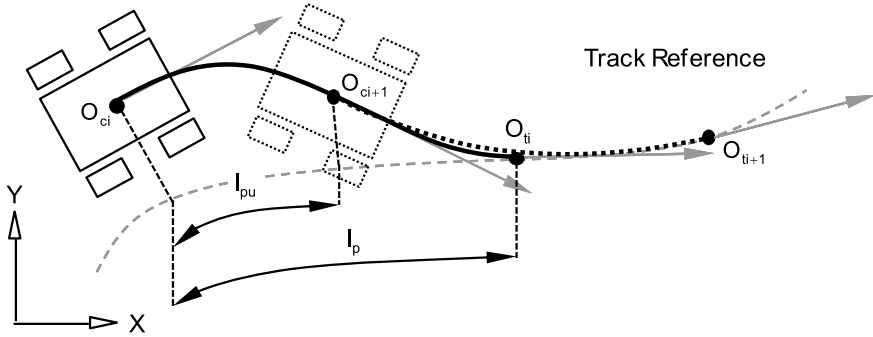
Fig. 1.9 Schematic representation of the preview distance and trajectory

where $\sigma(s_j) \in [-1, +1]$ and vector $\mathbf{b}(s_j)$ is normal to the track centerline tangent vector in each nodal point, as observed in Fig. 1.8b. Although the track width is considered constant in this work, such restriction is not strictly necessary.

1.5 Vehicle Trajectory and Speed Control

The controller implemented here is based on the work of Antos and Ambrósio [2]. In the original controller does not account for previewing or traction and braking actions. Here, the preview distance used to control the vehicle steering, shown in Fig. 1.9, is not only a natural way of driving but also a way to smooth the vehicle steering. A controller with previewing is generally more stable, especially when the vehicle is far from the prescribed position. Instead of trying to find the closest point in the trajectory, the controller looks for a point further ahead, O_t, using a predefined preview distance. From the current vehicle position, O_c, and orientation, the controller computes a new trajectory for the vehicle to follow by using a cubic polynomial.

Besides the control of the trajectory it is also necessary to control the vehicle velocity, deemed here as speed profile. Unlike the previewing method, the speed profile controller is a modification of the original controller by Antos and Ambrósio [2], although it is still a Linear Quadratic Regulator (LQR). To perform the best time in a race track there is the need to accelerate and brake the car, which requires the controller to ensure that the vehicle follows a predefined speed profile for the longitudinal velocity of the vehicle. For a detailed description of the controller implemented the interested reader is directed to the work by Marques [13] in which the methodology is presented and demonstrated.
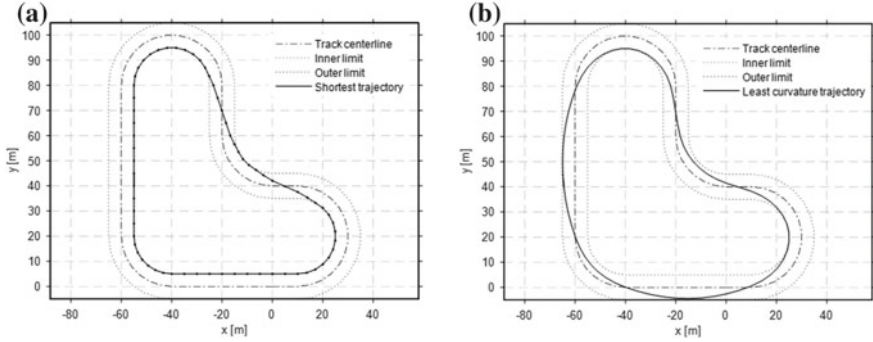
Fig. 1.10 Optimal trajectories about a speed track: **a** Shortest trajectory; **b** Least curvature trajectory

1.6 The Optimal Time Lap Problem

The optimal time lap problem has been addressed by different authors when dealing with vehicle competition [4–7]. The optimal trajectory consists in finding the best compromise between the shortest trajectory and the least curvature trajectory, which allows the vehicle to have higher velocities while turning. The best combination between trajectory and speed profile is the final goal of the process.

The shortest trajectory, shown in Fig. 1.10a, is the shortest possible line that can be described within the right and left limits of the track. This seems to be a good manner of minimizing the lap time, since the travelling distance is minimized. The shortest trajectory is found by minimizing the total trajectory arc-length, approximated by the sum of the distances between consecutive points of a discretized trajectory. The shortest trajectory optimal problem is stated as

$$\min F_{st}\big(\sigma_j\big) = \sum_{k=1}^{n_k-1} \left[({}^{sp}x(s_{k+1}) - {}^{sp}x(s_k))^2 + ({}^{sp}y(s_{k+1}) - {}^{sp}y(s_k))^2 \right]$$
$$s.t. \ -1 \leq \sigma_j \leq 1, \quad j = 1, \ldots, n_p \tag{1.16}$$

in which the track trajectory defined by n_p control points, as in Eq. (1.12), is interpolated using cubic splines and, afterwards, discretized with n_k points, with $n_k \gg n_p$. The n_p variables of the optimization problem are defined in Eq. (1.15).

The shortest trajectory inside the race track may not allow the vehicle to reach high speeds because it usually leads to trajectory segments with high curvature, which induce higher lateral accelerations on the car. The least curvature trajectory, depicted in Fig. 1.10b, is an alternative approach that allows the vehicle to reach higher velocities while cornering. Taking into account Eq. (1.14), the least curvature trajectory, defined as the optimal problem

$$\min F_{lc}(\sigma_j) = \sum_{k=1}^{n_k-1} \|k(s_k)\|^2 = \sum_{k=1}^{n_k-1} \left\| \frac{^{sp}x'(s_k)\,^{sp}y''(s_k) - ^{sp}y'(s_k)\,^{sp}x'(s_k)}{\sqrt{^{sp}x'(s_k)^2 + ^{sp}y'(s_k)^2}} \right\|^2 \tag{1.17}$$
$$s.t. \ -1 \le \sigma_j \le 1, \quad j = 1, \ldots, n_p$$

Assuming that the vehicle has its maximum lateral acceleration limited by the tyre grip, it is clear that when the curvature is lower, the velocity can reach higher values. Hence, with higher velocities lower lap times may be achieved. The least curvature trajectory length is longer than the shortest trajectory but it allows for higher velocities during curving. As none of the two trajectories is optimal, Braghin [6] suggests that a combination of the two may have good results and reduce the lap time by dividing the problem into path optimization and speed profile optimization, and by solving the problem iteratively. Let the best trajectory for the vehicle be a linear combination of the shortest and least curvature trajectories, defined as

$$\mathbf{r}(\tau, s_j) = \mathbf{r}_{center}(s_j) + \tfrac{1}{2}l_{tw}\big[(1-\tau)\sigma_{st}(s_j) + \tau\,\sigma_{lc}(s_j)\big]\mathbf{b}(s_j), \quad j = 1, \ldots, n_p \tag{1.18}$$

where $\sigma_{st}(s_j)$ are the optimal parameters for the shortest trajectory and $\sigma_{lc}(s_j)$ for the least curvature. The weight τ is now the variable that needs to be evaluated.

The minimal time lap is found by solving the optimal speed profile that leads to the lowest time required to complete track, subjected to limits in the lateral forces that can be developed by the tires, i.e., maximum lateral acceleration and traction and braking limits. The optimal velocity profile is described by the optimal problem

$$\min F(\tau, v(s_j)) = \sum_{k=0}^{n_k-1} \Delta t_k = \sum_{k=0}^{n_k-1} \frac{(s_{k+1} - s_k)}{\tfrac{1}{2}\big[^{sp}v(s_{k+1}) + ^{sp}v(s_k)\big]}$$
$$s.t. \ a_{long_{min}} \le ^{sp}a_{long}(s_k) \le a_{long_{max}}$$
$$0 \le \big|^{sp}a_{lat}(s_k)\big| \le a_{lat_{max}}$$
$$v_{min,\,j} \le ^{sp}v(s_k) \le v_{max,\,j} \tag{1.19}$$

where it is implied that a discretization of the vehicle velocity profile obtained by spline interpolation of the vehicle velocities on the n_p control points is done. The same type of discretization is implied for the longitudinal acceleration $^{sp}a_{long}(s_k)$ and for the lateral acceleration $^{sp}a_{lat}(s_k)$. The lower limit for the longitudinal acceleration is associated with the vehicle braking capabilities while the higher limit is associated to its traction capabilities. The higher limit for the lateral acceleration is associated to the maximum cornering acceleration of the vehicle while the velocity limits are associated with the maximum velocity that the vehicle can develop and the minimum velocity at which it is allowed to travel before stalling.

The optimal trajectory for the racetrack, which is the solution of the optimal problem described by Eq. (1.19) being shown in Fig. 1.11a, corresponds to the optimal weight, in Eq. (1.18), of $\tau = 0.00025$. This is a geometry for the trajectory
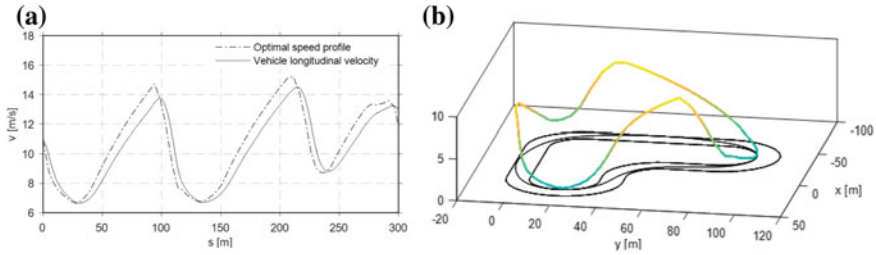
Fig. 1.11 Optimal velocity profile for optimal trajectory **a** Velocity versus distance travelled; **b** Velocity along the trajectory

Table 1.3 Lap times for the different trajectories of the demonstration track

Reference of trajectory	Lap time [s]
Centerline	37.15
Shortest trajectory	31.33
Least curvature trajectory	28.95
Optimal trajectory	28.54

similar to that of the least curvature. The optimal speed profile, for the optimal trajectory is depicted in Fig. 1.11b. The solution of the optimal problem is obtained considering limits in the longitudinal accelerations of 1.5 m/s^2, for traction, and $-$5.0 m/s^2, for braking. The limit of the lateral acceleration for the problem is 2.7 m/s^2.

The optimal speed profiles for the different trajectories considered in this work are also calculated. To each one of these trajectories corresponds the minimal lap times shown in Table 1.3. It is observed, as expected, that the lowest lap times are obtained for the optimal and least curvature trajectories with 28.54 s and 28.95 s, respectively.

1.7 Demonstration

The controller developed and implemented in this work is used to steer the vehicle model, presented in Sect. 1.3, along the optimal trajectory in the racetrack while following the optimal velocity profile. Figure 1.11a shows that the velocity profile effectively imposed by the controller is close to that of the optimal velocity profile, but without matching it perfectly. It is observed in Fig. 1.12 that the controller is able to steer the vehicle to closely follow the prescribed trajectory.

A better form to appraise the ability of the controller to steer the vehicle along the track is to measure the errors in the lateral position and alignment of the vehicle with respect to the prescribed trajectory. Figure 1.13 shows the lateral and angular errors as well as the steering angle. The controller has a smooth behavior in terms

Fig. 1.12 Optimal trajectory corresponding to the best velocity profile and actual trajectory followed by the vehicle with the controller
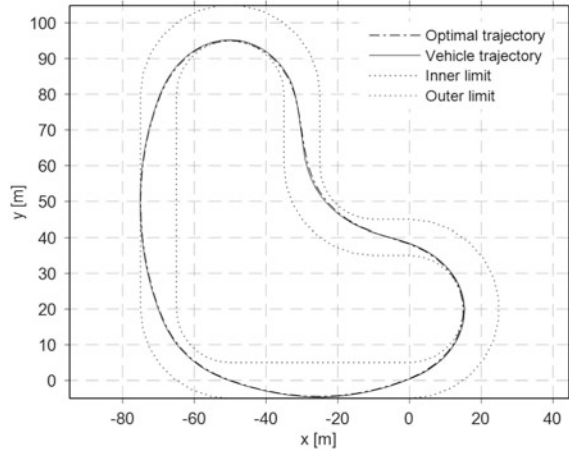
of the correction of the position errors with respect to the prescribed trajectory, but presents a, somehow, 'energetic' steering angle evolution.

It takes 30.7 s for the vehicle to complete the entire lap, which is different from the expected 28.54 s of optimal lap time. This difference can be explained by the constant trajectory errors correction by the controller, which does not ensure that the vehicle trajectory is the exact optimal trajectory, and by the difference between the optimal velocity profile and the actual velocity profile enforced by the controller.

1.8 Conclusions

The optimal time lap problem for a race vehicle along a racetrack has been addressed in this work by developing a methodology to obtain the optimal trajectory and velocity profiles for the vehicle and by developing and implementing a suitable planar vehicle model and a control strategy. Based on a multibody dynamics methodology the planar vehicle model developed in this work has all the features required to describe its longitudinal and lateral dynamics being the wheel/tyre dynamics handled by equations of motion that are uncoupled from those of the remaining vehicle system. The Pacejka magic formula tyre model is used in the process assuming a constant normal force on the tyre and a null camber angle. A linear quadratic regulator controller is used to steer the vehicle along a prescribed trajectory in the racetrack and to enforce a prescribed velocity profile. The ability to use previewing of the trajectory in the controller is implemented. The optimal time lap problem is solved by finding the optimal trajectory that can be traveled at the highest velocity. The problem is divided in two sub-problems, solved iteratively: The trajectory is obtained as a weighted sum of the shortest and the least curvature trajectories along the track, in which the weighting factor is the design variable. The velocity profile is obtained,

Fig. 1.13 Steering angle
and lateral and angular errors
along the track
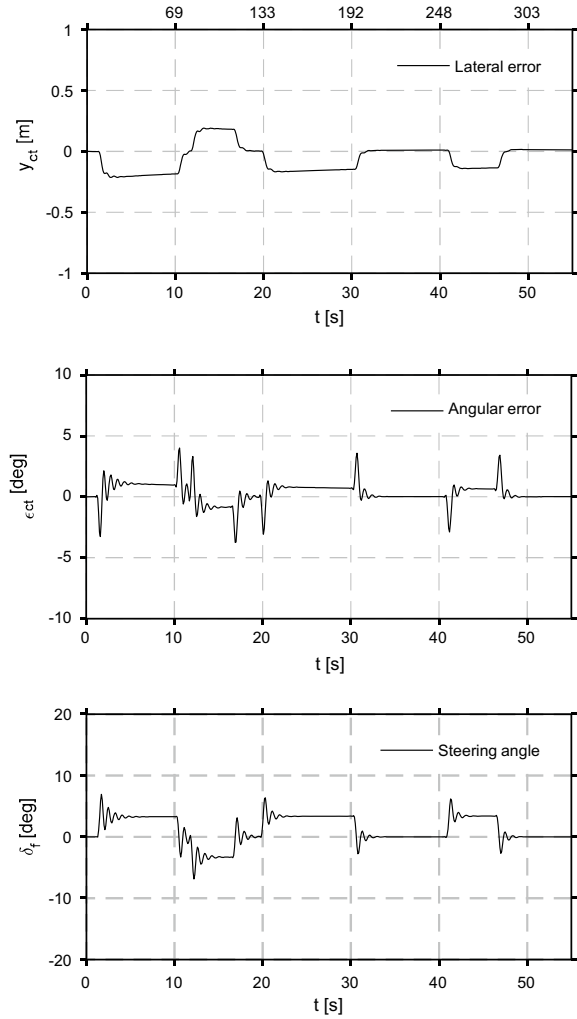
for each trajectory, as the velocity that the vehicle can handle without exceeding its physical limits, i.e., with limitations on its lateral accelerations and braking and traction abilities.

The demonstration of the methodology proposed here shows the feasibility of the strategy pursued and some of its actual limitations. All in all, it was possible to steer the vehicle around the racetrack following closely the optimal trajectory with a velocity profile close to the optimal one. The actual time lap obtained in the demonstration is 7.5% higher than the optimal time lap. Such difference is associated to the controlled steering actions that appear to be too 'energetic' leading to constant small changes in the steering angle. Although the controller forces the vehicle to

follow a prescribed velocity profiles, this is never completely matched leading to a travel velocity always slightly lower than the prescribed velocity. It is also observed that the preview strategy implemented in the controller needs to be improved. Future work addressing this problem is expected to include: the identification of a control strategy that leads to smoother steering and traction/braking actions, eventually by using improved gains for the LQR control algorithm; a suitable strategy for the trajectory preview with improved compatibility with the remaining steering control actions; the implementation of a spatial demonstration scenario in which the complete tyre mechanics plays a role, i.e., camber angle, variation of the normal tyre load and three dimensional track geometry.

Appendix 1.1: Pacejka Magic Formula Parameters

The Pacekja Magic Formula coefficients appearing in Eqs. (1.5) through (1.10) need to be evaluated based on the tyre specific data. The normalized vertical load increment, df_z, calculated as

$$df_z = (f_z - f'_{z0})/f'_{z0} \tag{1.20}$$

For the longitudinal force, in pure slip conditions, evaluate the parameters:

$$
\begin{aligned}
\mu_x &= (p_{Dx1} + p_{Dx2}\, df_z)\lambda^*_{\mu x} \\
K_x &= f_z\,(p_{Kx1} + p_{Kx2}\, df_z)\exp(p_{Kx3}\, df_z)\,\lambda_{Kx} \\
C_x &= p_{Cx1}\,\lambda_{Cx} \\
D_x &= \mu_x\, f_z\, \zeta_1 \\
B_x &= K_x/(C_x D_x) \\
E_x &= (p_{Ex1} + p_{Ex2}\, df_z + p_{Ex3}\, df_z^2)(1 - p_{Ex4}\,\mathrm{sgn}s_x)\lambda_{Ex} \\
S_{Hx} &= (p_{Hx1} + p_{Hx2}\, df_z)\lambda_{Hx} \\
S_{Vx} &= f_z(p_{Vx1} + p_{Vx2}\, df_z)\lambda_{Vx}\,\lambda'_{\mu x}\,\zeta_1
\end{aligned}
\tag{1.21}
$$

For the lateral force, in pure slip conditions, evaluate the parameters:

$$
\begin{aligned}
\mu_y &= (p_{Dy1} + p_{Dy2}\, df_z)\lambda^*_{\mu y} \\
K_y &= p_{Ky1}\, f'_{z0}\,\sin\!\big[p_{Ky4}\arctan\big(f_z/(p_{Ky2}\, f'_{z0})\big)\big]\lambda_{Ky\alpha}\,\zeta_3 \\
C_y &= p_{Cy1}\,\lambda_{Cy} \\
D_y &= \mu_y\, f_z\, \zeta_2 \\
B_y &= K_y/(C_y D_y) \\
E_y &= (p_{Ey1} + p_{Ey2}\, df_z)(1 - p_{Ey3}\,\mathrm{sgn}\alpha_y)\lambda_{Ey}
\end{aligned}
$$

$$S_{Hy} = (p_{Hy1} + p_{Hy2}\, df_z)\lambda_{Hy} + \zeta_4 - 1$$
$$S_{Vy} = f_z(p_{Vy1} + p_{Vy2}\, df_z)\lambda_{Vy}\, \lambda'_{\mu y}\, \zeta_4 \qquad (1.22)$$

For the aligning torque, in pure slip conditions, evaluate the parameters:

$$C_r = \zeta_7$$
$$D_r = f_z\,(q_{Dz6} + q_{Dz7}\, df_z)R_0\,\lambda_r + \zeta_8 - 1$$
$$B_r = (q_{Bz9}\,\lambda_{Ky}/\lambda_{\mu y} + q_{Bz10}\,B_y C_y)\zeta_6$$
$$C_t = q_{Cz1}$$
$$D_t = f_z(q_{Dz1} + q_{Dz2}\, df_z)R_0\,\lambda_t\,\zeta_5/f'_{z0}$$
$$B_t = (q_{Bz1} + q_{Bz2}\, df_z + q_{Bz3}\, df_z^2)\lambda_{Ky}/\lambda_{\mu y}$$
$$E_t = (q_{Ez1} + q_{Ez2}\, df_z + q_{Ez3}\, df_z^2)\big[1 + \tfrac{2}{\pi} q_{Ez4} \arctan(B_t C_t\, \alpha_t)\big]$$
$$S_{Ht} = q_{Hz1} + q_{Hz2}\, df_z$$
$$S_{Hf} = S_{Hy} + S_{Vy}/K_y \qquad (1.23)$$

For the longitudinal force, in combined slip conditions, evaluate the parameters:

$$B_{x\alpha} = r_{Bx1}\, \cos[\arctan(r_{Bx2}\, s)]\lambda_{x\alpha}$$
$$C_{x\alpha} = r_{Cx1}$$
$$E_{x\alpha} = r_{Ex1} + r_{Ex2}\, df_z$$
$$S_{Hx\alpha} = r_{Hx1}$$
$$G_{x\alpha0} = \cos\{C_{x\alpha} \arctan[B_{x\alpha} S_{Hx\alpha} - E_{x\alpha}(B_{x\alpha} S_{Hx\alpha} - \arctan(B_{x\alpha} S_{Hx\alpha}))]\}$$
$$G_{x\alpha} = \cos\{C_{x\alpha} \arctan[B_{x\alpha}\alpha_s - E_{x\alpha}(B_{x\alpha}\alpha_s - \arctan(B_{x\alpha}\alpha_s))]\}/G_{x\alpha0} \qquad (1.24)$$

For the lateral force, in combined slip conditions, evaluate the parameters:

$$B_{ys} = r_{By1}\, \cos\big[\arctan(r_{By2}(\alpha - r_{By3}))\big]\lambda_{ys}$$
$$C_{ys} = r_{Cy1}$$
$$E_{ys} = r_{Ey1} + r_{Ey2}\, df_z$$
$$D_{Vys} = \mu_y\, f_z\,(r_{Vy1} + r_{Vy2}\, df_z) \cos\big[\arctan(r_{Vy4}\,\alpha)\big]\zeta_2$$
$$S_{Hys} = r_{Hy1} + r_{Hy2}\, df_z$$
$$S_{Vys} = D_{Vys}\, \sin\big[r_{Vy5} \arctan(r_{Vy6}\, s)\big]\lambda_{Vys}$$
$$s_s = s + S_{Hys}$$
$$G_{ys0} = \cos\{C_{ys} \arctan\big[B_{ys} S_{Hys} - E_{ys}(B_{ys} S_{Hys} - \arctan(B_{ys} S_{Hys}))\big]\}$$
$$G_{ys} = \cos\{C_{ys} \arctan\big[B_{ys}s_s - E_{ys}(B_{ys}s_s - \arctan(B_{ys}s_s))\big]\}/G_{ys0} \qquad (1.25)$$

In the current use of the Pacejka Magic Formula it is assumed that the camber angle of the tyre is null and that the spin has small values. Consequently the turn-slip

Table 1.4 Basic Hoosier slick tire parameters

Parameters description	Symbol	Value
Nominal load [N]	f'_{z0}	1000
Unloaded tyre radius [m]	R_0	0.2667
Pressure [N/m^2]	p	14

Table 1.5 Tyre force coefficients for Hoosier slick racing tyre

Longitudinal force coefficients for pure slip

p_{Cx1}	−1.52584385	p_{Dx1}	−2.34680276	p_{Dx2}	−0.01901445	p_{Ex1}	0.03423689
p_{Ex2}	−0.02047066	p_{Ex3}	0.08026912	p_{Ex4}	12.94786189	p_{Kx1}	55.78576126
p_{Kx2}	−22.91717877	p_{Kx3}	0.78407478	p_{Hx1}	−0.00218633	p_{Hx2}	−0.00125411
p_{Vx1}	0.09011039	p_{Vx2}	0.13576578				

Lateral force coefficients for pure slip

p_{Cy1}	1.41805682	p_{Dy1}	−2.34564200	p_{Dy2}	0.58326693	p_{Dy3}	2.24951822
p_{Ey1}	−0.32926304	p_{Ey2}	−0.85752501	p_{Ey3}	−0.14258620	p_{Ey4}	−2.69179310
p_{Ey5}	0.58076203	p_{Ky1}	44.0025828	p_{Ky2}	3618.54091	p_{Ky3}	45.3363303
p_{Ky4}	3838.76713	p_{Ky5}	2530.72180	p_{Ky6}	2.12263754	p_{Ky7}	2.14394481
p_{Vy1}	−0.04075721	p_{Vy2}	0.03378133	p_{Vy3}	1.79355906	p_{Vy4}	1.05813771
p_{Hy1}	0.00228401	p_{Hy2}	−0.00255717				

Aligning moment coefficients for pure slip

q_{Bz1}	8.96400000	q_{Bz2}	−1.10600000	q_{Bz3}	−0.84200000	q_{Bz4}	–
q_{Bz5}	−0.22700000	q_{Bz6}	0.00000000	q_{Bz9}	18.4700000	q_{Bz10}	0.00000000
q_{Cz1}	1.18000000	q_{Dz1}	0.10000000	q_{Dz2}	−0.00100000	q_{Dz3}	0.00700000
q_{Dz4}	13.0500000	q_{Dz6}	−0.00800000	q_{Dz7}	0.00000000	q_{Dz8}	−0.29600000
q_{Dz9}	−0.00900000	q_{Dz10}	0.00000000	q_{Ez1}	−1.60900000	q_{Ez2}	−0.35900000
q_{Ez3}	0.00000000	q_{Ez4}	0.17400000	q_{Ez5}	−0.89600000	q_{Hz1}	0.00700000
q_{Hz2}	−0.00200000	q_{Hz3}	0.14700000	q_{Hz4}	0.00400000		

Longitudinal force coefficients for combined slip

r_{Bx1}	39.44374319	r_{Bx2}	29.1009714	r_{Bx3}	445.725208	r_{Cx1}	0.97915523
r_{Ex1}	0.00587889	r_{Ex2}	−0.10191520	r_{Hx1}	−0.01836582		

Lateral force coefficients for combined slip

r_{By1}	904.062492	r_{By2}	335.010345	r_{By3}	−0.11645527	r_{By4}	0.00034250
r_{Cy1}	0.90692545	r_{Ey1}	−0.28019022	r_{Ey2}	1.02588381	r_{Hy1}	−0.00229000
r_{Hy2}	−0.00728891	r_{Vy1}	−0.03540290	r_{Vy2}	−0.08858785	r_{Vy3}	−1.59736545
r_{Vy4}	25.1678576	r_{Vy5}	2.95319383	r_{Vy6}	−8.17697406		

and parking parameters are $\zeta_i = 1$, $i = 1,\ldots,8$. It is also assumed that no modification of the tires properties are used and, consequently, the scaling factors for pure slip are all unitary, i.e., all $\lambda = 1$.

Appendix 1.2: Hoosier Slick Racing Tyre Coefficients

See Tables 1.4, 1.5.

References

1. Ambrósio, J., Gonçalves, J.: Complex flexible multibody systems with application to vehicle dynamics. Multibody Sys. Dyn. **6**, 163–182 (2001)
2. Antos, P., Ambrósio, J.: A control strategy for vehicle trajectory tracking using multibody models. Multibody Sys. Dyn. **11**, 365–394 (2004)
3. Baumgarte, J.: Stabilization of constraints and integrals of motion in dynamical systems. Comput. Methods Appl. Mech. Eng. **1**, 1–16 (1972)
4. Bertolazzi, E., Biral, F., Da Lio, M.: Symbolic numeric indirect method for solving optimal control problems for large multibody systems: the time-optimal racing vehicle example. Multibody Sys. Dyn. **13**(2), 233–252 (2005)
5. Bertolazzi, E., Biral, F., Da Lio, M.: Real time motion planning for multibody systems: real life application examples. Multibody Sys. Dyn. **17**(2–3), 119–139 (2007)
6. Braghin, F., Cheli, F., Melzi, S., Sabbioni, E.: Race driver model. Comput. Struct. **86**(13–14), 1503–1516 (2008)
7. Cardamone, L., Loiacono, D., Lanzi, P., Bardelli, A.: Searching for the optimal racing line using genetic algorithms. In: Proceedings of the 2010 IEEE Conference on Computational Intelligence and Games, 18–21 Aug., Copenhagen, Denmark, pp. 388–394 (2010)
8. Fiala, E.: Seitenkräfte am rollenden Luftreifen. VDI Zeitschrift, 96 (1954)
9. Genta, G., Morello, L.: The Automotive Chassis-Volume 1: Components Design. Springer, Heidelberg (2009)
10. Gim, G., Nikravesh, P.E.: Analytical model of pneumatic tyres for vehicle dynamic simulations—Part 1: pure slips. Int. J. Veh. Des. **11**(6), 589–618 (1990)
11. Jazar, R.N.: Vehicle Dynamics: Theory and Applications. Springer, New York (2008)
12. Lot, R., Bianco, N.: Lap time optimisation of a racing go-kart. Veh. Syst. Dyn. **54**(2), 210–230 (2016)
13. Marques, L.: Optimal lap time for a race vehicle. M.Sc. thesis, Instituto Superior Técnico, University of Lisbon, Lisbon, Portugal (2016)
14. Nikravesh, P.: Computer-Aided Analysis of Mechanical Systems. Prentice-Hall, Englewood-Cliffs, New Jersey (1988)
15. Otto, S., Seifried, R.: Real-time trajectory control of an overhead crane using servo-constraints. Multibody Sys. Dyn. **42**(1), 1–17 (2018)
16. Pacejka, H.B.: Tyre and Vehicle Dynamics, 2nd edn. Butterworth-Heinemann, Burlington, Massachussetts (2006)
17. Sharp, R.S.: Optimal preview speed-tracking control for motorcycles. Multibody Syst. Dyn. **18**(3), 397–411 (2007)
18. Sharp, R.S.: A method for predicting minimum-time capability of a motorcycle on a racing circuit. J. Dyn. Syst. Meas. Contr. **136**(4), 0410072014 (2014)

19. Thommyppillai, M., Evangelou, S., Sharp, R.S.: Advances in the development of a virtual car driver. Multibody Sys. Dyn. **22**(3), 245–267 (2009)
20. Thommyppillai, M., Evangelou, S., Sharp, R.S.: Car driving at the limit by adaptive linear optimal preview control. Veh. Syst. Dyn. **47**(12), 1535–1550 (2009)

Chapter 2
The Influence of Axle Kinematics on Vehicle Dynamics

Georg Rill and Abel Arrieta Castro

Abstract The automotive industry employs many different kinds of axle suspension systems at modern passenger cars. Important criteria are costs, space requirements, kinematic properties, and compliance attributes. This paper illustrates that in particular the kinematic properties of a suspension system have a significant influence on the dynamics of vehicles. As a consequence, the kinematics of a suspension system must be modeled very precisely and nonlinear. Typical kinematical features of a suspension system are discussed by analyzing the most common double wishbone axle suspension system. The influence of the axle kinematics on vehicle dynamics is finally demonstrated by simulation results generated with a fully nonlinear and three-dimensional multibody vehicle model.

Keywords Suspension kinematics · Vehicle dynamics · Multibody system · Double wishbone suspension system

2.1 Axle Kinematics

The double wishbone suspension represents a very popular suspension system, Fig. 2.1. Although it represents a good compromise between design properties and costs, it is mainly applied in upper class or full size cars because the upper control arms limit the space for the engine or the trunk respectively. Revolute joints in (a) and (b) attach each lower and upper control arm to the chassis or an appropriate subframe respectively. Ball joints in A and B connect the control arms to the wheel body or knuckle. The link P-Q controls the rotation of the wheel body about the axis A-B (kingpin). The ball joint in P is attached to the chassis or the steering linkage.

G. Rill
OTH Regensburg, Galgenbergstr. 30, 93053 Regensburg, Germany
e-mail: georg.rill@oth-regensburg.de

A. Arrieta Castro (✉)
PUC-Rio – OTH Regensburg, Galgenbergstr. 30, 93053 Regensburg, Germany
e-mail: abel.arrietac@gmail.com
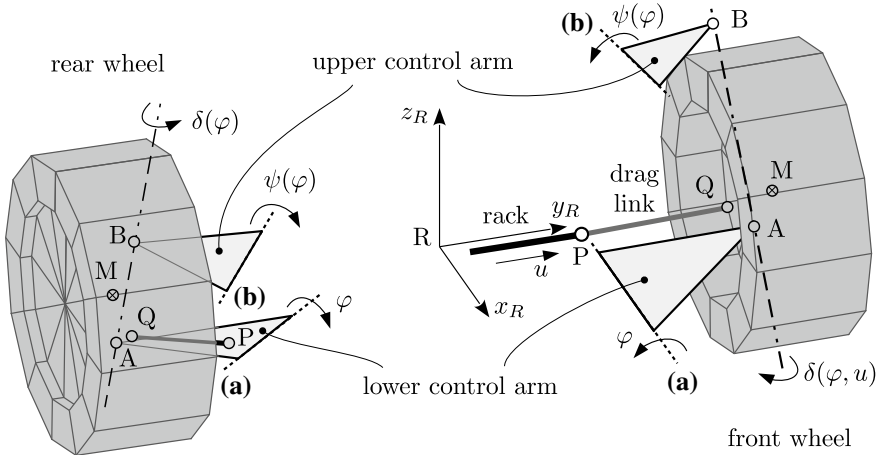
Fig. 2.1 Typical layouts of double wishbone suspensions at the front and the rear wheels

By using appropriate generalized coordinates the kinematics of a double wishbone suspension system can be solved analytically, [1].

The rotation angle of the lower control arm φ about the axis (a) is used as generalized coordinate. A first kinematical loop delivers the rotation angle of the upper control arm $\psi = \psi(\varphi)$ about the axis (b). If P is attached to the steering linkage its momentary position is defined by the steering angle in general or by the rack displacement u in particular. A second kinematical loop involves the link P-Q and yields the "steering angle" about the axis A-B (kingpin) as $\delta = \delta(\varphi)$ or $\delta = \delta(\varphi, u)$ if the wheel is steered. In the end, the kinematical analysis delivers the momentary position of the wheel center M and the orientation of a knuckle fixed reference frame as functions of the generalized coordinates φ and u or just as a function of φ only. In test rig measurements the movements x and y of the wheel center in longitudinal and lateral directions as well as the rotation angles α and γ of the wheel body about the longitudinal and the vertical axis are monitored when a piston forces the wheel to perform a vertical z-displacement.

Figures 2.2 and 2.3 shows the signals described before, considering a typical double wishbone suspension layout of a standard car [1], together with the movements of the geometric contact point. This contact point is defined as the point on the intersection line between the rim center plane and the local road plane that has the shortest distance to the wheel center, [2]. Two-dimensional plots of the rotation angles α (camber angle) and γ (toe angle) can be found in, [1]. The kinematical analysis of a MacPherson suspension system is described in [3] and the model of a multi-link wheel suspension is provided in [4].

Within the plots (a) and (b) the vertical coordinate z is shifted such that $z = 0$ defines the vertical position of the geometric contact point in the design position where the vehicle is loaded by the weight of two passengers at the front seats. Small circles mark the design position of the geometric contact point and the wheel center
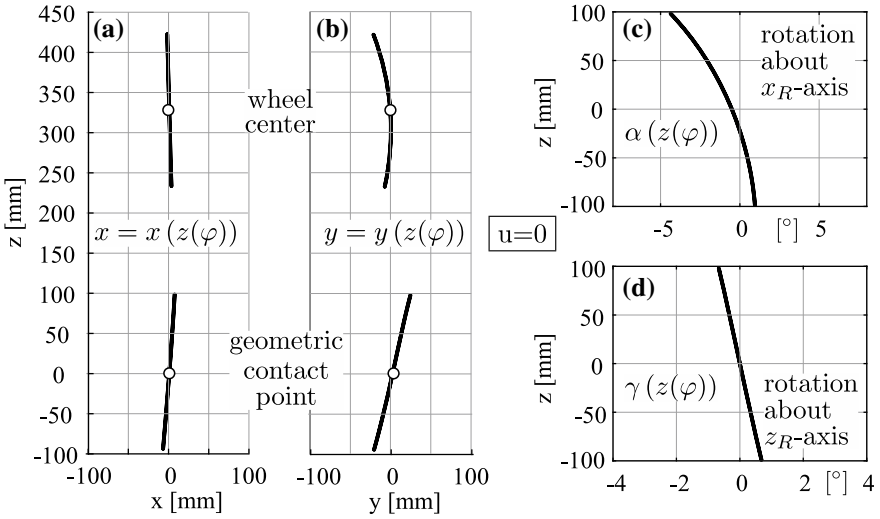
Fig. 2.2 Kinematic properties of the double wishbone suspension at the front wheels
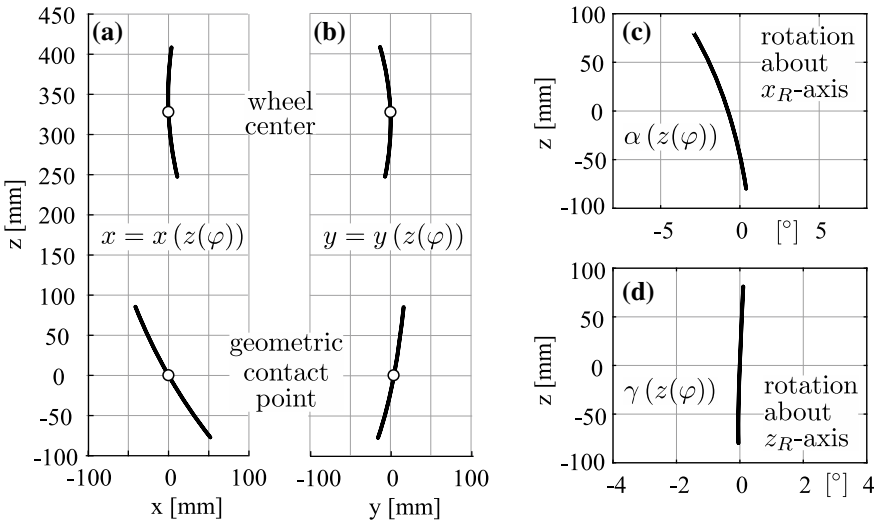
Fig. 2.3 Kinematic properties of the double wishbone suspension systems at the rear wheels

respectively. However, $z = 0$ indicates the design position of the wheel center within the plots (c) and (d).

By inspecting the plots (c) in Figs. 2.2 and 2.3 it can be seen that the wheels at the front and rear perform a significant rotation about the x_R-axis when moving up and down. This motion is called camber compensation because it at least partly counteracts the roll motion of the chassis when cornering and hence reducing the

tire camber angle. The typical layout of a double wishbone suspension where the upper control arm is significantly smaller than the lower one automatically produces this effect. In practice, a distinct camber compensation is realized on sportive or race cars only. As shown here, normal passenger cars usually employ just a moderate camber compensation. Because otherwise an unwanted tire wear is produced when the vehicle is simply driving straight ahead on normal roads and the wheels will be forced to rotate also about the x_R-axis when the wheels have to move up and down in order to compensate the road irregularities.

The plots (d) in Figs. 2.2 and 2.3 show a very common layout. Whereas the front wheels perform a small but distinct rotation about the z_R-axis (steering movement), $\alpha\left(z(\varphi)\right) \approx \frac{\partial \alpha}{\partial z} z$ when the wheel is moving up and down, the rear wheels remain practically un-steered, $\alpha\left(z(\varphi)\right) \approx 0$. The distinct steering movement at the front wheels realized here increases the understeer tendency of the vehicle and thus improves the stability of the vehicle when approaching the limit range. Steering effects at the rear wheels caused by up and down movements of the wheels would worsen the straight-ahead behavior of a vehicle when running on uneven roads.

The longitudinal and lateral movements of the geometric contact point affect the dynamics of a vehicle in particular and shall be discussed in the next section.

2.2 Results

The influence of the axle kinematics on the dynamics of vehicles is illustrated by simulations performed with a fully nonlinear and three-dimensional multibody system vehicle model, Fig. 2.4. Model details can be found in [1, 5].

The axle kinematics of the standard car, described in Sect. 2.1, was modified to a simple fictitious one where each wheel just performs a plain up and down motion z characterized by the trivial constraints $x = 0$, $y = 0$, $\alpha = 0$, and $\gamma = 0$.
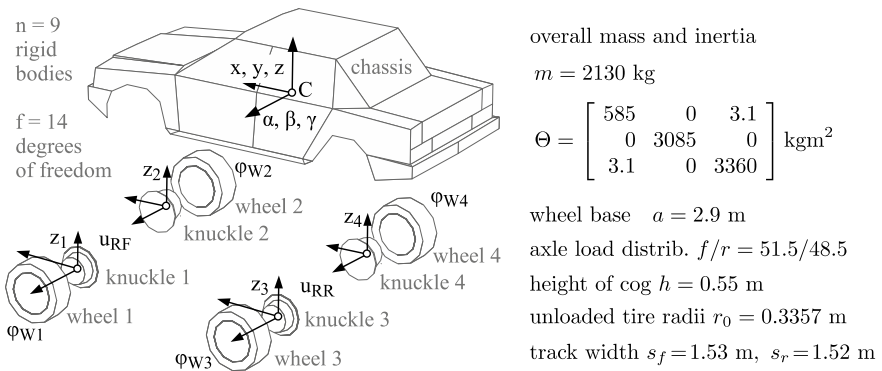
Fig. 2.4 Multibody vehicle model and characteristic data

As a consequence, the steering motion of the front wheels just depends on the rack displacement, $\delta = \delta(u)$ but maintains the full maneuverability of the fictitious vehicle model.

2.2.1 Brake Pitch

The pitch of the vehicle caused by braking will be felt as annoying, if too distinct. A proper layout of the axle kinematics, as realized in nearly every standard car, reduces the pitch angle significantly, Fig. 2.5. The pitch angle is the consequence of a jounce motion (positive suspension travel) at the front wheels and a rebound motion (negative suspension travel) at the rear wheels. By moving the contact points at the front and the rear wheels forward on compression and rebound respectively the suspension travel and hence the pitch angle is reduced significantly during a braking maneuver. These longitudinal motions of the contact point, realized in Figs. 2.2a and 2.3a are generated by an appropriate rotation of the wheel body about the y_R-axis. That is why, the rotation axis (a) and (b) of the control arms are not parallel but inclined against each other, Fig. 2.1. This layout avoids distinct longitudinal motions of the wheel center that would force the wheel to spin faster or slower when riding on a rough road and may excite drive train vibrations. In addition, a front axle designed with a distinct forward motion of the wheel center will cause severe problems when crossing a bump in forward drive, because knuckle and wheel will be moved toward the bump on compression then.
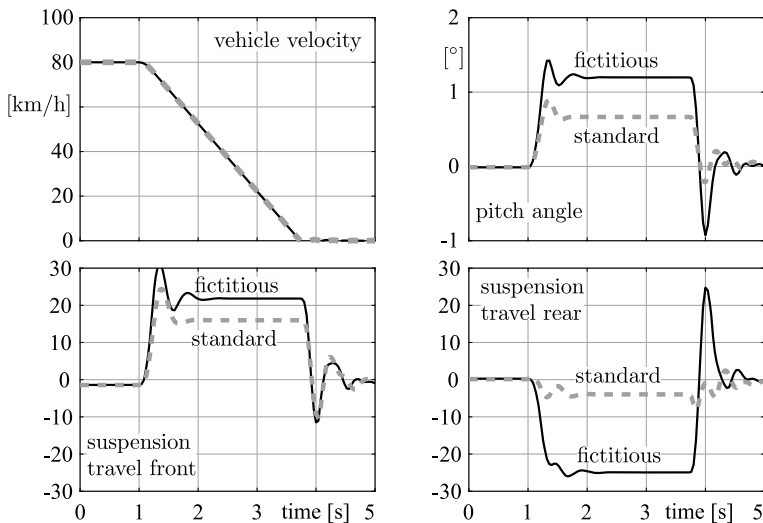
Fig. 2.5 Braking scenario with a standard vehicle and a fictitious vehicle with a simple kinematics

2.2.2 Steering Tendency

In field tests and in simulations the steering tendency of a vehicle is assessed by the driving maneuver steady state cornering. The maneuver is performed quasi-static, in general. The driver or an appropriate driver model keeps the vehicle on a given curve radius R when he slowly increases the driving speed v and due to $a_y = v^2/R$ the lateral acceleration too until reaching the limit. The plot steering wheel angle δ_{SW} versus the normalized lateral acceleration a_y/g indicates the steering tendency of the vehicle by its slope, left plot in Fig. 2.6.

As realized here, the design of the axle kinematics intensifies the understeer tendency (positive slope) in general. In this particular case it is mainly achieved by the kinematical steering effect (rotation about the z_R-axis) of the front wheels, Fig. 2.2d. In addition, the lateral movement of the contact points, plotted in Figs. 2.2b and 2.3b reduce the roll angle when cornering, right plot in Fig. 2.6.

2.2.3 Camber Compensation

The camber compensation is an important kinematic property to take into consideration especially in high-performance cars. This type of vehicles employs sophisticated suspensions and these layouts includes, among the normal suspension components, extra mechanical and force elements, e.g. the push-rod, the rocker and the drop-link, see Fig. 2.7. The rocker rotates around an axis fixed on the chassis, see the detailed view in Fig. 2.7. This component transmits via the push-rod rigid link the wheel up/down motion to the force element and by a drop-link to the anti-roll bar. Then, an extra suspension stiffness is achieved by the activation of the additional force element in order to compensate the downforces generated at high speeds. Additionally, by the activation of the anti-roll bar, the body roll angle is reduced during cornering.

In order to show the influence of the camber compensation only, a fictitious suspension system (similar to the one described previously) was modeled. This fictitious
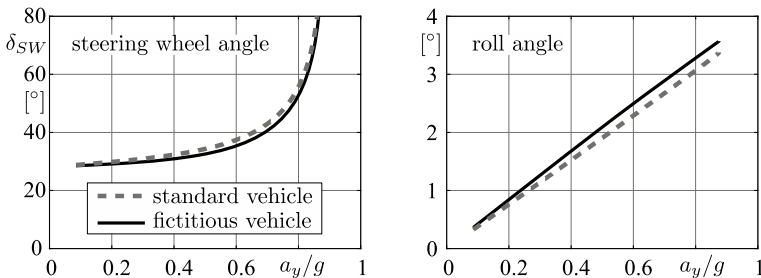
Fig. 2.6 Steady state cornering performed on a radius of $R = 100\,\mathrm{m}$
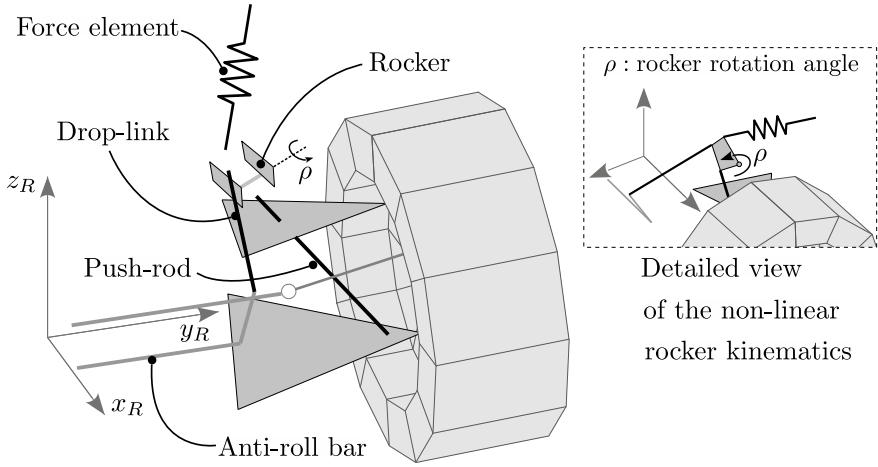
Fig. 2.7 Typical suspension system for high-performance cars
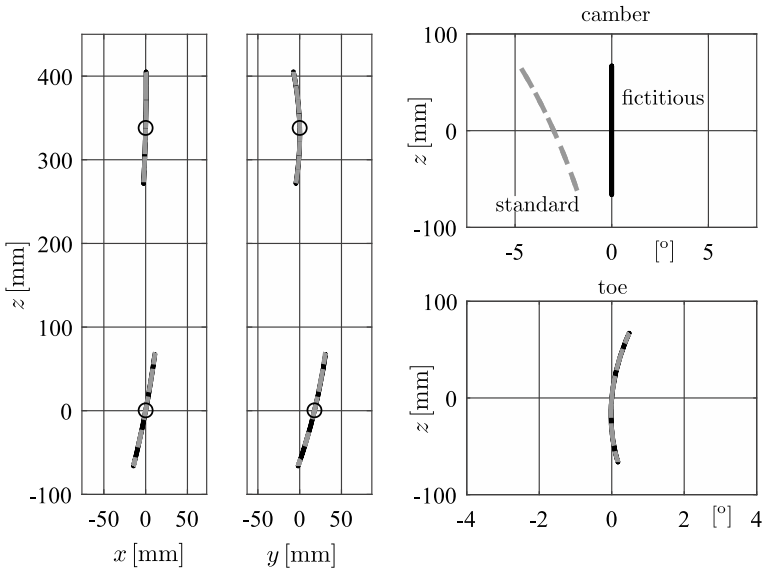
Fig. 2.8 Kinematic properties of the standard and fictitious sophisticated suspension system for high-performance cars at the front wheels

suspension is capable of removing the camber angle and keeps the other suspension kinematic properties.

In the upper right plot of Fig. 2.8, we can see that the fictitious suspension correctly removes the camber compensation while it keeps the contact point movement and the toe angle equal to the standard suspension system.

Table 2.1 Overall characteristic parameters of a high-performance car

Parameter	Value	Units
Mass	1750.2	kg
Inertia at COG	$\Theta = \begin{bmatrix} 525.6 & 0.0 & 6.2 \\ 0.0 & 682.9 & 0.0 \\ 6.2 & 0.0 & 1534.0 \end{bmatrix}$	kg.m^2
Wheel base	2.7	m
Axle load distrib.	$f/r = 59.2/40.8$	–
Height of COG	0.12	m
Unloaded tire radius	0.3268	m
Track width front/rear	1.67/1.59	m
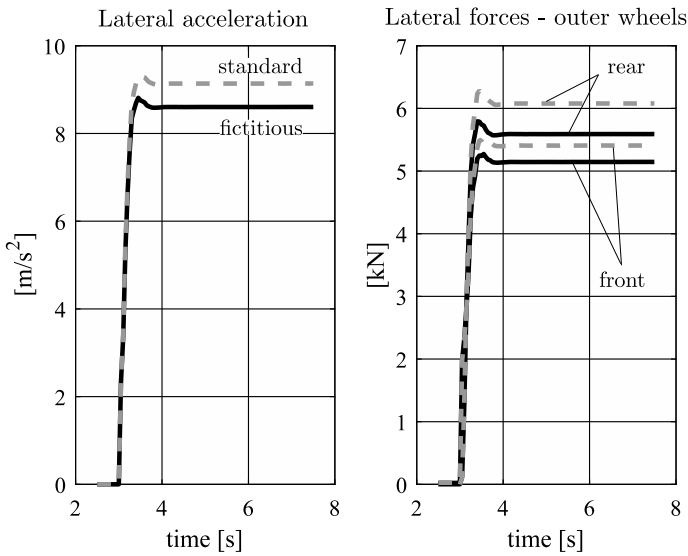
Fig. 2.9 Step-steer performance maneuver at 120 km/h of a high-performance car

The step-steer maneuver at 120 km/h is employed in order to analyze the camber influence in two high-performance cars, i.e. one with the fictitious suspension system and the other with the standard one. The overall parameters of this type of cars are shown in Table 2.1.

As can be seen in the left plot of Fig. 2.9, a larger lateral acceleration is achieved in the case of the vehicle with the standard suspension. This is because, with the camber compensation, it is possible to have a better tire-road contact and in consequence, greater lateral forces can be transferred to the road, see right plot of Fig. 2.9.

2.3   Conclusion

The influence of the axle kinematics on vehicle dynamics is wide-ranging and employed in most passenger and high-performance cars. As a consequence, vehicle models that are supposed to be valid in a wide range of applications have to take into account the nonlinear kinematics of the wheel suspension systems. By considering these nonlinearities and a proper tire model, it is possible to obtain a good conformity between simulations and measurements [6]. Therefore, using a simplified description of the axle kinematics, i.e. a pure wheel up/down motion, in a vehicle model can produce too inaccurate results. Additionally, in sophisticated suspension systems, it is also necessary to consider the nonlinearities of the extra components, e.g. the rocker kinematics. Finally, studies involving complex scenarios require the complete description of the axle kinematics in order to have a fully nonlinear and three-dimensional vehicle model, and consequently obtain reliable results [7].

References

1. Rill, G.: Road Vehicle Dynamics - Fundamentals and Modeling. Taylor & Francis, Boca Raton (2011)
2. Rill, G.: Sophisticated but quite simple contact calculation for handling tire models. In: Multibody System Dynamics (2018). (To appear)
3. Rill, G., Schaeffer, Th: Grundlagen und Methodik der Mehrkörpersimulation, 3rd edn. Springer Vieweg, Wiesbaden (2017)
4. Rill, G.: Multibody systems and simulation techniques. In: Lugner, P. (ed.) Vehicle Dynamics of Modern Passenger Cars, CISM International Centre for Mechanical Sciences Courses and Lectures. Springer, Cham (2018). (To appear)
5. Castro, A.: Development of a robust and fault tolerant integrated control system to improve the stability of road vehicles in critical driving scenarios, Ph.D-Thesis. PUC-Rio, Rio de Janeiro (2018)
6. Hirschberg, W., Palacek, F., Rill, G., Sotnik, J.: Reliable vehicle dynamics simulation in spite of uncertain input data. In: Proceedings of 12th EAEC European Automotive Congress, Bratislava (2009)
7. Castro, A., Rill, G., Weber, H.: Development of a robust integrated control system to improve the stability of road vehicles. In: Carvalho, J., et al. (eds.) Proceedings of the MUSME Conference in Florianópolis Brasil, pp. 506–516. Springer, Cham (2017)

Chapter 3
Automotive Mechanisms for Improving Fuel Economy

Madhusudan Raghavan

Abstract This paper presents two mechanism innovations in the area of advanced propulsion systems. The first is a mechanism arrangement that couples the two cranks of an opposed piston variable compression ratio engine. This arrangement can vary the relative phasing between the two cranks to achieve compression ratio change. This strategy has been shown to improve fuel economy by approximately 5%, in certain engine applications. Secondly, the paper describes a high-speed flywheel system coupled to an automotive transmission. Its use as an alternative energy storage system for capturing vehicle kinetic energy has the potential to improve fuel economy by 15–20% when coupled to the driveline via a three-speed clutched transmission system.

3.1 Introduction

The 2016 International Energy Outlook [1] states that global population grows from 7.3 billion in 2015 to 9.0 billion in 2040. Total world marketed energy will grow by 42% from 575 quads in 2015 to 815 quads in 2040 (quad = quadrillion Btu). The transportation sector projected usage remains at about 18% of this total. Against this backdrop of increasing population and energy consumption, we continue to look for ways to improve vehicle fuel economy via mechatronic augmentation of the driveline. In this paper, we describe two innovations to enhance the operating modes of the propulsion system thereby improving fuel economy.

   In the first example, we are tasked with devising a variable compression ratio mechanism for a two-stroke opposed piston engine equipped with a Roots super-charger to facilitate the scavenging process. We present the kinematic details of the mechanism arrangement that serves to couple the two cranks. These cranks may be selectively phased relative to each other to achieve a variable compression ratio. In the second example, we describe a high-speed flywheel system that is mounted on a conventional automatic transmission and is used as an alternative energy storage

M. Raghavan (✉)
General Motors R&D, Warren, MI, USA
e-mail: madhu.raghavan@gm.com

system for capturing vehicle kinetic energy in the form of a low-cost mechanical hybrid system. Such a system has the potential to improve fuel economy by 15–20% when coupled to the driveline via a three-speed clutched transmission system.

3.2 Significance of the Present Work

Advanced propulsion system development and enhancement are trending towards higher levels of electrification. Such systems are often challenged from the standpoint of affordability and profitability. Various forecasts including the 2016 International Energy Outlook [1] suggest that despite the rapid adoption of electric vehicles as a new market segment, liquid fuels will continue to play a significant role in transportation systems for the next several decades. In the present work, we offer mechatronic schemes that could perhaps serve as affordable enhancements to conventional propulsion systems that make use of liquid fuels.

3.3 Mechanism Concept 1

Opposed piston engines have been studied by various research groups as a means to achieving higher fuel economy. Hofbauer [2] describes an opposed piston engine for a possible military truck application with a planned power level of 465 kW and with a best efficiency island of ~206 g/kWh. Zhang et al. [3] investigated the characteristics of the piston dynamics on an opposed-piston two-stroke folded crank train diesel engine. They found that a larger asymmetric angle is positive for the scavenging efficiency but negative for combustion. Wallace and Lux [4] describe a hydraulically actuated piston which increases output 50% without increasing maximum combustion pressure.

The opposed piston engine concept of interest in this paper is shown in Fig. 3.1, and was conceived at GM R&D [5]. It has pairs of cylinders that are placed in-line, head to head. There is no traditional cylinder head; the clearance volume when the piston is at the top of its stroke is effectively the gap between the tops of the respective pairs of pistons. There are two crankshafts which are coupled mechanically via a gear train as shown in Fig. 3.1. This gear train effectively converts this two-crankshaft system into a single crankshaft system and we may use either crankshaft as the engine output depending on vehicle architecture and packaging convenience.

Analysis showed that one could achieve additional engine efficiency improvements (approximately +5%) by introducing a single degree-of-freedom control input to this mechanical coupling, which would allow the crankshafts to be phased relative to one another. This phase change modifies the compression ratio by changing the clearance volume by appropriately phasing the piston motions. An embodiment of this adjustable mechanical coupling between the two crankshafts is a planetary gear set and a pair of sprockets and chains connecting the components of the gear set
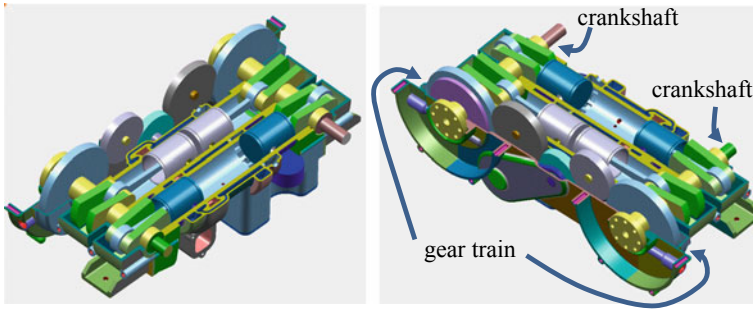
Fig. 3.1   Opposed piston engine concept
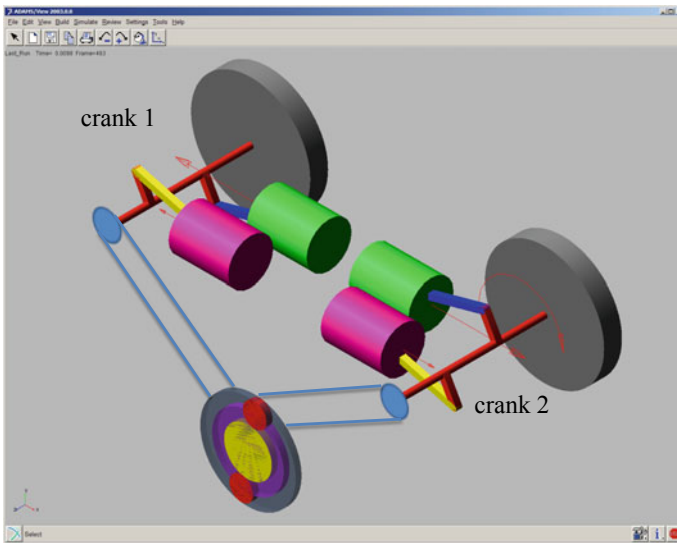
Fig. 3.2   Planetary gear set with chains to crankshafts

to the two crankshafts (see Fig. 3.2), in place of the original gear train connecting the sprockets. The shaft on the left (crank 1) is connected to the ring gear of the planetary set, and the shaft on the right (crank 2) is connected to the carrier of the planetary gear set. Kinematic and dynamic simulations of this embodiment of the opposed piston engine were conducted using ADAMS with the focus being on the design of the phaser mechanism coupling the 2 cranks. Power and exhaust cycles in one cylinder are accompanied by the intake and compression strokes in the other cylinder. In the simulations, a planetary gear set-based phaser with a ring-to-sun ratio of 2.0 was used.
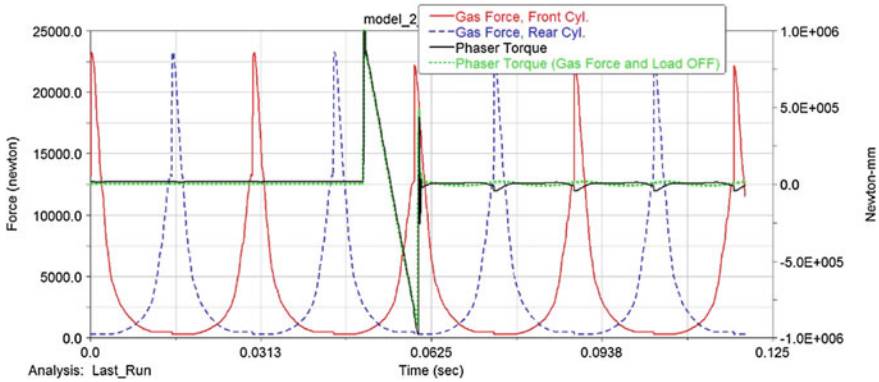
Fig. 3.3 Forces and torques during phase change maneuver

3.3.1   Simulation

In order to simulate the dynamics of the engine, the force produced by combustion was modelled. Cylinder pressure as a function of Crank Angle Degree (CAD) was available from GT-Power simulations and the force produced by combustion (in terms of pressure) was calculated from this data. In the ADAMS simulation, the force was represented in the form of a look-up table and varied as a function of the distance between the two pistons. The modelled force was used to simulate the combustion in both the cylinders with the proper phase difference. Forces at the bearings supporting the crankshafts, as well as the velocities and the displacements at various joints were recorded as functions of time.

One of the objectives of the phaser simulation was to calculate the torques and the forces acting on each component, particularly the sun gear. This was done to size the actuating device. Figure 3.3 shows the cylinder gas forces (left-side y-axis) and the phaser torque on the sun gear (right-side y-axis), during a phase change maneuver. The periodic gas forces in the cylinders show a constant phase difference. The sharp increase in the torque at the sun gear (solid green curve) is required to effect the phase change. Based on the high torque levels required (~1000 N-m), we selected a hydraulic actuation system to index the position of the sun gear to execute compression ratio changes. We will report on the outcomes from this approach once engine fabrication and testing are completed.

3.4   Mechanism Concept 2

Developments in flywheel technology have made it a credible alternative energy storage system (ESS) for hybrid vehicles [6–8]. The advantages of flywheel systems include high power density, durability, potentially lower material cost, and the
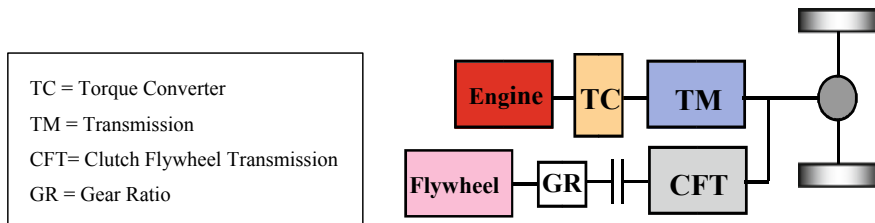
Fig. 3.4 Schematic of a post-transmission flywheel hybrid powertrain

elimination of energy conversion between the mechanical and electrical domains. A high-speed flywheel system works by recuperating vehicle kinetic energy that would normally be lost through braking. Note that the amount of stored energy, also known as the state-of-charge (SOC), can be easily and accurately computed from the rotational speed as follows.

$$SOC = \frac{KE_f}{KE_{max}} = \frac{\omega_f^2}{\omega_{f,max}^2} \tag{3.1}$$

where KE_f and KE_{max} are respectively the kinetic energy of the flywheel and its maximum allowed value, ω_f, is the flywheel speed, and $\omega_{f,max}$, is the maximum flywheel speed predetermined by the flywheel design.

In this study, a post-transmission (also-called P3) configuration (shown in Fig. 3.4) is chosen due to its practical advantages such as packaging, cost, and minimal design changes from the conventional vehicle. Figure 3.4 shows that both the engine and flywheel have dedicated transmissions, which allows the engine to operate independent of the flywheel speed as well as the vehicle speed. A conventional automatic transmission and a torque converter are used for the engine, and a clutch flywheel transmission (CFT) is used for the flywheel.

3.4.1 Simulation

A Simulink HEV model was developed based on the schematic in Fig. 3.4. The details are as follows. The model consists of a conventional driveline, flywheel driveline, and a supervisory controller. The conventional driveline includes an engine, torque converter, and a conventional automatic transmission, and the flywheel driveline includes the flywheel dynamics and the CFT. The supervisory controller coordinates two power sources, the engine and the flywheel, depending on the vehicle state and driver demand. The vehicle model is a generic mid-size vehicle with a 1.8L SI engine and a 6-speed automatic transmission.

The CFT (see Fig. 3.5) has three clutches with different gear ratios across them, and it has a multi-stage speed reduction gear connecting the CFT output to the
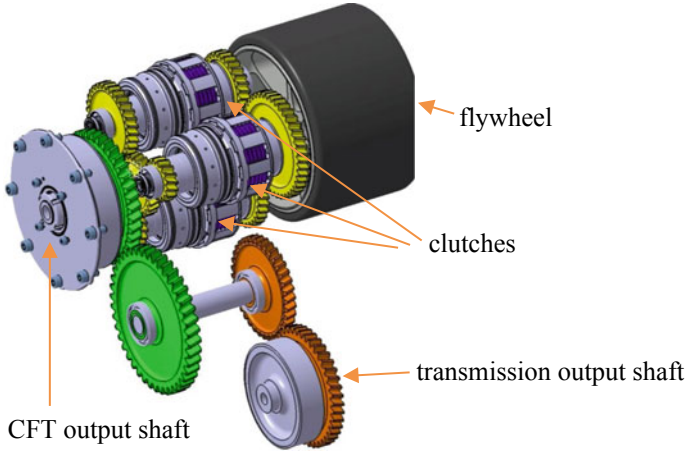
Fig. 3.5 Three dimensional view of the CFT

automatic transmission output shaft. The CFT chooses between the three available ratios across its clutches in order to reduce clutch slip during energy transfer between the input (flywheel side) and output (transmission side) shafts, resulting in minimal losses. The input shaft of the CFT is the shaft carrying the flywheel and the output shaft of the CFT (shown at the center of Fig. 3.5) is connected to the transmission output shaft through the afore-mentioned set of speed reduction gears. The flywheel inertia is quite small and can store 76.8 Wh (276 kJ) at the maximum operating speed of 60,000 rpm.

A quasi-static model is used for the transmission. Transmission output torque is computed as follows.

$$T_{o,TM} = \eta_{GR} TGR \cdot T_{i,TM} - C_{TM} \omega_{i,TM} \tag{3.2}$$

where $T_{o,TM}$ is output transmission torque, $\eta_{GR} =$ gear efficiency, *TGR* is the transmission gear ratio, C_{TM} is the spin (viscous) loss coefficient, and $\omega_{i,TM}$, is the transmission input shaft speed. It is related to $\omega_{o,TM}$, the transmission output shaft speed, as follows.

$$\omega_{i,TM} = TGR \cdot \omega_{o,TM} \tag{3.3}$$

The longitudinal vehicle dynamics is described by

$$\frac{dV}{dt} = \frac{F_D - F_B - F_R}{M_r}, \text{ with } F_R = f_0 + f_1 V + f_2 V^2 \tag{3.4}$$

and

Fig. 3.6 Energy loss
analysis of the simulation
results over the FTP urban
drive cycle
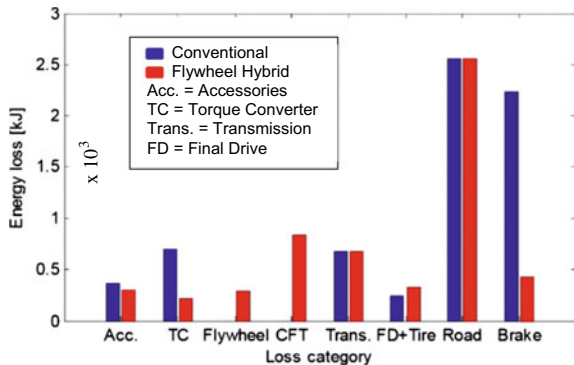
$$T_{sum} = T_{o,TM} + T_{o,CFT} \tag{3.5}$$

V is vehicle speed, F_D is the tractive force, F_B is the braking force, F_R is the road
load, M_r is the vehicle mass, f_0, f_1, f_2 are coefficients defining the road load, T_{sum}
is the summation of the two torques applied at the final drive, and $T_{o,CFT}$ is the CFT
output torque.

$T_{i,CFT}$ is computed as follows

$$T_{i,CFT} = \frac{T_{o,CFT}}{GR_{SR}GR_{CFT,o}GR_{CFT,i}} \tag{3.6}$$

where GR_{SR} is the multi-stage speed reduction gear ratio, and $GR_{CFT,o}$, $GR_{CFT,i}$
are the output and input side gear ratios of the slipping clutch, respectively.

The control strategy basically stores vehicle kinetic energy during braking and
uses this up during the next vehicle launch. The control algorithm is designed as
follows.

> If SOC > 0.01 and $P_{dem} < 50$ kw and V < 50 mph $\rightarrow E_{on/off} = 0$
>
> Else $E_{on/off} = 1$ and $P_{eng} = P_{dem}$

where P_{dem} is the demanded power, $E_{on/off}$ is the engine on/off flag.

Figure 3.6 shows the energy loss breakdown comparison between a conventional
vehicle (blue bars) and the flywheel hybrid vehicle (red bars), on the FTP Urban Driv-
ing Cycle. Fuel economy improvement for the hybrid comes from (1) idle stop/start,
(2) recuperation of the braking energy, and (3) higher engine efficiency by launch-
ing the vehicle with the flywheel. Figure 3.6 shows that the braking energy loss has
been reduced for the flywheel hybrid due to regenerative braking via kinetic energy
recuperation. However this gain is partly offset by the flywheel bearing losses (bar
labeled Flywheel) and CFT clutch slipping losses (bar labeled CFT).

Figure 3.7 shows the so-called "kite" diagram obtained from plotting vehicle
speed versus flywheel speed during FTP operation. Zone I features torque boosting

Fig. 3.7 Vehicle speed
versus flywheel speed
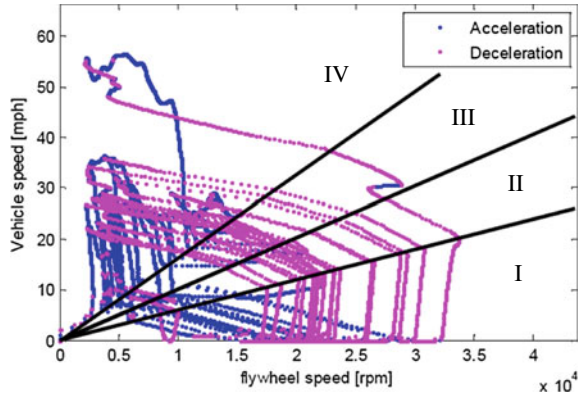
only (wherein the flywheel adds power to the driveline), zones II and III allow both boosting and recuperation, while zone IV features only recuperation. We found that the idle stop/start gain alone is 6%, with an additional 9% attributable to recuperation and hybrid launch. Although total component losses are not significantly reduced, the elimination of the idle stop/start and low-efficiency engine operation during deceleration and launch results in significant fuel economy improvement.

3.5 Conclusions

We have presented a planetary phaser-based scheme for a variable compression ratio engine and a high-speed flywheel system coupled to an automotive driveline via a three-speed layshaft transmission. Our key conclusions are as follows.

- A hydraulic actuation system would be suitable for use on the variable compression engine due to the relatively high actuation torques required to effect compression ratio changes.
- The high-speed flywheel system is a viable hybridization architecture offering a 15–20% fuel economy improvement, subject of course to packaging, safety and drive quality constraints.

References

1. International Energy Outlook 2016, DOE/EIA-0484(2016). https://www.eia.gov/outlooks/ieo/pdf/0484(2016).pdf (2016)
2. Hofbauer, P.: Opposed piston opposed cylinder (OPOC) engine for military ground vehicles. SAE 2005-01-1548

3. Zhang, Z., Zhao, C., Wu, D., Zhang, F., et al.: Effect of piston dynamic on the working processes of an opposed-piston two-stroke folded-cranktrain engine. SAE Technical Paper 2014-01-1628 (2014) https://doi.org/10.4271/2014-01-1628
4. Wallace, W., Lux, F.B.: A variable compression ratio engine development. SAE 640060
5. Maguire, J., Bucknor, N., Raghavan, M., Najt, P.: Hybrid powertrain. US Patent 7611432 (2009)
6. Wright, P.: F1 moves toward hybridization. Automot. Eng. Int. 60–63 (2008)
7. Hebner, R., Beno, J., Walls, A.: Flywheel batteries come around again. IEEE Spectr. 46–51 (2002)
8. Barr, A., Veshagh, A.: Fuel economy and performance comparison of alternative mechanical hybrid powertrain configurations. SAE 2008-01-0083

Chapter 4
Detection of Surface Texture with an Artificial Tactile Sensor

Moritz Scharff, Jorge H. Alencastre and Carsten Behn

Abstract Animals, e.g., rodents can detect multiple information with their vibrissae. Among other things, the vibrissae can be used to detect information about a surface texture by a tactile stimuli. Inspired by the natural example of mystacial vibrissae, an artificial tactile sensor is designed. To identify the relation between measured signal and surface texture, a simulation respecting a quasi-static sensor displacement is performed. The sensor is modeled as an one-side clamped Euler-Bernoulli whose surface contact is described within the limits of Coulomb's law of friction. Gathering the support reactions, the friction coefficient between beam and surface can be determined. The theoretical model is verified by an experiment.

4.1 Introduction

Animals use different types of senses for data reception. Next to, e.g., vision and audition the somatosensation is significant. Especially, the tactile data perception with mystacial vibrissae is a distinguished feature of the somatosensory system of various animals, for example cats, see Fig. 4.1a. The mystacial vibrissae are placed in a certain arrangement around the muzzle of the animal [5]. Gaining an insight of

M. Scharff (✉) · C. Behn
Department of Mechanical Engineering, Technische Universität Ilmenau, Max-Planck-Ring 12, 98693 Ilmenau, Germany
e-mail: moritz.scharff@tu-ilmenau.de

C. Behn
e-mail: carsten.behn@tu-ilmenau.de

J. H. Alencastre
Department of Engineering, Pontifical Catholic University of Peru, Av. Universitaria N° 1801, San Miguel, Lima, Peru
e-mail: jalenca@pucp.edu.pe

(a) Natural example: cat.　　(b) Theoretical model.　　(c) Artificial sensor.
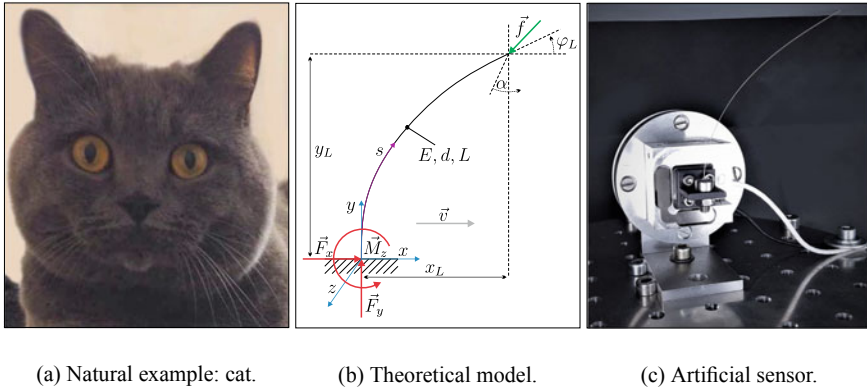
Fig. 4.1 Natural mystacial vibrissae of a cat (**a**), an abstracted theoretical model of a single vibrissa (**b**), and the experimental set-up (**c**)

this arrangement, the geometric dimensions of the vibrissal hair shaft vary, but the fundamental shape of each hair shaft is not changing.

The vibrissal hair shafts are characterized by a cylindrical tapered body with an inherent curvature. The length of the body is much larger than it's diameter. A hair shaft consists of different layers of material and is partially hollow. The outside is covered with scales [13]. Each hair shaft is supported by its own follicle-sinus complex (FSC) [7]. The FSC itself shows a particular structure: it is made of different types of tissue and blood vessels that result in a visco-elastic behavior. Furthermore, the FSC includes multiple kinds of mechanoreceptors to transduce the mechanical stimuli (collected by the vibrissa shaft) into an action potential for further processing [17]. This sophisticated combination of hair shaft and FSC enables to fulfill several tasks mentioned above. In [3] it is shown that vibrissae can be used to detected the distance to an object, to recognize it's shape and to classify the surface texture. The *Kinetic Signature Hypothesis* describes the process of surface texture detection [1]. It is assumed that the information about the surface texture is coded in a signal described by a temporal sequence of acceleration events. This hypothesis is extended in [16] and takes the stick-slip effect into account. It is reported that animals can differ surface structures with a dimension of approximated $30\,\mu\mathrm{m}$ [4]. Adapting the natural paragon, several theoretical models and artificial sensors are developed, e.g., [2, 6, 14, 15]. First approaches in describing the process of surface texture detection are done in [10, 12].

Here, the tip of a beam is in touch with a surface. The beam is characterized by the Euler-Bernoulli beam theory and takes large deflections into account. Assuming a point contact between beam tip and surface, Coulomb's law of friction is used to summarize all surface properties and related effects in the friction coefficient. This model is addressed to Sect. 4.2.

The goal is to design an artificial sensor with the whole functionality of a natural mystacial vibrissa. This work focuses exclusively on the aspect of surface texture

detection. Section 4.2 introduces details about the theoretical beam model and the performed experiment. The data of the simulation is compared to the experiment in Sect. 4.3. Finally, the findings and results are summarized in Sect. 4.4.

4.2 Methods

The natural vibrissa hair shaft is simplified to a straight (length L), cylindrical (diameter d) beam that consists of an isotropic, homogenous Hooke's material (Young's modulus E), see Fig. 4.1b. Geometric properties like tapering and an inherent curvature are theoretically examined in [8, 9] but not considered in this work. The elasticity of the FSC is neglected, the FSC is assumed to be ideal stiff (support is a clamping). The process of surface texture detection is assumed as a sequence with multiple steps. First, the beam is bent under the surface and it's tip stays in contact with the surface respecting Coulomb's law of friction (4.1):

$$\tan{(\alpha)} = \frac{|F_x|}{|F_y|} = \mu \leq \mu_s = \tan{(\alpha_s)} \tag{4.1}$$

For this initial position, it is furthermore assumed that the beam is loaded by a normal force f_y only. So, the angle of friction α is equal to zero, see Fig. 4.1b. Out of this position, the clamping gets displaced. For the simulation, this displacement is quasi-static and, for the experiment, a constant velocity is used. While the clamping is displaced, the beam tip is sticking to the surface and loaded by a tangential force f_x caused by friction, too, until the coefficient of static friction μ_s is reached. Passing this limit, the tip starts sliding under the influence of the dynamic friction coefficient μ_d. So, a finite support displacement results a finite number of stick-slip cycles. During the displacement of the clamping, the support reactions are measured (detailed description in Sects. 4.2.1 and 4.2.2). Evaluating this data the present friction coefficient can be determined. For the experiment, the contact surface is represented by a sandpaper with statistical distributed particles. The relation between grit size of the sandpaper and present friction coefficient is analyzed.

4.2.1 Simulation

The static equilibrium state of the beam while touching the surface is given by (4.2):

$$\left. \begin{array}{ll} \rightarrow: & F_x + f_x = 0 \Longleftrightarrow F_x = -f_x \\ \uparrow: & F_y + f_y = 0 \Longleftrightarrow F_y = -f_y \\ \circlearrowleft: & M_z + f_y \cdot x_L - f_x \cdot y_L = 0 \Longleftrightarrow M_z = -f_y \cdot x_L + f_x \cdot y_L \end{array} \right\} \tag{4.2}$$

with: $\qquad f_x = \sin(\alpha) \cdot f \quad ; \quad f_y = -\cos(\alpha) \cdot f$

Applying the method of sections for the bending moment in combination with the Euler-Bernoulli beam theory for large deflection forms the system of Eq. (4.3):

$$\left.\begin{aligned} x'(s) &= \cos(\varphi(s)) \\ y'(s) &= \sin(\varphi(s)) \\ \varphi'(s) &= \frac{f}{E \cdot I_z}(\sin(\alpha)(y(s) - y_L) + \cos(\alpha)(x(s) - x_L)) \end{aligned}\right\} \quad (4.3)$$

According to the assumption of a cylindrical beam (see Sect. 4.2), the second moment of area I_z is:

$$I_z = \frac{\pi d^4}{64}$$

For the described scenario, the tip of the beam is located at $(x_L; y_L)$ with a slope angle φ_L of the elastica and the clamping at $(x_0; 0)$, where x_0 changes in consequence of the displacement of the clamping. Accordingly to these assumptions, the boundary conditions are given by:

$$\left.\begin{aligned} x(0) &= x_0 &;& \quad x(L) = x_L \\ y(0) &= 0 &;& \quad y(L) = y_L \\ \varphi(0) &= \frac{\pi}{2} &;& \quad \varphi(L) = \varphi_L \end{aligned}\right\} \quad (4.4)$$

Applying a Shooting-Method in combination with the Runge-Kutta-Method of 4th order the boundary value problem (4.3) and (4.4) is solved. This procedure is implemented into *MATLABR2017b* using the functions *fsolve()* and *ode45()*.

4.2.2 Experiment

Based on the natural paragon, the artificial sensor is moved while it stays in contact with the fixed surface in the experiment. The experimental set-up includes a hexapod of type PI M-850.50 for displacing the sensors. A maximal travel distance of ±50 mm with a repeatability of $\pm2\,\mu$m can be realized using this robot platform. The hexapod carries the following sensors:

- ME-Meßsysteme torque sensor TD70, accuracy class 0.1, nominal load ±1 Nm,
- ME-Meßsysteme 3D force sensor K3D40, accuracy class 0.5, nominal load ±2 N

and further components. The force sensor is mounted onto the torque sensor, see Fig. 4.1c. This arrangement of the sensors causes an interacting between them and

Table 4.1 The sandpapers are classified by: ISO 6344-2:2013, ISO 6344-3:2013 and FEPA-Standards 43-1:2006. The pictures are taken with a magnification of ×60

Type	P120	P150	P180	P240	P320	P400	P600
Average particle diameter μm	125	100	82	58.5	46.2	35.0	25.8
Picture							

Type	P800	P1000	P1200	P1500	P2000	P2500	P3000
Average particle diameter μm	21.8	18.3	15.3	12.6	10.3	8.4	6
Picture							

finally an error in the measured signals. Because this error is quite small it is neglected. While the sensors and clamping are representing the FSC, the natural vibrissa is replaced by a spring steel wire. The material properties of the spring steel are given by DIN EN 10270-1:2017-09. The Young's modulus of the spring steel is 206000 MPa, it's length L is set to 100 mm and a diameter d of 0.3 mm is chosen. To verify different levels of surface textures, 14 sandpapers with different grit sizes are used, see Table 4.1.

The sensor is displaced by a distance of 100 mm with a constant velocity $v = 5\frac{mm}{s}$. The distance between the clamping and the surface is 55 mm. Each sandpaper is measured 5 times with a sample rate of 1000 Hz for each signal. The corresponding μ and number of stick-slip cycles n are determined. A normal distribution of the measured values and corresponding confidence interval of $\zeta \pm 3\sigma$, with ζ as mean and σ as standard deviation, is assumed for the determined μ. Furthermore, only values in the interval $x_0 \in 20$ mm, 80 mm are considered to minimize effects of the start and end of the displacement. Besides that, the measured forces are edited using a simple moving average of 10th order and all frequencies larger than 10 Hz are filtered out.

4.3 Results

The measured forces F_x and F_y are shown in Fig. 4.2. There are differences between the measured data and the simulation. The amplitude and the frequency of the signal are changing in case of the experimental data while the quasi-static simulation shows
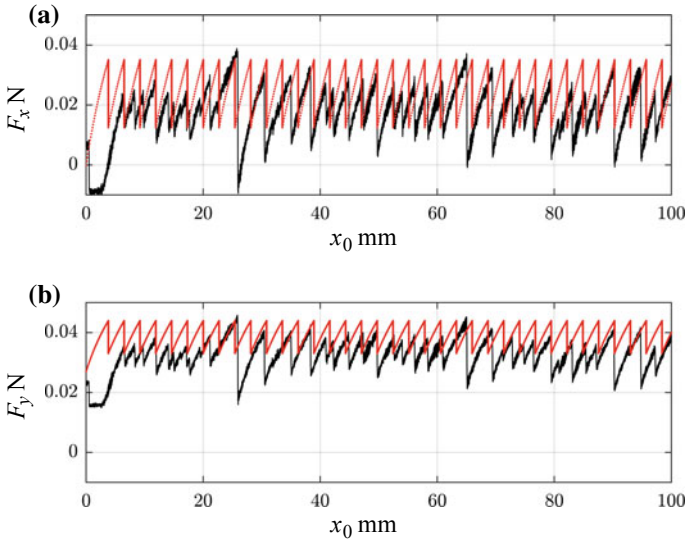
Fig. 4.2 Support reactions F_x (**a**) and F_y (**b**) versus the displacement x_0 of the clamping during scanning a surface of sandpaper (type P800)—simulation data (red) and experimental data (black)

ideal behavior. Especially, the start of the clamping displacement is influenced by a running-in behavior and finally excluded from the signal used for further processing (see Sect. 4.2).

The values for μ_s and μ_d are not examined because of the large change in the amplitude of the signal. A mean μ_m of all values for μ (including μ_s and μ_d) is assumed as a representation for the contact properties. Figure 4.3a shows the values for μ_m for every sandpaper type. Regarding some exceptions, a larger μ_m corresponds to a sandpaper with a larger average particle diameter. Large changes in the grit size are determined well, e.g., P120/Ø125 μ m versus P800/Ø21.8 μm, while small changes are not detectable, e.g., P240 / Ø58.5 μm versus P600/Ø25.8 μm. This effect is noticeable in Fig. 4.3b, too. In Fig. 4.3b, μ_m is compared to the number of stick-slip cycles n. For the measured data, there are large deviations of n. Furthermore, the matching between experimental data simulation is inadequate. This is caused by multiple disturbances in the experiment, e.g., a parasitic motion of the steel wire in the z-dimension. Here, n is not a reliable source of information of the surface texture. Also, the simulated data shows difficulties. There are two values of μ_m for one n. The maximal resolution of μ_m depends on the used step size for x_0 and x_L, fine changes need very small step sizes.
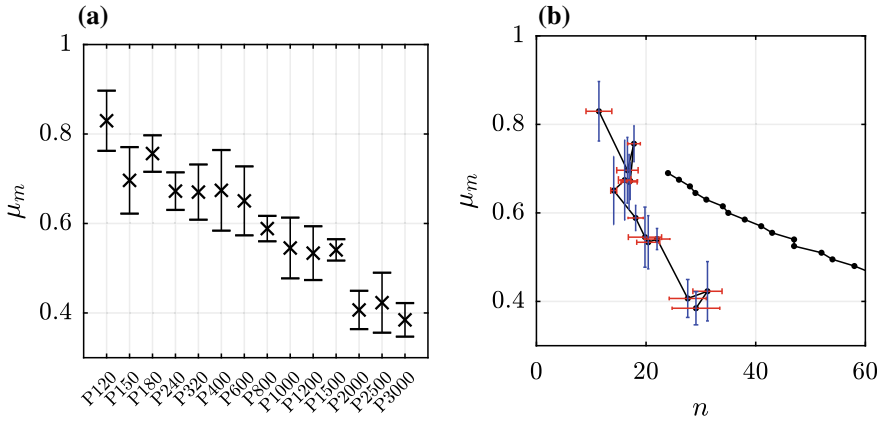
Fig. 4.3 Mean of the friction coefficient μ_m versus sandpaper type (**a**) and versus the number of stick-slip cycles n (**b**). The relation between μ_m and n is analyzed by simulations (black dotted line) and experiments (red bars-standard deviation of n, blue bars-standard deviation of μ_m)

4.4 Conclusion

A first approach for a novel artificial sensor for detection of surface texture properties is presented. The approach is analyzed in an experiment and simulation. Different levels of sandpaper grit sizes are classified based on the measurement of the support reactions. There is a relation between average particle diameter of the sandpaper and the present friction, whereby a larger particle diameter corresponds to larger friction effects. The resolution of the discriminability of the sandpapers is limited to large changes in the dimension of the particles. The analysis of the number of stick-slip cycles and related friction coefficient, grit size respectively, shows large standard deviations and is not a reliable source for the surface texture properties. The different sources of information have to be combined to identify a surface texture well. These findings are in accordance to biological ones [18]. The simulation shows a qualitative similar behavior compared to the experimental data but is not suitable for quantitative analysis.

In a further step, there are various possibilities to optimize the experiment and simulation, e.g., in the case of the experiment the parasitic rotation and displacement of the contact plane have to be prevented. The mechanical model is advanced to take dynamic effects into account [11].

But, also a change in the principal concept have to be mentioned. Changing the direction of the displacement of the sensor support, in the way that the sensor tip is pulled over the surface will analyzed in detail.

References

1. Arabzadeh, E., Zorzin, E., et al.: Neuronal encoding of texture in the whisker sensory pathway. PLoS Biol. **3**, e17 (2005)
2. Boubenec, Y., Claverie, L.N., et al.: An amplitude modulation/demodulation scheme for whisker-based texture perception. J. Neurosci. **34**(33), 10832–10843 (2014)
3. Brecht, M., Preilowski, B., et al.: Functional architecture of the mystacial vibrissae. Behav. Brain Res. **84**(1–2), 81–97 (1997)
4. Carvell, G.E., Simons, D.J.: Biometric analyses of vibrissal tactile discrimination in the rat. J. Neurosci. **10**(8), 2638–2648 (1990)
5. Dörfl, J.: The musculature of the mystacial vibrissae of the white mouse. J. Anat. **135**(1), 147–154 (1982)
6. Quist, B.W., Hartmann, M.J.Z., et al.: Modeling forces and moments at the base of a rat vibrissa during noncontact whisking and whisking against an object. J. Neurosci. **34**(30), 9828–9844 (2014)
7. Rice, F.L., Mance, A., et al.: A comparative light microscopic analysis of the sensory innervation of the mystacial pad. I. Innervation of vibrissal follicle-sinus complexes. J. Comp. Neurol. **252**(2), 154–174 (1986)
8. Scharff, M., Behn, C., et al.: Towards the development of tactile sensors for surface texture detection. In: Martin, A., Gonçalves, G., et al. (eds.) Proceedings of the 5th International Conference on Intelligent Systems and Applications (INTELLI). Barcelona, Spain, 18–22 Feb (2016) (ThinkMind)
9. Scharff, M., Alencastre, J.H., et al.: Investigations on the mechanical relevance of prominent vibrissa features for surface texture detection. In: Scharff, P., Weber, C., et al. (eds.) Engineering for a Changing World: 59th IWK, Ilmenau Scientific Colloquium, Technische Universität Ilmenau, Germany, 11–15 Sept (2017) (ilmendia)
10. Scharff, M., Darnieder, M., et al.: Towards the development of tactile sensors for determination of static friction coefficient to surfaces. In: Zentner, L., Corves, B., et al. (eds.) Microactuators and Micromechanisms. Mechanisms and Machine Science, vol 45. Springer, Cham (2017)
11. Scharff, M., Darnieder, M., et al.: Theoretical investigations on the behavior of artificial sensors for surface texture detection. Springer Proceedings in Mathematics & Statistics (to be published)
12. Steigenberger, J., Behn, C., et al.: Mathematical model of vibrissae for surface texture detection. Preprint No. M 15/03. Institute of Mathematics, Technische Universität Ilmenau, Germany (2015)
13. Voges, D., Carl, K., et al.: Structural characterization of the whisker system of the rat. IEEE Sens. J. **12**(2), 332–339 (2012)
14. Volkova, T., Zeidis, I., et al.: Analysis of the vibrissa parametric resonance causing a signal amplification during whisking behaviour. J. Bion. Eng. **13**(2), 312–323 (2016)
15. Will, C., Behn, C., et al.: Object contour scanning using elastically supported technical vibrissae. ZAMM J. Appl. Math. Mech./Zeitschrift für Angewandte Mathematik und Mechanik (2017). https://doi.org/10.1002/zamm.201600161
16. Wolfe, J., Hill, D.N., et al.: Texture coding in the rat whisker system: slip-stick versus differential resonance. PLoS Biol. **6**(8), e215 (2008)
17. Zucker, E., Welker, W.I.: Coding of somatic sensory input by vibrissae neurons in the rat's trigeminal ganglion. Brain Res. **12**(1), 138–156 (1969)
18. Zuo, Y., Perkon, I.: Whisking and whisker kinematics during a texture classification task. Philos. Trans. R. Soc. B Biol. Sci. **366**(1581), 3058–3069 (2011)

Chapter 5
Analysis of the Dynamic Behavior of Beams Supported by a Visco-Elastic Foundation in Context to Natural Vibrissa

Jhohan Chavez Vega, Moritz Scharff, Thomas Helbig, Jorge H. Alencastre, Valter Böhm and Carsten Behn

Abstract Rodents use their mystacial vibrissae, e.g., to recognize the shape or determine the surface texture of an object. The vibrissal sensory system consists of two components: the hair shaft and the follicle-sinus complex (FSC). Both components affect the collection of information, but the impacts of the different properties are not completely clear. Borrowing the natural example, the goal is to design a powerful artificial sensor. The influence of a continuous visco-elastic support is analyzed for an artificial sensor following hypotheses about the FSC. Starting with a theoretical treatment of this scenario, the vibrissa is modeled as an Euler-Bernoulli bending beam with a partially continuous visco-elastic support. The numerical simulations are validated by experiments. Using a steel strip as a technical vibrissa and a magneto-sensitive elastomer (MSE) as representation of the artificial continuous visco-elastic support, FSC respectively, the first resonance frequency is determined.

J. Chavez Vega (✉) · M. Scharff (✉) · T. Helbig · V. Böhm · C. Behn
Department of Mechanical Engineering, Technische Universität Ilmenau, Max-Planck-Ring 12, 98693 Ilmenau, Germany
e-mail: jhohan-harvey.chavez-vega@tu-ilmenau.de

M. Scharff
e-mail: moritz.scharff@tu-ilmenau.de

T. Helbig
e-mail: thomas.helbig@tu-ilmenau.de

V. Böhm
e-mail: valter.boehm@tu-ilmenau.de

C. Behn
e-mail: carsten.behn@tu-ilmenau.de

J. H. Alencastre
Department of Engineering, Pontifical Catholic University of Peru, Av. Universitaria N° 1801, San Miguel, Lima, Peru
e-mail: jalenca@pucp.edu.pe

5.1 Introduction

The animal world shows several concepts of sensory systems, e.g., the eyesight, olfaction and sense of touch. Especially, rodents have a sophisticated tactile sensory system. Using this system, obstacles and objects can be located and identified in terms of the determination of distance to the object, the recognition of its shape and the detection of its surface texture [19]. On this way, the functional principle and structure of the sensory system have to be analyzed to adapt it for an artificial sensor. This work focuses on the influence of a continuous visco-elastic support on the first resonance frequency.

For this, the paper is arranged as follows: Sect. 5.2 gives a short review on the biological aspects as well as on associated aspects from a technical point of view. Section 5.3 focuses on the theoretical modeling of the problem and the experimental setup. The results of the simulation and the experiments are described and discussed in the Sect. 5.4. Finally, a brief summary and evaluation are done in Sect. 5.5.

5.2 State of the Art

Rodents have tactile hairs at different places all over their body. One type of these tactile hairs are the vibrissae. Vibrissae are located, e.g., near above the paws (carpal vibrissae) or around the snout (mystacial vibrissae) [10]. The mystacial vibrissae are part of the mystacial pad. There is one mystacial pad on each side of the snout. The mystacial pad is a particular arrangement consisting of arcs and rows of mystacial vibrissa [8]. Every hair shaft is supported by its own follicle-sinus complex (FSC) [15], see Fig. 5.1. The FSC itself is embedded in the mystacial pad and surrounded by several types of muscles and different elastic tissues. Using the muscles the vibrissae can be swept actively [8]. The FSC consists of different parts: there are different types of nerve cells, elastic tissue and bloodvessels [13]. To change the sensitivity of the sensory system, the visco-elastic properties of the FSC seems to be adjustable by controlling the blood pressure inside the bloodvessels [13]. It is assumed that white noise of unknown stimuli is excluded from essential signals by controlling the blood pressure in the vessel [17]. All components are annular arranged around the hair shaft in the FSC. The hair shaft has a tapered body (decreasing diameter from base to tip) and its length is much larger than its diameter. The whole vibrissa is three dimensional pre-curved. The interior of the hair shaft is structured by different layers, e.g., medulla. The outside is covered with scales [16]. Using the combination of vibrissa and FSC, the animals can collect various information about the environment, like mentioned in Sect. 5.1. Source of theses information are the deflection, vibration and motion pattern of the vibrissae. All information is relatively affected by the dynamic properties of the combination of vibrissa and FSC. For example, for the procedure of surface texture detection, two hypotheses are assumed: the *Resonance Hypothesis* as well as the *Kinetic Signature Hypothesis* deal with highly dynamical

(a) Sliced FSC of a rat.   (b) Theoretical model.   (c) Strip embedded on MSE.
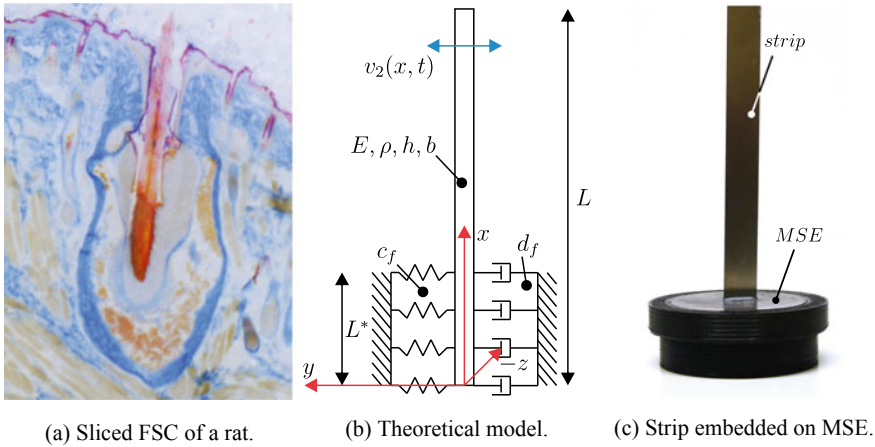
Fig. 5.1 Longitudinal section of a natural FSC of a rat (**a**), model for simulation (**b**), and sample used for experiments (**c**)

signals, and the resonance frequency of vibrissa and FSC has a significant influence [1, 12].

Based on these biological findings from literature, there are several theoretical models of bending beams including a visco-elastic support, e.g., [4, 5, 11] and experiments, e.g., [7, 14], too.

5.3 Methods

To analyze the relation between the visco-elastic properties of the support and the first resonance frequency f_1 of the coupled system (beam and its support), several simulations and an experiments are performed, see Sects. 5.3.1 and 5.3.2. For the theoretical model the natural hair shaft is assumed as an Euler-Bernoulli beam, see Fig. 5.1a. The amplitudes of the vibrations of the beam are expected to be low. Furthermore, it is assumed that:

- the material behavior is a linear elastic one, with Young's modulus E and density ρ;
- the beam is straight (length L) with a constant rectangular cross section, whereby the width b refers to z-dimension and the height h to the y-dimension.

The FSC is modeled by a continuous visco-elastic support with spring rate c_f, damping coefficient d_f and an extent of L^* in x-dimension, all represented by an MSE in experiments.

The rectangular cross section of the beam is used because of circumstances of the experimental setup. For the experiment, a strip of spring steel is used as a beam

to facilitate the signal detection, see Fig. 5.1c. The spring steel strip is supported by a magneto-sensitive elastomer (MSE). The MSE changes its stiffness and damping properties in dependence on the applied magnetic field [3, 9, 18]. The assembly of spring steel strip and MSE is mounted onto an electrodynamic shaker, see Sect. 5.3.2.

5.3.1 Simulation

According to the Euler-Bernoulli beam theory and the structure of the system, see Fig. 5.1b, there are two beam sections. Section one is described by (5.1) and includes the elastic foundation:

$$\rho A \ddot{v}_1(x, 1) + E I_z v_1''''(x, t) + d_F \dot{v}_1(x, t) + c_F v_1(x, t) = 0 \tag{5.1}$$

The second beam section (5.2) oscillates without any further effects:

$$\rho A \ddot{v}_2(x, 1) + E I_z v_2''''(x, t) = 0 \tag{5.2}$$

The resulting (boundary) conditions are:

$$\left.\begin{array}{lll}
 & v_1(L^*, t) = v_2(L^*, t) & \\
 & v_1'(L^*, t) = v_2'(L^*, t) & \\
v_1''(0, t) = 0 & v_1''(L^*, t) = v_2''(L^*, t) & v_2''(0, t) = 0 \\
v_1'''(0, t) = 0 & v_1'''(L^*, t) = v_2'''(L^*, t) & v_2'''(0, t) = 0
\end{array}\right\} \tag{5.3}$$

The whole problem consisting of (5.1), (5.2) and (5.3) is solved by separation of the variables:

$$v(x, t) = T(t) \cdot X(x) \qquad \forall (x, t) \tag{5.4}$$

The solution is adapted from [2].

5.3.2 Experiment

In the experiments, a steel strip (100.15 mm × 9.65 mm × 0.1 mm, $E = 206$ GPa, $\rho = 7.850e - 6$ kg/mm^3) is embedded into a cylindrical MSE-sample (diameter: 40 mm, height: 15 mm, partially encased by housings on the circumferential and bottom surfaces). The isotropic MSE consisting of silicone rubber (Alpa-Sil Classic, Alpina Silicone Corp.), silicone oil (Xiameter® PMX-200, 500 cSt), and carbonyl iron particles (BASF®, CIP CC, average particle size: 6 μm) is used. The composition for the fabrication of the MSE-sample results from former investigations [6, 18] (silicone oil cSt: 29 vol.%, carbonyl iron particles: 40.3 vol.%). To characterize the

Fig. 5.2 Experimental
setup: MF induced by
permanent magnets, input
amplitude measured by a
triangulation lasersensor and
oscillating response of the
strip measured by a second
triangulation lasersensor
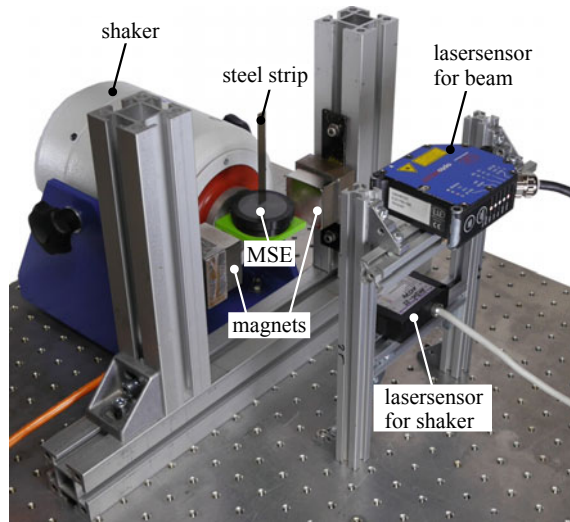
effect of the magnetic field on the first resonance frequency f_1 and damping ratio D
of the steel strip embedded on the MSE-sample, tests are performed to measure its
response to the presence of a forced vibration under three conditions of magnetic field
(MF): without MF, regular MF (average: 63 mT) and strong MF (average: 180 mT).
The magnitude of MF at the MSE-sample, induced by a pair of permanent magnets
(NdFeB, 40 mm × 40 mm × 20 mm), is controlled by the distance between the MSE-
sample and both permanent magnets, see Fig. 5.2.

In order to experimentally find an approximation of the first resonance frequency
f_1 (tests of type I), the MSE-sample is fixed to a shaker which provides a sinusoidal
waveform. A constant amplitude of 0.5 mm (measured by a triangulation lasersensor)
in the frequency range of 2...20 Hz is the input of the experiments. The response of the
steel strip is measured through a second lasersensor. The value of f_1 is approximated
to the frequency where the end of the strip has the biggest response amplitude, see
Fig. 5.3a. For every frequency, the amplitude of the oscillation of the end of the strip
is recorded. A second type of experiments (tests of type II) is performed to approach
the damping ratio D. A pulse signal is given by the shaker on the bottom of the MSE,
the strip oscillates with amplitude decreasing in time. In this period, the coefficients
for the damping ratio can be found.

5.4 Results

The results from the experiments of type I show that for every condition of induced
MF to the MSE, there is a excitation frequency where the oscillation of response
reaches a maximum value (see Fig. 5.3a), at frequency f_1. The result of every

(a) Amplitude versus frequency
for three induced MF.

(b) Amplitude versus time.
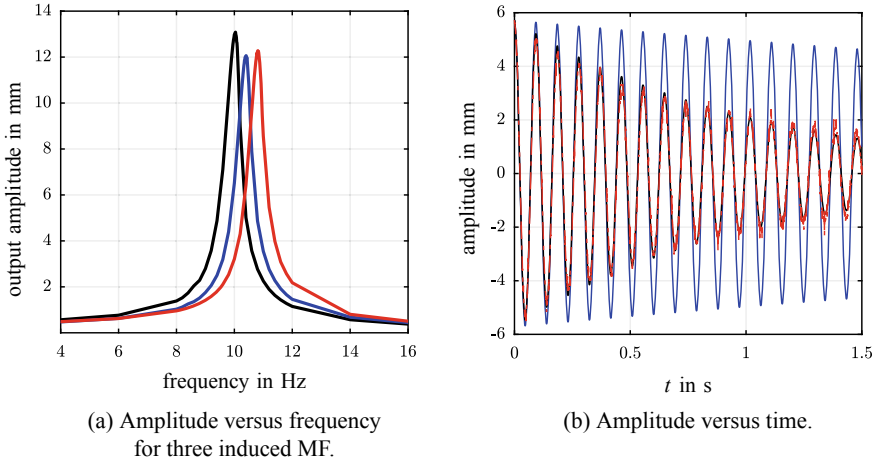
Fig. 5.3 Results for the amplification of the amplitude (**a**)—black curve: 0 mT, blue curve: 63 mT and red curve: 180 mT. Response of the strip to a pulse (**b**) for a MF: 180 mT—experimental data (red curve), Simulation data with $d_f = 0.00212$ kg/s (blue curve) and $d_f = 0.015$ kg/s (black curve)

Table 5.1 Experimental data of f_1 and D for both experiments

MF	Test I: f_1				Test II: D	
	f_1	s. dev.	D	s. dev.	f_1	s. dev.
mT	Hz	–	–	–	Hz	–
0	10.03	0.0167	0.00825	0.0001	10.00	0.0026
63	10.41	0.0207	0.00865	0.0001	10.50	0.0016
180	10.81	0.0114	0.01298	0.0001	10.83	0.0032

experiment of type II is the typical oscillation of an underdamped system, see Fig. 5.3b. The average values and standard deviation of f_1 and D from five measurements are summarized in Table 5.1. The resonance frequency f_1 can also be calculated from curves fits from the experiments of type II. However, after few seconds from the pulse signal, the error on the measurement of the strip oscillation (resolution of triangulation lasersensor) has a significant influence on the parameters of the fitted curve since the oscillation amplitude is already decreased. Hence, the frequencies f_1 found in the experiments of type I are more reliable.

The experimental results are used to verify the theoretical model, see Figs. 5.3b and 5.4. There are large deviations for the case of the decaying vibration in Fig. 5.3b. In the beginning there is a good coincidence of experiment and simulation in all cases, but with increasing time it is getting worse. The damping is stronger in the experiment.

(a) f_1 versus c_f and d_f.   (b) D versus c_f and d_f.
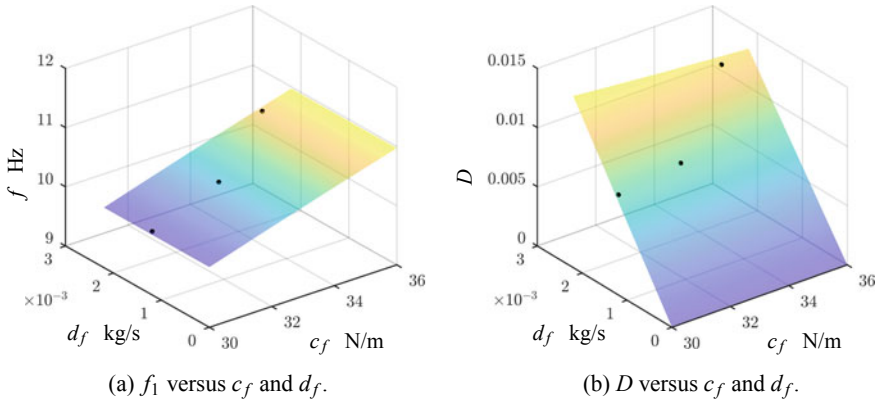
Fig. 5.4 Simulation data of **a** f_1 and **b** D in comparison to the experimental data (black dots)

Table 5.2 Change of c_f and d_f in consequence of different MF's

MF mT	c_f N/m	$\Delta\%$	d_f kg/s	$\Delta\%$
0	30.09		0.00125	
63	32.39	≈7.5	0.00136	≈8.8
180	34.95	≈16	0.00212	≈69.6

A reason for this can be frictional effects between the steel strip and the surface of housing of the MSE. The damping ratio D as well as f_1 are depending on the properties d_f and c_f of the continuous visco-elastic support. Combining the experimental results with the simulation data there is one set of c_f and d_f that matches the experimental values for f_1 and D. Table 5.2 summarizes the changes of c_f and d_f for the different levels of the MF.

5.5 Conclusion

In the present study, investigations on the potential use of the effect of magnetic fields on the change of resonance frequency and damping ratio for a steel strip embedded into an MSE sample were considered. It can be concluded, that the resonance frequency and the damping factor can be tuned under the presence of a magnetic field, and the considered effect can be used to realize a vibrissal sensory system which can vary its properties (on its own). The experimental data for the resonance frequency matches the simulation data well, but in the case of the damping ratio there are large deviations considering the whole decaying process. Further investigations focus on tests with various compositions for the MSE-samples, e.g., diverse levels

of MSE-samples visco-elasticity by varying the viscosity of the used silicone oil. These considerations include also tests with a wider range for the induced magnetic field as well as more geometries as representation of the vibrissa.

References

1. Arabzadeh, E., Zorzin, E., et al.: Neuronal encoding of texture in the whisker sensory pathway. PLoS Biol. **3**, e17 (2005)
2. Baldeweg, D., Will, C., et al.: Transversal vibrations of beams in context of vibrissae with foundations, discrete supports and various sections. In: Scharff, P., Weber, C., et al. (eds.) Shaping the future by engineering: 58th IWK, Ilmenau Scientific Colloquium, Technische Universität Ilmenau, Germany, 8–12 Sept (2014). (ilmendia. urn:nbn:de:gbv:ilm1-2014iwk-081:7)
3. Becker, T.I., Raikher, Y.L., et al.: Dynamic properties of magneto-sensitive elastomer cantilevers as adaptive sensor elements. Smart Mater. Struct. **26**, 1–9 (2017)
4. Behn, C.: Adaptive control of vibrissae-like mechanical sensors. Commun. Nonlinear Sci. Numer. Simul. **16**(5), 2254–2264 (2011)
5. Behn, C., Scharff, M., et al.: Modeling of controllable support stiffness bio-inspired by tactile sensor systems. In: Stépán, G., Csernák, G. (eds.) Proceedings of the 9th European Nonlinear Dynamics Conference, Budapest, Hungary, 25–30 June. CongressLine Ltd. (2017). http://congressline.hu/enoc2017/abstracts/313.pdf
6. Chavez Vega, J., Kaufhold, T., et al.: Field-induced plasticity of magneto-sensitive elastomers in context with soft robotic gripper applications. Proc. Appl. Math. Mech. **17**, 23–26 (2017)
7. Conn, A.T., Pearson, M.J., et al.: Dielectric elastomer vibrissal system for active tactile sensing. In: Bar-Cohen, Y. (ed.) Electroactive polymer actuators and devices (EAPAD), San Diego, United States, pp. 12–15. March. SPIE, Bellingham, United States (2012)
8. Dörfl, J.: The musculature of the mystacial vibrissae of the white mouse. J. Anat. **135**(1), 147–154 (1982)
9. Han, Y., Hong, W., et al.: Field-stiffening effect of magneto-rheological elastomers. Int. J. Solids Struct. **50**(14–15), 2281–2288 (2013)
10. Helbig, T., Voges, D.: Characterizing the substrate contact of carpal vibrissae of rats during locomotion. In: Duff, A., Lepora, N.F., et al. (eds.) Biomimetic and Biohybrid Systems. Living Machines 2014. Lecture Notes in Computer Science, vol. 8608. Springer, Cham (2014)
11. Mitchinson, B., Gurney, K.N.M.L., et al.: Empirically inspired simulated electro-mechanical model of the rat mystacial follicle-sinus complex. Proc. R. Soc. B Biol. Sci. **271**(1556), 2509–2516 (2004)
12. Moore, C.I., Andermann, M.L.: The vibrissa resonance hypothesis. In: Ebner, F.F. (eds.) Neural Plasticity in Adult Somatic Sensory-Motor Systems. Frontiers in Neuroscience. CRS Press, Taylor & Francis (2005)
13. Rice, F.L., Mance, A., et al.: A comparative light microscopic analysis of the sensory innervation of the mystacial pad. I. Innervation of vibrissal follicle-sinus complexes. J. Comp. Neurol. **252**(2), 154–174 (1986)
14. Valdivia y Alvarado, P., Bhat, S.: Whisker-like sensors with tunable follicle sinus complex for underwater applications. In: Lakhtakia, A., Martn-Palma, R.J. (eds.) Bioinspiration, Biomimetics, and Bioreplication. Proceedings of SPIE, vol.9055. SPIE, Bellingham, United States (2014)
15. Vincent, S.B.: The tactile hair of the white rat. J. Comp. Neurol. **23**(1), 1–34 (1913)
16. Voges, D., Carl, K., et al.: Structural characterization of the whisker system of the rat. IEEE Sens. J. **12**(2), 332–339 (2012)

17. Wrobel, K.H.: Bau und Bedeutung der Blutsinus in den Vibrissen von Tupaia glis. Zentralblatt für Veterinärmedizin Reihe A **12**(9), 807–899 (1965) [Transboundary and Emerging Diseases]
18. Zimmermann, K., Böhm, V., et al.: Investigations and simulations on the mechanical behaviour of magneto-sensitive elastomers in context with soft robotic gripper applications. Int. Sci. J. IFToMM "Problems of Mechanics" **4**(65), 13–26 (2016)
19. Zucker, E., Welker, W.I.: Coding of somatic sensory input by vibrissae neurons in the rat's trigeminal ganglion. Brain Res. **12**(1), 138–156 (1969)

Chapter 6
Design of a Cable-Driven Device for Elbow Rehabilitation and Exercise

Marco Ceccarelli, Lucia Ferrara and Victor Petuya

Abstract The paper presents a new rehabilitation device for elbow motion as based on a cable-driven parallel manipulator. The kinematic design is presented as characterized with a numerical evaluation of motion performance and an experimental validation. A CAD design is simulated as the basis for a prototype construction. Tests with a built prototype are discussed to show its feasibility and operation characteristics.

Keywords Service robotics · Rehabilitation device · Cable parallel manipulators · Design · Testing

6.1 Introduction

Movement disorders or weakness are neurological syndromes that may give excess of movement or a paucity of movement that is not connected to weakness, paralysis or spasticity of the muscles. They affect the speed, fluency or smoothness, quality and ease of movement. The help of robotics in movement disorders and post-stroke patients' rehabilitation as well as in elderly people exercise has been investigated intensively like for example in [1–7]. In fact, medical therapies have highlighted the need of rehabilitation procedures with key features such as effectiveness of repetitive and repeatable performance for motion tasks, since a specific rehabilitation strategy can allow the progressive recovery of specific motion functions, and can achieve a

M. Ceccarelli (✉)
Beijing Advanced Innovation Center for Intelligent Robots and Systems, Beijing Institute of Technology, Beijing, China
e-mail: marco.ceccarelli@unicas.it

M. Ceccarelli · L. Ferrara
LARM, Laboratory of Robotics and Mechatronics, University of Cassino and South Latium, Cassino, Italy

V. Petuya
Department of Mechanical Engineering, University of Basque Country UPV/EHU, Leioa, Spain
e-mail: victor.petuya@ehu.com

minimum muscular tone, [2]. Parallel cable-driven robots can provide cost-effective solutions with automated and controlled structures with suitably large workspaces [2]. They are able to perform several kinds of movements similarly to anthropomorphic robotst with higher payloads. Illustrative well-known examples are NeReBot [5], MEDARM [6] and Carex [7].

In this paper, a new rehabilitation device is proposed as based on a cable-driven parallel manipulator for assisting elbow motion with user-oriented wearable light design and direct operation. The main design features are presented together with a numerical characterization of performance as a basis for the construction of a prototype. Test results with a lab prototype show the feasibility and operation efficiency of the proposed design.

6.2 Requirements for Elbow Exercise Rehabilitation

The elbow articulation is a complex hinge joint that is formed between the distal end of the humerus in the upper arm and the proximal ends of the ulna and radius in the forearm [8, 9]. The elbow allows the flexion and extension of the forearm relative to the upper arm, as well as rotation of the forearm and wrist, [8]. Flexion is the movement that drives the forearm forward so that the front face of the forearm approaches the front face of the arm. In general, the breadth of the active flexion is 145°, while the passive bend breadth is 160° as reported in [9].

The main goals of elbow rehabilitation and exercise are the recovery of stability, mobility and strength to levels enough to carry out daily work activities that are related to work and hobbies, all without pain. Rehabilitation of elbow motion is usually achieved by a physiotherapist, who strongly assists the arm motion. But not always a physiotherapist is able to perform this therapy efficiently since it sometimes involves very long and repetitive exercises. Thanks to robotic equipment a personalized exercising is possible to achieve a total recovery with repetitive exercise even within home environments as pointed out in [7]. Thus, requirements for an assisting device can be identified in a design structure that can be fairly easily adjusted to the patient specific needs and can be operated by the patient himself with suitable operation characteristics during the therapy as indicated by a therapist. Those requirements can be summarized in expected goals in terms of proper size and operation user-oriented features, easy transportation and wearable design, comfort operation with sensor-assisted controlled supervision.

6.3 The Proposed Design

A parallel robot consists of an end-effector that is connected to a fixed base by at least two independent kinematic chains [10]. In the case of cable driven parallel manipulator robots, the kinematic chains are constituted by cables and platform

Fig. 6.1 A scheme of the proposed kinematic design with main parameters
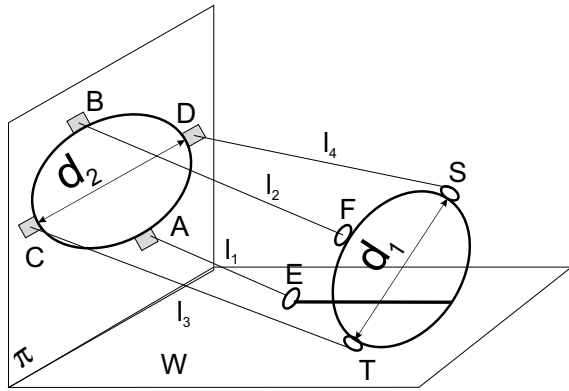
bodies. Therefore, the kinematic structure of the parallel manipulator under design will consist of the following parts:

- A platform acting as fixed base with suitable shape for wearing it on the user's arm;
- An end-effector platform with suitable shape for wearing it on the user's forearm;
- A certain number of cables connecting the above two platforms.

The operation task as assisting device consists in an elbow different movement for flexion and extension of the forearm through angular motions of the forearm, with the elbow joint as the rotation center. The trajectory that is traced by the middle point of the forearm is a circular arc in the plane that is defined in sagittal plane, [9], in the model of Fig. 6.1 as the plane orthogonal to π and W planes.

The kinematic design in Fig. 6.1 is characterized by the upper ring platform ABCD of diameter d_2, the lower ring platform FST of diameter d_1, the four cables l_1, l_2, l_3 and l_4 that are actuated by the motors at points A, B, C and D, respectively. The two ring platform structures will avoid a risk of tweaking due to the cables around the arm. The cables l_3 and l_4 are used to avoid or guide a lateral motion of the forearm, while the cables l_1 and l_2 can be used for extension/flexion motion of the forearm.

The elbow exercise requires a motion planning of the end-effector ring platform with a suitable actuation of the cables. The inverse position problem can be solved to find the cable lengths as function of the end-effector platform position. For the flexion-extension movement, the kinematic scheme for the motion of cables l_1 and l_2 is shown in Fig. 6.2a. The length of the cable l_1 is defined by points A and E which are the attachment points of the cables to the motor and the end-effector platform. Similarly, the length of the cable l_2 is defined by points B and F which represent the attachment points of the cable to the motor and the end-effector platform. Sizes L and Q indicate the lengths of the forearm. ϑ represents the angular displacement of the forearm. Considering a reference frame Gxy fixed in the center G of the upper platform (as in Fig. 6.2b), the circular motion of the cable attachments during flexion-

(a)

(b)
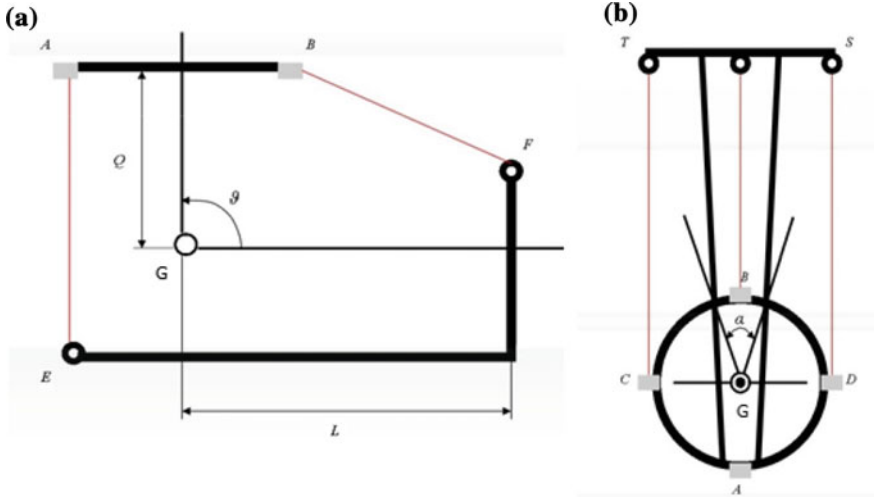
Fig. 6.2 Schemes for cable motion modeling in Fig. 6.1: **a** in the plane π; **b** in plane W

extension arm movements can give the length of the cables in a straight forward way. For example, the length of the cable l_1 can be computed by

$$l_1 = \sqrt{AE_x^2 + AE_y^2} \tag{6.1}$$

with

$$AE_x = E_x + \frac{d_2}{2} \quad AE_y = (E_y - Q) \tag{6.2}$$

where the position vector of E can be expressed as

$$\left\{ \begin{matrix} E_x \\ E_y \end{matrix} \right\} = \left[\begin{matrix} \cos \vartheta & -\sin \vartheta \\ \sin \vartheta & \cos \vartheta \end{matrix} \right] \left\{ \begin{matrix} -\frac{d_2}{2} \\ -\frac{d_1}{2} \end{matrix} \right\} \tag{6.3}$$

Similar calculation can be used for l_2 when referring to points B and F.

Figure 6.3 shows a CAD mechanical design of the device that is based on a proper modeling of human arm as suggested in [11, 12], and it used also for simulating operation performance. The device is composed by an upper ring platform, a lower ring platform, four cables, four pulleys and four servomotors with proper sizes and shapes with commercial components in agreement with the kinematic design in Fig. 6.1. The ring platforms are designed in such way that a patient can wear them with the forearm at 90°. The beam in the lower platform is used to attach cable l_1 safely without interference with the patient arm, and it can be properly shaped for a comfort positioning of the patient arm. Comfort and position stability of the platforms are ensured by using a soft elastic cover inside the platform surface in
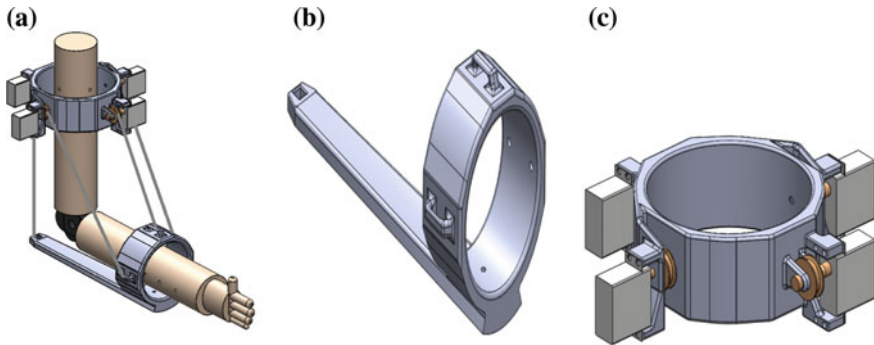
Fig. 6.3 A CAD mechanical design of the proposed device in Fig. 6.1: **a** the overall design installed on an arm model; **b** lower ring platform with forearm support beam; **c** upper ring platform with cable servomotors

contact with the patient arm by a proper fixing that ensures no relative motion but no excessive pressure on the arm body.

6.4 Performance Evaluation via Simulation

A mechanical design has been defined also by means of a dynamic simulation of the operation performance. Results of the simulation are used to characterize the device operation and to discuss the design peculiarities as referring to the main operation modes such as flexion-extension of the assisted forearm.

The length of each cable is calculated as function of the rotation angle of the forearm by means of Eqs. (6.1)–(6.3). The simulated movement consists of a flexion of the forearm from 0° to 50° and extension from 50° to 0° as shown in Fig. 6.4.

Numerical results of a simulation are reported in Figs. 6.5 and 6.6. In Fig. 6.5a and b the time histories of the cables l_1 and l_2 are shown during the flexion motion indicating that the cable length l_2 decreases over time as related to the fact that motors reel the cables while l_1 increases correspondingly.

In Fig. 6.6a and b the cable lengths change during the extension movement similarly to the flexion motion but with opposite variations indicating that the cable lengths increase or decrease over time as related to the fact that motors release or reel the cables.

The simulation results, as the reported ones, show smooth motion with suitable time history for the forearm motion and cable pulling action.
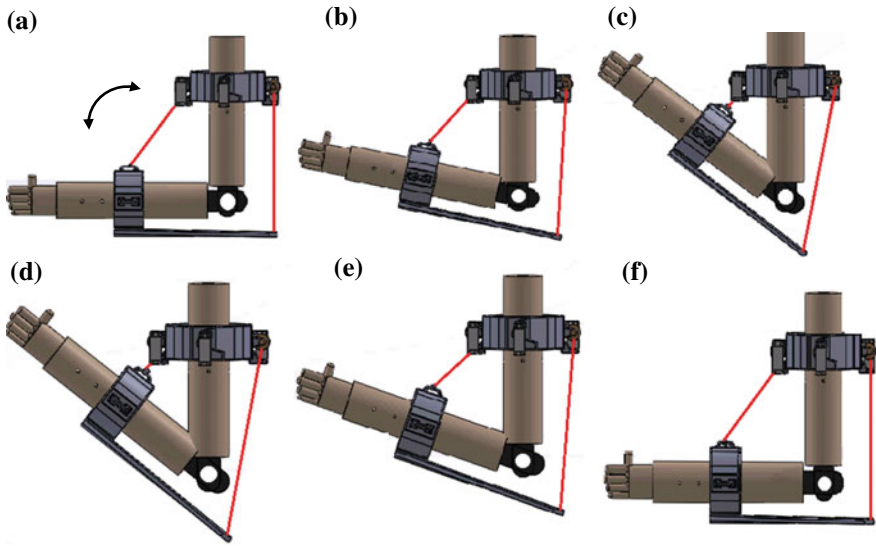
Fig. 6.4 Simulated motion of forearm flexion-extension: **a** start at sec 0.00 s; **b** at sec 0.30; **c** at sec 1.00; **d** at sec 1.10; **e** at sec 1.50 and **f** end at sec 2.00
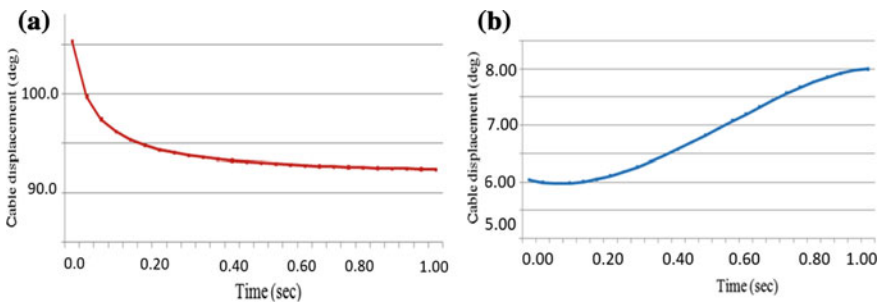
Fig. 6.5 Computed results from flexion motion simulation in Fig. 6.4 for cables l_1 (**a**) and l_2 (**b**)
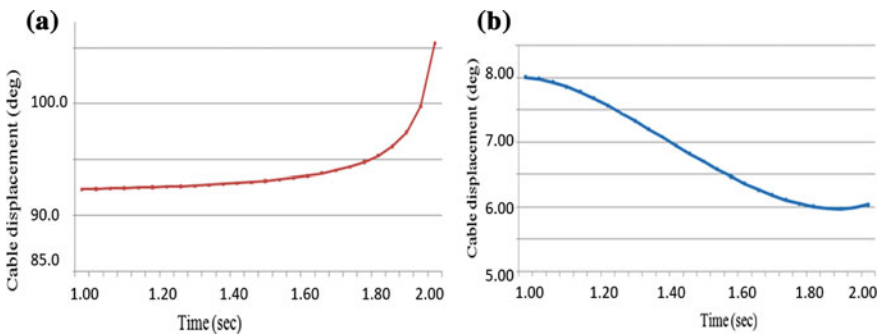
Fig. 6.6 Computed results from extension motion simulation in Fig. 6.4 for cables l_1 (**a**) and l_2 (**b**)
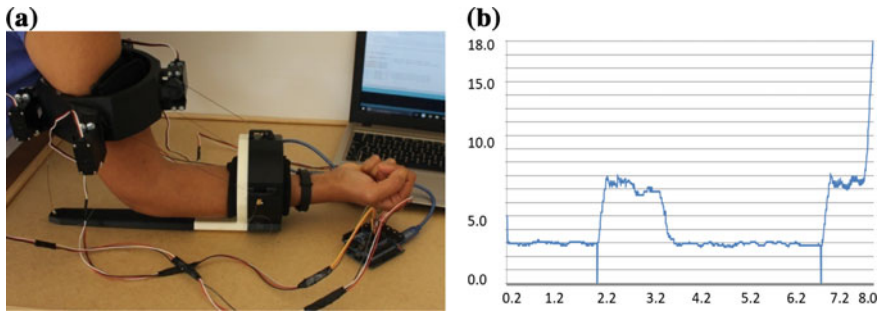
Fig. 6.7 Validation experience: **a** the lab setup for future testing; **b** computed power consumption (W vs seconds) for motion simulation test in Fig. 6.4

6.5 Prototype Construction and Test

A prototype in Fig. 6.7a has been built referring to the proposed design in Fig. 6.1 in agreement also to a patent submission, [13], through a 3D printing manufacturing of the structure parts at the University of Basque Country UPV/EHU. Four SpringRC SM-S4315R servomotors are installed in the upper ring platform with corresponding four pulleys with diameter of 23 mm rolling a nylon cable with a maximum tension of 89 N. The four servomotors are controlled by means of an Arduino Uno card. A prototype in Fig. 6.7a will be used in future experiments with human arms both for experimental validation and performance characterization.

Once the prototype has been built and correctly assembled, the lab set-up has been settled for testing in order to validate experimentally the device. Figure 6.7b shows results in terms of power consumption during the simulated flexion-extension-motion of the forearm in Fig. 6.4. In the plot from 2.1 to 3.8 s the slow flexion movement is computed with a maximum of 7.93 W and from 6.8 to 7.9 s the extension is computed with a maximum in 11.93 W. This simulation test shows that the built device has a proper power consumption that can be afforded by a commercial Li-Poly battery for a suitable wearable solution. Measurements of cable lengths during tests are obtained by using the rotation angle of the pulley. These values when compared to the ones that are obtained through the above kinematics analysis and simulation results demonstrate that the kinematics of the proposed assisting device is efficient for a proper fairly user-oriented operation.

6.6 Conclusions

In this paper a new device for motion exercise and rehabilitation of elbow motion is proposed as based on a cable driven parallel manipulator. The rehabilitation device is designed with two ring platforms that can be wearable by users with low-cost design

and fairly simple comfort operation for home application. Performance of the device has been characterized through simulation and experimental results. A prototype for testing is presented with low-cost user-oriented features. Simulation results are discussed to show the feasibility and efficient characteristics of the proposed device design.

References

1. Kollen, B.J., Krebs, H.I., Kwakkel, G.: Effects of robot-assisted therapy on upper limb recovery after stroke: a systematic review. Am. Soc. Neurorehabilitation: Neurorehabilitation Neural Repair **22**(2), 111–121 (2008)
2. Eschweiler, J., Gerlach-Hahn, K., Jansen-Troy, A., Leonhardt, S., Maciejasz, P.: A survey on robotic devices for upper limb rehabilitation. J. Neuro-Eng. Rehabil. **11**(3), 2–29, (2014)
3. Kawasaki, H., Cox, D., Jeon, D., Saint-Bauzel, L., Mouri, T.: Rehabilitation robotics. J. Robot. **2011**, 1–3 (2011). Article ID 937875, Hindawi
4. Stephenson, A., Stephens, J.: An exploration of physiotherapists' experiences of robotic therapy in upper limb rehabilitation within a stroke rehabilitation centre. J. Disabil. Rehabil. Assist. Technol., 1–8 (2017)
5. Rosati, G., Gallina, P., Masiero, S.: Design, implementation and clinical tests of a wire-based robot for neurorehabilitation. IEEE Trans. Neural Syst. Rehabil. Eng. **15**(4), 560–569 (2007)
6. Ball, S.J., Brown, I.E., Scott, S.H.: MEDARM: a rehabilitation robot with 5DOF at the shoulder complex. In: IEEE International Conference on Advanced Intelligent Mechatronics, Zurich (2007)
7. Mao, Y., Agrawal, S.K.: Design of a cable-driven arm exoskeleton (CAREX) for neural rehabilitation. IEEE Trans. Robot. **28**(4), 922–931 (2012)
8. Halim, A.: Human Anatomy—Upper Limb and Thorax, pp. 19–52. I.K. International Publishing House Pvt., New Delhi (2008)
9. Tözeren, A.: Human Body Dynamics: Classical Mechanics and Human Movement. pp. 84–112, 150–183. Springer, Dordrecht (2008)
10. Ceccarelli, M.: Fundamentals of Mechanics of Robotic Manipulation. Springer, Dordrecht (2004)
11. Captain, E.P., Hanavan, JR.: A mathematical Model of the human body. Air Force Aerospace Medical Research Lab Wright-Patterson AFB OH (1964)
12. Barter, J.T.: Regression Equations for Determining Body Segment Weights, Estimation of the Mass of Body Segments, Technical Report, Air Development Center, Wright-Patterson Air Force Base, Ohio, pp. 57–260 (1957)
13. Ceccarelli, M., Ferrara, L., Petuya, V.: Device for elbow rehabilitation, patent n.102017000083887, 24 July 2017, Italy. (in Italian)

Chapter 7
Transoral Robotic Surgery (TORS) Emulation Using a Highly Flexible Robotic System

**Catalina Almeida, Nikolas Bufe, Stefan Mattheis, Stephan Lang
and Andrés Kecskeméthy**

Abstract The gap between the progress of transoral robotic surgery (TORS) adoption and training, has encouraged the industry to develop a variety of multiple-scenario endoscopic procedures without the need of a physical environment, in other words, surgical simulation platforms. Consequently, the authors aimed at developing the initial form of a virtual platform for the reproduction of TORSs, by embedding a highly flexible robotic manipulator, in a patient's head and neck three-dimensional (3D) model, acquired from Computed Tomography (CT) images, to simulate a surgery. This platform intents to provide experienced and inexperienced surgeons and medical students a way of pre-planning, replaying, or practicing a surgery, outside the operating room (OR). This platform is developed in C++ under the Windows operating system using the MobileBody SDK simulation system, using two C++ program libraries, Open Inventor and Mobile. At this stage, the virtual system developed provides a total visualization of the patient's head and neck anatomy, in different perspectives (different camera views), and provides all the movements possible of the robotic system, as in reality. This training tool will allow a proper placement of the robot with the shortest path possible, significantly influencing the success of the operation. Also, this platform, can be efficient as an educational tool for medical students and doctors who are inexperienced in TORSs.

C. Almeida (✉)
School of Engineering, University of Minho, R. da Universidade, 4610-057 Braga, Portugal
e-mail: A68369@alunos.uminho.pt; catalina.almeida@outlook.com

N. Bufe (✉) · A. Kecskeméthy
Department Mechanics and Robotics, University of Duisburg-Essen, Lotharstr. 1, 47058
Duisburg, Germany
e-mail: nikolas.bufe@uni-due.de

A. Kecskeméthy
e-mail: andres.kecskemethy@uni-due.de

S. Mattheis · S. Lang
University Hospital Essen, Hufelandstraße 55, 45147 Essen, Germany
e-mail: stefan.mattheis@uk-essen.de

S. Lang
e-mail: stephan.lang@uk-essen.de

7.1 Introduction

The surgery field is under relentless evolution, thus, medical professionals and researchers continue to investigate novel methods to upgrade and enhance outcomes for patients and doctors, by making the procedures safer, more effective, and shorter [13]. Head and neck cancers (HNCs) have been treated with traditional open surgery procedures; to successfully perform a traditional open surgery in the head and neck areas, a surgeon needs to make long incisions through the patient's jaw and throat, accompanied by the insertion of long instruments [33]. These actions can cause deformities in the patient's head and neck structures, as well as difficulties eating, speaking and swallowing. Additionally, plastic or reconstructive surgery might have to be performed to rebuild bones and/or tissues removed during the surgery [22, 23]. Contemporary technology has made overcoming these challenges easier by introducing better fibreoptics and microscopes [23]. Despite these technological innovations, certain areas are still difficult to visualize and operate without the need of surgically radical approaches [23].

A different approach would be a minimally invasive transoral surgery, consisting of the insertion of a laryngoscope to access and expose the pharynx, while long and rigid surgical tools are maneuvered within the boundaries of the laryngoscope [23]. To achieve a successful visualization and manipulation of the instruments in the pharynx area, a method of visual inspection and tissue resection is necessary [23]. Drs. Weinstein and O'Malley, at the University of Pennsylvania, applied the da Vinci® Surgical System to tumors of the head and neck and introduced the term TORS, in 2004 [31], to describe these procedures [32]; over the next several years, researches were conducted by Weinstein et al., to prove the efficacy and safety of the TORS techniques [19, 20, 29, 30]. TORS has become valued as an additional, innovative, and effective approach in head and neck surgery [11, 25], granting the surgeon the execution of procedures equivalent to traditional (open) surgery, with the advantages of augmented 3D visualization, wide field of motion, reduction of hand tremors and fatigue, possibility of navigating around corners through angled scopes, and telesurgery and teaching opportunities to inexperienced doctors and medical students with more favorable learning curves [24]. At present, the da Vinci® Si HD (Intuitive Surgical, Sunnyvale, CA) is the most used robotic system to accomplish transoral resections of head and neck tumors, proving to be feasible for a widespread range of surgical interventions within the head and neck region, and has been used since 2005 [7, 11, 25]. Even though visualization and anatomical access have been enhanced with the use of the da Vinci®, this system has several major limitations, such as its overall bulkiness and rigidity to support instrument articulation and manipulation (not providing ideal access to all of the anatomical sites), elevated costs, and limited number of cutting devices available [10, 11, 14, 23, 24].

Unhindered access to the laryngopharynx is best accomplished with the help of a flexible instrument that can be introduced through the oral cavity [23]. In contrast to the da Vinci® system, a deeply flexible robot was developed for minimally invasive surgical applications and developed to gain visual and surgical access to any

required site [7], at Carnegie Mellon University (Pittsburgh, PA) [23]. This deeply flexible robotic system, Medrobotics® Flex® Robotic System (Medrobotics Corp., Raynham, MA), is the currently available alternative to overcome the da Vinci®'s robotic system impediments. It is especially developed for head and neck surgery and incorporates the benefits of a flexible endoscope with flexible tools to successfully perform a trans-oral surgery [11]. Briefly, this robotic manipulator incorporates a flexible endoscope (with more than 150 degrees of freedom) that allows the surgeon and the operating room staff to access and visualize the anatomy of interest within the oral cavity, oropharynx, hypopharynx, and larynx, and two externally-mounted accessory guides that open to ports at the distally-mounted endoscope's camera, for the insertion of different flexible tools with tactile feedback that help the surgeon to conduct the surgery [11, 15]. Further information on this robotic system can be seen in [7] and [23]. This "computer-assisted operator-controlled flexible endoscope" [17], has been extensively tested in preclinical animal and cadaveric studies [25], and achieved the Conformité Européenne in 2014, and US Food and Drug Administration (FDA) clearance in 2015 [11]; it was first used to treat (with success) a T2 squamous cell carcinoma (SCC) of the lower lateral wall of the oropharynx, in 2014, in Europe [11, 23]. Subsequently, it has been used to perform hundreds of procedures around the world.

Surgical education aims its attention at the paradigm "see one, do one, teach one" [12]; on one hand, this teaching approach is excellent for practice as the trainee will be fortunate to engage in a specific surgery, but on the other hand it might not be optimal for patient care [12]. Although for rarer diseases or extremely complicated procedures the trainee might lose his/her chance to participate in the procedure, the arrival of robotic surgery has brought the incorporation of surgical simulation, and, consequently, the opportunity to train a variety of multiple-scenario endoscopic procedures without the need of a physical environment [5, 12].

The gap between the progress of robotic surgery adoption and training has encouraged the industry to develop robotic simulation platforms. Taking into consideration that there is no register of a platform that simulates the Medrobotics® Flex® Robotic System, a training, planning, and replaying platform prototype began its development in this project. The motivation of this project relies on granting experienced and inexperienced surgeons and medical students opportunities to learn to maneuver a robotic system virtually. Acknowledging the user about the platform, before operating on an actual real patient, or, simply, to replay a previously conducted surgery as a way of analyzing what was done and could have been done differently during the whole procedure in a surgical simulation within a safe virtual milieu is a means of optimizing this technology.

7.2   Materials and Methods

To accomplish a successful 3D virtual simulation environment that replicates the surgical training environment, consenting an efficient use of time and medical staff, limiting costs, and reducing patient's risks, three steps were followed: (1) emulating the robotic manipulator in a clinical environment that could be controlled by the user; (2) analyzing a patient's head and neck CT scan data and segmenting it into an interactive 3D model; and (3) embedding steps (1) and (2) in the same virtual environment to recreate a surgical procedure in the patient's head and neck region, by either mapping the surgeon's hand control data to the manipulator's joints (replaying the surgery), or using it as a preoperative planning or training tool.

7.2.1   Highly Flexible Robotic System Emulation

To accurately develop an interactive 3D kinematic model of the Flex® Robotic System, controlled by the user, a theoretical concept was made. The theoretical concept is comprised of three groups: TMS and Flex® Base, Flex® Drive and Flex® Instruments; each group's structure, function, and user control being defined to accurately emulate the robotic system (Fig. 7.1).

Attached to the surgical table's side, the TMS can translate, perpendicularly to the surgical table top and rotate around several axes, providing support to the Flex® Base. The Flex® Drive component, attached to the Flex® Base, is divided into two subcomponents. A head, used to control the direction of the whole system's flexible body and capable of rotating around X, Y and Z axes and translating forward and backward. And a snake-like flexible body that follows the movement of the head to help it reach the target site, so the user can conduct the surgery. Along the sides of the system's body, two channels are introduced to ports at the distally mounted camera where the user can insert two third-party flexible instruments to perform the surgery; without the Flex® Instruments, the surgeon would not be able to complete the surgery. The instruments represented are two lasers and can be operated (rotation around X, Y, and Z axes) separately by the user. As a predecessor of the 3D interactive kinematic model, a simple 2D environment was developed, using two C++ program libraries, Open Inventor [34] and Mobile [9]. At this stage, the system is represented by several rigid links, connected by 2D revolute joints, forming a chain. This chain is attached to a prismatic joint, to endow the model with motion along the X axis (Fig. 7.2).

The subsequent step consisted on transforming the 2D chain into a 3D kinematic model, capable of moving within a 3D environment. At this stage, the user controls the first frame (head) of the kinematic chain, acting as "the leader". The remaining part of the chain follows the movement of the head and composed by several rigid links, connected by a single point of articulation at their central point (Fig. 7.3).
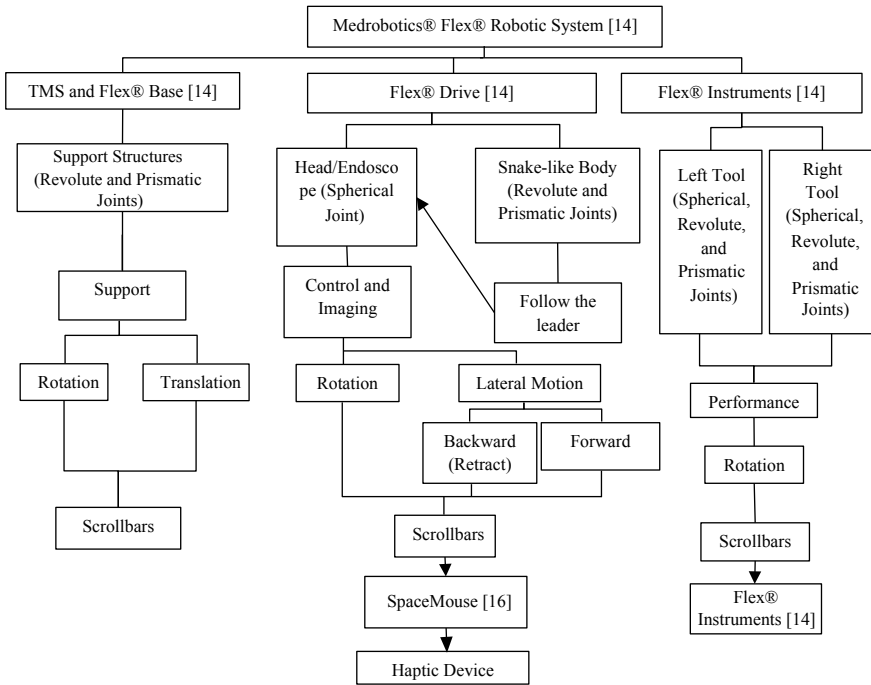
Fig. 7.1 Although the original system consists of five components [7], only four are represented because one of them is not needed in this simulation (Flex® Console). The TMS is an adjustable support stand allowing the surgeon to position the Flex® Base in the position required to access the oral cavity. The Flex® Drive, that is mounted on the Flex® Base, contains a flexible endoscope, allowing the user to access and visualize the anatomy of interest. The Flex® Instruments are flexible tools that help the surgeon conduct the surgery. The whole structure is represented by prismatic, revolute and spherical joints and controlled by scrollbars in the simulation scene and later by a SpaceMouse [16]. As a future development and final goal, this virtual environment would be controlled by the haptic device [7] and Flex® Tools [7] used in the OR
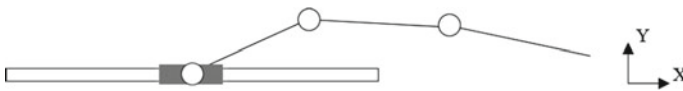
Fig. 7.2 Representation of the 2D chain. Each joint was defined to be controlled by a scrollbar in the simulation scene. The scene was composed of four scrollbars; one for the prismatic joint and the other three for the revolute joints

Fig. 7.3 Representation of the Flex® Drive, in MobileBody SDK; **a** represents the head/endoscope (spherical joint) and **b** represents one section of the snake-like body (revolute joint) that follows the manipulator's head. On the left side, one can see the scrollbars that control each variable of the head. Rotation around the X, Y, and Z Axes and "Move Robot" that allows the robot's body to move forward and to retract to a previous position (backward)

7.2.2 Patient's Head and Neck Segmentation

The capability of 3D medical imaging with computer reconstruction, rendering and analysis, has confirmed to be a beneficial tool to clinicians and researchers in all stages of successful planning and executing of complicated surgeries. From an anonymized CT image data set (DICOM [21]) of a patient's head and neck region, a 3D model of the area was generated (segmentation) (Fig. 7.4) using a medical image viewer software, InVesalius [3] and exported in a file format (STL [28]/OBJ [18]) that could be incorporated in the OR simulation using a computer graphics software, Blender [6]. File size is an important concern in terms of a program's performance. The exported file from InVesalius had approximately 300 Mb. The STL surface was imported to an editing software, MeshLab [2], to reduce the surface's size and remove unwanted structures, to improve the program's image data processing and speed. Consequently, a method to reduce the overall size of the 3D structure was successfully accomplished [1].

7.2.3 Embedding the Robotic System in the Patient's Head and Neck Model

After building the robotic system's skeleton and making sure it was working according to its performance demands, as well as confirming that the patient's model was
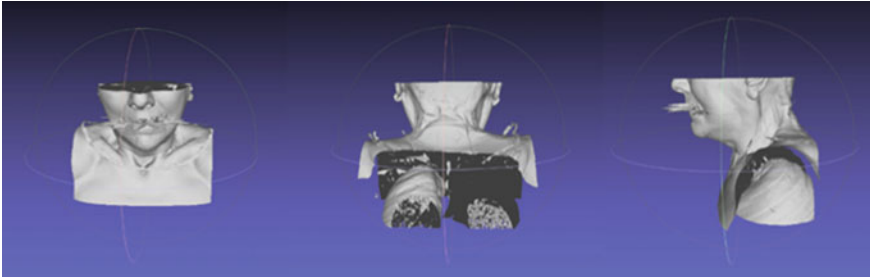
Fig. 7.4 Patient's head and neck model (front, back and left side, respectively), using MeshLab

in its optimal form, the next step was the conceptualization of a 3D model of the OR to mimic the reality as close as possible. The final form of the environment (Fig. 7.5) was obtained in three steps. At first, the robotic system's components and operating table were designed, separately, using a computer-aided design software, AutoCAD [26]. Subsequently, the 3D components of the OR were exported from AutoCad (STL format) to Blender, where the whole scene was put together, adjusted and scaled according to the patient's head and neck 3D model. At last, the model was exported from Blender and imported to a simulation system, MobileBody SDK [8], as a Virtual Reality Modeling Language (VRML/WRL [4]) file. The default camera view offered by MobileBody SDK is a Third-Person Point of View (POV) (Fig. 7.5a), which would be useful when replaying a surgery. Since the camera is not fixed, so the user can zoom in and out and pan the scene. This camera view would allow the surgeon to see what was done during the whole procedure (surgery replay) including the control of the endoscope and flexible tools from an outside position, giving him/her a perspective how the endoscope was taken from the entrance of the oral cavity to the target site to conduct the operation. This could inform the user if the target was reached in an optimal way and what he/she could have done differently. For planning and training, or sometimes replaying, a First-Person POV (Fig. 7.5b) is mandatory, to simulate the procedure in the closest way to reality. This type of view refers to a graphic perspective rendered from the Flex® Drive portion; the user cannot see the Flex® Drive's body, though he/she is able to see the tip of the Flex Tools, as well as the patient's oral cavity and throat. The First-Person POV allows the immersion in the scene and places the user at the tip of the endoscope. In this manner, an optional camera was added to the scene, that would set the position of the screen at the distal tip of the Flex® Drive, as in a real procedure.
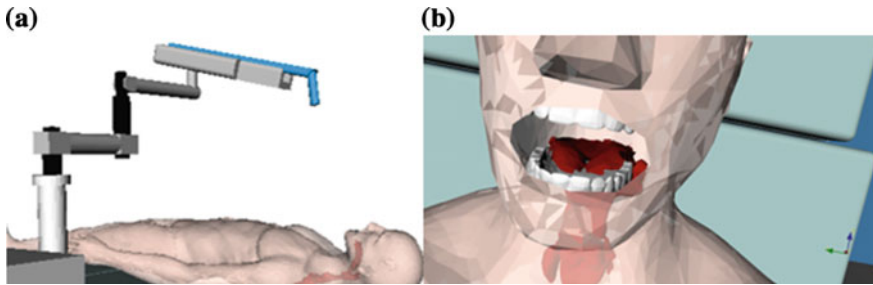
Fig. 7.5 Partial representation of the final form of the virtual environment. **a** Third-person POV; **b** First-person POV

7.3 Discussion

Prior to an operation, the time that a surgeon dedicates to a meticulous preoperative plan is of crucial importance and often determines the success or failure of the procedure. At this stage, a surgeon can take all the time needed to delineate the surgical problem, to completely identify all the anatomical structures involved as well as technical aspects of the robotic procedure and then plan the solution. This platform has the purpose of reducing surgery time by preparing and warning the doctors beforehand about the difficulties and obstacles they might be facing during the real procedure, as well as providing them a robotic surgical simulation tool that transfers the training from the operating room to an office without the need of a patient and medical staff, as illustrated in Fig. 7.6. Several benefits are brought with the development of this preoperative planning system for TORS. In addition to robotic surgical procedures, where the doctor decides how to execute the operation by observing and analyzing the patient's CT/MRI (Magnetic Resonance Imaging) images, the actual placement of the surgical robot is simulated by placing it into a 3D virtual space of the OR with a 3D model built from the patient's CT/MRI images. By embedding the geometrical structure of the patient and the surgical robot in the same virtual space, surgeons and assistants can confirm the movability of the surgical robot in the OR. Using this virtual system, surgeons, assistants, and nurses can develop an intuitively common perception about how to drive and position the manipulator in the target site, thus reducing the time spent in the OR. This training tool will allow a proper placement of the robot with the shortest path possible, significantly influencing the success of the operation. This planning system can also be efficient as an educational tool for medical students and doctors who are inexperienced in TORSs.
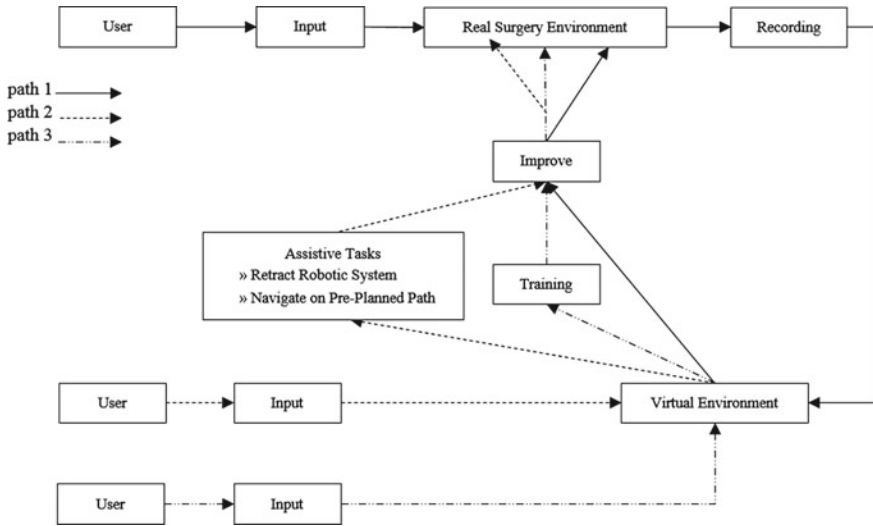
Fig. 7.6 In the OR, the Flex® Robotic System is controlled by the surgeon's hand motion (input) which is translated to guide the Flex® Drive into the patient's oral cavity until it reaches the target site. Thus, this platform's goal can be divided in three paths: Path 1 involves recording the surgeon's input and connecting them to the manipulator's joints in the virtual environment, thus replaying the surgery; this path can help experienced surgeons make conclusions on the surgery they conducted. At the same time, this could be used by inexperienced surgeons and medical students to help them learn how a surgery should be conducted. Path 2 offers the opportunity to train a variety of multiple-scenario endoscopic procedures without the need of a physical environment. Path 3 uses the virtual environment as an intermediate tool to fruitfully complete a real surgery: the patient's 3D model can be uploaded into the virtual environment and be used to train a surgery taking place in the future, or to control the manipulator to follow a path automatically and retract the robotic system automatically once the surgery has finished

7.4 Conclusion and Future Developments

To help reduce the learning curve regarding the use of robotic surgical systems, surgical training simulation systems can be developed to embody an effective addition to workplace training. These simulation systems allow the categorization of the practice of robotic surgery with objective performance reporting in a safe environment.

A first concept of the Flex® Robotic System was successfully generated, i.e., it can mimic the real system's movement, by a "follow-the-leader" motion. The system's appearance is similar to reality, though improvements in appearance, number of sections, and overall scale need to be made.

The patient's 3D model developed mimics the patient's anatomy as close to reality as possible; however, the patient's tissues do not have the capability of being deformed in real-time. Currently, one can only modify the patient's anatomy, for example, applying pressure in the patient's hyoid bone to straighten the pharynx anatomy before embedding the 3D model. This is a good start to getting to know the model's

anatomy and will possibly lead to the development of a collision detection and deformation method in the future.

To improve the head and neck 3D model developed, one needs to implement a method to simulate deformations that result from collision, either from the surgeon's hand or the Flex® Robotic System's tools. Also, the dynamics of the tissues depend on forces from surrounding tissues and organs, as well as physiological movements such as heart motion or breathing. Subsequently, further research must be done to find out how crucial these physiological movements would be in the emulation of the surgery. Another important step would be to develop an algorithm or use existing libraries, such as VTK [27], that would make the segmentation of the 3D model semi or completely automatic.

Disclaimer
No patients were involved throughout the course of this study.

References

1. Almeida, C.: Transoral Robotic Surgery (TORS) Emulation Using a Highly Flexible Robotic Manipulator (Unpublished Master's Thesis) (2017)
2. Cignoni, P., Callieri, M., Corsini, M., Dellepiane, M., Ganovelli, F., Ranzuglia, G.: Meshlab: an open-source mesh processing tool. In: Eurographics Italian Chapter Conference, pp. 129–136 (2008)
3. de Moraes, T.F., Amorim, P.H., Azevedo, F.S., da Silva, J.V.: InVesalius: an open-source imaging application. Comput. Vis. Med. Image Process. Vip IMAGE **2011**, 405 (2011)
4. Dhillon, R., Green, M.A.: Three dimensional flow visualization in virtual reality. In: 23rd AIAA Computational Fluid Dynamics Conference, p. 3807 (2017)
5. Fisher, R.A., Dasgupta, P., Mottrie, A., Volpe, A., Khan, M.S., Challacombe, B., Ahmed, K.: An over-view of robot assisted surgery curricula and the status of their validation. Int. J. Surg. **13**, 115–123 (2015)
6. Hess, R.: The Essential Blender: Guide to 3D Creation with the Open Source Suite Blender. No Starch Press (2007)
7. Johnson, P.J., Serrano, C.M., Castro, M., Kuenzler, R., Choset, H., Tully, S., Duvvuri, U.: Demonstration of transoral surgery in cadaveric specimens with the medrobotics flex system. Laryngoscope **123**(5) (2013)
8. Kecskemethy, A.: Integrating efficient kinematics in biomechanics of human motions. Procedia IUTAM **2**, 86–92 (2011)
9. Kecskemethy, A., Hiller, M.: An object-oriented approach for an effective formulation of multibody dynamics. Comput. Methods Appl. Mech. Eng. **115**, 287–314 (1994)
10. Lanfranco, A.R., Castellanos, A.E., Desai, J.P., Meyers, W.C.: Robotic surgery. Ann. Surg. **239**(1), 14–21 (2004)
11. Lang, S., Mattheis, S., Hasskamp, P., Lawson, G., Güldner, C., Mandapathil, M., Schuler, P., Hoffmann, T., Scheithauer, M., Remacle, M.: A European multicenter study evaluating the flex robotic system in transoral robotic surgery. Laryngoscope **127**(2), 391–395 (2016)
12. Lendvay, T.S., Hannaford, B., Satava, R.M.: Future of robotic surgery. Cancer J. **19**(2), 109–119 (2013)

13. Loevner, L.A., Learned, K.O., Mohan, S., O'Malley, B.W., Scanlon, M.H., Rassekh, C.H., Weinstein, G.S.: Transoral robotic surgery in head and neck cancer: what radiologists need to know about the cutting edge. RadioGraphics **33**(6), 1759–1779 (2013)
14. Mackenzie, M.: The Use of the Laryngoscope in Diseases of the Throat. Lindsay & Blakiston (1869)
15. Mandapathil, M., Duvvuri, U., Güldner, C., Teymoortash, A., Lawson, G., Werner, J.A.: Transoral surgery for oropharyngeal tumors using the Medrobotics® Flex® System—a case report. Int. J. Surg. Case Rep. **10**, 173–175 (2015)
16. Martins, M., Cunha, A., Morgado, L.: Usability test of 3D connexion 3D mice versus keyboard mouse in second life undertaken by people with motor disabilities due to medullary lesions. Procedia Comput. Sci. **14**, 119–127 (2012)
17. Mattheis, S., Hasskamp, P., Holtmann, L., Schäfer, C., Geisthoff, U., Dominas, N., Lang, S.: Flex robotic system in transoral robotic surgery: the first 40 patients. Head Neck **39**(3) (2016)
18. McHenry, K., Bajcsy, P.: An overview of 3d data content, file formats and viewers. Natl. Cent. Supercomput. Appl. **1205**, 22 (2008)
19. O' Malley, B.W., Weinstein, G.S., Hockstein, N.G.: Transoral robotic surgery (TORS): glotticmicrosurgery in a canine model. J. Voice **20**(2), 263–268 (2006)
20. O'Malley, B.W., Weinstein, G.S., Snyder, W., Hockstein, N.G.: Transoral robotic surgery (TORS) for base of tongue neoplasms. Laryngoscope **116**(8), 1465–1472 (2006)
21. Pianykh, O.S.: Digital Imaging and Communications in Medicine (DICOM): A Practical Introduction and Survival Guide. Springer Science & Business Media (2009)
22. Preim, B., Botha, C.: Chapter 20—visual computing for ENT surgery planning. Vis. Comput. Med. **2**, 61–100 (2014)
23. Remacle, M., Prasad, V.M.N., Lawson, G., Plisson, L., Bachy, V., Van der Vorst, S.: Transoral robotic surgery (TORS) with the Medrobotics Flex™ System: first surgical application on humans. Eur. Arch. Otorhinolaryngol. **272**(6), 1451–1455 (2015)
24. Rinaldi, V., Pagani, D., Torretta, S., Pignataro, L.: Transoral robotic surgery in the management of head and neck tumours. ecancermedicalscience **7** (2013)
25. Schuler, P., Duvvuri, U., Friedrich, D., Rotter, N., Scheithauer, M., Hoffmann, T.: First use of a computer-assisted operator-controlled flexible endoscope for transoral surgery. Laryngoscope **125**(3), 645–648 (2014)
26. Seidler, D.R.: Digital Drawing for Designers: A Visual Guide to AutoCAD® 2017. Bloomsbury Publishing USA, Chicago (2016)
27. Sun, M., Wu, S.: A software development of DICOM image processing based on QT, VTK and ITK. In: 2013 IEEE International Conference on Medical Imaging Physics and Engineering (2013)
28. Szilvśi-Nagy, M., Matyasi, G.Y.: Analysis of STL files. Math. Comput. Model. **38**(7–9), 945–960 (2003)
29. Weinstein, G.S., O'Malley, B.W., Hockstein, N.G.: Transoral robotic surgery: supraglottic laryngectomy in a canine model. Laryngoscope **115**(7), 1315–1319 (2005)
30. Weinstein, G.S., O'Malley Jr., B.W., Snyder, W., Hockstein, N.G.: Transoral robotic surgery: supraglottic partial laryngectomy. Ann. Otol. Rhinol. Laryngol. **116**(1), 19–23 (2007)
31. Weinstein, G.S., O'Malley, B.W.: Transoral Robotic Surgery (TORS). Plural Publishing (2011)
32. Weinstein, G.S., O'Malley, B.W., Magnuson, J.S., Carroll, W.R., Olsen, K.D., Daio, L., Holsinger, F.C.: Transoral robotic surgery: a multicenter study to assess feasibility, safety, and surgical margins. Laryngoscope **122**(8), 1701–1707 (2012)
33. Yarlagadda, B., Grillone, G.: Anatomic considerations in transoral robotic surgery. In: Robotic Surgery of the Head and Neck, pp. 13–27 (2014)
34. Wernecke, J.: The inventor mentor: programming object-oriented 3D graphics with open inventor, release 2. Addison-Wesley, Reading, MA (2005)

Chapter 8
Characteristics of a Lower Limb Exoskeleton for Gait and Stair Climbing Therapies

Dante A. Elias, Diego Cerna, Christian Chicoma and Renato Mio

Abstract The first exoskeleton development in Peru was performed at Pontificia Universidad Católica del Perú (PUCP), supported by health professionals, with the aim of treating locomotion disability which is the second main limitation affecting Peruvians these days. It is a lower limb exoskeleton for assisting normal gait and stair climbing in the sagittal plane whose dynamic model was obtained from data collected from over 40 Peruvian young adults. The proposed mechanical design is a hip-knee-ankle device that is electrically actuated and which also allows for passive rotation of hip and ankle in the frontal plane. Additionally, the system includes a trolley and a telescopic guide which allow for horizontal and vertical movement of patient's center of mass; therefore, these parameters can also be controlled in order to obtain customized therapies. Currently, a simplified model of this design is being implemented in order to verify exoskeleton proper behavior and its response to control system commands.

Keywords Lower limb · Exoskeleton · Normal gait

8.1 Introduction

At present, there is a specific need to support medicine and rehabilitation from the field of engineering and technology, and the Peruvian context is not the exception.

The lower limb rehabilitation therapies require special time and dedication, therefore the physiotherapist accompanies the patient during the whole treatment, recreating the gait patterns, holding their legs or guiding the patient while he walks leaning against a railing [1]. Thus, the quantity of individuals that can be treated by a medical professional during one day is limited and these repetitive activities cause fatigue on the physiotherapist. Besides, the offer of public and private rehabilitation services in Perú is not able to meet the demand. According to the National Register of Health

D. A. Elias (✉) · D. Cerna · C. Chicoma · R. Mio
Laboratory of Research in Biomechanics and Applied Robotics, Department of Mechanical Engineer, Pontificia Universidad Católica del Perú, Av. Universitaria 1801, Lima, Peru
e-mail: delias@pucp.pe
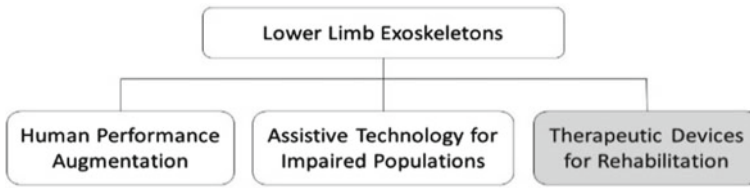
Fig. 8.1 Classification of lower limb exoskeletons according to Young and Ferris [4]

Services Provider Institutions [2] only 194 from 21,145 institutions provide rehabilitation treatments and, among them, 152 (78% of the total) are private institutions. Finally, the second main limitation affecting Peruvians is related to locomotion [3]. For this reason, assisting people with this type of disability is a great opportunity to generate a positive impact in Peru.

The lower limb exoskeleton development is of growing interest due to its powerful impact on people's capabilities [4]. These devices can be classified in three categories according to their intended use (Fig. 8.1). Human performance augmentation devices allow users to increase strength, endurance and other physical capabilities. The second category is composed of assistive devices for people with disabilities that allow them to recover movement autonomy for life daily activities. The third category devices are therapeutic exoskeletons for rehabilitation (indoors or outdoors) allowing health professionals to create an environment that can assist user's movement to achieve a specific exercise.

Some of the most relevant stationary therapeutic devices developed in universities are LOwer-extremity Powered ExoSkeleton (LOPES), Active Leg Exoskeleton (ALEX), Cable Driven Active Leg Exoskeleton (C-ALEX) and the University of Michigan Lower Limb Exoskeleton [5–8]. On the other hand, Lokomat 6th Generation and AlterG Bionic Leg are stationary and wearable exoskeletons respectively, which are commercially available and were developed by private companies.

Some exoskeletons can be considered in both the second category and the third category, for example ExoAtlet®, eLEGS, Rewalk, TWICE, Autonomyo and Indigo Therapy. These devices allow to control the movements of extension and flexion of the hip and knee for rehabilitation purposes or to help the autonomous walking of the patient with the help of crutches for the forearms, or without crutches as in the case of Rex Bionics. There are also devices that act on the movement of rotation of the hip for rehabilitation purposes, such as the cases of HIBSO and Honda Walking Assist Device.

In this paper, the mechanical design characteristics of a lower limb exoskeleton are presented. This motorized exoskeleton belongs to the third category: therapeutic devices for indoors rehabilitation. The main objective is to develop a robotic exoskeleton for the lower limbs which allows reproducing human movement patterns in the sagittal plane during normal gait or assisted movements. The project was divided in four phases, as shown in Fig. 8.2. The scope of the mechanical design stage involves
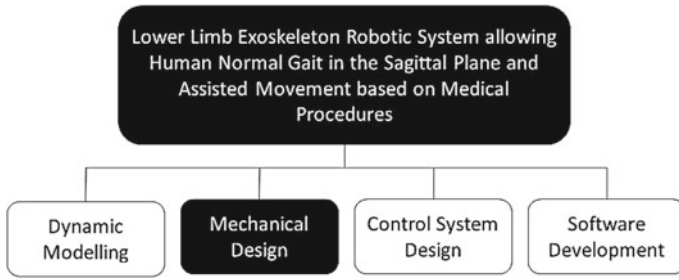
Fig. 8.2 Lima lower limb exoskeleton robotic system development stages

the design, selection and construction of mechanical elements or components of the exoskeleton robotic system prototype.

8.2 Preliminary Design

A preliminary exoskeleton was proposed considering a five-link model, which uses the double-link model for each leg and adding a link for the upper body (Fig. 8.3). In this model, it is assumed that patients will use any type of support that holds the upper body with the objective of compensating forces and moments generated in that part. To perform the dynamic analyses for the swing phase, the model used is a double pendulum, whereas for the stance phase the model used is a double inverted pendulum, as shown in Fig. 8.3.

For kinematics, analysis is performed by positions vectors in a closed loop, which are differentiated to get first the velocities, and then accelerations:

$$\vec{R_p} + \vec{R_m} - \vec{R_4} - \vec{R_1} = 0 \tag{8.1}$$

$$\frac{d}{dt}\left[\vec{R_p} + \vec{R_m} - \vec{R_4} - \vec{R_1}\right] = 0 \tag{8.2}$$

$$\frac{d^2}{d^2t}\left[\vec{R_p} + \vec{R_m} - \vec{R_4} - \vec{R_1}\right] = 0 \tag{8.3}$$

$$\vec{R_m} + \vec{R_p} - \vec{R_8} - \vec{R_5} = 0 \tag{8.4}$$

$$\frac{d}{dt}\left[\vec{R_m} + \vec{R_p} - \vec{R_8} - \vec{R_5}\right] = 0 \tag{8.5}$$

$$\frac{d^2}{d^2t}\left[\vec{R_m} + \vec{R_p} - \vec{R_8} - \vec{R_5}\right] = 0 \tag{8.6}$$
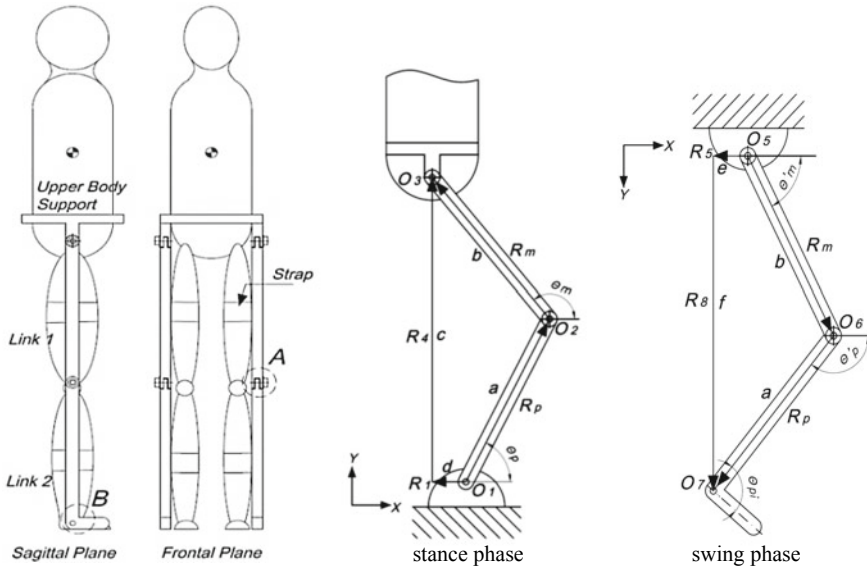
Fig. 8.3 Preliminary exoskeleton proposal [9]

In the case of kinetics, the Newton-Euler equations are used to get forces and torques. First, a general free-body diagram is proposed to consider masses and inertias of the exoskeleton mechanism and the body segments of the legs, as well as the ground reaction forces. Then, a free-body diagram is done for each leg component. As part of the preliminary design proposed, the hip is as well analyzed, considering that there is a type of "ring" that wraps around the upper body, based on the assumption that the person will auto compensate remaining external forces and moments on the trunk through a kind of "sky hook" support that absorbs those effects (Fig. 8.4) [9].

Information available on the kinematic and external forces of human gait provided by Winter [10] was considered to develop the preliminary model proposed. The direct dynamics trajectory is generated for hips and toe for a person of 65 kg and 1.80 m height [9]. As well, torques at hips and knees and the torques on upper body were calculated, in order to design the mechanical system. The inverse dynamics is performed using a normal gait trajectory for a person of 80 kg, as shown in Fig. 8.5.

8.3 Design and Model of Lima Lower Limb Exoskeleton

The internal forces and momentums calculated were used to design the mechanical system [11]. It is important to remark that the proposed design is based on a seven-limb exoskeleton with rotation in the sagittal plane for ankle, knee and hip, beside
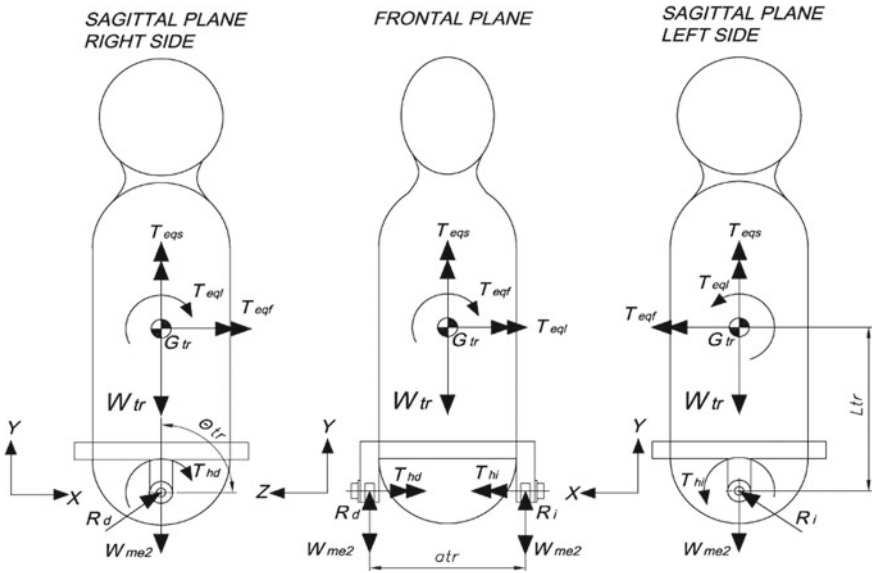
Fig. 8.4 Upper body support free-body diagram [9]
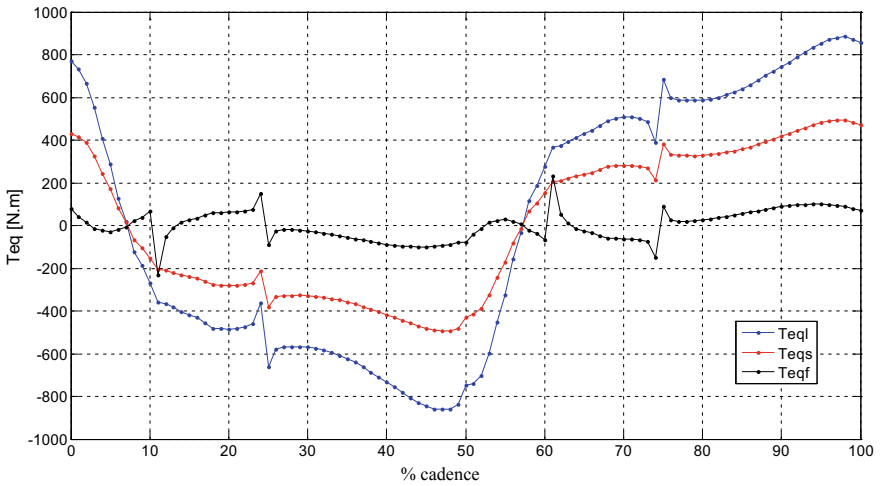
Fig. 8.5 Momentums of equilibrium in Upper Body of a person of 80 kg [9]

Table 8.1 Height and Mass

Requirement	Unit	Max.	Min.
Height	mm	1700	1600
Mass	kg	80.0	60.0

Table 8.2 Limb length

Limb	Unit	Max.	Min.
Foot	mm	256	241
Calf	mm	409	385
Thigh	mm	411	387
HAT[a]	mm	446	419

[a]HAT: Head, arms and trunk

Table 8.3 Temporal parameters

Parameter	Unit	Max.	Min.
Gait cycle	s	1.714	1.333
Step period	s	0.857	0.667
Stance period	s	1.063	0.827
Swing period	s	0.651	0.507
Frequency	steps/min	90	70

Table 8.4 Spatial parameters

Parameter	Unit	Max.	Min.
Linear speed	m/s	1.10	0.81
Linear acceleration	m/s^2	4.12	3.01
Stride	cm	121.68	114.52
Step length	cm	60.84	57.26
Step width	cm	6	5

trunk vertical translation. The technical requirements are shown in Tables 8.1, 8.2, 8.3 and 8.4.

Lima Lower Limb Exoskeleton is a stationary and electrically actuated machine to help human gait rehabilitation procedures in the sagittal plane through of two therapy modes: walking and stair climbing. It has four main components: a lower limb exoskeleton, a trolley, a telescopic guide and a structure (Fig. 8.6).

As mentioned in Table 8.5, each component performs a specific function. The Lima Lower Limb Exoskeleton allows for reproducing normal gait and stair climbing patterns, while the trolley allows for displacement on the horizontal axis according to normal speeds during human gait and stair climbing. The telescopic guide allows for displacement on the vertical axis. Finally, the structure holds up all the weight involved and it also acts as a guide for the trolley.

The Lima Lower Limb Exoskeleton designed allows reproducing normal gait and stair climbing patterns while providing a safe environment for executing rehabili-
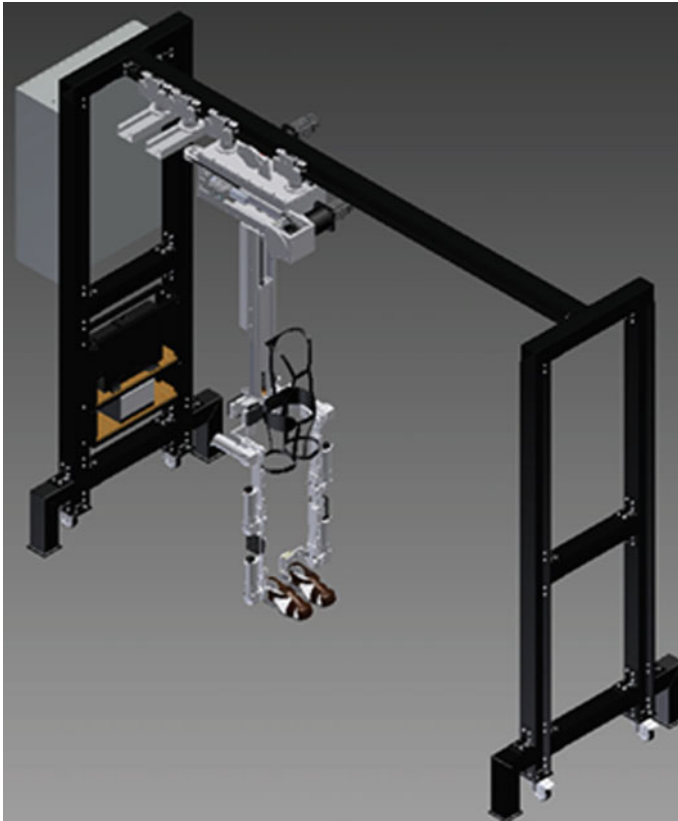
Fig. 8.6 Lima Exoskeleton 3D model. Four main components are shown: lower limb exoskeleton, trolley, telescopic guide and structure [11]

Table 8.5 Lima lower limb exoskeleton main components

Component	Specific function
L.L. Exoskeleton	Reproduce human normal gait and stair climbing patterns
Trolley	Allow for translation of the patient's center of mass horizontally
Telescopic guide	Allow for translation of the patient's center of mass vertically
Structure	Hold up total weight: patient, trolley and telescopic guide

tation therapies. It is important to remark that the system includes a trolley and a telescopic guide for horizontal and vertical translation of patient's center of mass. These parameters can be controlled to obtain customized therapies: for example, a slow horizontal speed (trolley) and holding 50% of patient's weight (telescopic guide and cable) condition.

8.4 Implementation of Lima Lower Limb Exoskeleton

This phase is currently under development and it has started with the implementation of a simplified model of the proposed design which only includes the lower limb exoskeleton, as shown Fig. 8.7. The robotic mechanism implemented has three degrees of freedom in the sagittal plane to reproduce the extension-flexion movements of the hip, knee and ankle. It includes the first kinematic pattern of the Peruvian gait cycle obtained with the VICON® motion capture system [12]. This mechanism is installed in a stationary structure to perform passive therapies (without the need for voluntary movement of the patient).

This first design allowed assistance of hip, knee and ankle rotation by means of six DC motors aligned with the corresponding joints. The part attached to the patient is meant to remain static (that is, no horizontal or vertical movement is supported). To provide hip support, an additional structure was soldered above the machine, from which the patients would be attached through a derrick belt. The main structure was made of steel plates for the leg links a mechanical mobile structure made of steel rectangular profiles. This component interacts directly with the patient; therefore the objective of the preliminary development is to verify proper behavior of the exoskeleton: joints range of motion, limbs kinematics, response to control system commands and confirm protection devices function.

A communication system was designed to control the device and to allow the main controller to drive each joint motor and to coordinate movements synchronously. A UDP protocol connection was established between the User Interface Computer and the Main Controller, and two CAN bus were installed between the Main Controller and the six drivers, one for each leg and a set of three drivers. Figure 8.8 shows the complete control system architecture.

8.5 Experiences with a Prototype

The first simplified prototype was built and evaluated for functionality. No tests have been performed yet with actual human subjects. Position values were sent from the user interface to the main CPU via UDP protocol and then converted to CANopen commands to be interpreted and executed by the motor drivers. After verifying the functioning of position control, gait trajectories were included to be sent from user the interface (see Fig. 8.9a) with a normal cadence. These trajectories

Fig. 8.7 Lima lower limb exoskeleton robotic system prototype. The figure shows how a user should be positioned in the prototype. The prototype has not been yet tested with actual human subjects

were then tested on the prototype (see Fig. 8.9b) to evaluate the performance of the PID trajectory following algorithm, which is embedded on the drivers. In general, the exoskeleton moves normally within the range of motion, but exhibits following error due to vibrations in the structure, which could be mitigated with tuning of the control parameters.
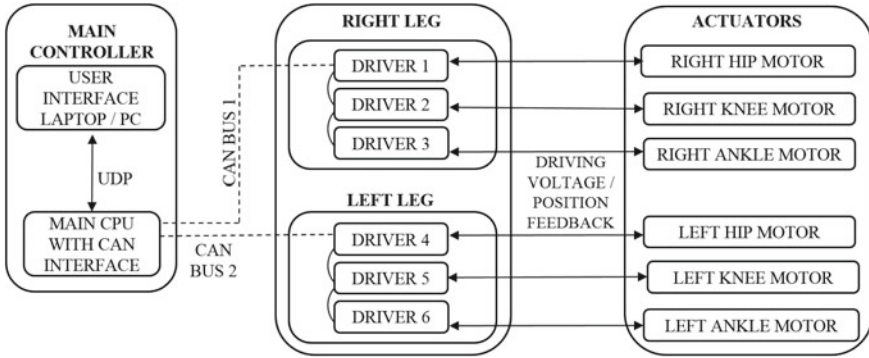
Fig. 8.8 Control system architecture of the Lima lower limb exoskeleton prototype
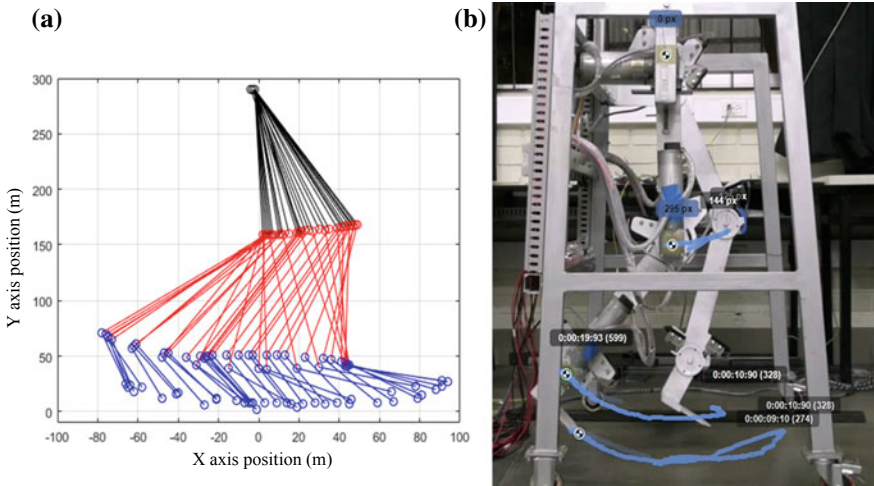
Fig. 8.9 **a** Snapshots of the gait trajectory for one leg in the sagittal plane. **b** Exoskeleton moving according to the trajectory

8.6 Conclusions

The Lima Lower Limb Exoskeleton designed allows reproducing normal gait and stair climbing patterns while providing a safe environment for executing rehabilitation therapies. A remarkable difference with other therapeutic exoskeletons in the state of the art is that PUCP's design includes a foot limb to control ankle rotation in the sagittal plane, thus three degrees of freedom of the lower limb can be controlled using a kinematic pattern of the human gait cycle or assisted movements. Another relevant feature is that it allows controlling vertical displacement and vertical load on patient's lower limbs due to the cable that is inside the telescopic guideline, which is

attached to the trunk limb. This body weight support system, using a harness, allows the patient to perform rehabilitation therapy while maintaining correct posture.

Immediate step involves testing the simplified lower limb exoskeleton that was constructed with the aim of identifying gaps related to: kinematics, response to control system, and comfort. This will be followed by the optimization of the lower limb exoskeleton and the construction of the trolley, telescopic guide and structure according to final design. Also this developed mechanism must be tested considering the human-exoskeleton interface to evaluate the support forces at the person's skin as well as the sufficient comfort for prolonged use.

References

1. Ministerio de Salud: Norma Técnica de Salud de la Unidad Productora de Servicios de Medicina de Rehabilitación. 079 MINSA/DGSP-INR V.01. Lima, Perú (2009). Available via MINSA. http://www.dgiem.gob.pe/norma-tecnica-de-salud-de-la-unidad-productora-de-servicios-de-medicina-de-rehabilitacion/. Accessed 3 Nov 2017
2. Superintendencia Nacional de Salud: Registro Nacional de Instituciones Prestadoras de Servicios de Salud. Lima, Perú (2017). Available via SUSALUD. http://app12.susalud.gob.pe. Accessed 3 Nov 2017
3. Consejo Nacional para la Integración de la Persona con Discapacidad: Anuario Estadístico del Registro Nacional de la Persona con Discapacidad. Lima, Perú (2015). Available via CONADIS.http://www.conadisperu.gob.pe/observatorio/index.php/informacion-de-base/registro-nacional-de-la-persona-con-discapacidad/anuario-estadistico-2000-2014. Accessed 3 Nov 2017
4. Young, A.J., Ferris, P.: State-of-the art and future directions for robotics lower limb exoskeletons. IEEE Trans. Neural Syst. Rehabil. Eng. **25**(2), 171–182 (2017)
5. Frumento, C., Messier, E., Montero, V.: History and future of rehabilitation robotics. Worcester Polytechnic Institute, 2010. Available via DigitalCommons@WPI. https://digitalcommons.wpi.edu/atrc-projects/42/. Accessed 10 Jun 2017
6. Balana, S.K., Agrawal, S.K., Scholz, J.P.: Active Leg Exoskeleton (ALEX) for gait rehabilitation of motor-impaired patients. In: Driessen, B., Herder, J.L., Gelderblom, G.J. (eds) Proceedings of the 2007 IEEE 10th International Conference on Rehabilitation Robotics, Noordwijk, The Netherlands (2007)
7. Jin, X., Cui, X., Agrawal, S.K.: Design of a Cable-driven Active Leg Exoskeleton (C-ALEX) and gait training experiments with human subjects. In: Proceedings of the 2015 IEEE International Conference on Robotics and Automation (ICRA), Seattle, WA, USA (2015)
8. Jones, R.K.: Pneumatically powered lower limb exoskeletons. University of Michigan. https://deptapps.engin.umich.edu/open/rise/getreport?pid=5&fv=2&file=Pneumatically%20Powered%20Lower%20Limb%20Exoskeletons_Final.compressed.pdf. Accessed 11 Jun 2016
9. Pujada, E.: Modelación y simulación dinámica de un mecanismo exoesquelético para personas con dificultades en la marcha. Mechanical Engineering Thesis, Pontificia Universidad Católica del Perú. Lima, Perú (2009)
10. Winter, D.A.: The Biomechanics and Motor Control of Human Gait: Normal, Elderly and Pathological, 2nd edn. University of Waterloo Press, Waterloo, Ont (1991)

11. Garces, A.: Diseño de un mecanismo del tipo exoesqueleto de miembros inferiores que permita reproducir patrones de movimiento. Mechanical Engineering Thesis, Pontificia Universidad Católica del Perú. Lima, Perú (2017)
12. Dongo, R., Moscoso, M., Callupe, R., Pajaya, J., Elías, D.: Normal human gait patterns in Peruvian individuals: an exploratory assessment using VICON® motion capture system. In: Romero, E., Lepore, N., Brieva, J., García, J.D. (eds) Proceedings of the 2017 SPIE 13th International Conference on Medical Information Processing and Analysis, San Andres Island, Colombia, vol. 10572 (2017)

Chapter 9
A 3D-Printed Prosthetic Hand
with Modular Reconfigurable Fingers

Renato Mio, Marlene Bustamante, Giancarlo Salazar and Dante A. Elias

Abstract Partial hand and transradial amputations are among the most common levels of amputation. In the former case, a mechanical prosthesis is prescribed, while in the latter case either a mechanical or a myoelectric one are used depending on the patient's preference and access to the technology. While a variety of prostheses designs are aimed to transradial amputees and plenty others are for partial hand amputations, like the 3D-printed open-source concepts that are activated by the user's wrist, for a faster and more efficient treatment of hand amputations, one design should be adaptive for different levels of amputation without compromising the prosthesis performance. This work describes a powered prosthesis design with modular fingers and space constraints that allow it to be adapted to different levels of amputation. The prosthesis finger lengths could also be customized to user-specific anthropometry and, besides shafts, bolted connections and electronic components, the whole hand can be 3D printed.

9.1 Introduction

In the recent years, there have been many new approaches to prosthetic hand design, many of which have been driven by the appearance of the disruptive technology of 3D-printing, more compact actuators and new promising materials. Highly dexterous and biomimetic hands are being designed [1], but the increasing number of actuators needed for this type of prosthesis make the hand too heavy or large, which is not a suitable option for a prosthesis. Because of this problem, most hand prostheses utilize underactuated finger mechanisms [2, 3], such as four-bar linkages or pulley systems. In most cases, the proximal joints of the fingers are active degrees-of-freedom (DoF) while the distal joints are non- actuated with geometric restrictions. In the case of

R. Mio · M. Bustamante · G. Salazar · D. A. Elias (✉)
Laboratory of Biomechanics and Applied Robotics, Pontificia Universidad Católica del Peru, Universitaria 1801, 15088 Lima, Peru
e-mail: delias@pucp.pe

R. Mio
e-mail: r.mioz@pucp.edu.pe

transmetacarpal amputees, there is even less space available to fit all the components of the prosthesis, but it is not an impossible task. Thus, in this work we propose a design for a customized powered hand prosthesis aimed for transmetacarpal amputees which can also be adapted for transradial levels of amputation. We show a method for customizing prosthetic fingers to match a user-specific anthropometry. Furthermore, silicon rubber components are designed to be attached to the prosthetic fingers in order to increase the prosthetic hand maximum payload.

9.2 Mechatronic Design

The following sections describe the main features of the implemented prototype. A previous design of this hand prototype was presented in preceding work [4]. A summary of the design features and the changes made to the latest version are explained in the following sub-sections.

9.2.1 Anthropometry

To customize the fingers lengths, the digits II to V (all fingers except for the thumb) were designed to be parametric based on the hand total length (L_H) measured from the wrist to the tip of the middle finger. First, the proximal phalanx length (L_{pp}) of each finger was determined using the phalanges lengths as percentage of hand length values proposed by Davidoff and Frievalds [5], which are shown in equation form in (9.1)–(9.4) where the II, III, IV and V superscripts correspond to the index, middle, ring and little fingers respectively. Then, the length of medial phalanx (L_{mp}) and distal phalanx (L_{dp}) for each finger were calculated based on the corresponding proximal phalanx length (L_{pp}) using the ratios proposed by Littler [6], which are shown in equation form in (9.5)–(9.7) where i = II, III, IV, V.

$$L_{pp}^{II} = 0.218 L_H \tag{9.1}$$

$$L_{pp}^{III} = 0.245 L_H \tag{9.2}$$

$$L_{pp}^{IV} = 0.222 L_H \tag{9.3}$$

$$L_{pp}^{V} = 0.177 L_H \tag{9.4}$$

$$L_{mp}^{i} = 0.565 L_{pp}^{i} \tag{9.5}$$

$$L_{dp}^{i} = 0.435 L_{pp}^{i} \tag{9.6}$$

Fig. 9.1 **a** Segments
conforming the parametric
finger. **b** The segments'
lengths translated to the first
CAD model
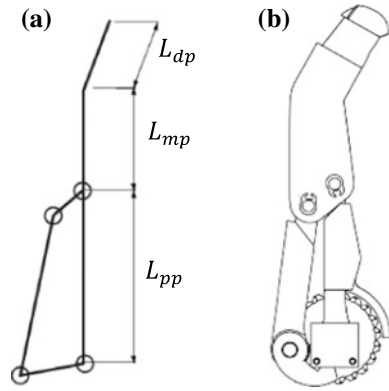
$$L_{mp}^V = L_{dp}^V = 0.5L_{pp}^V \tag{9.7}$$

Finally, the finger bases, which correspond to the metacarpophalangeal (MCP) joints, are positioned in such a way that the fingertips lie in the same plane parallel to the frontal plane when the fingers are fully flexed, as proposed in [7]. Additionally, the computed L_{pp} values are used to determine the dimensions of the four-bar linkage mechanism, which allows underactuated motion of the MCP and proximal interphalangeal (PIP) joints, while the DIP joint is fixed and flexed 20° (see Fig. 9.1).

9.2.2 Modular Fingers

The mechanisms of the fingers (worm drive and four-bar linkages) and the thumb (worm drive and gears) are explained in [4]. Small changes made in this version include an overall size improvement and replacement of the thumb rotation spur gears for helical gears with a reduction of only two stages, while the previous had three. Figure 9.2 shows the new version mechanisms.

To determine the positions of the finger segment at all times, two angles need to be measured: the MCP and PIP joints flexion angles. The former is measured directly on the MCP axis using a magnet attached to the proximal phalanx lower link while the latter is measured indirectly by means of a helical gear coupled to the worm gear rotation. This gear has a second magnet attached and its rotation can be related with the PIP joint rotation.

For an easier assembly, the fingers are designed as modular units, which includes the DC micromotor, worm drive transmission, position and force sensors and the finger links (see Fig. 9.2). The thumb has two levels of modularity: the proximal and distal phalanx are a unit with one degree of actuation for the distal phalanx flexion powered by the embedded DC micromotor; the thumb flexion unit is then mounted
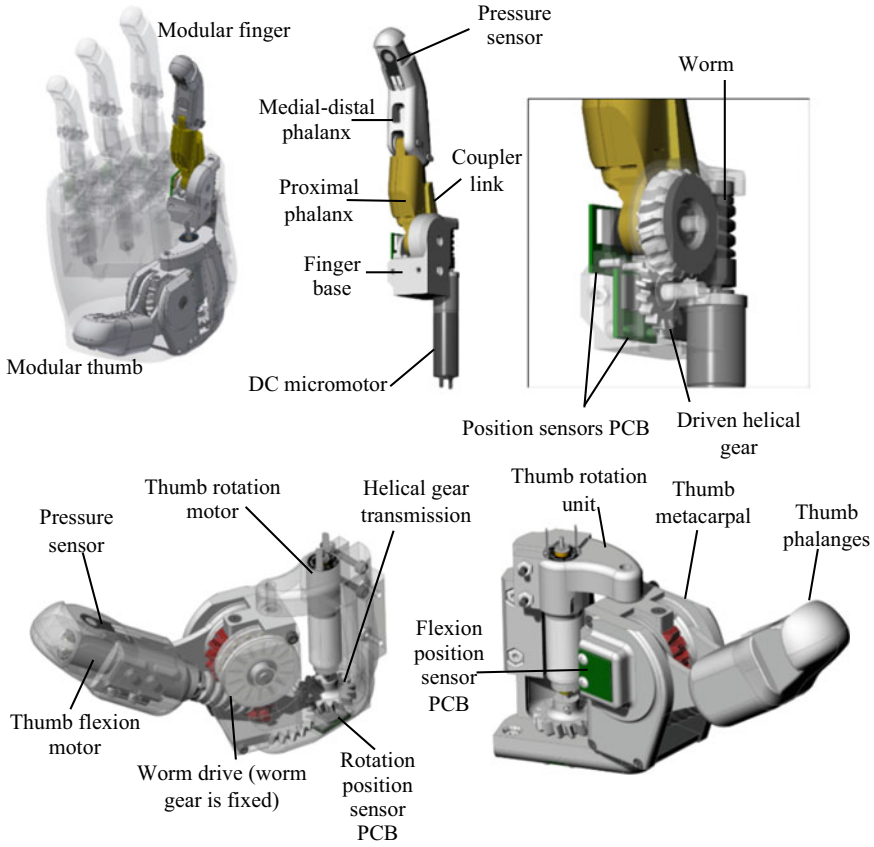
Fig. 9.2 Mechanisms of the modular fingers and thumb

on the rotation unit, which includes a base (thumb CMC) and its abduction-adduction or rotation actuator. The flexion unit can be easily detached from the metacarpal.

9.2.3 Electronics and Control

Two types of sensors were included for the control of each DoF: a Hall Effect absolute rotary position sensor and force sensitive resistors (brand and models are also stated in [4]). Each finger has two position sensors: in the II, III, IV and V digits, they measure the MCP and PIP joints angles; in the thumb, one position sensor for the rotation is located in the carpometacarpal joint of thumb (CMC) and the second for the flexion is located in the MCP joint. The force sensors are located at the tip of each finger as shown in Fig. 9.2.

Table 9.1 Actuation and transmission features for each degree of actuation

Stage/feature	Degrees of actuation			
	Thumb F/E	Thumb rotation	II and III digits F/E	IV and V digits F/E
Motor	Maxon DCX 10L	Maxon DCX 10 S	Maxon RE 10	Maxon DCX 8 M
Gearhead	Maxon GPX 10 16:1	Maxon GPX 10 256:1	Maxon GP 10 K 16:1	Maxon GPX 8 16:1
Transmission	Wormdrive 20:1	Helical gears 1.4:1	Wormdrive 10:1	Wormdrive 10:1
Output velocity[a] (RPM)	21	11	38	26
Output torque[a] (mNm)	300	196	150	102.5

[a]Theoretical values

DC micromotors of the Maxon series were selected for powering each finger. The index and middle fingers have actuators with larger torque than the ring and little fingers to match the strength of their biological counterparts. The actuations and transmissions per finger are described in Table 9.1.

Regarding the electronic architecture, the system is composed of a main controller and local controllers. The control circuit board comprises an independent controller unit for each finger with motor drivers for the micromotors. A host controller, which executes the main control loop, will send desired position and force values for each finger to the corresponding local controller. These controllers read the values sent by the host controller and move each finger independently from the others using a control algorithm based on a Proportional-Derivative (PD) controller.

9.2.4 Materials

Besides the bolted connections, shafts and electronic components, every part of the prosthesis was made using fused filament fabrication (FFF) 3D-printing. The two materials used for fabrication were ABS and PLA plastic. The former was used for external parts because of its higher impact resistance, while the latter was utilized for parts that required hardness such as the worm drive and helical gears transmission. The 3D-printer used was an Ultimaker 2 Extended+.

Additionally, silicon rubber finger gloves were designed to cover the fingers similar to a skin. Three different food grade liquid silicon rubber were evaluated for use: RTV1500 [8], RTV1510 [8] and L20 [9]. The main difference among them was the hardness and elasticity, and the criteria for selecting the best consisted in an evaluation of the quality of the force sensing signal when a force sensor was placed on

the fingertip under the finger glove. It was proved that the RTV1510 gave the signal with less noise.

9.2.5 Finger Gloves

The finger glove has the purpose of increasing the friction coefficient and cover the fingers without compromising their function. The exterior shape of these gloves was inspired on the fingerprints of the human hand, copying features such as the texture pattern, which consists on concentric circles, and the size of the ridges, which have a thickness of 200 μm [10, 11] (see Fig. 9.3a). The fingers are designed to hold a force sensor in the fingertip and, to properly transmit the force to the sensor, silicone pads integrated in the finger glove design, similar to the ones in [12]. Thus, when the objects are grasped, the deformation of the pad allows adapting to the geometry of the object while maintaining the structure that transmits the force to the sensor. Two extra pads were placed on the middle and proximal phalanx to increase the grip zones (see Fig. 9.3b). After adding this feature, the external shape of the glove was modified to improve its aesthetic and better mimic the human finger shape (see Fig. 9.3c). Besides, a single finger glove design can adapt to the geometry of the four fingers by just cutting its length. Another glove was designed only for the thumb's dimensions with a similar integrated pad. In addition, to cover the thumb's metacarpal, an accordion-shaped silicone protection was added (see Fig. 9.3d).

9.2.6 Stump Fitting

The prosthetic hand allows fitting of a stump typical from partial hand amputees or wrist disarticulation (see Fig. 9.4). In these cases, power supply should be placed externally due to the limited space. However, in the case of a transradial amputee, the battery could be embedded on the socket.

9.3 Results

First, to prove the effectiveness of the silicone rubber finger gloves in enhancing the friction coefficient, we evaluated the maximum payload of the prosthetic hand when performing a cylindrical grasp in a horizontal posture (see Fig. 9.5) with and without the gloves. The holding of an object was considered successful if after closing the hand and grasping the cylindrical object no slippage was observed. Three objects made of glass, plastic (polyethylene) and metal were evaluated.

When the prosthesis was tested without the finger gloves (i.e. ABS plastic was in contact with the cylindrical object), the maximum payload values before slippage
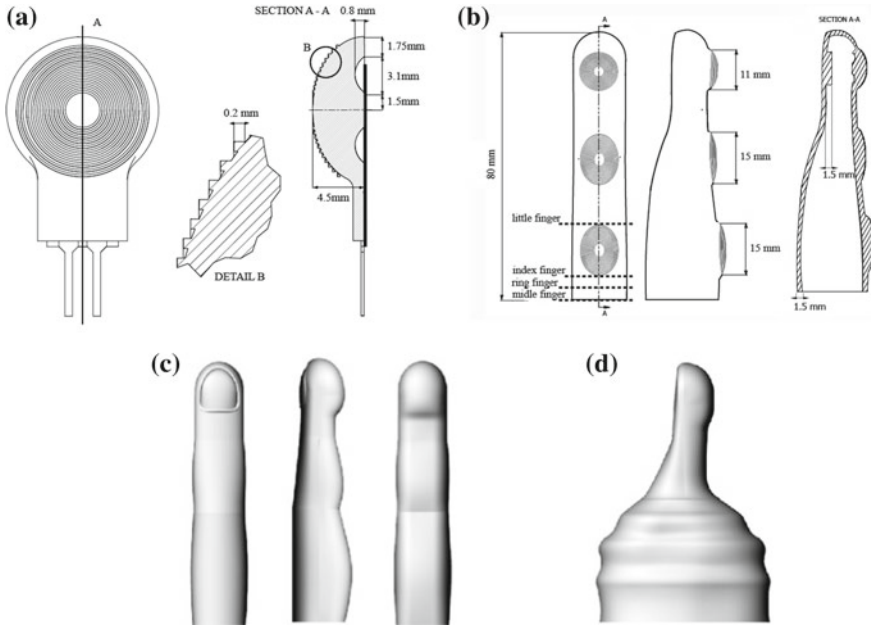
Fig. 9.3 Finger gloves design features

Fig. 9.4 Components distribution inside the hand prosthesis in order to fit a stump

Modular fingers actuators and sensors

Main PCB's

Partial hand amputee's stump
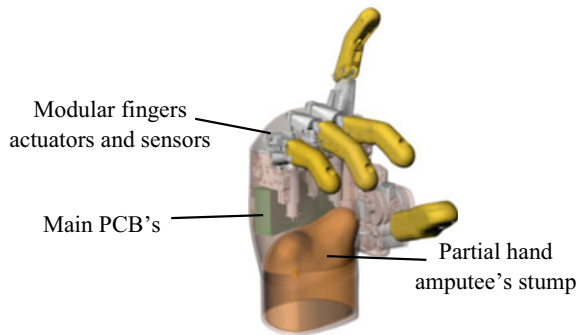
were 335 g, 430 g and 325 g for metal, plastic and glass respectively (see Fig. 9.5a–c). On the other hand, when the prosthesis was tested with the silicon rubber finger gloves, a significantly higher compliance was noticed and the highest tested payload of 900 g did not show any slippage for any of the three materials (see Fig. 9.5d–f).

A prototype was fabricated to match a partial hand amputee's specific anthropometry, with a total length of 183 mm and a weight of 435 g. Due to its degrees of actuation and kinematic configuration, it was able to perform precision (pinch, tripod, lateral) and power grasps (cylindrical, spherical and palmar extension) as depicted in Fig. 9.6a–f. A prosthetic socket was fabricated to serve as interface between the user's stump and the prosthesis. Due to the convenient distribution of components
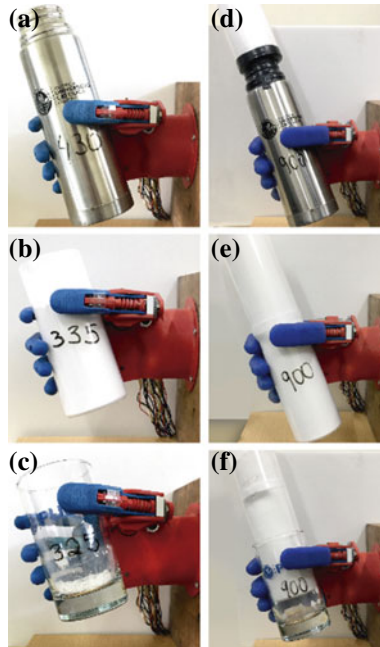
Fig. 9.5 Prosthesis payload test without the finger gloves holding the **a** metallic, **b** plastic and **c** glass objects. Prosthesis payload test with the finger gloves holding the **d** metallic, **e** plastic and **f** glass objects

within the palm, no offsets were needed to fit the user's stump, which is the same as the one shown in Fig. 9.4. No discomfort was experienced by the user during the use of the prosthesis and, thanks to the socket flexibility, both pronation and supination movements were performed without any inconvenience (see Fig. 9.6g).

9.4 Conclusion

A method for customizing the dimensions of the fingers of a prosthesis with just the hand length as an input was presented. As can be seen in the images of the prototype, the result is an anthropomorphic hand that mirrors the user healthy hand thanks to the parameterization procedure. Additionally, it is demonstrated that not only the silicon rubber but also the texture pattern, surface roughness and compliance of the gloves that cover the fingers are important factors that greatly improve the payload of a hand prosthesis and are an interesting topic for further research. Furthermore, the modularity of the fingers allows to test different kinematic configurations of the hand by just changing the design of the palm to which they are attached.
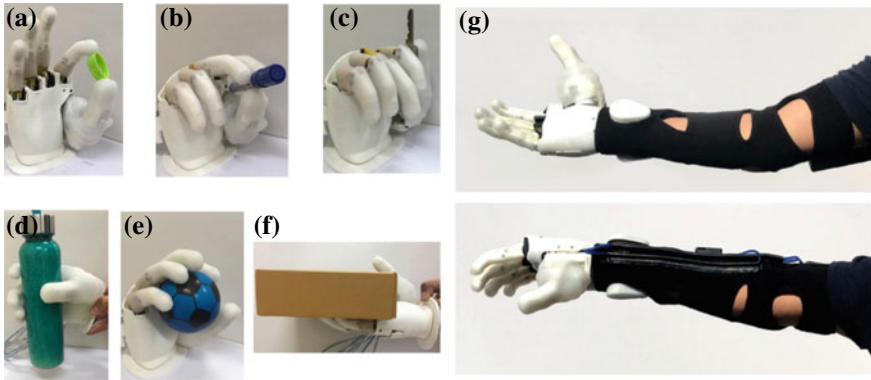
Fig. 9.6 Gestures the prosthesis can perform. **a** Pinch. **b** Tripod. **c** Lateral. **d** Cylindrical. **e** Spherical. **f** Palmar extension. **g** Prosthesis fitted to a user with partial hand amputation

References

1. Xu, Z., Torodov, E.: Design of a highly biomimetic anthropomorphic robotic hand towards artificial limb regeneration. In: 2016 IEEE International Conference on Robotics and Automation (ICRA), Stockholm (2016)
2. Rea, P.: On the design of underactuated finger mechanisms for robotic hands. In: Advances in Mechatronics, Shanghai, InTech, pp. 131–155 (2011)
3. Jin, J., Zhang, W., Sun, Z., Chen, Q.: LISA hand: indirect self-adaptive robotic hand for robust grasping and simplicit. In: International Conference on Robotics and Biomimetics, Guangzhou (2012)
4. Mio, R., Villegas, B., Ccorimanya, L., Flores, K.M., Salazar, G., Elías, D.: Development and assessment of a powered 3D-printed prosthetic hand for transmetacarpal amputees. In: 3rd International Conference on Control, Automation and Robotics (ICCAR), Nagoya (2017)
5. Frievalds, A.: Biomechanics of the Upper Limbs: Mechanics, Modeling and Muskuloskeletal Injuries, p. 204. CRC Press LLC, Florida (2004)
6. Hutchinson, A.L., Hutchinson, R.L.: Fibonacci, littler, and the hand: a brief review. Hand **5**(4), 364–368 (2010)
7. Gerruti, G., Chablat, D., Gouaillier, D., Sakka, S.: Design method for an anthropomorphic hand able to gesture and grasp. In: 2015 IEEE International Conference on Robotics and Automation (ICRA), Seattle, Washington (2015)
8. RongXingDa: Liquid Silicone Rubber for Food GradeMold RXSILICONE (2016). http://www.rtv-2.com/project/food-grade-silicone-rubber-for-mold-making. Accessed 12 Apr 2017
9. Silika: Silicona RTV Platino Silika Moldes e Insumos. http://silikamoldeseinsumos.com/productos/caucho-silicona-rtv-platino/. Accessed 17 Apr 2017
10. Oddo, M., Beccai, L., Wessberg, J., Backlund, H., Mattioli, F., Chiara, M.: Roughness encoding in human and biomimetic artificial touch: spatiotemporal frequency modulation and structural anisotropy of fingerprints. Sensors **11**(6), 5596–5615 (2011)

11. Duvefelta, K., Olofssona, U., Johannessona, C., Skedungb, L.: Model for contact between finger and sinusoidal plane to evaluate adhesion and deformation component of frictio. Tribol. Int. **96**, 289–394 (2016)
12. Kargov, A., Pylatiuk, C., Martin, J., Schulz, S., Doderlein, L.: A comparison of the grip force distribution in natural hands and in prosthetic hands. Disabil. Rehabil. **26**(12), 705–711 (2004)

Chapter 10
Design and Analysis of a Lower Limb Exoskeleton for Rehabilitation

Giancarlo Villena Prado, Raimo Yli-Peltola and Miguel B. Castro Sanchez

Abstract Nowadays, the growing development of technologies has led to look for optimal and efficient solutions to activities that are done by human precision. Particularly, in a medical environment, it should be ensured that the technologies used in patients provide the acceptable conditions in health, safety and care; with high precision. Exoskeletons for medical use are designed to provide therapies for patients with walking disabilities. The purpose is to assist patients in the recovery of their motor capacity through the movements that the device performs. In Peru, most of the therapies are performed manually, involving a routine of movements in which the physical effort of a physiotherapist is required. The technology of exoskeletons makes possible use its precision to achieve controlled movements with a given speed, to produce consecutive homogeneous repetitions, to generate opposition forces or resistance to some kind of movement in a rehabilitation routine, among others. This paper focuses on the design and evaluation of a lower limb exoskeleton which can help in the rehabilitation of patients with some mobility problem, thus contributing to the social insertion, psychological well being, and improvement of the quality of life of patients in Peru. The designed exoskeleton, based on a pneumatic artificial muscle actuator, will serve to an average 11 years old child to an adult and has a four degrees of freedom (DoF) in each lower limb.

10.1 Introduction

Innovative robotic devices that satisfy the diverse clinical needs has helped to improve the quality of life of people with problems in the limbs. Robotics has become very useful in medicine, it is a very appropriate tool since it is programmable and has a

G. Villena Prado (✉) · M. B. Castro Sanchez
Universidad de Piura, Piura, Peru
e-mail: gvillenap@pucp.edu.pe

M. B. Castro Sanchez
e-mail: miguel.castro@udep.pe

R. Yli-Peltola
Seinajoki University of Applied Sciences, Seinajoki, Finland
e-mail: raymond988@me.com

high precision compared to human hand, thus allowing a better access to delicate areas where there is no possibility of an error. In the last two decades, there has been an increase in the amount of research on the use of robots in physical therapies [1]. The goal of rehabilitation is to recover the patient from an impairment or disability and to improve mobility, functional capacity and quality of life. An exoskeleton is a structure to be used on the human body as a garment, as defined by its term "wearable robots", either to complement the function of a limb or to replace it completely.

In Peru, 5.2% of the total population present some type of disability, according to the National Institute of Statistics and Informatics (INEI). The motor disability is the most frequent disability affecting Peruvians (equivalent to 59.2%). In addition, INEI reports that 88.6% of the population with some disability does not receive treatment and/or rehabilitation therapy [2]. The most serious problem for people with disabilities is that rehabilitation services are scarce and are offered mainly in the capital of Peru [3].

Traditional methods are being used, which require the assistance of a person to facilitate the movements of the limbs. Therefore, in this paper we will develop and analyze a lower limb exoskeleton structure in order to enhance the situation in therapy rehabilitation in Peru. The robotic exoskeleton has two active and two passive DoF in each lower limb. The former ones represent the active rotation of the hip and knee in the sagittal plane. The latter movements are located in the ankle, where a torsion spring is used to return to a 90° position of the foot with respect to the shank in each step, and the hip, where the abduction and adduction restricted movements allow a much more natural gait.

10.2 Related Works

Emerging robots are increasingly in contact with people: interacting, helping, serving, and exploring with human. There are several manufactures of exoskeletons for rehabilitation therapies. The main features and modes of operation of the three most outstanding exoskeletons worldwide will be detailed below.

10.2.1 Hybrid Assistive Limb (HAL)

The company Cyberdyne was established in 2004 in Japan in order to disseminate the result of the research of Professor Yoshiyuki Sankai of the University of Tsukuba. His research is about the use of Robot Suit HAL (Fig. 10.1a) for benefits of humankind in the field of medicine, caregiving, welfare, labor, heavy work, entertainment, and so on [4]. User physical functions can be improved, supported and/or enhanced. This exoskeletons helps a person with physical disabilities to move and allows him to exert more torque than usual [5].

Fig. 10.1 Exoskeletons used for rehabilitation purposes in the industry. **a** HAL [5] **b** Lokomat [12] **c** ReWalk [13]

(a) HAL [5]   (b) Lokomat [12]   (c) ReWalk [13]
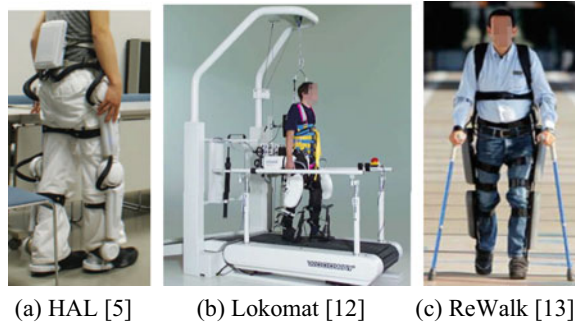
HAL has two types of control movements [6], cybernic voluntary control system and a robot-like cybernic autonomous control system. The former detects very weak biolectrical signals on the surface of the skin, called myoelectric signals. This signal causes the contraction of the muscle fiber and occurs before its visible movement. Depending on the signal, the power unit that generates the assistive power is controlled by amplifying the torque and supporting movement. The latter control strategy is applied when the signals are unable to be detected. It provides an humanlike movement.

10.2.2 Lokomat

Hocoma is a world-class company for the development, manufacture and marketing of robotic devices and sensors for functional movement therapy. The Swiss-based medical technology company was founded in 1996 by electrical and biomedical engineers Gery Colombo and Matthias Jorg respectively, and the economist Peter Hostettler [7]. It has several products for rehabilitation, but the most well-known is the exoskeleton called Lokomat.

The Lokomat (Fig. 10.1b) is a robotic orthotic device that provides variable support of body weight and relief to the lower limbs of patients while walking on a treadmill [8]. It consists of four main components: body weight support, lower limb orthoses, the treadmill and the virtual reality environment. The patient is installed on a body weight support system through a harness, which allows patients to walk despite the degree of weakness they present at the top. The lower limbs exoskeleton is used around the legs for orientation and movement of the legs. The therapy consists of the movements of the legs in the sagittal plane through its two joints actuated by each limb, one for the hip and the other for knee flexion. The new version of the exoskeleton is called LokomatPro [9], which allows lateral translation and transverse rotation of the pelvis up to 4° for a more natural gait.

10.2.3 ReWalk

The ReWalk exoskeleton was developed in Israel when mechanical engineer Dr. Amit Goffer became tetraplegic due to a car accident in 1998. The company, which has the same name of the exoskeleton, was founded in 2001 to help people with paraplegia [10]. The lower limbs exoskeleton provides power to the hip and knee joints in order to generate movement for people with spinal cord injury (SCI). It allows them to stand erect, walk, turn, and go up and down stairs. The latest version of the portable robot provides independent, controlled walking while mimicking the natural gait pattern of the legs. ReWalk (Fig. 10.1c) system operates with a tilt sensor which detects changes in the user balance and helps in the movement control algorithm through the subtle changes in their center of gravity [11]. That is, if the system detects forward tilt of the upper body, it starts its first forward step. The repeated displacement of the body generates a sequence of steps that mimics a natural functional gait of the legs. Its battery system is lightweight and powers the motors that are positioned at the hip and knee joints. If the tilt sensor does not detect inclination, the exoskeleton is held in its upright position.

10.3 Conceptual Design

Through the conceptual design process, an exoskeleton solution is sought based on the proposed specifications and requirements. The following are the design parameters necessary for its elaboration. Anthropometry, responsible for measuring the human body and its proportions, provides data to determine main body dimensions. The relationship of the segments of the human body respect to the height of a person used in the following design was proposed by Drillis et al. in [14].

The adjustable exoskeleton must fit an average Peruvian, from a 11 year old child to an adult. Dr. Isaac Crespo, former president of the Peruvian Society of Endocrinology, mentions in [15] that in recent years there has been an increase in the average height in Peru, the average height of peruvian women and men are 1.68 and 1.72 m respectively. Cossio-Bolaños et al. [16] carried out a cross-sectional and descriptive study in school children in Arequipa, Peru. The universe consisted of 5,627 school children from the urban areas of the district Jose Luis Bustamente y Rivero. The anthropometric variables evaluated were body mass (kg), height (m), tricipital skin fold (mm) and arm circumference (cm). The maximum height of an 11 years old kid found is 1.44 m, corresponding to the girls average.

Based on the information of the heights and considering the lengths of the human body segments, the main dimensions of the adjustable lower limbs exoskeleton were selected and are shown in Table 10.1.

The definition of the degrees of freedom that the hip, knee, and ankle joint have can be found in [17, 18] and are detailed in Table 10.2. The system will provide the active motions through actuators with a high torque and light weight which exert the

Table 10.1 Segments dimensions of the lower limb exoskeleton structure

Lower limb segment	Peruvian male average (cm)	11-years old Peruvian average (cm)	Total displacement (cm)
Hip	32.852	27.313	5.539
Transversal hip[a]	13.247	11.014	2.233
Thigh	42.140	35.035	7.0105
Shank	42.312	35.178	7.134
Foot	26.144	21.736	4.408

[a]Because this measure was not found in the literature a scaled real human being model from SolidWorks software was used to determine an approximate displacement

Table 10.2 Degrees of freedom of the exoskeleton

Joint	Movement	Range of freedom (°)	Type
Hip	Flexion	0–90	Active
	Extension	0–30	Active
	Abduction	0–10	Passive
	Adduction	0–10	Passive
Knee	Flexion	0–90	Active
Ankle	Plantar flexion	0–40	Passive
	Dorsiflexion	0–30	Passive

necessary force so that the exoskeleton links reach the desired position. Finally, the structure will have an anthropomorphic and ergonomic design for patient comfort and ease of rehabilitation therapies.

10.4 Methodology

The prototype should be as light as possible, so the commercial aluminum 6061-T6 will be used. Aluminum and its alloys are among the most versatile from the point of view of manufacturing, The 6061-T6 is an aluminum of medium/high strength with a high resistance to corrosion, to tension and easily machined. It has a tensile yield strength of 275 MPa, an ultimate tensile strength of 310 MPa, a density of 2700 kg/m^3 and a Young modulus of 69 GPa as its main mechanical properties.

The adjustable length will be possible using telescopic bars with sliding common faces. This method will be used for hip, transversal hip, thigh and shank segments. The desired length will be fixed by using a pressure screw as shown in Fig. 10.2.

The active movements with the range described in Table 10.2 will be performed through two pneumatic artificial muscles (PAM) in each joint. The neumatic system has two principal advantages: lightweight and it is easy to recharge. The PAM is a tube type actuator that decreases its length when is pressurized with compressed air

Fig. 10.2 Telescopic bars of the thigh
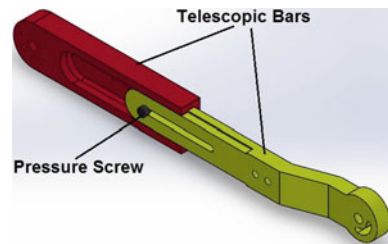
Fig. 10.3 Active movement of the exoskeleton with PAM actuator. **a** Reference ideal position. **b** Anticlockwise rotation. **c** Clockwise rotation
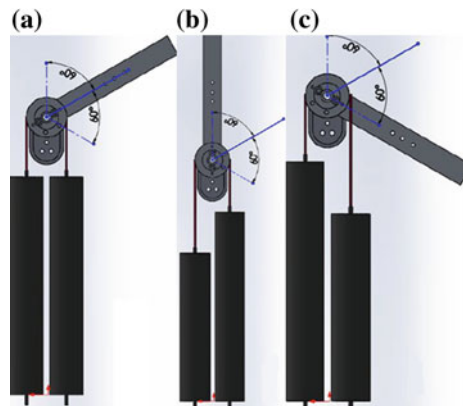
and thus generates a force [19]. As it only generates a compression force, but not traction, it will be necessary the use of two actuators with a configuration (Fig. 10.3) that allows controlling not only the anticlockwise rotation, but also the clockwise. Figure 10.3a represents the reference position for the movements, when both muscles are unpressurized. The figure only represents an ideal situation. In a real one, the thigh will not stay in that position because of the gravity force and the weight of patient and structure. Figure 10.3b shows only the first PAM pressurized, whose compression force allows the anticlockwise rotation, and Fig. 10.3c shows only the second PAM pressurized, allowing a flexion movement of the hip joint. Thus all the complete range is reached; the same method is used in the knee joint. Notice that both PAMs are attached to the hip pulley, and the movement of the thigh is generated by the rotation of the pulley.

The exoskeleton will need a total of 8 PAMs that will be placed in a backpack. The force will be transmitted using a brake cable and cable guides near the pulleys. The hip joint for the abduction/adduction movement and the knee joint will have a security mechanical stop in order to control their range of movements. To accomplish this important feature an inner guide at the end of the thigh link is added, such that one guide screw of the pulley defines its movement as seen in Fig. 10.4 for the right limb. The same method is used in the hip joint (see Fig. 10.5).

The maximum torque supported by both joints, the force, and the maximum length of contraction of the PAM must be known to select the radio of both pulleys. Accord-

Fig. 10.4 Knee mechanical
stop for security
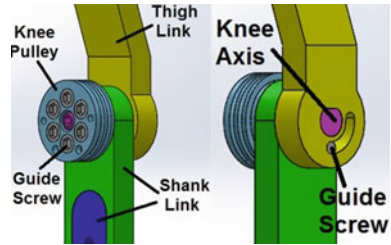
Fig. 10.5 Hip mechanical
stop for security
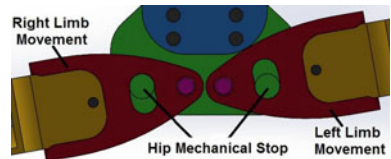
Fig. 10.6 Free body
diagram of the extended leg.
The weight and the lenght of
the foot is included
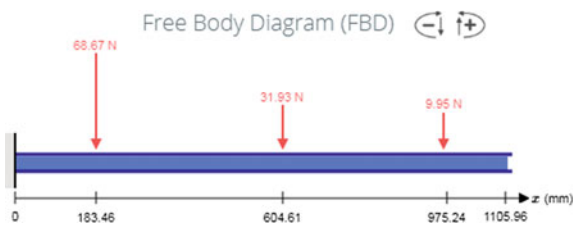
ing to the pneumatic actuator datasheet, found in [20], the maximum contraction is
the 20% of the total length for a load of 30 kg; thus for a 30 cm PAM length, the
maximum length contraction considered is $L_{con} = 6$ cm.

In order to calculate the maximum torque generated at the hip and knee pulleys, the
limb is analyzed at its critic position, that is, when the leg is completely extended in a
90° position. The determination of the weight of the segments and their center of mass
is based on the method presented in [21], where a review of several investigations
is presented. Figure 10.6 is the free body diagram used to calculate the maximum
torque supported by the shank and the thigh.

The maximum torque generated by the hip and the knee joint is 41.5 N-m and 11.36
N-m respectively. Replacing it in the basic torque formula, the minimum radio of the
pulley at the joint is calculated. $T = F \times r_{min}$, where T is the torque generated in the
joint (N-m), F is the force generated by the PAM (N), and r_{min} is the minimum radio
of the pulley (m). To calculate the maximum radius, the arc length formula of a circle
$(L_{con} = \theta_{max} \times \dfrac{\pi}{180} \times r_{max})$ is applied since the actuator contracts the same length
of arc of the pulley, and it is also reflected in the rotation angle. Each muscle will
need to cover half of the total active movement shown in Table 10.2, consequently,
the maximum hip angle is 60° and the maximum knee angle is 45°. The pulleys radio
range in millimetres are $23.05 < r_{HIP} < 57.3$ for the hip and $6.31 < r_{KNEE} < 76.4$

Fig. 10.7 Profile of the
telescopic bar used
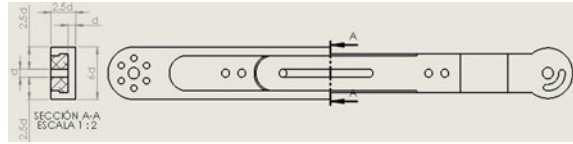
for the knee. With the range of radios for both pulleys known, a radio of 24.5 mm for the hip pulley and of 22 mm for the knee pulley is chosen.

To determine the normal bending stresses in the links with the limb in the critical position, the equations for normal bending stresses in straight beams were used, these equations are based on the following assumptions [22]:

- The shear force is zero and there is no torsion nor axial loads.
- The link or beam is initially straight with a constant cross section through the link or beam length.
- The beam has an axis of symmetry in the plane of bending.
- The cross-section is rectangular with a minimum base to height ratio of 1:2.

The maximum bending stress occurs in the part of the profile where the distance to the centroid is the largest, and is given by the following formula $\sigma_{\max} = \dfrac{M \times C}{I}$, where M is the bending moment, C is the distance from the centroid to the top and I is the second moment of the cross section with respect to the x-axis.

The shape of the cross section used for the determination of the dimensions of both, the thigh and shank links is shown in Fig. 10.7. The second moment of the cross section is calculated with the expression (10.1). The area of the hole that fixes the length of the bar is considered in the calculations. The hole represents a discontinuity called stress raiser, and the region in which it occurs is called area of stress concentration. A theoretical stress-concentration factor Kt is used to relate the actual maximum stress at the discontinuity to the nominal stress [22].

$$I_X = I_{\text{total}} - I_{\text{hole}} \tag{10.1}$$

$$I_X = 44.875d^4 \tag{10.2}$$

$$C = 3d \tag{10.3}$$

The nominal value of the bending stress is the maximum value calculated with the maximum bending stress formula. To determine the actual stress value, the nominal value is multiplied by a factor Kt = 2.1 obtained from Table A-15 in [22]. This value must be lower than the tensile yield strength of the material, considering a safety factor (SF).

Taking into account that the analysis does not consider the weight of the structure and the instrumental equipment of neither the exoskeleton nor the torque generated by the foot, a SF of 7 was considered. Another factor to take a high SF is the fact

that the exoskeleton will be used by rehabilitation patients. Using expression (10.4) and the maximum bending stress formula, the minimum profile of the telescopic bar for the thigh and the shank is calculated: $d_{\text{thigh}} \geq 5.3$ mm and $d_{\text{shank}} \geq 3.5$ mm.

$$\sigma_{\max} \times K_t \leq \frac{S_y}{SF} \tag{10.4}$$

Since the dorsiflexion and plantarflexion movements are not active; a torsion spring of 2 N-m is used to cushion the normal gait and repetitive therapeutic movements as shown in Fig. 10.8a. Thus, a 90-degree foot position with respect to the shank is always sought. A single row ball bearing is used in the hip and knee joints to allow radial movement with minor friction. A contact seal type is selected for a better control of grease contamination. To prevent linear displacement, retaining rings are used as shown in Fig. 10.8b. Finally, important components in the assembly are the guides for the power transmission cables of the PAM. They are positioned on each side of the hip and knee joint and serve as a guide for attaching the cables to the pulleys (Fig. 10.8c).

10.5   Results

Numerical analyses of the main pieces subjected to critical loads were performed to verify that the material chosen and the design of the pieces were the appropriate. The software SolidWorks 2015 was used to perform a finite element and buckling analysis. In the case of the hip area, the stops must resist the maximum force generated by the patient. The resulting distribution of stresses is shown in Fig. 10.9 and the maximum stress value is 148.3 MPa, which is located in the cylindrical face corresponding to the stop. The maximum displacement is 5.56 mm and occurs at the same point. The safety factor of the complete assembly is 1.9.

A simulation of the lower limb in its critical position was performed. The loads applied were the weights of the thigh, shank, and foot of the patient, and a torque generated by the foot length. The Von Mises stress analysis gives a maximum stress value of 65.25 Mpa, the results are shown in Fig. 10.10. Finally, the displacement analysis gives a maximum value of 5.71 mm. The assembly has a safety factor of 4.2.

The prototype was designed to work in parallel with patients whose upper limb mobility is not affected. A flexural analysis (buckling) of the lower limb structure was performed considering a critical force equal to the maximum upper body weight based on the chart found in [21]. This force is applied at the highest point of the limb (at the top) represented as an Euler's critical load. The conditions assumed at the ends of the column were: one end free and the other fixed, even though the exoskeleton does not support this total force. Four possible failure modes, shown in Fig. 10.11, were analyzed with SolidWorks 2015 software to verify the load factor (strength of the structure) of the lower limb. The resulting load factors for the mode 1, 2, 3 and 4 are 3.0197, 24.928, 47.239 and 92.83 respectively, showing that the structure supports the maximum weight.

The back structure is conformed by a support base, in which there are two cases to place four pneumatic artificial muscles in each of them. The main power source

Fig. 10.9 Equivalent Von Mises stress of the hip system of the exoskeleton
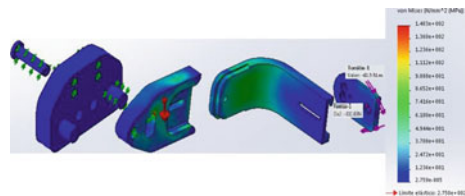
Fig. 10.10 Equivalent Von Mises stress of the thigh-shank pieces
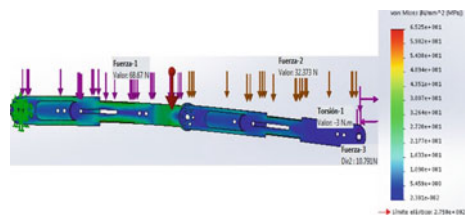
Fig. 10.11 Buckling
simulation results: mode 1,
mode 2, mode 3 and mode 4
(from left to right)
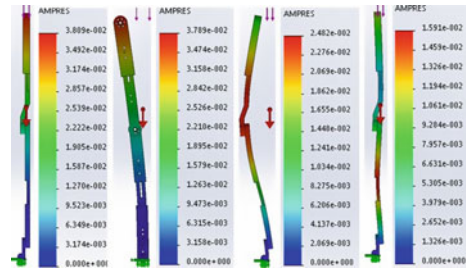
Fig. 10.12 Lower limb
exoskeleton prototype of an
11-year-old child
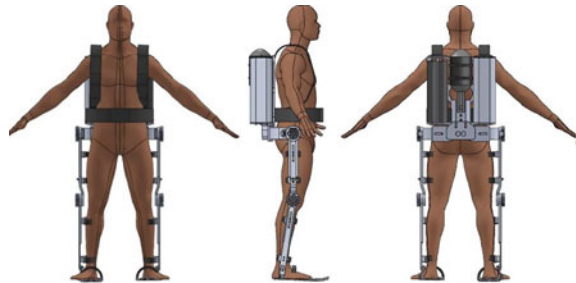
of the system is pressurized air from a compressed air tank made of fiber carbon to reduce the weight of the complete device, Fig. 10.12 shows the prototype adjusted to its minimum size to fit the model of the size of an average 11-year-old Peruvian child. The cover of the left backpack has been taken out in order to see the actuators inside.

10.6   Conclusion

A design and strength analysis of a lower limb exoskeleton for rehabilitation was presented in this paper. A patient of 70 kg of weight and 1.72 m of height was considered for the strength analysis with SolidWorks 2015 software. The results obtained guarantee the correct performance of the exoskeleton with an appropriate safety factor and imperceptible minimum movements. Fatigue analyzes were obviated since the rehabilitation therapy is slow and smooth. The exoskeleton allows 7 types of movement: three controlled, which represent the sagittal displacement of the hip and the knee, and four passive, where the abduction and adduction present a motion range of $10°$ and the ankle movements are damped by a torsion spring of 2 N-m. Among the different types of actuators used in the exoskeleton industry, the PAM was selected as the main actuator because of their lightness and their ability to produce the force required to raise an adult lower limb. Through the contraction of the PAMs, the pulleys are turned to generate the sagittal movements.

References

1. Xie, S.: Advanced Robotics for Medical Rehabilitation: Current State of the Art and Recent Advances, vol. 108. Springer (2015)
2. Primera Encuesta Nacional Especializada sobre DISCAPACIDAD 2012. Instituto Nacional de Estadstica e Informtica. http://www.regionlalibertad.gob.pe/ineiestadisticas/, Mar 2014
3. Laguna, J.: Derecho a la salud de las personas con discapacidad, ser. Colección Estudios sobre discapacidad en el Perú. Comisión Especial de Estudio sobre Discapacidad del Congreso de la República. https://books.google.com.br/books?id=V70UAQAAIAAJ (2006)
4. HAL corporate identification. https://www.cyberdyne.jp/english/company/index.html. Accessed 10 June 2017
5. Zelinsky, A.: Robot suit hybrid assistive limb [industrial activities]. IEEE Robot. Autom. Mag. **16**(4), 98–98, 102 (2009)
6. Sankai, Y.: Hal: hybrid assistive limb based on cybernics. In: Robotics Research, pp. 25–34. Springer (2010)
7. Hocoma about us. https://www.hocoma.com/hocoma/about-us/. Accessed 10 June 2017
8. Neckel, N., Wisman, W., Hidler, J.: Limb alignment and kinematics inside a lokomat robotic orthosis. In: 2006 International Conference of the IEEE Engineering in Medicine and Biology Society, August 2006, pp. 2698–2701 (2006)
9. Functional robotic gait therapy. https://www.hocoma.com/wp-content/uploads/2016/08/bro_LokomatPro_141008_en.pdf. Accessed 10 June 2017
10. Spungen, A.M., Asselin, P., Fineberg, D.B., Kornfeld, S.D., Harel, N.Y.: Exoskeletal-assisted walking for persons with motor-complete paraplegia. Res. Technol. Organ. Hum. Factors Med. Panel N. Atl. Treaty Organ. (2013)
11. Talaty, M., Esquenazi, A., Briceo, J.E.: Differentiating ability in users of the ReWalkTM powered exoskeleton: an analysis of walking kinematics. In: 2013 IEEE 13th International Conference on Rehabilitation Robotics (ICORR), June 2013, pp. 1–5 (2013)
12. Gardner, A.D., Potgieter, J., Noble, F.K.: A review of commercially available exoskeletons' capabilities. In: 2017 24th International Conference on Mechatronics and Machine Vision in Practice (M2VIP), November 2017, pp. 1–5 (2017)
13. Bernhardt, M., Frey, M., Colombo, G., Riener, R.: Hybrid force-position control yields cooperative behaviour of the rehabilitation robot lokomat. In: 9th International Conference on Rehabilitation Robotics, ICORR 2005, June 2005, pp. 536–539 (2005)
14. Drillis, R., Contini, R., Bluestein, M.: Body Segment Parameters. New York University, School of Engineering and Science Research Division, NY (1966)
15. Sulca, R.: Da mundial de la talla baja: los peruanos ahora son ms altos? http://vital.rpp.pe/expertos/dia-mundial-de-la-talla-baja-subio-talla-promedio-de-peruanos-noticia-907951#section-comment. Accessed 12 June 2017. RPP vital, October 2015
16. Cossio-Bolaos, M., Figueroa, P., Cossio-Bolaos, W., Lzari, E., Arruda, M.: Parmetros del crecimiento fsico de nios que viven a moderada altitud. Revista Medica Herediana, vol. 23, pp. 96–105. http://www.scielo.org.pe/scielo.php?script=sci_arttext&pid=S1018-130X2012000200004&nrm=iso, April 2012
17. Marrero, R., Rull, I.: Biomecnica clnica de las patologas del aparato locomotor Masson. https://books.google.com.br/books?id=bBZyst1al68C (2006)
18. Nordin, M., Frankel, V.H., Forssén, K.: Biomecánica básica del sistema musculoesquelético. McGraw-Hill. Interamericana (2004)
19. Zhang, D., Zhao, X., Han, J.: Active modeling for pneumatic artificial muscle. In: 2016 IEEE 14th International Workshop on Advanced Motion Control (AMC), April 2016, pp. 44–50 (2016)
20. Kanda Tsushin Kogyo pneumatic artificial muscle datasheet. http://www.kanda.co.jp/jp/examples/medical/muscle/air-muscle.pdf. Accessed 10 June 2017
21. Winter, D.A.: Biomechanics and Motor Control of Human Movement. Wiley (2009)
22. Shigley, J.E.: Shigley's Mechanical Engineering Design. Tata McGraw-Hill Education (2011)

Chapter 11
A Method to Identify the Difference in Kinematic Behavior of Human Model Lower Extremities with Respect to Muscle Activation During Crash Impact

Kishan Srinivas Indrani, Nils A. Hakansson and Hamid M. Lankarani

Abstract The main objective of this study is to develop a computational human musculoskeletal model, used to investigate the change in the kinematic behavior of the model's lower extremities under the influence of activated (active) and deactivated (passive) muscles, during a representative frontal collision using the *OpenSim* software. Since OpenSim is seldom used in crash simulations, an appropriate model evaluation is performed by comparing the model's kinematics, obtained from the OpenSim's inverse dynamic simulation, against the LS-DYNA's explicit non-linear side impact simulation of a finite element model for a car-pedestrian collision. The required musculoskeletal model is constructed in OpenSim and scaled to meet the requirements of the Hybrid III 50th percentile crash test dummy. For evaluating the developed model, the kinematics from both programs (OpenSim and LS-DYNA), containing identical displacement data, are compared by visual observation of identical time frames. Using the evaluated model in the forward dynamics domain of OpenSim, representative frontal crash simulations are conducted for the active and passive muscle states of the musculoskeletal model, and the kinematic differences in the human model's lower extremities are extracted and compared.

11.1 Introduction

Computational human body models (HBMs) are globally accepted and utilized by researchers and major industries such as the automotive, aerospace etc., with an

K. S. Indrani · N. A. Hakansson · H. M. Lankarani (✉)
Wichita State University, 1845 Fairmount St, 67260 Wichita, KS, USA
e-mail: hamid.lankarani@wichita.edu

K. S. Indrani
e-mail: kxsrinivasindrani@wichita.edu

N. A. Hakansson
e-mail: nils.hakansson@wichita.edu

intention to reconstruct accidents and to identify model's biomechanical responses under varied impact conditions.

Over the past few decades, mathematical models have been preferred over the traditional cadaver and anthropomorphic test dummies (ATDs) to simulate the effect of design parameters and corresponding human behavior during vehicle crash events. Also, during this period, different platforms have emerged to aid in human musculoskeletal modeling and dynamics simulation, in order to better understand the details behind the science of human body movement and focus on the causes.

Toyota motor corporation and Toyota research group have jointly developed an active finite element human body model called 'The Total HUman Model for Safety', abbreviated as 'THUMS', which is a simplified and accurate mathematical representation of human musculoskeletal structure [1]. This model is intended to simulate ideal human kinematics, and document reactions to various injury scenarios, including internal organ failures [2].

OpenSimulator, abbreviated as *OpenSim*, is a powerful musculoskeletal modeling platform, an open source software which uses a combination of springs, dampers, diverse types of joints, controllers, actuators etc. to create a human musculoskeletal model [3]. This platform uses a modified version of Hill-type muscle model, called the Thelen2003Muscle model, which captures the active and passive behavior of the muscles, and efficiently demonstrates muscle-tendon dynamics. This platform also enables one to perform inverse kinematics, kinetics, static optimization, and forward dynamic simulations of human movement.

11.2   Methodology

In this study, the musculoskeletal software OpenSim has been chosen which serves the needs of frontal crash simulation, along with providing a suitable control over the model's muscle properties. The model development has the following requirements: 1. The musculoskeletal model used for this study needs to represent the physical dimensions and weight of the 50th percentile adult male finite element model. 2. It should contain all the major muscles in lower extremities, and 3. Appropriate constraints and degrees of freedom should be defined between the geometries to simulate actual motion within OpenSim. Hence, the musculoskeletal model has been created per the physical requirements of a Hybrid III Anthropomorphic Test Dummies (ATD). The developed model is then evaluated and subjected to forward dynamics, in order to analyze the kinematic behavior of the model's lower extremities at active and passive muscle states. For simplicity, the muscle states of the upper extremity have been neglected in this study.
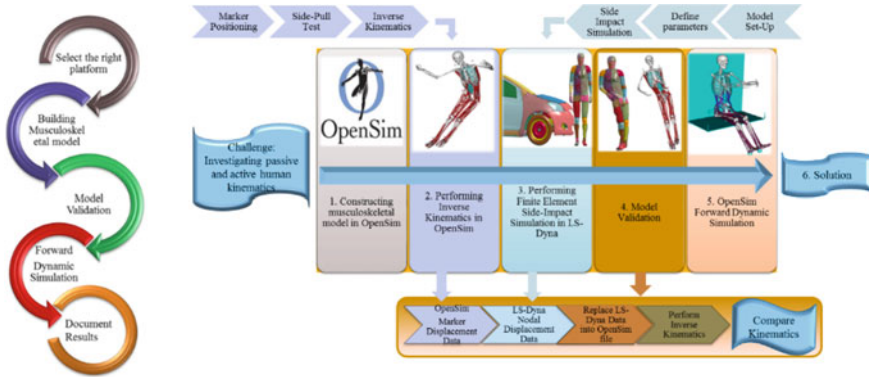
Fig. 11.1 The overall (left) and the detailed methodology (right) adopted for this study

11.2.1   Overall and Detailed Approach

A well-constructed approach (Fig. 11.1) has been utilized to study the effect of muscle activation properties on the human kinematics during a frontal crash scenario.

11.2.2   Muscle Definition and Activation Properties

The muscles used for this study are differentiated based on their function and location in the body. The muscle naming conventions are identical to the OpenSim's standard naming conventions, based on the muscle's location and function. Eighty-four muscles have been defined in the developed musculoskeletal model, aiding in the abduction, adduction, eversion, inversion, flexion, extension, rotation, plantarflexion, and dorsiflexion movements of the lower extremities. The muscle activation has been defined using a unit-less value between 0 and 1, where 0 represents no muscle activation and 1 represents peak muscle activation.

11.2.3   Contact Model Definitions

The Elastic-Foundation model and Hunt-Crossley force model are the two contact models used in this study (Table 11.1) [4, 5]. Choice of suitable contact model has been decided based on the simulation conditions, contact surface, contact behavior, and distance between the surfaces. Contact parameters such as stiffness, dissipation, static friction, dynamic and viscous friction, and transition velocity have been held constant for both the contact models.

Table 11.1 Contact model selection for various parts of the developed model

Bodies	Contact model
Thorax, sled	Elastic-foundation model
Pelvis, sacrum, sled	Elastic-foundation model
Femur, sled	Hunt-Crossley model
Tibia, sled	Hunt-Crossley model
Foot, sled	Hunt-Crossley model

Fig. 11.2 Process used to evaluate the OpenSim model

11.3 Model Evaluation

Since its inception, OpenSim, as a modeling platform, has seldom been used to analyze vehicle occupant's response during impact crash scenarios. Therefore, there is little known information about the output accuracy from the OpenSim, as compared to traditionally used simulation platforms such as the LS-DYNA.

The 50th percentile adult male along with a compact car finite element (FE) model have been utilized to perform evaluation in the LS-DYNA post-processor. The compact car, accelerating at 30 miles per hour, is made to impact the THUMS pedestrian model. Nodal data from 27 desired locations on the THUMS are extracted from the crash simulation, and used as input to perform the inverse kinematic analysis in OpenSim, on the developed model. The evaluation is performed based on the accuracy of the kinematics obtained from both platforms, using identical displacement data. The process used to evaluate OpenSim model is shown in Fig. 11.2.

To facilitate ideal replication of the kinematics in both the platforms, 27 marker positions have been chosen at prescribed points on the developed musculoskeletal as well as the THUMS models (Fig. 11.3).

The marker displacement data file is obtained as a result of the OpenSim inverse kinematic simulation. An inverse kinematic experiment is conducted on a human volunteer in a laboratory setting (Fig. 11.4). The volunteer has been subjected to a side pull force of around 60 N, during which the motion has been recorded using 12 motion capture cameras at 200 frames per second. This data has been refined using the CORTEX software, and later, used as an input file (motion data) to perform an inverse kinematic simulation involving the developed OpenSim model. The result of this simulation is a motion identical to that of the volunteer's test. The motion capture camera stores the motion data; i.e. the marker displacements, in the marker displacement file. The purpose of this experiment was to obtain the marker displace-
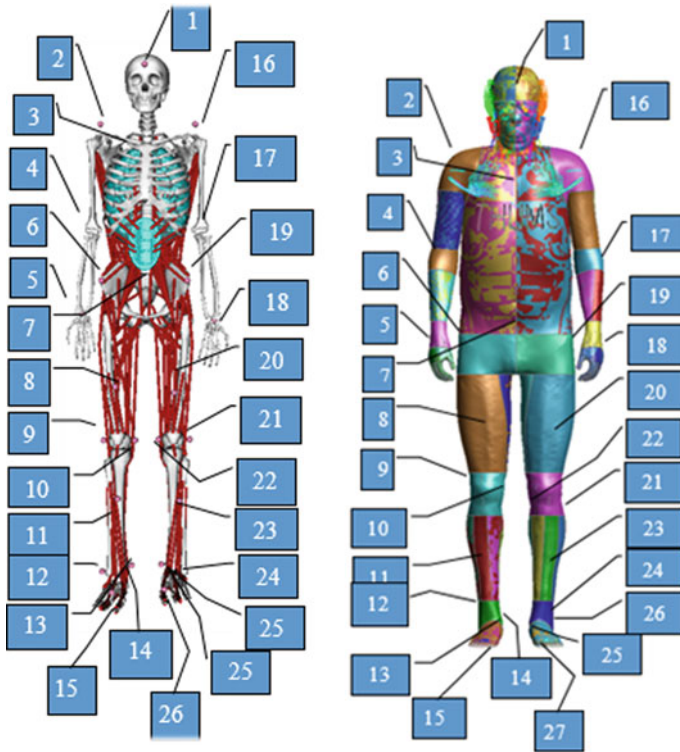
Fig. 11.3 Marker position on the OpenSim model (left), and the nodal data points on the THUMS model (right)

ment file, which can be used as a standard template to replicate the FE simulations in OpenSim.

Since LS-DYNA is commonly used to perform crashworthiness simulations in order to analyze occupant and pedestrian safety, a side impact simulation has been performed using this software. The THUMS pedestrian FE model has been subjected to 30 miles per hour impact from a compact FE car model (Fig. 11.5), and 27 nodal displacement data were produced.

OpenSim successfully utilized the nodal displacement output from an explicit simulation, input into its marker displacement file, in order to replicate kinematics of the human model from the LS-DYNA simulation.

From Fig. 11.6, visible differences in the kinematic behavior of the models in the regions above the pelvis, including upper extremities, has been observed. However, these differences are negligible, as the bodies under consideration do not deviate by a large margin. It can be concluded that the OpenSim and THUMS models have shown reasonably similar kinematic response for identical displacement data.
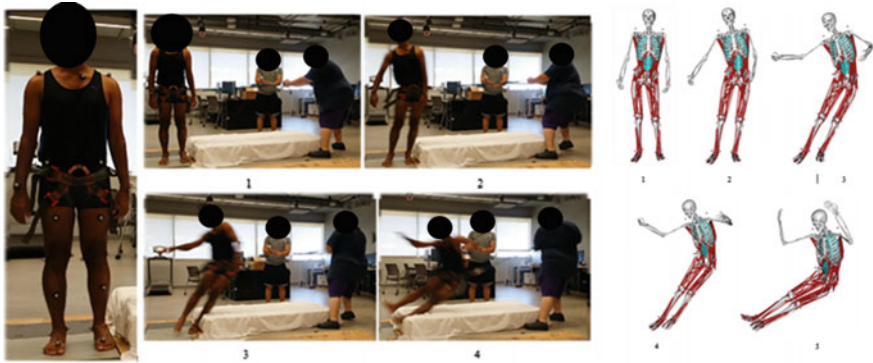
Fig. 11.4 (Left) 27 marker positions on the human volunteer, (center) side-pull test, and (right) replication of the human volunteer's motion in OpenSim's inverse kinematic simulation. [Ethical approval of the human subjects activities are on file by the institutional IRB no. 4329.]
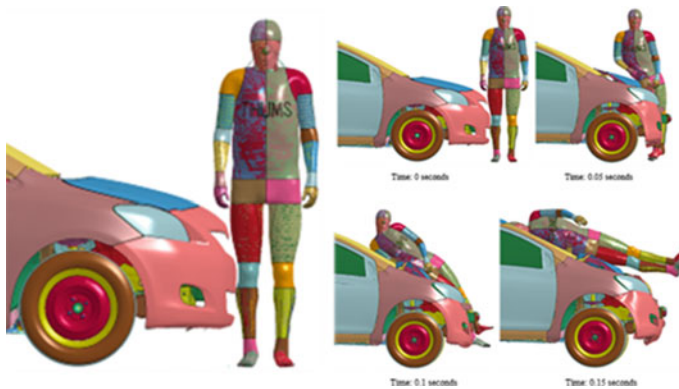
Fig. 11.5 (Left) Model set-up in LS-DYNA, and (Right) crash kinematics at different time frames

11.4 Frontal Crash Simulation

The evaluated model is then used to identify differences in kinematic behavior of a car occupant under active versus passive muscle states during a frontal impact.

A simple sled test, with a lap belt, has been used to replicate an impact of a car occupant. The sled is modeled using a contact half spaces in OpenSim, and the developed model is super imposed over it, with appropriate contact models defined between the sled, human, and the lap belt. Forces extracted from a frontal impact tests [6] have been used to prescribe the motion of the sled. Simulations are then conducted for identical crash conditions with and without muscle activation. Results are then compared to identify the kinematic difference during these states (Fig. 11.7).

In the interest of accuracy and achieving robust results, it is necessary to bring the human model to equilibrium with the stationary sled. Once the correct contacts are
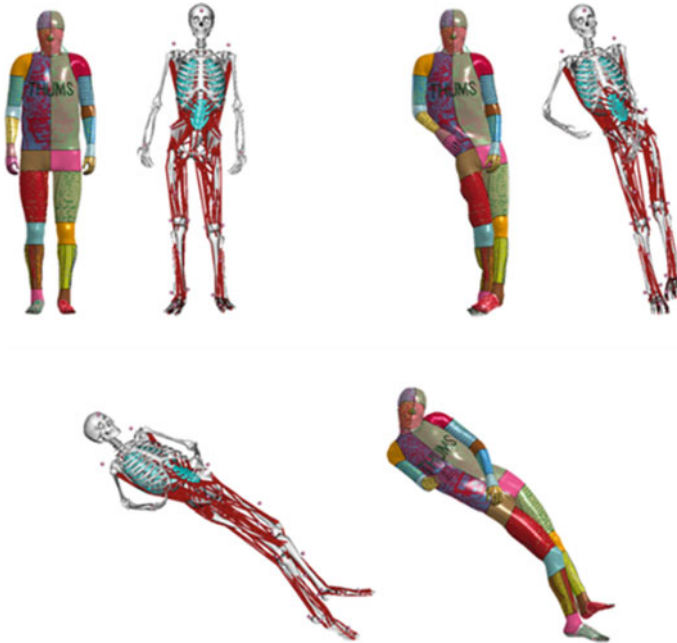
Fig. 11.6 Comparing the kinematic simulations obtained from OpenSim's inverse dynamic approach and LS-DYNA's explicit simulation using identical displacement data
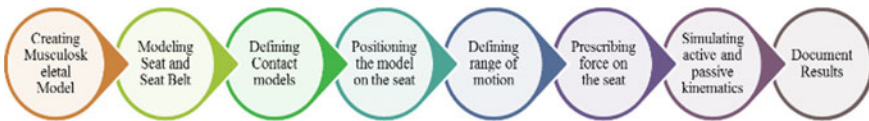
Fig. 11.7 Sequence of steps followed to identify the kinematic difference during a sled test with varying muscle activation levels

defined, the developed model is shaped to the required seated position upon the sled, but with negligible gap between the body and sled. The simulation is conducted with the sled locked in place, and the model falling into position onto the sled with only gravitational force acting on it. Over the simulation duration, the model achieves an ideal equilibrium position, which is standardized as an initial position, to perform further analysis.

Figure 11.8 shows the initial position of the OpenSim model on the sled with a lap belt. The lap belt is initially constructed as a 3-dimensional model and then meshed into a finite element model in order to define Elastic-Foundation contact with other geometries.

The New Car Assessment Program (NCAP), in the year 1999, performed a frontal barrier impact test on a typical sedan [6]. Data from an accelerometer placed under
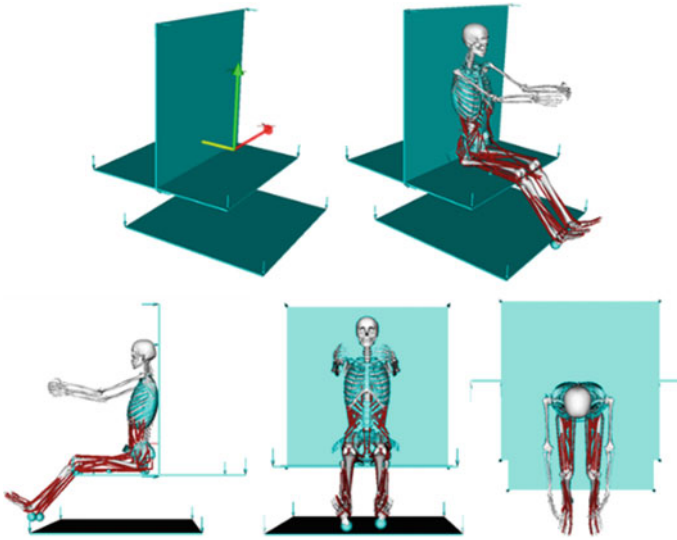
Fig. 11.8 Initial position of the developed model attained before starting the impact crash simulation

the driver's seat has been extracted and converted into force data using Newton's second law of motion, which is then used to prescribe the sled's motion in this study.

Two simulations have been conducted, with and without muscle activation, to compare the kinematics of the model's lower extremities. First simulation, to identify the kinematics of the musculoskeletal model with activated muscles, the activation values for all the muscles in the lower extremities is assumed to be maximum; i.e. 1, throughout the simulation duration, with an activation time constant of 0.01 s. Second simulation is conducted without considering any muscle activation.

11.5   Results for Active and Passive Models

The kinematics of the developed musculoskeletal model are recorded during sled deceleration tests for two muscle cases:

1. Activated Muscles and
2. Deactivated (Passive) Muscles
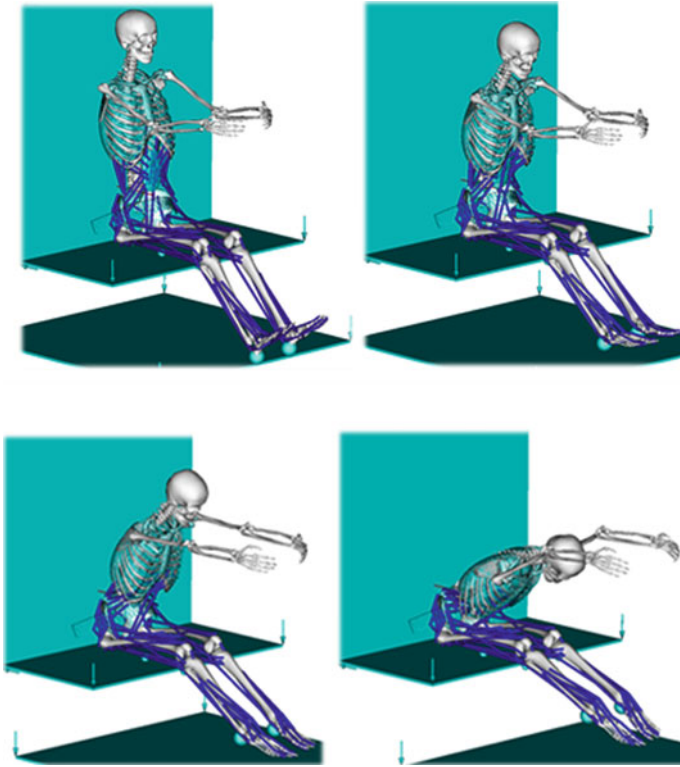
Fig. 11.9 Passive kinematics of the model with deactivated muscles at various time frames of 0, 0.075, 0.1 and 0.125 s during the simulation

11.5.1 Simulation Using Passive Muscles

The positioned musculoskeletal model is prepared to perform a negative sled deceleration with deactivated muscles. The passive kinematics of the model are recorded for a duration of 0.125 s (Fig. 11.9).

By visual observation of the kinematics, maximum displacements are noticed in the torso, head, neck, and the upper and lower extremities of the musculoskeletal model. Also, the right and left ankle are displaced by 84.6 and 81.7° from their initial positions, respectively. Similarly, the right and left knee are displaced by 22.4 and 20.2°, respectively. Over the simulation duration, the sled is displaced by 0.59 m, whereas, the pelvis is displaced by 0.58 m. The positions of the other bodies and joints have been ignored, as they are deemed insignificant in magnitude when compared to the displacements of the knees and ankles.
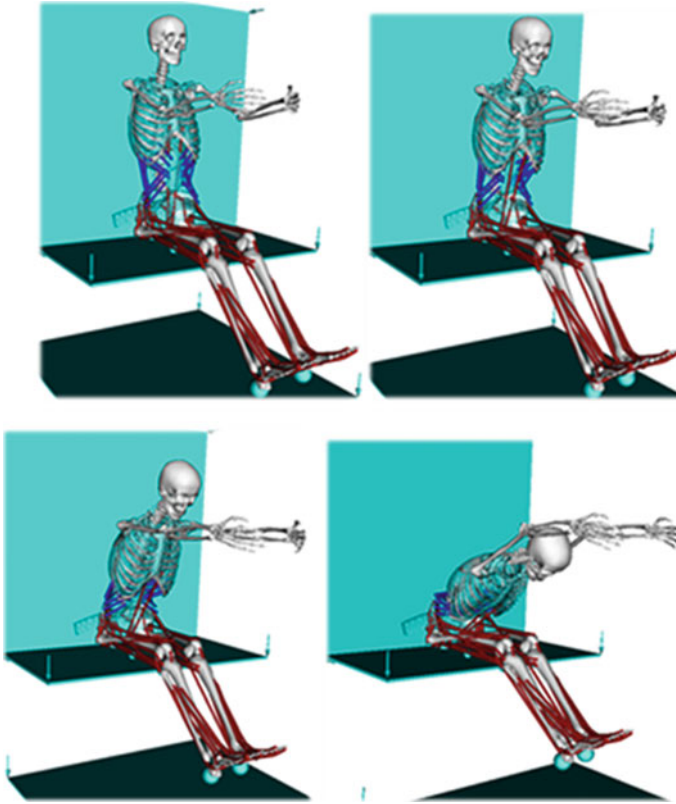
Fig. 11.10 Active kinematics of the model with activated muscles at various time frames of 0, 0.075, 0.1 and 0.125 s during the simulation

11.5.2 Simulation Using Activated Muscles

The positioned musculoskeletal model with muscle activation properties is prepared to perform a negative sled deceleration. The model kinematics are recorded for a duration of 0.125 s (Fig. 11.10).

Similar to the observation from the passive kinematic simulation, maximum displacements are observed in the torso, head, neck, the upper and lower extremities of the musculoskeletal model. When compared to the initial positions, it is observed that the right and left ankle are displaced by 15.1 and 14.7°, and the right and left knee are displaced by 37.0 and 37.3° respectively.
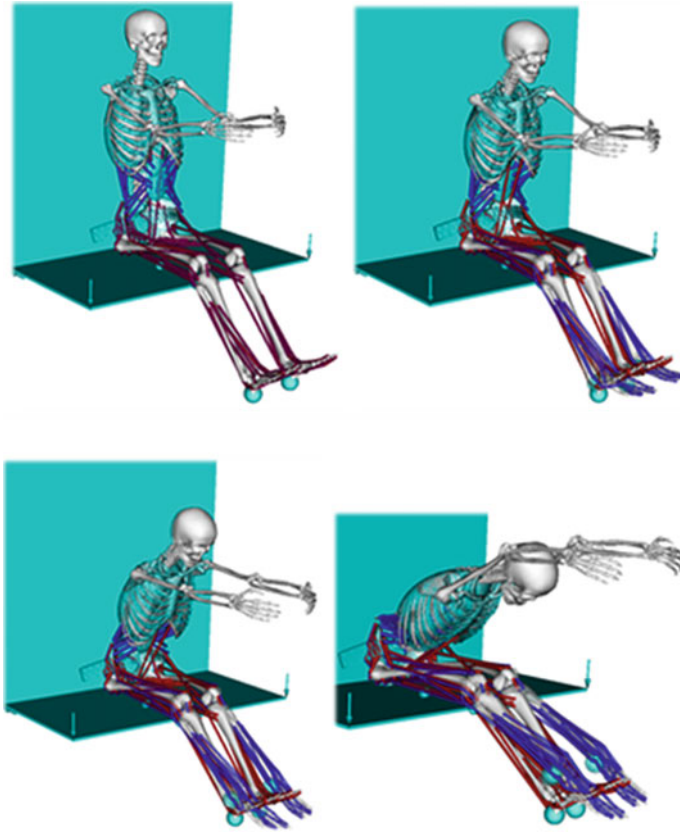
Fig. 11.11 Comparative kinematics of the model with activated and deactivated muscles at various time frames of 0, 0.075, 0.1, and 0.125 s during the simulation

11.5.3 Comparing Active and Passive Muscle Kinematics

Figure 11.11 shows that there is significant visible difference in the kinematics of the lower extremities of the human musculoskeletal model when subjected to muscle activation, as compared to the kinematics with deactivated muscles. The most significant kinematic difference can be observed in the regions of the tibia, ankle, and foot (talus, calcaneus, toes etc.).

When comparing the kinematics of the lower extremities under the active and passive muscle states, it is observed that the largest difference occurs in the regions of the knee and ankle. The relative displacements between the active and passive muscle states are noticed where the right and the left knees are displaced by 14.6 and 13.4°, respectively, and, the right and the left ankles are displaced by 69.5 and 67.0°, respectively. The kinematics of the human model under active muscle state exhibits smaller displacements in the body and the joints of the lower extremities,

Table 11.2 Difference in the kinematics of the musculoskeletal model, with and without activated muscles in the lower extremities

Body and joints	Tx[a]	Ty[a]	Tz[a]	Θx[a]	Θy[a]	Θz[a]
Pelvis	X	−0.005	X	X	−0.335	−1.975
Right hip	X	X	X	−0.468	X	4.535
left hip	X	X	X	−0.083	X	1.053
Right knee	X	X	X	−14.630	X	X
Left knee	X	X	X	−13.364	X	X
Right ankle	X	X	X	69.542	X	X
Left ankle	X	X	X	67.000	X	X

[a]Represents the translational and rotational displacements in the x, y and z directions, respectively

when compared to the kinematics of the OpenSim model under the passive muscle state (Table 11.2).

11.6 Conclusions

All standardized injury criteria currently used for evaluating occupant injuries are based on traditional test results involving cadavers and ATDs. It has since been argued that the accuracy of such criteria is questionable or otherwise incomplete, because of the inherent absence of consideration of human factors such as the in situ biomechanical human reactions, and the associated physical behaviors they induce in the crash response. Therefore, this study aimed, within this discussed context, to identify the difference between the human kinematics with and without muscle activation, could be a crucial aspect to consider within current injury criteria. This research demonstrates OpenSim's capabilities to model and simulate human musculoskeletal impact response performance. One challenge faced during this work was to identify the correct software which can model a human and perform muscle activation. Then, the selected software had to be evaluated alongside an existing finite element software, one used extensively in crash test simulations. Upon evaluating the OpenSim model, a novel approach was identified which can be used to study the effect of different muscle properties upon the kinematics of FE human model simulations. In the region of the lower extremities, such as the tibia, heel, and toes, the results obtained clearly indicate the presence of kinematic differences due to muscle activation. The most significant differences in kinematics were observed in the knee

angle and ankle positions, with approximate magnitudes of 14 and 67° respectively. Therefore this study indicates that the role of muscle activation in a human body during a collision could be a crucial factor in the application and consideration of associated injury criteria. Overall, the study demonstrates that the novel approach, in conjunction with the use of OpenSim, can be utilized for the investigation of human crash injury biomechanics.

References

1. Livermore Software Technology Corp (2017). Total Human Model for Safety—THUMS. http://www.lstc.com/thums
2. Oasys Software (2017). THUMS model. http://www.oasys-software.com/dyna/en/fe-models/THUMS.shtml
3. OpenSim (2017). OpenSim's Capabilities. https://simtk-confluence.stanford.edu:8443/display/OpenSim/OpenSim%27s+Capabilities
4. Flores, F., Lankarani, H.M.: Contact force models for multibody dynamics. In: Springer Book Series on Solid Mechanics and its Applications, vol. 226, 171p (2016)
5. Machado, M., Moreira, P., Flores, P., Lankarani, H.M.: Compliant contact force models in multibody dynamics: evolution of the Hertz contact theory. Mech. Mach. Theory **53**, 99–121 (2012)
6. Sasikumar, N.: Performance comparison of human and dummy models in various vehicle crash scenarios based on federal regulatory standards. Wichita State University, Wichita (2012)

Chapter 12
Modeling for the Design of a Lower Limb Exoskeleton for People with Gait Impairments

Christian Chicoma, Oscar Cieza, Enrique Pujada and Dante A. Elias

Abstract As part of the research efforts carried out at the Pontificia Universidad Católica del Perú, proposed models of lower limb exoskeletons were developed and simulated with the aim of getting valuable information for later mechanical design, and control system design, of the Lima lower limb exoskeleton for rehabilitation cases, which should replicate human gait and help people with gait impairments in the attempt to recover gait ability. This paper describes the process of modeling proposed for the Lima lower limb exoskeleton and shows simulation results that are important for future works.

Keywords Lower limb · Exoskeleton · Normal gait

12.1 Introduction

Disability refers to some restrictions and limitations in movement or displacement that part of the population suffers. CONADIS, an entity specialized in all issues related to disability in Peru, estimates that there are around 1.6 million of people with any kind of disability in Peru, where just 120 thousand people have been registered [1]. According to CONADIS, locomotion is the second main disability on Peruvian population registered.

Human gait is divided in two phases: stance and swing [2], as shown in Fig. 12.1. Physical and dynamic models have been proposed to materialize the way of human walking. In human gait, a periodic movement of each foot from one support position to next is necessary [3]. Multijoint pendulum is a physical model to represent whole body center of mass (COM) motion at the top of one leg during gait: a double pendulum fixed on the hip for swing phase and a double inverted pendulum for stance phase with foot fixed to the ground [4].

C. Chicoma · O. Cieza · E. Pujada · D. A. Elias (✉)
Laboratory of Research in Biomechanics and Applied Robotics, Department of Mechanical Engineer, Pontificia Universidad Católica Del Perú, Av. Universitaria 1801, Lima, Peru
e-mail: delias@pucp.pe
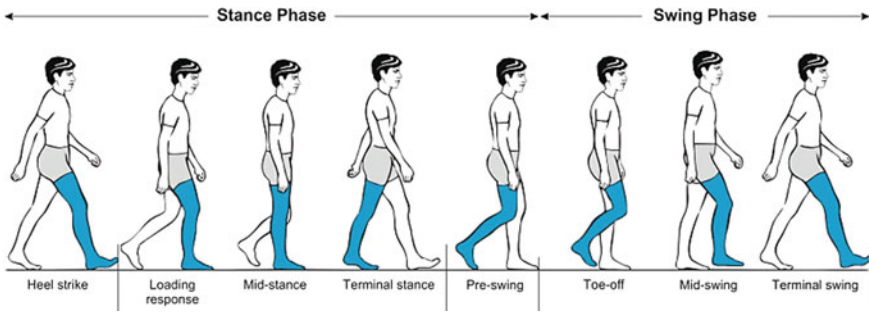
Fig. 12.1 Phases and events of gait cycle [2]

(a) Seven links   (b) Eight/Nine Links   (c) Roll-over shape approach
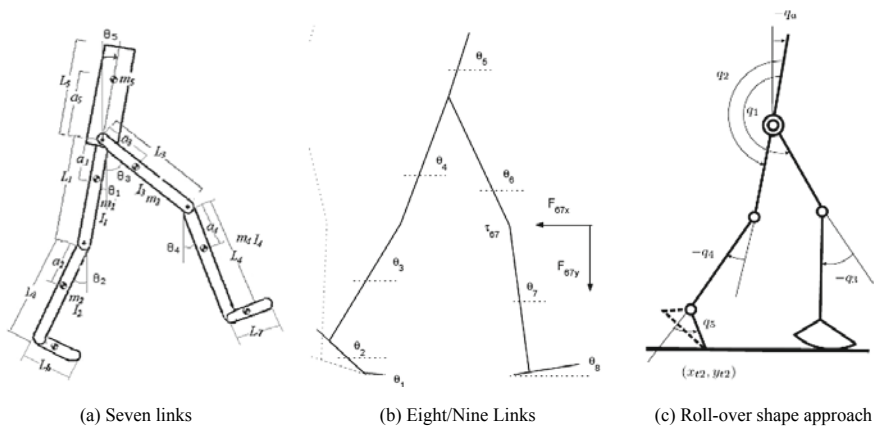
Fig. 12.2 Physical models proposed for human gait

Mechanical models have been developed to represent dual leg implementation for gait motion in sagittal plane. Link segment models consisting in rigid bodies and joints are need to represent the normal gait. As shown in Fig. 12.2: (a) 7-link model consisting on one head-arms-trunk (HAT) segment plus two legs each with a thigh, a shank and a foot [4], (b) eight/nine links model where additionally each foot consists of two segments: the toe and the hindfoot joined by metatarsal joint [5] and (c) 7-link model similar to (a) with foot roll-over shape approach for stance with Cartesian coordinates of the rolling point, the swing heel, and the trailing toe [6].

Motorized lower limb exoskeletons are first simulated as Nacy et al. [7] with one leg as a 3-link robotic manipulator (thigh, shank and foot), while the equations of motion were differentiated using Euler-Lagrange (E-L) method. Also the energy approach and the ground reaction forces were estimated as external forces acted on contact points on the foot. As well, Baluch et al. [8] proposed an 8-DOF model with four degrees of freedom (DOF) for each leg. Forward and Inverse kinematics of the proposed exoskeleton has been performed using E-L to calculate the expressions for the joint torques. Majeed et al. [9] proposed an angular position tracking control for a

Fig. 12.3 Stance (left) and swing (right) phases of 5-link model [10]
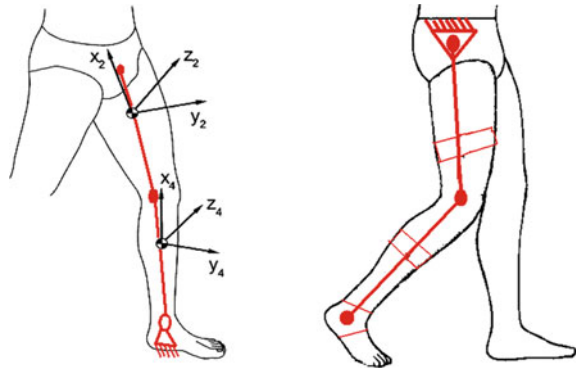
dynamic system consisting in a 3-link lower limb exoskeleton for gait rehabilitation, which the human-machine interaction assumed seamless and free from frictional elements.

12.2 Preliminary Proposed Modeling

In this research, a preliminary lower limb exoskeleton for gait rehabilitation was proposed considering a 5-link model, as shown in Fig. 12.3, considering a HAT and two legs, joined at the hip, each with a thigh and a shank [10]. It is assumed that patient will use walking sticks or any type of support and hold the upper body with the objective of compensating forces and moments generated at the hip joint.

For stance motion of the exoskeleton leg, the kinematic analysis is performed upwards by positions vectors of each link center of mass (COM), starting at the shank because foot is fixed to the ground. In case of kinetics, forces and torques are computed using Newton-Euler (N-E) equations.

A general free-body diagram (FBD) of the whole exoskeleton, shown in Fig. 12.4a, considering only external forces for the stance phase. Also, Fig. 12.4b shows a FBD for a leg links of the 5-link exoskeleton [10]. In both FBD, weights of human body segments (HAT, thigh and shank) are located at respective COM relative to the proximal joint are indicated as external loads over each link of the lower limb exoskeleton. The effect of the HAT segment over the two hip joints during gait is also analyzed by considering internal forces and moments of the upper body [10].

Motion data of joint positions and external forces of human gait is available and considered from Winter [11, 12] to evaluate the proposed 5-link model, which should be able to perform the same trajectory and support all internal forces and moments. Data from hip, knee and ankle of a person of 65 kg and 1.80 m height, a gait cadence of 90 stride/min and an exoskeleton mass of 20 kg [10] were used to generate angular trajectories of the exoskeleton joints.

(a) Whole model

(b) Exoskeleton links: thigh and shank
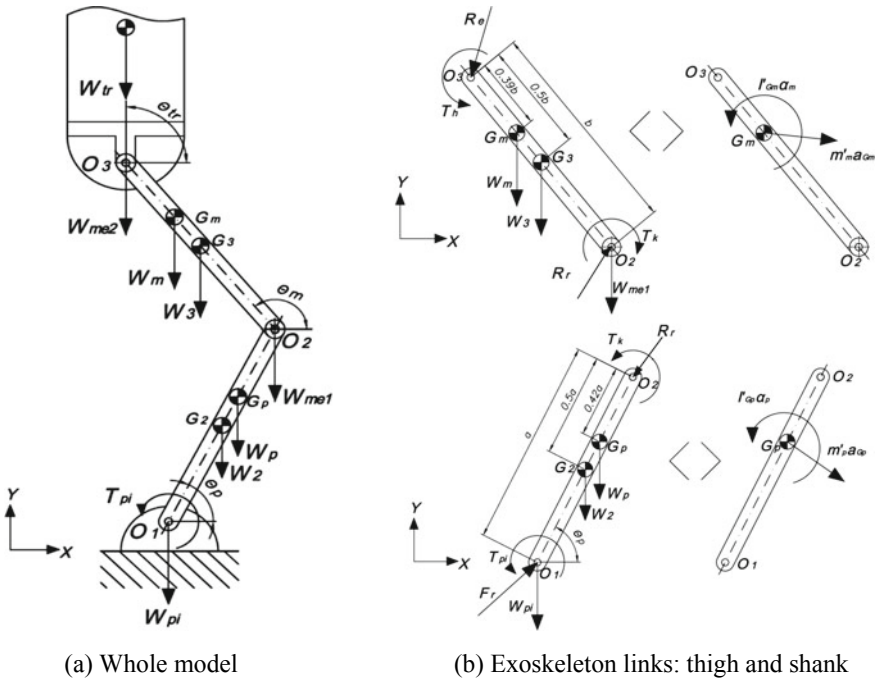
Fig. 12.4 Free-body diagram of 5-link exoskeleton for stance phase

Based on the dynamic results, Fig. 12.5 shows the highest hip joint moments when one leg is on loading response (between 0 and 10% of gait cycle), the terminal stance (between 40 and 60% of gait cycle) and when the opposite leg is on terminal swing (between 90 and 100% of gait cycle).

12.3 Focused Modeling for Analyses

As the moments on the hip are high, thus a new model has to consider that the hip has to be suspended and kept by an upright device to support fully or partly body weight. Also a foot-link is added to the 5-link model, as shown in Fig. 12.6, for a better approximation of ground contact, thus the new physical model is a 7-link model. The geometry of the 7-link lower limb exoskeleton model considers length of the HAT, thigh, shank and foot. Both legs are considered ideally equal. For kinematic analyses, the cardinal positions method is used to relate the human body segment COM of the hip (c1), the knee (c2) and the ankle (c3) in Eqs. (12.1)–(12.6). Also position of the metatarsal (R4) and the heel (R5) are considered in Eqs. (12.7)–(12.10). Furthermore, the angle links for HAT (β0), thigh (β1), shank (β2) and foot (β3) are included in Eqs. (12.1)–(12.10). The equations are referenced to the position of the
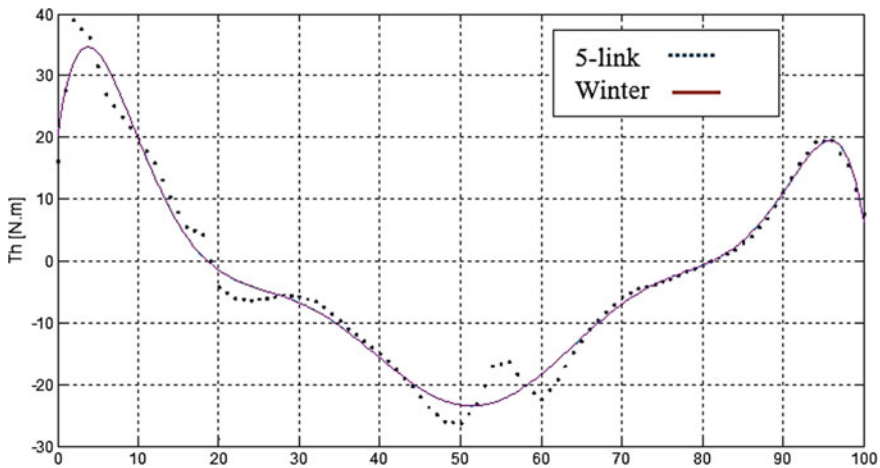
Fig. 12.5 Hip moment (Th) in N.m during gait cycle

Fig. 12.6 Seven-link model: right leg
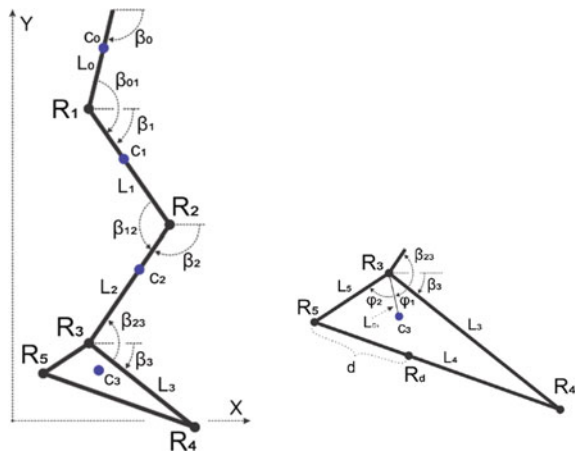
hip because both legs start from it, which is also linked to a higher support that generates a movement in the sagittal plane (X-Y) as the hip motion during normal gait. Differentiating the Eqs. 12.1–12.10, and arranging the equations in a matrix, the COM velocities of each link and velocities of the metatarsal and heel are obtained, as shown in Eqs. 12.11 and 12.12, respectively. Then, accelerations of COM of each link and velocities of the metatarsal and heel are obtained by differentiating the Eqs. 12.11 and 12.12 as shown in Eqs. 12.13 and 12.14.

$$C_{1x} = R_{1x} + L_{C1} \cos \beta_1 \tag{12.1}$$

$$C_{1y} = R_{1y} + L_{C1} \sin \beta_1 \tag{12.2}$$

$$C_{2x} = R_{1x} + L_1 \cos \beta_1 + L_{C2} \cos \beta_2 \tag{12.3}$$

$$C_{2y} = R_{1y} + L_1 \sin \beta_1 + L_{C2} \sin \beta_2 \tag{12.4}$$

$$C_{3x} = R_{1x} + L_1 \cos \beta_1 + L_2 \cos \beta_2 + L_{C3} \cos(\beta_3 + \varphi_1) \tag{12.5}$$

$$C_{3y} = R_{1y} + L_1 \sin \beta_1 + L_2 \sin \beta_2 + L_{C3} \sin(\beta_3 + \varphi_1) \tag{12.6}$$

$$R_{4x} = R_{1x} + L_1 \cos \beta_1 + L_2 \cos \beta_2 + L_3 \cos \beta_3 \tag{12.7}$$

$$R_{4y} = R_{1y} + L_1 \sin \beta_1 + L_2 \sin \beta_2 + L_3 \sin \beta_3 \tag{12.8}$$

$$R_{5x} = R_{1x} + L_1 \cos \beta_1 + L_2 \cos \beta_2 + L_5 \cos(\beta_3 + \varphi_1 + \varphi_2) \tag{12.9}$$

$$R_{5y} = R_{1y} + L_1 \sin \beta_1 + L_2 \sin \beta_2 + L_5 \sin(\beta_3 + \varphi_1 + \varphi_2) \tag{12.10}$$

$$\dot{c} = J_1 . \dot{q} \tag{12.11}$$

$$\dot{P} = J_2 . \dot{q} \tag{12.12}$$

$$\ddot{c} = J_1 . \ddot{q} + \dot{J}_1 . \dot{q} \tag{12.13}$$

$$\ddot{P} = J_2 . \ddot{q} + \dot{J}_2 . \dot{q} \tag{12.14}$$

Then, based on the described kinematic, FBD are made for the whole system from the trunk support device to the foot of the exoskeleton, as shown in Fig. 12.7. Where, in addition to the internal forces and torques between the links of the exoskeleton, it is consider body segments weights and the resulting ground reaction forces (GRF).

Also, considering that the terminal stance is being analyzed for the right leg, so the left leg is in terminal swing; in Fig. 12.7, the FBD the force of the left leg plus the force of the upper body support are included and tagged as Fa.

From Winter [11, 12], input angle data of body segment angles β_{01}, β_{12}, β_{23} for thigh, shank and foot, respectively which are related to angle link positions. Then, accelerations of the COM are determined by Eqs. 12.13 and 12.14.

Fig. 12.7 Free-body
diagram for each element
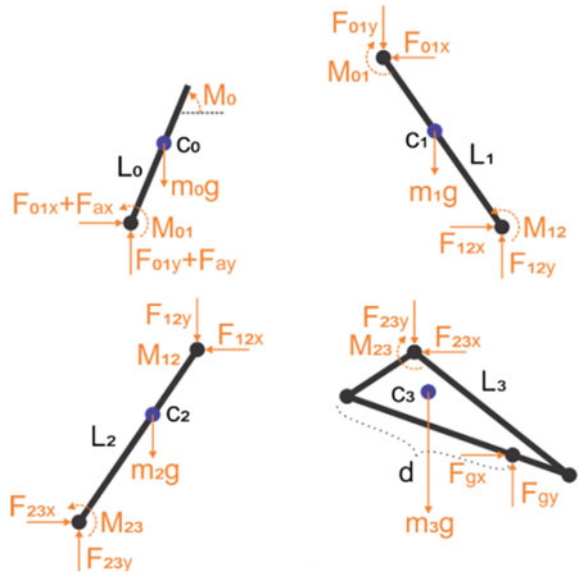
$$
\begin{bmatrix}
F_{23x} \\
F_{12x} \\
F_{01x} \\
F_{ax} \\
F_{23y} \\
F_{12y} \\
F_{01y} \\
F_{ay}
\end{bmatrix}
=
\begin{bmatrix} Z & 0 \\ 0 & Z \end{bmatrix}^{-1}
\begin{bmatrix}
m_3\ddot{C}_{3x} - F_{gx} \\
m_2\ddot{C}_{2x} \\
m_1\ddot{C}_{1x} \\
m_0\ddot{C}_{0x} \\
m_3(\ddot{C}_{3y} + g) - F_{gy} \\
m_2(\ddot{C}_{2y} + g) \\
m_1(\ddot{C}_{1y} + g) \\
m_0(\ddot{C}_{0y} + g)
\end{bmatrix};
$$

$$
Z =
\begin{bmatrix}
-1 & 0 & 0 & 0 \\
1 & -1 & 0 & 0 \\
0 & 1 & -1 & 0 \\
0 & 0 & 1 & 1
\end{bmatrix}
\tag{12.16}
$$

Using N-E equations to calculate inverse dynamics, equations are arranged in a matrix, to obtain the dynamic model of the system as shown in Eq. 12.16. To determine internal forces (F_{01}, F_{12}, F_{23}) of each joint of the 7-DOF model lower limb exoskeleton, and Fa for a gait cycle, it was necessary to introduce GRF in X and Y axis from Winter and accelerations.

Results of Eq. (12.16) are shown in Fig. 12.8, where internal forces of opposite leg and upper body partial body weight support in x axis (Fa_x) and in y axis (Fa_y) are shown in Fig. 12.8a. The internal forces on the hip joint (F_{01x}, F_{01y}) are shown in Fig. 12.8b. These results are for a person with 80 kg of body mass, a height of
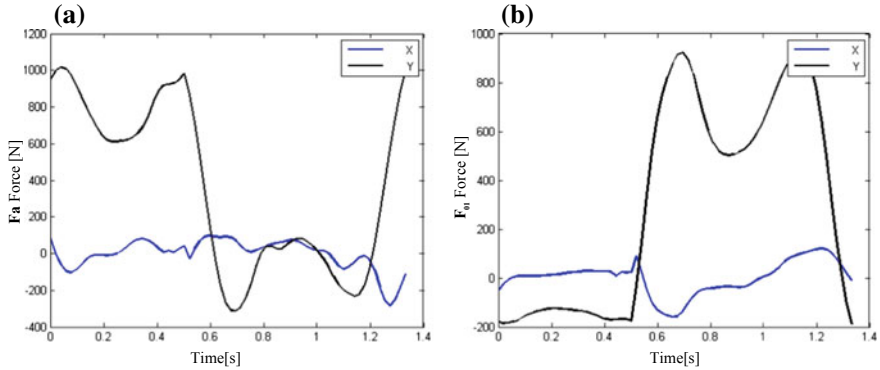
Fig. 12.8 Internal reaction forces of (**a**) Fa and (**b**) F_{01} in XY axis

1.65 m, a exoskeleton mass of 20 kg (10 kg each leg), a cadence of 121 stride/min and stride length of 0.76 m.

A mathematical model of the dynamic of the mechanism, that allows a preliminary implementation of a control algorithm as well as simulations of internal forces and moments, is required to optimize the mechanical design. In this case the 7-DOF lower limb exoskeleton model is more complex because the proposed model includes a foot-link, therefore it was considered the Euler-Lagrange Method [13], as shown in Eq. 12.18, to obtain preliminary results that allow to optimize the development of the Lima lower limb exoskeleton.

$$\frac{d}{dt}\frac{\partial L}{\partial \dot{\tilde{q}}} - \frac{\partial L}{\partial \tilde{q}} - \frac{\partial \Gamma}{\partial \tilde{q}}\Lambda = \tilde{Q} \tag{12.18}$$

where Λ is lagrange multipliers vector, Γ are movement restrictions ordered in a vector, $\tilde{q}$ is the vector of generalized coordinates, $\dot{\tilde{q}}$ is time differentiated of coordinates vector, and $\tilde{Q}$ is a vector of Forces and Torques generalized. Proceeding with the formulation, the dynamic model is shown in Eq. 12.19.

$$M\ddot{\tilde{q}} + C\dot{\tilde{q}} + G = \tilde{Q}_1 + J_2\tilde{Q}_2 \tag{12.19}$$

The direct dynamic is obtained using the Eq. (12.19) to calculate the acceleration vector $(\ddot{\tilde{q}})$, and then the position vector $(\tilde{q})$. Through of the direct dynamic and the information about the positions and the external forces of the human gait, provided by Winter [12], a simulation of the normal gait was obtained as shown in Fig. 12.9.

The case of torques is of great importance in the calculation of the power in the selection of actuators (motors). By generating new trajectories of segment angles it is possible to change cadence values (86.8, 105.3, 123.1 stride/min), in order to evaluate different gait parameters. Then, applying the dynamic balance of torques, and the corresponding information of Winter [11, 12], the torque and angular velocity
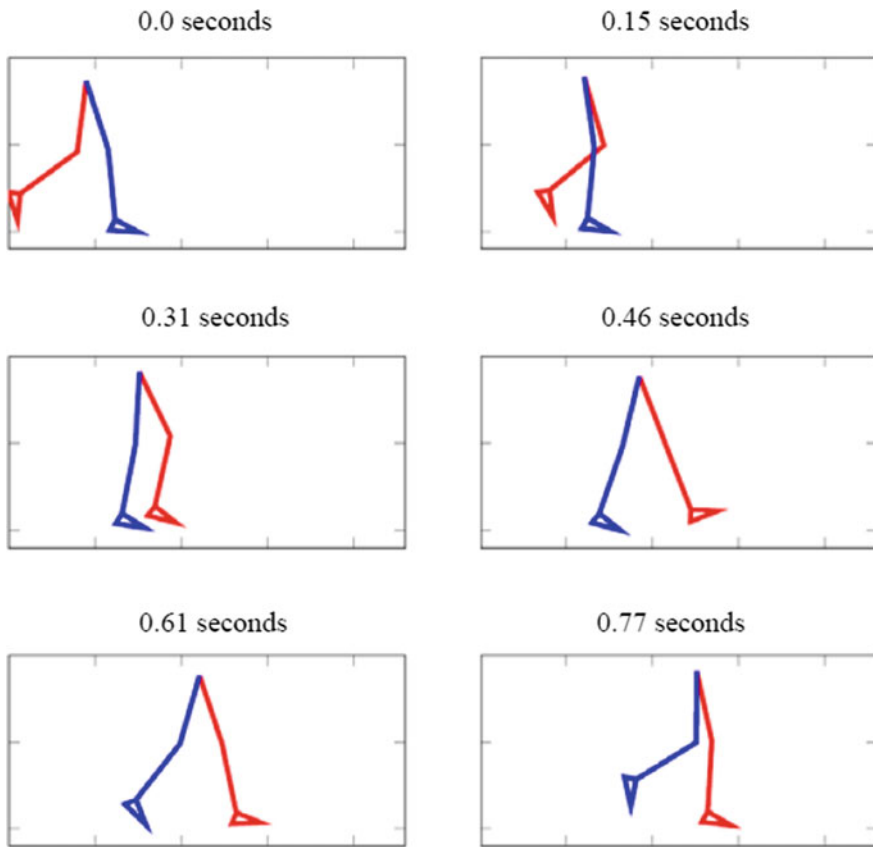
Fig. 12.9 Human gait model simulation with direct dynamics of the proposed 7-link model

curves for each joint are obtained. Figure 12.10 shows the angular velocity and torque curves for hip, knee and ankle of the 7-link lower limb exoskeleton.

12.4 Conclusions

A dynamic model for the design of an exoskeleton for lower limbs was obtained based on a seven-link physical model, which considers joints in the ankle, knee and hip, and that the pelvis can be suspended by an upright device that supports fully, or partly, the weight. The proposed modeling could be close to a human gait, and generated data could be used to optimize the mechanical design of the Lima lower limb exoskeleton. In that sense, the design must consider a device which would support all the moments of upper-body due to the high instability during the attempt of walking by a person with gait disability. Additionally, this design should also
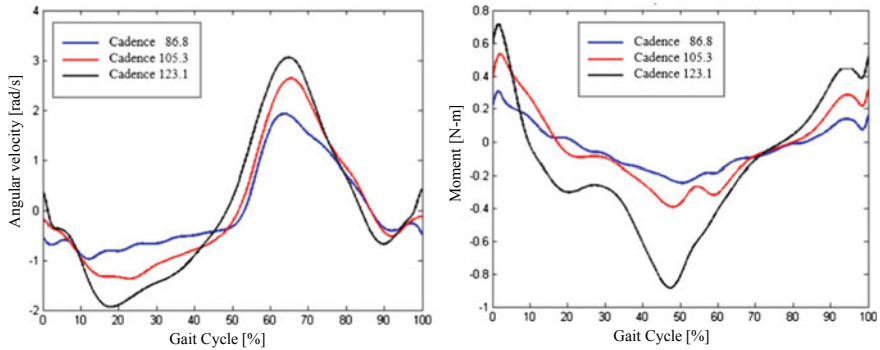
Fig. 12.10 Angular velocities and moments of the hip for different cadence values

consider a device to protect the ankle during the terminal stance, mainly from 40 to 60% of gait process, due to in that moment higher torques are generated internally in the ankle, because the ankle is supporting all the effort to propel body for the next step, where the left leg will start stance phase, this should be considered as critical to avoid any injury in patients.

It is important that the exoskeleton makes the greatest efforts in the cyclic rehabilitation of human gait. This decreases the risk of injury to patients during rehabilitation, therefore it is critical to establish adequate parameters for the exoskeleton control system according to the rehabilitation conditions for each patient. The design of the exoskeleton, and its operation, must be optimized for each user by determining, with the proposed dynamic model, the internal forces and moments in the joints of the lower limbs.

References

1. Consejo Nacional para la Integración de la Persona con Discapacidad: Anuario Estadístico del Registro Nacional de la Persona con Discapacidad. Lima, Perú (2015). http://www.conadisperu.gob.pe/observatorio/index.php/informacion-de-base/registro-nacional-de-la-persona-con-discapacidad/anuario-estadistico-2000-2014. Accessed 3 Nov 2017
2. Pirker, W., Katzenschlager, R.: Gait disorders in adults and the elderly. Wiener Klinische Wochenschr. **129**(3–4), 81–95 (2017)
3. Vaughan, C., Davis, B., O'Connor, J.: Dynamics of Human Gait, 2nd edn. Kiboho Publisher, South Africa (1999)
4. Contreras, L., Roa, M.: Modelamiento de la marcha humana por medio de gráficos de unión. Revista Tecnura **8**(16), 26–42 (2005)

5. Hu, T., Lin, Z., Abel, M.F., Allaire, P.E.: Human gait modeling: dealing with holomonic constraints. In: Proceedings of the 2004 American Control Conference, Boston, MA, USA, vol. 3, 2296–2301 (2004)
6. Srinivasan, S.: Low-dimensional and analysis of human gait with application to the gait of transtibial prosthesis users. Doctor of Philosophy Dissertation, Ohio State University, OH, USA (2007)
7. Nacy, S.M., Hassan, S.S., Hanna, M.Y.: A modified dynamic model of the human lower limb during complete gait cycle. Int. J. Mech. Eng. Rob. Res. **2**(2), 8–19 (2013)
8. Baluch, T., Masood, A., Iqbal, J., Izhar, U., Khan, U.: Kinematic and dynamic analysis of a lower limb exoskeleton. Int. J. Mech. Aerosp. Ind. Mechatron. Manuf. Eng. **6**(9), 1945–1949 (2012)
9. Majeeda, A., Tahaa, Z., Abidinb, A., Zakariaa, M., Khairuddina, I., Razman, M., Mohamed, Z.: The control of a lower limb exoskeleton for gait rehabilitation: a hybrid active force control approach. Procedia Comput. Sci. **105**, 183–190 (2017)
10. Pujada, E.: Modelación y simulación dinámica de un mecanismo exoesquelético para personas con dificultades en la marcha. Mechanical Engineering Thesis, Pontificia Universidad Católica del Perú. Lima, Perú (2009)
11. Winter, D.A.: The Biomechanics and Motor Control of Human Gait: Normal, Elderly and Pathological, 2nd edn. University of Waterloo Press, Waterloo, Ont (1991)
12. Winter, D.A.: The Biomechanics and Motor Control of Human Gait: Normal, Elderly and Pathological, 4th Edition. Wiley, Hoboken (2009)
13. Tsai, Lung-Wen: Robot Analysis: The Mechanics of Serial and Parallel Manipulators. Wiley, New York (1999)

Chapter 13
Human Modeling for Biomechanical Analysis of Closed Kinetic Chain Exercises of the Leg

Christian G. Chicoma, Fabricio G. Canales, Jose G. Garcia, Marco Morales, Dante A. Elias and Elizabeth R. Villota

Abstract This paper presents the development and validation of a tridimensional 7-DOF human body model for the representation and study of closed kinetic chain exercises (CKCE) performed with the feet fixed in space, i.e. low posture exercises. The biomechanical model, a link-segment model, is based on an Euler-Lagrange formulation and employs a generalized joint coordinate system. A top-down mechanical analysis provides an estimation of the internal joint moments, along with the vertical ground reaction forces, using kinematical data collected by inertial sensors. The model is validated by correlating estimated ground reaction forces to kinetic experimental data from force plates. Pearson correlation coefficients were calculated for four CKCE types (150 trials in total). In all cases, a median correlation $r > 0.90$ was found, hence proving that the proposed model is quite satisfactory for CKCE movement representation and analysis. Volleyball serve reception in low posture, a type of CKCE, is also analyzed using the results of the model.

Keywords CKCE · Body model · Experimental validation · Biomechanical analysis

---

C. G. Chicoma · F. G. Canales · J. G. Garcia · M. Morales · D. A. Elias (✉) · E. R. Villota
Pontificia Universidad Catolica del Peru, Av. Universitaria 1801, San Miguel, Lima 32, Peru
e-mail: delias@pucp.pe

C. G. Chicoma
e-mail: christian.chicoma@pucp.pe

F. G. Canales
e-mail: giaf.can@gmail.com

J. G. Garcia
e-mail: jggarcia@pucp.pe

M. Morales
e-mail: marco.morales@pucp.pe

E. R. Villota
e-mail: evillota@pucp.pe

13.1   Introduction

Closed kinetic chain exercises (CKCE) and open kinetic chain exercises (OKCE) have long been used by athletes as core exercises to enhance their performance in sports [4]. CKCE occur when the terminal segment in a kinetic chain meets resistance, muscle action and joint motion, e.g. if one end of the chain (the feet) is on the floor and thus fixed [14]. These type of exercises are characterized by requiring more stabilization and less acceleration than OKCE because either set of limbs is involved in supporting one's weight [7]. Specifically, CKCE of the leg are exercises in which the feet are fixed from moving, such as squats, legs press, deadlift and power lift. The functional and multijoint squat exercise has received considerable biomechanical evaluation. Several studies have examined its kinematics [12], dynamics [6], muscle recruitment pattern at the hip [9] and knee joints [5], for different strategies and resistance loads [8]. Nevertheless, the biomechanical study of other CKCE has received less attention, e.g. volleyball serve reception in low posture. Even for those CKCE found in the literature, studies of their ranges of motion and movement speeds are unclear or not well documented [10]; and it is also not known whether the findings are applicable to fast and large rotational trunk movements.

Besides being used in sports medicine, CKCE are also recurrent as therapeutic exercises in orthopedic medicine, including occupational health and physical therapy. Due to this, the study of the dynamics of CKCE motion is very beneficial in order to choose appropriate exercises depending on the needs of the athlete or patient. The choice of a given CKCE exercise will depend on the forces and internal moments produced in the body, which may be deemed fitting or not.

Several studies suggest that using biomechanical models and inverse dynamics calculations are valid for producing estimated profiles of human motion kinetic patterns and evaluating internal forces. These models may have various levels of complexity, being highly dependant on the accuracy needed. As such, studies of human movements have used two- (2-D) and three-dimensional (3-D) models for identification of net moments and reaction forces at the anatomical joints [13]. Models without muscles have estimated joint moments and forces utilizing linked body segments [1]. These link-segment models (LSM) estimate moments and forces by top-down inverse dynamics calculations, i.e. by measuring the external loads at one end of the chain and then working through the connected joints (elbow, shoulder, pelvis) to the floor, hence estimating forces and moments at each of these joints. The accuracy of the magnitude and direction of the estimated forces at the feet depends on the characteristics of the body segment, i.e. length, mass and center of mass, as well as the orientation in space of the various segments of the body (motion capture). Due to the complexity of 3-D movement analysis, most LSMs are restricted to one plane of motion, the sagittal plane. However, in asymmetric movements this may result in loss of relevant information.

This paper aims to develop and validate a 3-D link-segment model for representation of asymmetric CKCE of the leg. By using the validated model, a biomechanical analysis involving different CKCE at different movement speeds is performed.

13.2 Human Modeling

13.2.1 Link-Segment Model and Assumptions

CKCE of the leg studied herein are characterized by having both feet fixed to the floor in wide stance, see Fig. 13.1(left). A 3-D model of the human body with seven degrees of freedom (DOF) and six link-segments connected by revolute joints is considered for representation of these type of CKCE, as shown in Fig. 13.1(right). The kinematics of the 7-DOF human body model is described in three parts: lower limbs, trunk and upper limbs. The lower limbs are assumed to flex symmetrically with respect to the sagittal plane, hence a single branch can be used to describe the motion of the left (L) and right (R) lower limbs. The trunk is divided by the lumbar joint in two parts: pelvis and upper trunk (abdomen, thorax, neck and head). The pelvis height (a_3) is measured from the hip joint to the intervertebral disc (L5/S1), and the upper trunk from L5/S1 to vertex (d_5). The upper trunk is allowed to bend laterally and rotate. Finally, the upper limbs are also assumed to flex symmetrically so that both left and right limbs are also considered as a single branch.

Figure 13.1(right) also shows the joint angles represented in the 7-DOF model: ankle—q_1, knee—q_2, hip—q_3, lumbar joint—q_4—q_5, shoulder—q_6 and elbow—q_7, measured counterclockwise with respect to the $(i-1)$-th link. As such, segments included in the model are, segment I: shanks, II: thighs, III: pelvis, IV: upper trunk, V: arms, VI: forearms - see Fig. 13.1(left).

Symmetry assumptions for the model are valid because for CKCE with fixed feet position, such as squat, weight lifting or similar, lower limbs perform a symmetric motion in the sagittal plane. It should also be noted that the model does not present a segment associated with the foot; therefore, foot rotation is not considered; L/R feet
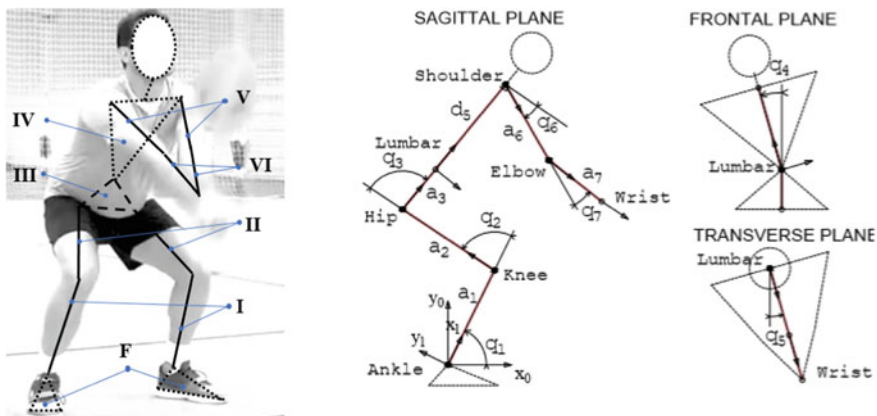
Fig. 13.1 (Left) Representative CKCE of the leg. (Right) 7-DOF human body link-segment model for CKCE of the leg with generalized joint coordinate system

are analyzed as a mass fixed to ground. Note also that the model also assumes that the upper trunk does not flex over the pelvis segment.

13.2.2 Equations of Motion

The body motion for the 7-DOF model is represented by a vector of generalized coordinates, $\mathbf{q} = [q_1, \ldots, q_7]^T \in R^7$. The Denavit-Hartenberg (D-H) method is used to describe the angular position and velocity of the center of mass (COM) of each model segment. Using the Lagrangian formulation, the equations of motion of the kinetic chain can be described as:

$$M(q)\ddot{q} + C(q, \dot{q})\dot{q} + D(q) = \Gamma. \tag{13.1}$$

In Eq. (13.1), $M(q)$ is a 7×7 matrix related to mass and inertial properties, Γ is a 7×1 generalized moment vector, $C(q, \dot{q})$ is a term related to centrifugal and Coriolis forces and $D(q)$ is the gravitational force vector. $C(q, \dot{q})$ and $D(q)$ can be calculated as in Eqs. (13.2) and (13.3).

$$C(q, \dot{q}) = \dot{M}(q) - \frac{1}{2}\dot{q}^T \left(\frac{\partial M(q)}{\partial q} \right), \tag{13.2}$$

$$D(q) = \left(\frac{\partial V}{\partial q} \right)^T. \tag{13.3}$$

13.2.3 Computational Aspects for the Simulation

For simulation purposes, input data such as mass, center of mass and inertia for each model segment are calculated according to [3]. Other kinematic data required for inverse dynamics calculation of internal joint moments is collected using a IMU-based motion capture system, see Sect. 13.3.3. By using the joints angular kinematic as input data in Eq. (13.1), internal joint moments are calculated.

In order to obtain the vertical ground reaction force (VGRF), the weight of the feet (segment F in Fig. 13.1 - left) must be added to the vertical component of the internal ankle joint force Fy_1. By adding an additional degree of freedom to the ankle joint, y_1, another equation similar to Eq. (13.1) is obtained [15], and from this Fy_1 can be estimated. This new equation relates the internal ankle force to the other joint angles and to the newly added degree of freedom y_1. The resulting Γ is an 8×1 vector comprised of joint moments and Fy_1. The internal ankle force Fy_1 is finally obtained by restricting the motion of the y_1 degree of freedom: $y_1 = \dot{y}_1 = \ddot{y}_1 = 0$.

Table 13.1 CKCE types, associated joint motions and other test descriptions

CKCE	AD	KF	HF	LLB	LIR	SF	EF	Hand clasp-ing	Ball contact
1	x	x	x	–	–	–	–	–	–
2	x	x	x	–	–	–	–	x	–
3	x	x	x	–	–	x	x	x	x
4	x	x	x	x	x	x	x	x	x

Ankle Dorsiflexion (DF), Knee Flexion (KF), Hip Flexion (HF), Lumbar Lateral Bending (LLB), Lumbar Internal Rotation (LIR), Shoulder Flexion (SF) and Elbow Flexion (EF)

13.3   Materials and Methods

13.3.1   CKCE Types

Four different types of CKCE have been chosen for evaluation, they present similar patterns to CKCE squat, that is varus lower leg position, feet flat and stable, and heels in contact with the ground at all times [11]. Table 13.1 shows the joint motions involved in each type of CKCE. CKCE type 1 consists of squatting with the upper trunk aligned with the pelvis in the sagittal plane and arms hanging down freely at the sides. CKCE type 2 consist of squatting as in type 1 but with both hands clasped and held at the front. CKCE type 3 consists of performing volleyball low posture serve reception technique with the whole body symmetrically to the sagittal plane and flexing the arms emulating ball contact. CKCE type 4 consists of performing movements as in type 3 but including lateral bending and rotation of the upper trunk at the lumbar joint.

13.3.2   Subject

A male amateur volleyball player, served as subject, aged 36, mass 87.5 kg and height 1.72 m. The subject performed all types of CKCE required. He signed a written informed consent statement giving his approval to participate in this study.

13.3.3   Testing Setup

A wearable inertial motion capture (mocap) system (Aktos-T, Myon®) was used to collect the kinematic data at 142 Hz and two force plates (AMTI OPT400600-2000) were used to measure the VGRF at 1000 Hz. The inertial mocap is comprised of 15 IMUs, each unit contains a 3-D accelerometer (± 8 g), a 3-D gyroscope ($\pm 1.000\,°/s$)

and 3-D magnetometer (±1 mT). IMU calibration consists of setting a global axis reference for each IMUs, and align the IMU's y-axis to force plate's y-axis. Force plates were calibrated by setting them to zero by hardware. The 15 IMUs were attached to the subject body using soft elastic straps around each body segment (L/R shanks, L/R thigh, pelvis and upper trunk, L/R arm, L/R forearm) and also bonded to skin with double-sided tape (L/R hand, L/R foot, head). Data from the IMUs was stored by the software SmartVisualizer (MobileBody®ITBB GmbH), whose output data are the anatomical angles for each spherical joint of a whole body 35-DOF, 15 link-segment model. Force data was recorded by the AMTI Netforce software, 3-D orthogonal ground reaction forces were obtained for each foot.

13.3.4   Data Collection

A single session test was carried out. Several tests were performed, each test consisted of 3 trials. In each test, the subject was asked to step upon the force plates and stand with legs apart at medium stance squat [5]. Starting from an upright posture (UP), the subject was instructed to "wait for the go-signal" to start performing an specific type of CKCE, once the CKCE ended the subject had to return to the initial position. In each trial, the subject squatted, without heeling-off, to reach the greatest depth by flexing his lower limbs symmetrically to the sagittal plane and also kept facing forward. At the end of each trial, the subject should remain still for 2 s, in an UP for CKCE1 and in $UP|q_6 = -40^{\circ}$ for the other CKCE, and be ready for the next go-signal. The subject was required to perform a type of CKCE at three different natural speeds (slow-medium-fast) for the tests.

13.3.5   Data Processing

Anatomical angles (flexion, abduction and rotation) were analyzed for symmetrical motion of the limbs, depending on the CKCE type executed. Left and right flexion of limbs, and 3-D trunk angles were averaged and smoothed with a 4th-order zero-phase lag Butterworth low pass digital filter with a cut-off frequency of 8 Hz. Averaged anatomical angles data was used to define each generalized coordinate of the 7-DOF model, q_i. Note that, for the coordinate system defined in Fig. 13.1(right), human upright posture corresponds to: $q_1 = 90^{\circ}$, $q_2 = 0^{\circ}$, $q_3 = 0^{\circ}$, $q_4 = -90^{\circ}$, $q_5 = -90^{\circ}$, $q_6 = -90^{\circ}$ and $q_7 = 30^{\circ}$.

Internal moments and estimated VGFR were calculated embedding the generalized coordinate vector **q** and its derivatives in the equation of motion, Eq. (13.1), as described in Sect. 13.2.3.

VGRF data was smoothed using a 4th-order zero-phase lag Butterworth low pass digital filter with a cut-off frequency of 10 Hz.

13.3.6 Data Analysis

The validity of the proposed 7-DOF link-segment model was analyzed by comparing the estimated VGRF with the measurements from the force plates. Two parameters were employed for the analysis: normalized absolute error and Pearson correlation coefficient (PCC). Data presented is grouped by the type of CKCE (4 types) and by the movement speed (slow-fast). The normalization parameter is the body mass (BM) of the subject.

The kinematics related to a representative CKCE type (CKCE3) were also analyzed, together with the corresponding internal joint moments. Magnitude of moments exerted at each body joint was obtained for each CKCE trial; however, mean values of moments for each CKCE type could not be determined because this requires a normalization with respect to time, as in gait analysis.

Other insights related to the biomechanics of the CKCE of the leg can be gained by plotting the range of motion (ROM) for each body joint, either by each CKCE type or by movement speed. The contribution of each body segment to the VGRF can also be assessed by calculating the product of the mass of the segment and the acceleration of its center of mass.

13.4 Results

Trials in which an IMU's signal got lost at some point were eliminated. This led to a total of 150 trials that were grouped according to each type of CKCE: 36 CKCE1, 45 CKCE2, 50 CKCE3 and 19 CKCE4. The selection of trials according to the movement speed led to a total of 74 fast and 28 slow CKCE. All the data was analyzed as described in Sect. 13.3.5 and the results are shown in this section.

13.4.1 Model Validation

Both estimated and measured VGRF have been considered for the validation of the 7-DOF body model. Figure 13.2 (left) shows a direct comparison of the VGRF for CKCE3, and Fig. 13.2 (right) shows the normalized absolute error. In general, Fig. 13.2 shows a good agreement between forces along the trial cycle, measured and estimated VGRF are very close at body weight (838 N) but estimated VGRF appears more damped at peak and valley values. Similar behavior was observed when comparing results from other trials. Specifically, the normalized error for the CKCE3 case has a valley of about -3 N/kg.

Pearson correlation coefficient r provides further insight with regards to the model validation by determining a measure of linear correlation between estimated and measured VGRF. Figure 13.3 shows the boxplot of the PCC for each CKCE type
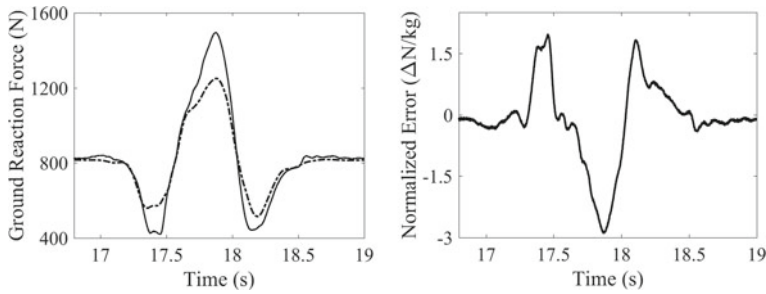
Fig. 13.2 (Left) Representative graph for VGRF: (−) measured versus (- -) estimated. (Right) Normalized absolute error
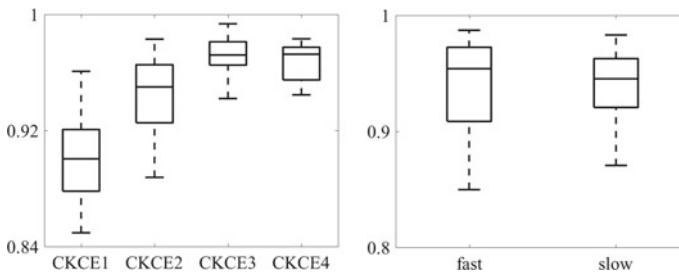
Fig. 13.3 Boxplot of Pearson correlation coefficient r. (Left) CKCE type. (Right) Movement speed

and movement speed. By type, all CKCE have a median r greater than 0.90 ($\tilde{r} > 0.90$), similar to [2] ($r > 0.88$). The $\tilde{r}$ increases from CKCE1 to CKCE4. CKCE3 and CKCE4 also present smaller interquartile ranges and they are above the ones of CKCE1 and CKCE2. This result implies that the 7-DOF model represents CKCE3 and CKCE4 more consistently. When analyzing the model validity by movement speed, $\tilde{r} > 0.95$ in both cases, none of the interquartiles are above the other and the interquartile range for fast speed is a bit smaller. Fast speed CKCE may seem to be much more consistently represented by the 7-DOF model.

13.4.2 Biomechanical Analysis

CKCE type 3, which emulates ball contact during a low posture volleyball reception technique, is used in this part for analysis purposes. Representative lower and upper limb kinematics (Fig. 13.4) and dynamics (VGRF - Fig. 13.2 and joint moments - Fig. 13.5) are considered for a quantitative evaluation. Serve reception cycle has been identified by observing the video of the reception execution; as such, the serve cycle lasted 1.56 s (starting from $t = 17.0$ s) and ball contact occurred at $t = 18.15$ s.
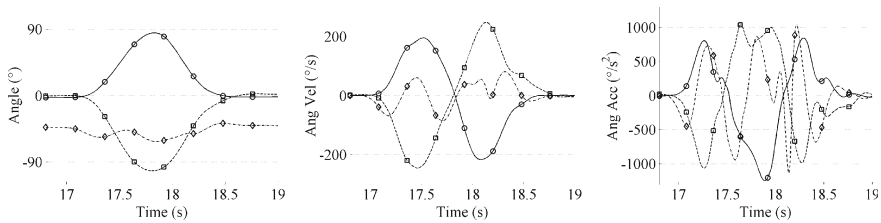
Fig. 13.4 Representative graph for joint angles, angular velocities and angular accelerations. (∘ Knee, □ Hip, ⋄ Shoulder)
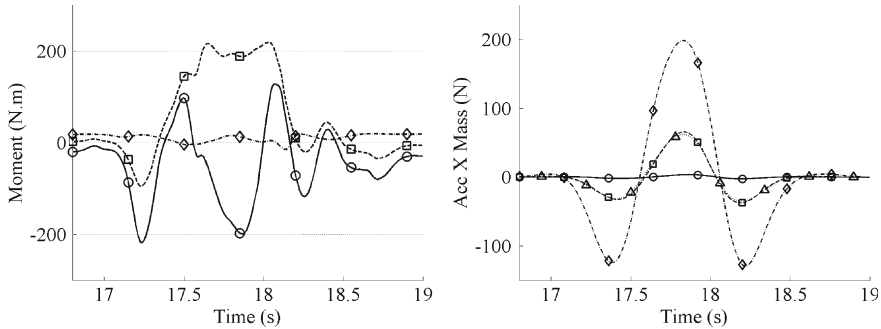
Fig. 13.5 (Left) Representative joint moments. (∘ Knee, □ Hip, ⋄ Shoulder). (Right) Mass × acceleration of center of mass for each body segment. (∘ Shank, □ Thigh, △ Pelvis, ⋄ Trunk)

The time characteristics of the kinematics show that knee and hip rotate together with similar magnitude but opposite direction, while the shoulder changes from $40°$ to $60°$; velocities for the knee and hip lay within $±220°/s$ and $±60°/s$ for the shoulder; and acceleration gets to $-1248°/s^2$ in the knee and $1001°/s^2$ in the hip, when preparing for ball contact.

Joint dynamics show that the knee and hip experience the greatest values of moments, the hip getting to 218 N.m and the knee to 128 N.m before ball contact. At ball contact, VGRF has passed its maximum peak (1495 N) and is about to settle on the subject body weight. Figure 13.5(right) shows that the trunk contributes the most to VGRF.

The range of motion (ROM) for each joint angle q_i is calculated for all trials. Figure 13.6 presents the ROM for each CKCE type and movement speed. For each q_i, similar ROM are obtained for all types of CKCE. In all CKCE types, q_1, q_4 and q_5 present smaller ROM in comparison to the other joint angles, with q_2 y q_3 having the largest ROM. A similar pattern is presented when analyzing CKCE by speeds. A quantitative analysis of the ROM for CKCE3 results in a mean (SD) ROM for the
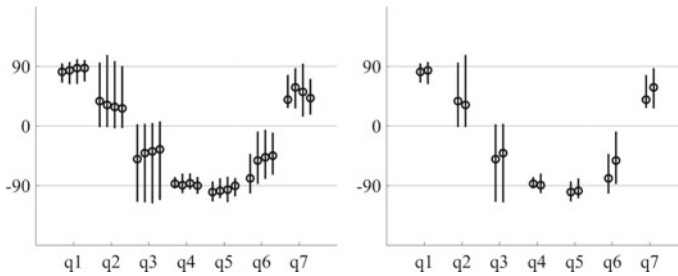
Fig. 13.6 ROM and mean for joint angles. (Left) CKCE type. (Right) CKCE speed

knee and hip of 91.48 (4.46) - q_2 and 107.12 (5.33) - q_3, respectively, and of 48.43 (16.57) - q_6 for the shoulder. In terms of speeds, the mean (SD) ROM for the low and fast speed of q_3 are 103.48 (3.22) and 108.11 (4.59), respectively.

13.5 Conclusions

In this study, a tridimensional 7-DOF human body model was developed to characterize CKCE of the leg with asymmetrical movements. Dynamic equations were derived using Lagrangian mechanics. The model was validated using the VGRF from force plates as a reference and comparing it with the VGRF estimated by the model. The validation procedure indicates that the VGRF can be adequately predicted by the model for all types of CKCE considered. In particular, VGRF in movements with significant lateral bending and rotation of the upper trunk are accurately described. Results from the model were further employed to characterize the serve reception gesture in volleyball, which was defined as a type of CKCE. Insight was gained regarding the kinematics and dynamics associated with volleyball reception. Kinematics data also provided information about the range of motion experienced by the joint angles during the execution of serve reception. In general, the validated model can provide an adequate description of internal dynamics for movements performed within the identified ranges. A more detailed analysis of these movements will be the topic of future research.

Compliance with Ethical Standards

Conflict of Interest The authors declare that they have no conflict of interest.

Ethical Approval All procedures performed with the human subject were in accordance with the ethical standards of the Comite de Etica de la Investigacion PUCP - Dictamen N°066-2017/CEI-PUCP.

References

1. Bernard, T.M., et al.: Evaluation of a biomechanical simulation model for sagittal plane lifting. Int. J. Ind. Ergon. **24**, 157–171 (1999)
2. De Looze, M.P., et al.: Validation of a dynamic linked segment model to calculate joint moments in lifting. Clin. Biomech. **7**(3), 161–169 (1992)
3. Dumas, R., et al.: Adjustments to McConville et al. and Young et al. body segment inertial parameters. J. Biomech. **40**(3), 543–553 (2007)
4. Escamilla, R.F., et al.: Biomechanics of the knee during closed kinetic chain and open kinetic chain exercises. Med. Sci. Sports Exercise **30**(4), 556–569 (1998)
5. Escamilla, R.F.: Knee biomechanics of the dynamic squat exercise. Med. Sci. Sports Exerc. **33**, 127–141 (2001)
6. Farris, D.J., et al.: Deconstructing the power resistance relationship for squats: a joint-level analysis. Scand. J. Med. Sci. Sports **26**, 774–781 (2015)
7. Gray, G.W.: Chain Reaction: Successful Strategies for Closed Chain Testing and Rehabilitation. Wynn Marketing, lnc., pp. 13–5 (1989)
8. Hoffman, J.R., et al.: Comparison of loaded and unloaded jump squat training on strength/power performance in college football players. J. Strength Cond. Res. **7**(4), 810–815 (2005)
9. Isear Jr., J.A., et al.: EMG analysis of lower extremity muscle recruitment patterns during an unloaded squat. Med. Sci. Sports Exercise **29**(4), 532–539 (1997)
10. Kingma, I., et al.: Segment inertial parameter evaluation in two anthropometric models by application of a dynamic linked segment model. J. Biomech. **29**, 693–704 (1996)
11. Kritz, M., et al.: The bodyweight squat: a movement screen for the squat pattern. Strength Cond. J. **31**, 76–85 (2009)
12. Lee, J.L., et al.: The kinematics of the lower leg in the sagittal plane during downward squatting in persons with pronated feet. J. Phys. Ther. Sci. **27**(1), 285–287 (2015)
13. Plamondon, A., et al.: Validation of two 3-D segment models to calculate the net reaction forces and moments at the L5/S1 joint in lifting. Clin. Biomech. **11**, 101–110 (1996)
14. Smidt, G.L.: Current open and closed kinetic chain conceptsclarifying or confusing? J. Orthop. Sports Phys. Ther. **20**(5), 235–235 (1994)
15. Stroe, I., Staicu, S.: Calculus of joint forces using Lagrange equations and principle of virtual work. Proc. Romanian Acad. Ser. A **11**(3), 253–260 (2010)

Chapter 14
VDI 2742: Electronic Motion Control Systems for Linkage Mechanisms: Principal Uses and Aspects of Realization

Burkhard Corves, Reinhard Braune and Rolf Blümel

Abstract Mechanisms, such as linkages with rotational or prismatic joints, cams, non-circular gear pairs and a variety of other mechanism types are classical mechanical means for generating complex movements of work elements in processing machines and thus often the "heart" of a machine for the performance of a certain technological process. As an alternative to these "classic" mechanisms, position-controlled servo drives with programmed motion control ("Motion Control Systems" or "MCS") are increasingly being used to solve demanding motion tasks. Sometimes, however, a combination of an MCS with a linkage can be a particularly favorable solution. Awareness of these opportunities that are presented here in the necessary brevity and in much greater detail in the VDI guideline to be published soon, is to encourage the design and development engineer to consider in appropriate cases such combination of solutions. Thus, some motion tasks may be solved easier or more elegantly than in the case of being restricted to just using an MCS without considering any mechanisms such as linkages, cams, linked gears or combinations thereof. Parts of this paper have been taken from a former German paper published in 2014 (Corves in VDI-Berichte 2237:27–39 (2014) [1]).

14.1 Introduction

The purpose of this article is to provide an overview of a new VDI Guideline (VDI 2742), which will be published this year and which will describe the joint use of MCS with linkage mechanisms and give suitable interpretations. It is intended to provide support for the realization of flexible solutions for demanding motion tasks

B. Corves (✉)
Institute of Mechanism Theory, Machine Dynamics and Robotics, RWTH Aachen University, Steinbachstr. 53B, 52074 Aachen, Germany
e-mail: corves@igmr.rwth-aachen.de

R. Braune
Leibniz University, Hannover, Germany

R. Blümel
Theegarten-Pactec GmbH & Co. KG, Dresden, Germany

with the stimulus to consider the combination of MCS with linkage mechanisms. The focus of this guideline is to demonstrate the basic benefits that can only be achieved by expanding an intended MCS by means of a linkage mechanism with nonlinear motion transmission. In addition, the principle of the design of electromechanical drive trains with an MCS will be discussed and special aspects of the dimensioning of the drive system and its control with regard to the special combination of the MCS and the linkage mechanism are presented.

14.2 Principle Setup of an Electro-Mechanical Drive Train with an MCS

MCS are electronic systems that control or regulate the motion of electromechanical drive train in machines and plants. Within the framework of a superior control concept for the entire machine or plant, it is intended to ensure that pre-programmed motions can be carried out with a high degree of precision and coordination.

Figure 14.1 shows schematically the most important components of an MCS with the Electro-Mechanical-Drivetrain shown in the lower part, which is called the motion axis. The function of the MCS with the main groups "Setpoint Generation", "Motion Controller" and "Current Controller and Power Electronics" and their coordination with other function groups of the machine is controlled by control signals S1 from a superordinate machine controller. The control signal S2 is supplied to the block "Setpoint Generation", so that setpoints S3 can be provided for the desired motion of the motor and passed on to the "Motion Controller". This block compares the setpoint and actual values of the motion state, whereby a measuring system usually records them directly from the motor shaft. As an alternative, the actual motion state can also be measured at different position of the drive train, which is indicated by the dashed signal lines designated as (S5). The consequences of this are discussed in more detail in VDI 2742.

Via the drive train shown in the lower part of the picture, the power output from the motor P_{mot} is transferred as P_{ab} to the actual working element and then transmitted as P_{pro} to the technological process performed in the machine or plant. The statements in the guideline relate in particular to whether, and to what possible advantages, a linkage could be integrated in this drivetrain. In order to indicate that a reduction gear unit is not necessarily required, the relevant block in Fig. 14.1 is only shown as a dashed block.

A substantial difference between a system with a linkage and a system with components with only uniformly transmitting gears is, that the mass moment of inertia J_{red}, reduced to the crank input of the linkage mechanism, is not constant but variable with time due to the time dependency of the drive angle $\varphi_{crank}(t)$. Figure 14.2a shows a centric slider-crank mechanism, in which only the rotational mass moment of inertia J_1 of the input crank 1 in relation to its axis of rotation A_0 and the translational mass m_3 of the output slider 3 are considered. The diagram in
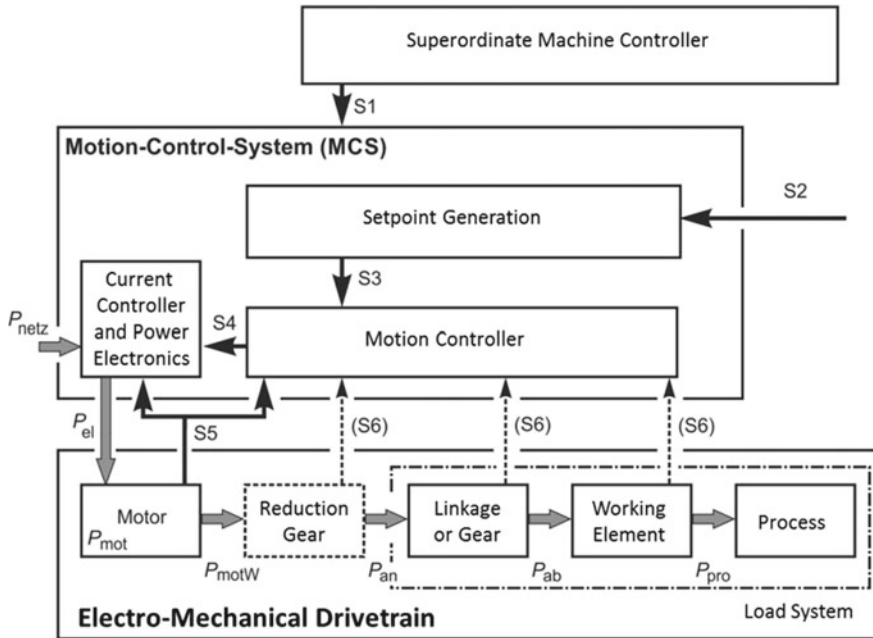
Fig. 14.1 Basic structure of an MCS
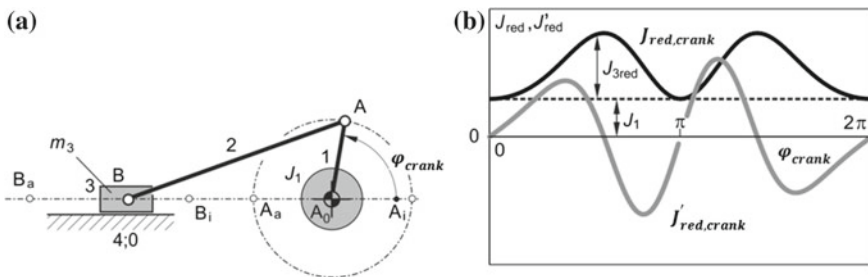
Fig. 14.2 Reduced mass moment of inertia of a centric slider crank **a** Considered inertias of the slider crank **b** Characteristics of the reduced mass moment of inertia and its derivation with regard to the drive angle

Fig. 14.2b then shows in black the total mass moment of inertia reduced to the drive shaft $J_{red,crank}$ of this mechanism, which is composed of the constant part J_1 and the variable reduced part J_{3red} of the slider mass m_3. The derivation $J'_{red,crank}$ with regard to the drive angle φ_{crank} is shown as an additional grey line.

Now in the case of non-uniform transmission according to VDI 2149, the input torque can be computed from the differential equation of the rigid mechanism:

$$M_{crank}(t) = J_{red,crank}(\varphi_{crank}) \cdot \ddot{\varphi}_{crank}(t)$$
$$+ \frac{1}{2} \cdot J'_{red,crank}(\varphi_{crank}) \cdot \dot{\varphi}^2_{crank}(t) + M_{red,crank}(t, \varphi_{crank}, \dot{\varphi}_{crank})$$

(14.1)

Additional force effects in the linkage mechanism such as friction or gravitational forces etc. are neglected but $M_{red,crank}(t, \varphi_{crank}, \dot{\varphi}_{crank})$ considers all the force and torque effects from the process and the working element.

14.3 Potentials for the Combined Use of MCS and Linkages

According to [2, 3], the possible benefits of combinations of an MCS with a linkage can essentially be assigned to the five main topics listed below. Only those additional benefits are mentioned that can be achieved by integrating a linkage mechanism together with an MCS instead of just using an MCS. VDI 2742 describes the following principle potentials of MCS/linkage mechanism combinations in more detail:

- Motion transfer and transformation of the motion type

  - Simple motion transfer and/or transformation from rotational motion of servo motors into a desired linear translational motion.
  - Use of a linkage mechanism with an approximate linear transmission ratio in a limited range of motion as a replacement for a linear reduction gear.

- motion limitation by dead-center positions

  - Simple, safe and precise limitation of the motion range of a working element using the dead-center positions of a linkage, e.g. in the case of a crank & rocker.

- Link guidance

  - Mechanically secured guidance of a working element on a desired trajectory by using a 1DOF linkage.

- Drive torque relief for static operating loads

  - Reduction of peak values of the required drive torque due to highly varying static process loads by making use of the non-linear transfer characteristic of a linkage.

- Drive torque relief for dynamic operating loads

  - Reduction of peak values of the required drive torque due to dynamic loads - i. e. loads caused by inertial forces - due to the following partial effects:
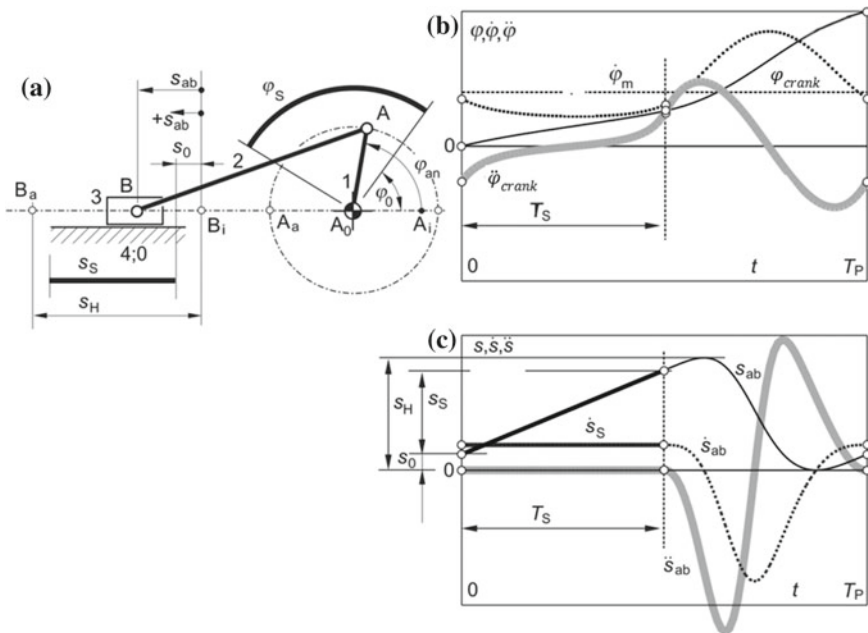
Fig. 14.3 Solution of the motion task "reverse dwell" with a slider-crank mechanism **a** Kinematic scheme **b** Diagram of the input crank angle, angular velocity and acceleration **c** Diagram of the slider position, velocity and acceleration

– Reduction of the drive torque by reduction of the drive acceleration
– Reduction of the output torque induced drive torque component by making use of the toggle position of a linkage close to its dead-center-positions.
– Reduction of peak values of the sum of the input and output torque components by temporal offset of the individual peak values.
– Approximate mutual compensation of the input and output torque components by similar but opposite course of action

VDI 2742 explains these individual potentials mainly by means of two exemplarily selected, typical practical tasks.

The first task "synchronous motion" is often referred to as "flying saw". In this case, a working element in straight-line guidance carries out an oscillating motion, whereby the motion in the middle section is to take place at exactly constant speed. With the second task "reverse dwell", a straight-line guidance with oscillating motion in both reverse positions is intended to realize a certain period of dwell. Figure 14.3 shows the motion task "reverse dwell" for the same slider-crank mechanism already depicted in Fig. 14.2. In practice, one often finds an integrated use of several of the above-listed effects realized with the same system combination of MCS and linkage. In fact, it is often just such a "usage mix" that makes the use of a combination of linkages with MCS particularly sensible.

Additionally, it should also be noted that combinations of MCS with linkages compared to MCS without linkages may have disadvantages, which have to be considered on a case-by-case basis in relation to the achievable advantages:

- **Limitations of flexibility**

MCS/linkage combinations can be very favourable, but they may also limit the flexibility of use. The more a linkage is optimised for a very specific operating case, the less it will generally be suitable for other operating cases. Thus, it makes sense to restrict it to simple linkages such as a crank & rocker or a slider-crank mechanism.

- **Design effort**

MCS/linkage combinations usually require a higher design effort and mechanism design expertise. Knowledge of the available technical rules, literature and the use of appropriate software tools will facilitate this task. The new VDI guideline also addresses the required knowledge of control structures and dimensioning of the electrical drive system.

- **Requirements for the control performance of a motion control system**

MCS/linkage combinations put special demands on the control behaviour of the MCS. In order to achieve sufficiently small motion errors and/or to avoid excessive torque peaks caused by the control scheme, special control engineering measures such as the "dynamic feedforward torque" may be required, although the implementation of such measures may not be part of the standard performance range of marketable MCS [4–6].

14.4   Electric Drive System

The Electric Drive system, i.e., the "Motor" block from Fig. 14.1 cannot be designed without taking into account the adjacent "Reduction Gear" and "Linkage or Gear" blocks on the motor output side [7, 8] and the "Current Controller and Power Electronics" block on the input side. Particular attention should be paid to the optimal synthesis of the gear ratio of the reduction gear unit, especially if the application requires a relatively high torque at low rotational speeds. Together with the question of how large the motor must be in order to produce the required process torque, the goal must be to enable an adaptation of rotational speed and torque in the sense of the smallest possible motor dimensioning. A compromise must therefore be found whereby the motor torque and its rotational speed are adapted by the reduction gear to the cycle time and the forces or torques required on the process side. Usually, the motor and the reduction gear (possibly a gear or geared motor as a fixed combination of motor plus gear [9, 10]) have to be selected from a defined set determined by the offers and catalogues of various manufacturers.

Based on the schematic structure of a drive train with variable inertia shown in Fig. 14.4 calculation methods are presented in the guideline which enable the design
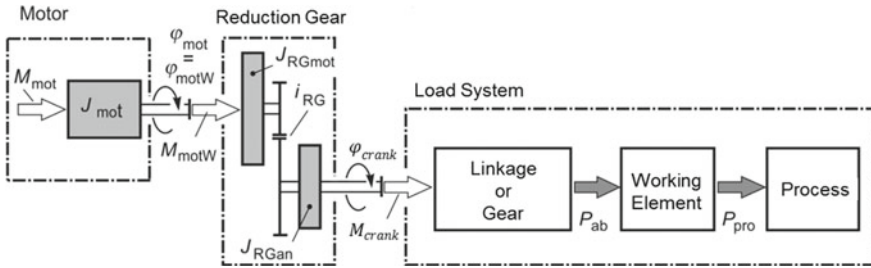
Fig. 14.4 Schematic structure of a drive train with a reduced inertia model for the reduction gear and subsequent linkage mechanism
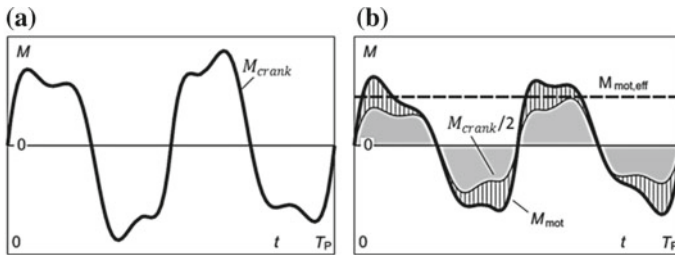
Fig. 14.5 Torque diagrams for "reverse dwell" with a slider-crank mechanism **a** Crank torque according to Eq. (14.1) **b** Motor torque according to Eq. (14.2)

engineer to carry out the drive optimization described above with relatively simple algorithms. Additionally a control calculation should be carried out based on the determined optimum transmission ratio and the motor and linkage parameters for the reduction gear unit and the parameters of the selected linkage. Based on the crank torque given through Eq. (14.1) the motor torque can be computed by

$$M_{mot}(t) = \left(J_{mot} + J_{RGred,mot}\right) \cdot \ddot{\varphi}_{mot}(t) + \frac{1}{i_{RG}} \cdot M_{crank}(t) \qquad (14.2)$$

taking into account the ratio i_{RG} of the reduction gear unit as well as its mass moment of inertia $J_{RGred,mot}$ and that of the motor J_{mot}. Figure 14.5 shows results of a calculation of crank torque $M_{crank}(t)$ and motor torque $M_{mot}(t)$ using the "reverse dwell" application case already depicted in Fig. 14.3 as an example. The motion diagram for the input crank angle φ_{crank}, angular velocity $\dot{\varphi}_{crank}$ and acceleration $\ddot{\varphi}_{crank}$ are from Fig. 14.3b. Additionally Fig. 14.5b shows the effective motor torque

$$M_{mot,eff} = \frac{1}{T_P} \cdot \int_0^{T_P} (M_{mot}(t))^2 \cdot dt \qquad (14.3)$$
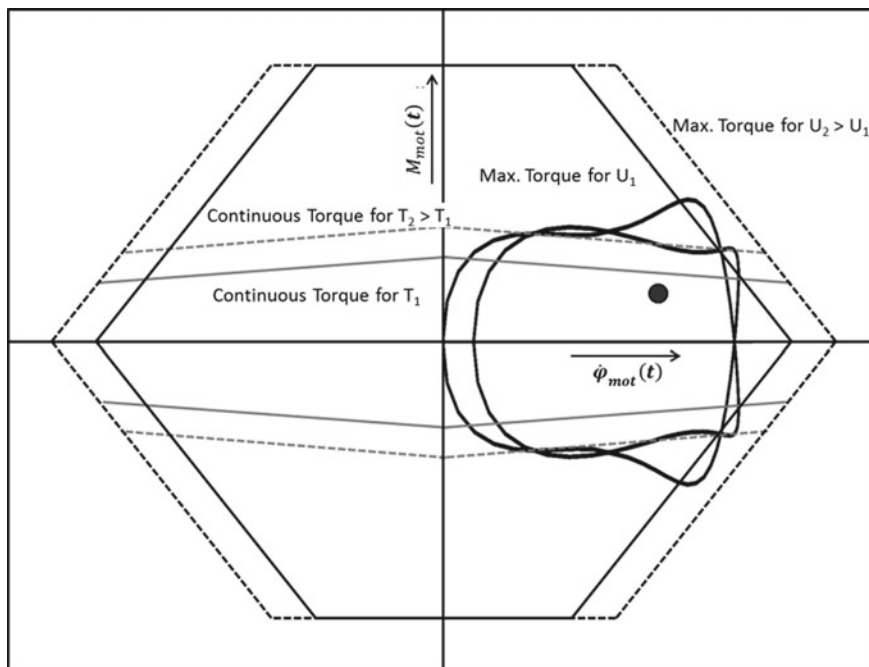
Fig. 14.6 Comparison of torque versus angular velocity requirements with the limit curves of a selected servomotor and equivalent continuous operation point

In order to check on the motor selection, it is advisable to draw yet another diagram with the required motor torque $M_{mot}(t)$ plotted against the angular motor velocity $\dot{\varphi}_{mot}(t) = i_{RG} \cdot \dot{\varphi}_{crank}(t)$ with the ratio i_{RG} of the reduction gear unit.

Figure 14.6 shows the diagram together with the equivalent continuous operation point based on the effective motor torque $M_{mot,eff}$ and the average angular motor velocity

$$\dot{\varphi}_{mot,av} = \frac{1}{T} \int_{0}^{T_P} |\dot{\varphi}_{mot}(t)| dt \tag{14.4}$$

In Fig. 14.6, the torque versus angular velocity diagram of a servomotor is shown, which can be operated with two different supply voltages $U_2 > U_1$. The solid black lines refer to the torque limit curves when operating with supply voltage U_1, the dashed lines refer to the supply voltage U_2. A distinction is made between the permissible torque for continuous operation and the short-time maximum torque. In the case of different engine-temperatures $T_2 > T_1$ tolerated by the user or approved by the engine manufacturer, also the permissible permanent torques are of different magnitude. This is shown in Fig. 14.6 by a continuous grey line for the engine temperature T_1 and a dashed grey line for T_2. Thus, a comparison between the performance
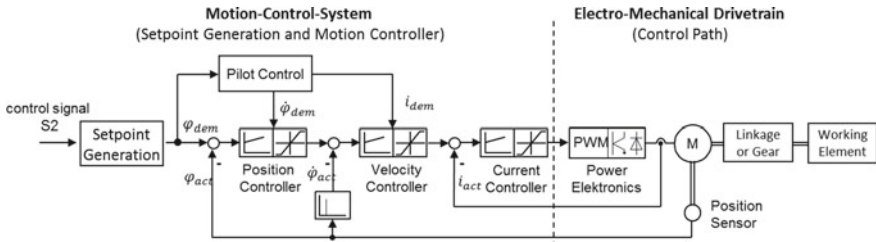
Fig. 14.7 Control diagram with cascaded control for current, velocity and position

limitations of the engine and the requirements for motor torque and angular velocity curve can be made. The total required torque versus angular velocity curve must be within the permissible torque limitations of the motor. Hence, in this example the motor version operated with U_2 should be selected. The example also shows that simply a selection on the basis of $M_{mot,eff}$ (Eq. (14.3)) and $\dot{\varphi}_{mot,av}$ (Eq. (14.4)) would be insufficient, since based on this point the operation with the supply voltage $U_2 > U_1$ may seems sufficient, although the associated torque versus angular velocity curve exceeds the maximum permissible permanent torque line for the supply voltage U_1 several times.

14.5 Control

A meaningful layout and design of the control function can only be done, if all the components involved such as the servo-electric drive, the downstream mechanical motion system and the controller are tuned in the best possible way. Assuming that the motion task finally requires a position control as part of the whole servo control strategy, a cascaded structure and thus the superposition of several control loops for motor current, velocity and position is selected as shown in Fig. 14.7.

Important reasons for the widespread cascaded control are the simple commissioning and optimization of the control loops from the inside (current control) to the outside (position control), the rapid control of disturbance as well as easy switching between position, speed and current control. In the dynamic case, i.e. during a setpoint or disturbance variable change there is always a control difference, i.e. set-point and actual value deviate from each other. The task of the controller design is now to design these dynamic deviations in such a way that the permissible tolerance of the motion task is satisfied.

Figure 14.8 shows the basic control loop as a graphical representation of the relationships with the transfer functions of the individual control loop elements in the sub-area of the Laplace transformation and directional graphs as connecting lines.

In such a basic control circuit the control path and the assigned controller are expressed through the Laplace transfer function $G_S(s)$ and $G_R(s)$. Design goals can be an optimal follower behavior with respect to the reference variable w, an opti-
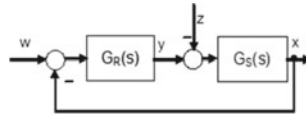
Fig. 14.8 Basic control circuit with Laplace transfer function $G_S(s)$ of the control path and the Laplace transfer function $G_R(s)$ of the controller

mal interference behavior with respect to the disturbance z or simply the stationary accuracy of the control. With the simple basic control circuit, generally no dynamic follower behavior with good suppression of disturbances acting on the controlled system is possible. Attention should be paid to any major control errors, which, in particular as positional errors, may limit the practical usability of such a system. But not only increased motion errors can be critical, but also much higher torque values than theoretically expected for a precisely executed motion. Frequently, only certain sections are functionally important in a required course of motion, and then, in less significant sections of motion, larger motion errors may be acceptable, but not substantial increases in torque peaks. In addition to possibly increased and possibly impermissible "motion errors", also possible and possibly impermissible "torque errors" must be taken into account [5]. An effective approach, which many MCS offer today, is to reduce increased motion and torque errors by applying "dynamic torque feedforward control " [2, 4, 5, 6, 11].

When using linkages, additionally the following three functional relationships are classified as relevant for the controller design:

- **Non-linear mechanical transfer characteristic of control deviations**

This means, that there is no longer any linear relationship between the motion input of the motor and the motion output towards the process.

Thus the control deviations on the motor shaft are no longer linked just to a constant factor to the output deviations. The requirement on the control quality (e.g. the positional accuracy of the slider crank) with respect to the motion tolerance should be determined for the entire motion as shown in Fig. 14.9b. From this, the permissible motion tolerance shown in Fig. 14.9c can be derived.

- **Position-dependent reduced moment of inertia**

The reduced moment of inertia is an important basic value for setting the controller parameters since in the case of linkages it is no longer constant (Fig. 14.2):

$$J_{mot,red}(\varphi_{crank}) = J_{mot} + J_{RG,mot} + \frac{1}{i_{RG}^2} \cdot \left(J_{RG,crank} + J_{red}(\varphi_{crank}) \right) \quad (14.5)$$

Typical for linkages are different step responses for different crank positions as shown in Fig. 14.10b and Fig. 14.10c.

- **Nonlinear-dynamic torque curve**
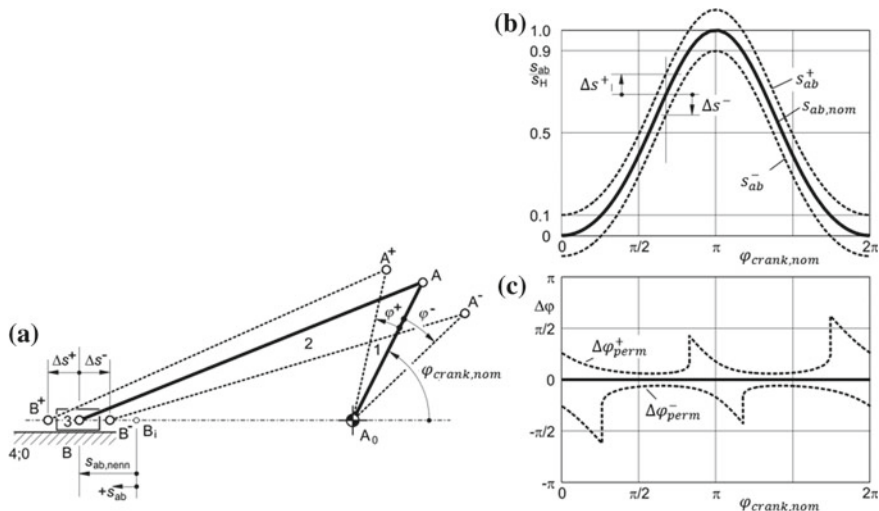
Fig. 14.9 Nonlinear transfer of control deviations **a** Definition of deviations Δs^+ and Δs^- of the output path s_{ab} and corresponding deviations $\Delta\varphi^+$ and $\Delta\varphi^-$ of the drive angle $\varphi_{crank,nom}$. **b** Permissible deviations of the output displacement of the slider crank plotted against the nominal crank angle $\varphi_{crank,nom}$ **c** Corresponding permissible, non-constant deviations $\Delta\varphi_{perm}$ of the drive angle φ_{crank} plotted against the nominal crank angle $\varphi_{crank,nom}$
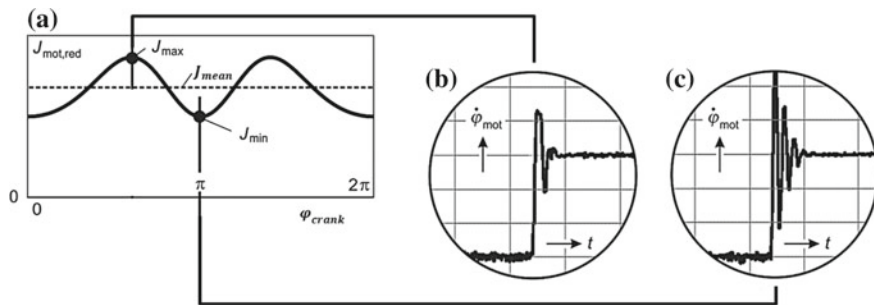
Fig. 14.10 Influence of the variability of the total inertia reduced to the motor shaft **a** Exemplary diagram of the total mass moment of inertia reduced to the motor shaft of the slider crank. **b** Step response to a change in the nominal angular velocity in the position with maximum reduced mass moment of inertia J_{max}. **c** Step response to a change in the nominal angular velocity in the position with minimum reduced mass moment of inertia J_{min}

The nonlinear-dynamic torque (see also Eq. (14.1) and Fig. 14.5) can be a significant disturbance, which often cannot be controlled with the usual functionality of an MCS. When using linkages, it can happen that a torque reversal occurs during acceleration and a braking torque is necessary for the specified positional change. Traditional control measures may not help, but may even worsen the resulting problems. A countermeasure, the "dynamic torque feedforward control" according to [2, 4, 5, 6] has proven to be effective. It provides the nominal required torque for the linkage as a function of the torque demand based on Eqs. (14.1) and (14.2). It requires the MCS to allow additive torque application at the input of the torque control loop with a sufficiently fast sampling rate (<1 ms). Such a feed forward control has no direct influence on the stability of the control loop since the stability depends only on the closed-loop controllers, controlled system parameters and filters (time constants). An indirect effect is that with a good feedforward control and thus small system deviations a more robust controller setting can be achieved, which is especially recommended for linkages.

14.6 Closing Remarks

The guideline VDI 2742 introduces for the first time a design guide in which a motion control system according to Fig. 14.1 is supplied to an integrative design process between the domains mechanism design, electrical engineering and control engineering. The guideline was developed as a joint effort between VDI and VDE. In the joint working committee the authors named here "only" served as the core group and big thanks for the intensive and fundamental cooperation goes to the other members.

References

1. Corves, B.: VDI 2741: Motion-Control-Systeme für ungleichmäßig übersetzende Getriebe: Prinzipielle Nutzungsmöglichkeiten und Aspekte der Realisierung. VDI-Berichte **2237**, 27–39 (2014)
2. Köster, M.: Der Antrieb ungleichmäßig übersetzender Koppelgetriebe durch Motion-Control-Systeme—Systemkonzipierung und praktischer Einsatz. Fortschritt-Berichte VDI, Reihe 8, Nr. 1168. Düsseldorf: VDI-Verlag (2010)
3. Braune, R., Köster, M.: Der Antrieb von ungleichmäßig übersetzenden Getrieben mit Motion-Control-Systemen – Systematik möglicher Nutzeffekte. VDI-Berichte **2116**, 3–19 (2010)
4. Köster, M., Braune, R., Callesen, M.: Die dynamische Momentenvorsteuerung – Eine wirksame Maßnahme zur Verbesserung des Betriebsverhaltens von Servo-Antrieben in Kombination mit ungleichmäßig übersetzenden Getrieben. VDI-Berichte **1845**, 283–302 (2004)
5. Braune, R.: Koppelgetriebe mit Servo-Antrieb in schnellen Verarbeitungsmaschinen. In: Tagungsband VVD 2006 zur Tagung Verarbeitungsmaschinen und Verpackungstechnik 2006, 311–348. Selbstverlag der TU Dresden, Professur Verarbeitungsmaschinen und Verpackungstechnik, Dresden (2006)

6. Callesen, M.: Der Antrieb ungleichmäßig übersetzender Koppelgetriebe durch Motion-Control-Systeme – Nutzungsaspekte, Betriebsverhalten und Bewegungsoptimierung. Fortschritt-Berichte VDI, Reihe 8, Nr. 1146. Düsseldorf: VDI-Verlag (2008)
7. Blümel, R.: Entwurf dezentraler Antriebe für Verarbeitungsmaschinen. Dissertation TU Dresden (2000)
8. Spohr, H.-H., Knöthig, J.: Vergleichsbetrachtung zwischen Getriebemotor und Direktmotor. Special Antriebstechnik, Konstruktion S **1**, 60–65 (2007)
9. N.N.: DYNABLOC Geared Servo Motors, Technical Catalogue, Moteurs Leroy-Somer SAS., Angoulême (2017)
10. N.N.: L-force, geared servo motors, Lenze Automation GmbH, Hameln, 2011
11. Köster, M., Braune, R.: Der Antrieb ungleichmäßig übersetzender Getriebe durch Motion-Control-Systeme – Bewegungsdesign und Systemauslegung. VDI-Berichte **2116**, 21–34 (2010)

Chapter 15
MechDev—A New Software
for Developing Planar Mechanisms

M. Müller, T. Mannheim, M. Hüsing and B. Corves

Abstract At the Institute of Mechanism Theory, Machine Dynamics and Robotics of RWTH Aachen University, software for the design of planar mechanisms is currently being prepared. This software aims to be easy to handle and at the same time include new functionalities. To allow a dynamical extension of the software, a special software architecture based on Plug-Ins is defined. One of these Plug-Ins is the kinematical analysis. It combines analytical and numerical computation methods. The basic approach of this functionality will be presented within this paper. It allows a powerful and modern handling during the mechanism design process.

15.1 Introduction

The invention of the steam engine in 1781 took a big part in the first industrial revolution [19]. This engine was based on a planar crank mechanism that was optimized by James Watt [12]. Ever since, the design and improvement of mechanisms was essential in the automation process in industry. Therefore, the field of kinematic and the use of mechanisms were taught in many different ways [3, 13]. From then until today, the two essential steps in the mechanism design is the synthesis and the analysis of mechanism [8].

Due to the increasing requirements on mechanisms in application, nowadays the engineering process is supported by special software [18]. This software can be divided into two different types: geometric software products and mechanism design software [10]. Geometric software like Cinderella [9] and GeoGebra [7] allow the

M. Müller (✉) · M. Hüsing (✉) · B. Corves
Institute of Mechanism Theory, Machine Dynamics and Robotics, Kackertstr. 16-18, 52072 Aachen, Germany
e-mail: mueller@igmr.rwth-aachen.de

M. Hüsing
e-mail: huesing@igmr.rwth-aachen.de

T. Mannheim · M. Hüsing · B. Corves
KHS GmbH, Juchostr. 20, 44143 Dortmund, Germany
e-mail: tom-philip.mannheim@khs.com

application of graphical methods of mechanism theory in a dynamic way. Therefore, explicit knowledge in mechanism design is required. Furthermore, the synthesis and analysis of mechanisms take a lot of effort. Mechanism design software like Optimus Motus [11] or GENESYS [2, 6] instead require less explicit knowledge and support the design process with special functionalities in the fields of mechanism synthesis and analysis. The mentioned software comes along with other deficits. Since the focus was on functions concerning mechanism design, the operation of the software is not intuitively, it is expensive or it has limitations concerning their functionality since a geometrical design is not possible [10].

According to these deficits, the Institute of Mechanism Theory, Machine Dynamics and Robotics of RWTH Aachen University provides a new software for the development of planar mechanisms—MechDev (**Mech**anism **Dev**eloper). This software aims to be easy to handle and at the same time to allow complex analysis, development and synthesis considering innovations and the actual state of the art. To be up to date, this software project should be extensible with different functions as well as different interfaces. Therefore, a special software architecture is considered.

This paper will give a short impression about the software architecture and different functionalities provided by the software so far.

15.2 Software Architecture

As mentioned before, MechDev is designed to be a software that is extendable with different functionalities to be up to date all the time. To meet those requirements, a special software architecture is required. Software architecture itself is the first artifact that can be analyzed to determine how well quality attributes are being achieved. It deals with the high-level structure of a software system [1].

Model-View-Controller (MVC) is an architecture that is recommended specially for user-interactive systems [5]. Essential for this design pattern is the capsulation of each part such as model, view and controller. The model provides the data of the system and includes the design intelligence. The view is the interface to the user and visualizes the data. The controller takes part in the interaction with the user and forwards the changes to the model. Figure 15.1 shows the interaction of a user with the three parts of the MVC software architecture.

The main advantage of this software architecture is that the model is independent of the user interface represented and loosely coupled by the controller. Each part can be updated or replaced individually. For the application of a mechanism design software, this means that the mechanical calculation including the methods for analysis and synthesis of mechanisms can be changed without updating the view itself. That simplifies the extension of the software enormously.

To add functions dynamically to the software a Plug-In-based approach was implemented. The software bases on the Rich Client Platform (RCP) of Java to provide a platform independent software with the possibility to add additional functions and update methods via Plug-Ins. To illustrate the Plug-Ins for the different MVC com-
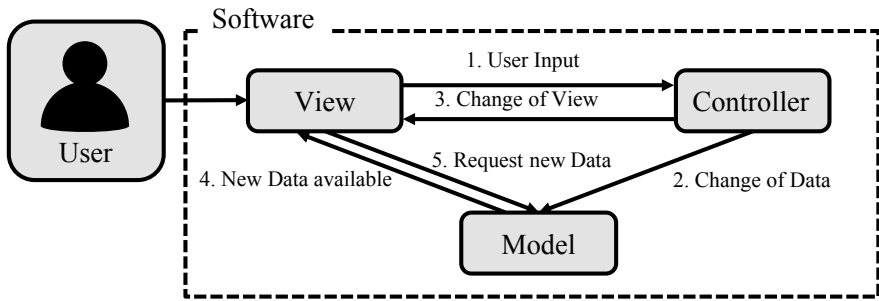
Fig. 15.1 Interaction of the components in a MVC-Architecture based on [5]

Table 15.1 Example of possible Plug-Ins for the different MVC components

Model	View	Controller
Data model	2-Dimensional view	Provided by RCP
Kinematical analysis	Analysis diagrams	
Kinetostatical analysis	Interactive diagrams	
Structural synthesis	Properties window	
Dimensional synthesis	Console	
…	…	

ponents Table 15.1 gives a short overview. The data model Plug-In is the core of the model. It includes the data structure and represents how a mechanism is composited within the software. The different plugins for the analysis and synthesis can be developed independently based on the data model Plug-In.

The Plug-Ins concerning the view components are visualized in Fig. 15.2.

The 2–Dimensional View shows the mechanism and visualizes its motion. The analysis diagram gives information about calculated data of an element such as the movement of a mass point. With an interactive diagram, the drive speed can be varied over time to create servo driven mechanisms. The property window allows the change of properties such as name and position of the selected element. The console gives a feedback to the user about the calculation and status of the program. The view components can be arranged individually and changed easily due to the decoupling of the view with the model.

The RCP framework itself provides the functionalities of the controller.
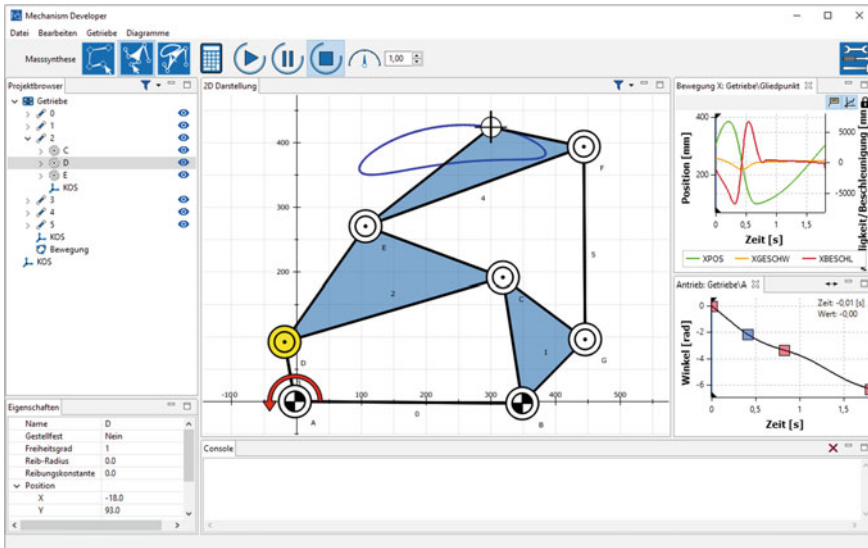
Fig. 15.2 Overview of the different view components

15.3 Kinematical Analysis of Mechanisms

The following chapter will focus on the MechDev Plug-In for the kinematical analysis of planar linkages. This Plug-In is based on [10]. This special approach differs between numerically and analytically computable loops of a kinematical structure. So if an analytical computation is possible, MechDev will use this kind of calculation to be as performant as possible.

15.3.1 Topological Analysis

To determine whether a numerical or an analytical computation is possible, the topology of a mechanism has to be analyzed. Results of this analyzation are the independent loops of the kinematical structure that have to be determined.

Figure 15.3 shows an example of an 8-bar mechanism, where one part can be calculated analytically and one part has to be calculated numerically. The topological analysis will determine three independent loops (*I–III*). A kinematical structure can also be represented by a topological graph where the linkages are represented by knots and the joints are represented by vertexes. Based on the graph theory the different loops can be found by a depth-first search starting with the frame. Next element of a loop is the adjacent element of the topological graph that was not visited yet. Elements of loop *I* in Fig. 15.3 are the joints A_0, A, B and B_0 as well as
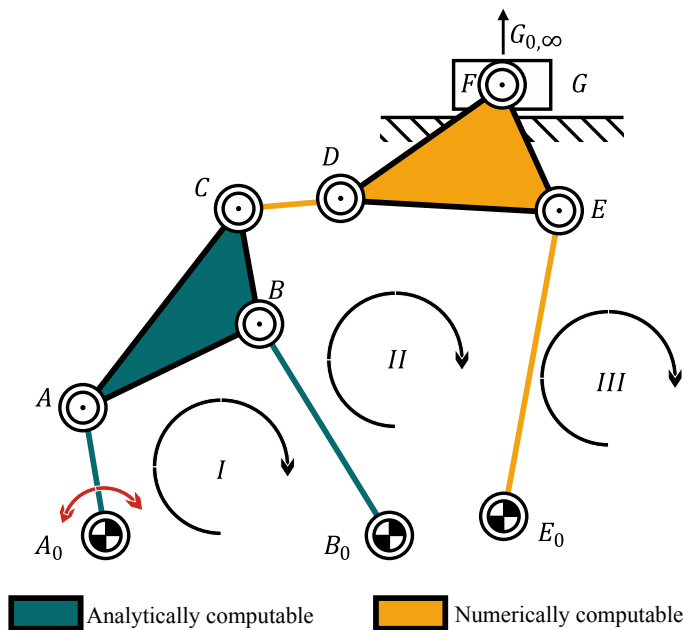
Fig. 15.3 Mechanism with analytical an numerical solvable loops

their connecting linkages. Loop *II* consists of the joints B_0, B, C, D, E, E_0 and the connecting linkages. The last loop *III* consists of the joints E_0, E, F, G and $G_{0,\infty}$ as well as the connecting linkages.

To conclude whether a loop can be calculated analytically, the elements of an independent loop that have a given position have to be determined. In loop *I* the joints A_0 and B_0 have a known position since they are located in the frame and do not change their position over time. In addition, the location of joint A is known because the link $\overline{A_0 A}$ is actuated with a defined motion. The only unknown joint is joint B. The kinematical properties of this joint can be determined analytically since it is the only unknown joint in loop *I*. In every other loop at least two joint locations are unknown (in loop *II* the unknown joints are D and E, in loop *III* the joint unknown joints are E, F and G). Loops with more than one unknown joint cannot be calculated analytically and have to be calculated numerically instead.

15.3.2 Kinematical Analysis

The previous chapter dealt with the topological analysis of the mechanism and the determination of analytically and numerically solvable loops. This chapter will explain how an analytically and a numerically computable loop will be calculated.
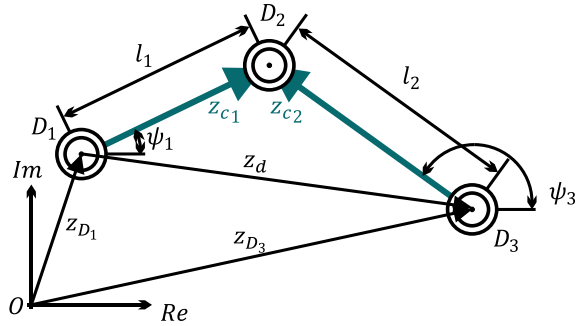
Therefore the approaches of [16, 17] are used for the analytical calculation. The
numerical calculation is based on the loop equation approach mentioned in [4, 14,
15].

15.3.2.1 Analytical Calculation

The German standards VDI 2142 [16] and VDI 2729 [17] give an approach for a
modular, analytical computation of dyads with revolute joints, prismatic joints and
cam joints. Since the calculation via complex numbers is more efficient the approach
described in [16] is chosen for the algorithm. The calculation will be described by
the example given in Fig. 15.4.

The kinematic properties (position, velocity and acceleration) of the two joints
D_1 and D_3 are known and represented by the complex vectors z_{D_1} and z_{D_3}. Besides,
the kinematic lengths l_1 and l_2 are input for the algorithm. The algorithm will then
compute the position, velocity and acceleration of joint D_2.

Equation 15.1 shows the basis loop equation. This equation includes the unknown
angles ψ_1 and ψ_3. They can be used to calculate the position of the unknown joint
D_2.

$$z_{D_1} + l_1 \cdot e^{i\psi_1} = z_{D_3} + l_2 \cdot e^{i\psi_3} \tag{15.1}$$

The solutions of this equation are the intersection points of two circles centered
in D_1 respectively D_3 with the radius l_1 respectively l_2. The analytical solution is
given in Eqs. 15.6 and 15.7 with the parameters presented in Eqs. 15.2–15.5. The
parameter K determines which intersection point will be chosen for the calculation.
K can have the two values $+1$ or -1.

$$z_d = z_{D3} - z_{D1} \tag{15.2}$$

$$Q_1 = \frac{l_1^2}{z_d \overline{z_d}} \tag{15.3}$$

$$Q_2 = \frac{l_2^2}{z_d \overline{z_d}} \tag{15.4}$$

$$w_1 = \frac{1 + Q_1 - Q_2}{2} + iK\sqrt{Q_1 - \left(\frac{1 + Q_1 - Q_2}{2}\right)^2} \tag{15.5}$$

$$\psi_1 = \arg(w_1 z_d) \tag{15.6}$$

$$\psi_3 = \arg((w_1 - 1)z_d) \tag{15.7}$$

The calculation of the velocity and acceleration as well as the calculation for dyads including prismatic joints will not be presented within this paper. It can be taken from [10] or [16].

15.3.2.2 Numerical Calculation

As mentioned before, the numerical approach is based on the loop equation. Each joint has a transformation matrix $^{i-1}T_i$. This matrix represents the transformation between link $i - 1$ and link i and depends on the positon of each joint q_i. For revolute joints q_i is the angular displacement between the two linkages. For a prismatic joint, q_i represents the linear displacement. Since the beginning and ending of a closed loop is the same, the product of every transformation matrix of one loop will end in the identity matrix I. So for one loop the zeros of a function $F(q)$ can be formulated as following:

$$T_{ges} = \prod_{i=1}^{n} {}^{i-1}T_i(q_i) = I \tag{15.8}$$

$$F(q) = T_{ges}(q) - I \tag{15.9}$$

Since only one solution is required and an initial solution of the problem is always given, the Newton's method is a suitable method to find the unknown joint positions q_i. Therefore, a Taylor series can be used to approximate the function up to the first derivative:

$$F(q) = T_{ges}^* - I + \sum_{i=0}^{n} \left(\frac{\partial F}{\partial q_i}\right)^* \Delta q_i^* + \boldsymbol{Res}(q, q^*) \tag{15.10}$$

The variables marked with a star (*) are variables of the previous iteration. The joint position of the actual iteration q can be calculated by the determination of Δq_i^* since the following equation is valid:

$$q = q^* + \Delta q^* \tag{5.11}$$

Also for the numerical approach, the determination of velocities and acceleration will not be part of this paper and can be taken from [10].

15.4   Conclusion

This paper dealt with the idea of a new software for mechanism design. It aims to be easy to handle and includes new functionalities. This software named MechDev was developed at the Institute of Mechanism Theory, Machine Dynamics and Robotics at RWTH Aachen University. To allow a continuous development and improvement, a special software architecture was considered. This architecture, based on MVC and different Plug-Ins, was presented within this paper. Furthermore, parts of the Plug-In for the kinematical analysis was presented. Core of this Plug-In is a special algorithm that combines analytical with numerical computation. Thus, advantages of both methods can be combined. Besides, the general outline of the different computation methods were presented.

References

1. Bass, L., Clements, P., Kazman, R.: Software architecture in practice, 2nd edn. Addison-Wesley, Boston, Mass (2010). [u.a.]: 14. print, ISBN 0-321-15495-9
2. Braune, R.: Das Projekt GENESYS. In: Verein Deutscher Ingenieure (ed.) Kurvengetriebe, Gelenkgetriebe, gesteuerte Antriebe, pp. 17–46. VDI Verlag, Düsseldorf (1996). ISBN 9783180912813
3. Burmester, L.: Lehrbuch der Kinematik. Verlag von Arthur Felix, Leipzig (1888)
4. Corves, B.: Simulation des kinematischen und dynamischen Verhaltens von Handhabungsgeräten mit geschlossenen kinematischen Teilketten, Dissertation, VDI-Verlag; VDI-Verl, Düsseldorf (1989). ISBN 3-18-147118-6
5. Goll, J.: Methoden und Architekturen der Softwaretechnik. Vieweg+Teubner Verlag, Wiesbaden (2011). ISBN 3834881643
6. Hüsing, M., Braune, R., Corves, B.: Dimensional synthesis with mechanism processing strategy. In: Flores, P., Viadero, F. (eds.) EUCOMES 2014, pp. 139–146. Springer (2014)
7. International GeoGebra Institute, GeoGebra, https://www.geogebra.org/?lang=de. Accessed 6 Nev 2017
8. Kerle, H., Corves, B., Hüsing, M.: Getriebetechnik, Grundlagen, Entwicklung und Anwendung ungleichmässig übersetzender Getriebe, Springer Fachmedien Wiesbaden, Wiesbaden, 5 Auflage 2015. ISBN 978-3-658-10056-8
9. Kortenkamp, U.: Cinderella. https://www.cinderella.de. Accessed 6 Nev 2017
10. Mannheim, T.-P.: Kombination analytischer und numerischer Berechnungsmethoden als Grundlage eines Softwaresystems zum Getriebeentwurf, Dissertation, RWTH Aachen University, Aachen, Institut für Getriebetechnik und Maschinendynamik (2015)
11. Nolte, R.: Optimus Motus. http://www.optimusmotus.de. Accessed 6 Nov 2017
12. Nuvolari, A., Verspagen, B., Tunzelmann, N.: The early diffusion of the steam engine in Britain, 1700–1800, a reappraisal. Cliometrica **5**(3), 291–321 (2011)
13. Reuleaux, F.: Lehrbuch der Kinematik. F. Vieweg & Sohn, Braunschweig (1900)

14. Stickeler, A.: Kinematische und kinetostatische Untersuchung räumlicher Kurbelgetriebe unter Berücksichtigung von Glied- und Gelenkfehlern, Dissertation, RWTH Aachen, Aachen, Techn. Hochschule, Institut für Getriebetechnik und Maschinendynamik (1996)
15. Uicker, J.J., Denavit, J., Hartenberg, R.S.: An iterative method for the displacement analysis of spatial mechanisms. J. Appl. Mech. **31**(2), 309 (1964). https://doi.org/10.1115/1.3629602
16. VDI 2142: Auslegung ebener Kurvengetriebe, Standard, Verein Deutscher Ingenieure. Beuth Verlag GmbH, Berlin (2002)
17. VDI 2729: Modular analysis of planar linkages with rotating and sliding joints Kinematic analysis, Standard, Verein Deutscher Ingenieure. Beuth Verlag GmbH, Berlin (2016)
18. Wohlenberg, P.: Auslegung von Koppelgetrieben mit wiederholtem Durchlauf interaktiv erstellter Bearbeitungsstrategien, VDI-Verlag, Düsseldorf (2001). ISBN 3183337010
19. Zanda, G.: Corporate management in a knowledge-based economy. Palgrave Macmillan, Basingstoke, 1. Publ (2012). ISBN 978-0-230-29425-7

Chapter 16
Shaking Force Balance
of the Peaucellier-Lipkin Straight-Line
Linkage

Volkert van der Wijk

Abstract This paper shows three different approaches for the shaking force balancing of the Peaucellier-Lipkin straight-line linkage. First the common approach to balance a linkage by modeling one link in each closed loop with two equivalent masses and subsequently adding countermasses is shown, requiring five countermasses in total. With the second approach the parallelogram in the Peaucellier-Lipkin straight-line linkage is considered a balanced pantograph with which three countermasses are required in total. The third approach consists of considering the parallelogram a mass-equivalent linkage for which the results only require two countermasses. It is also shown how with the second approach shaking force balance in a single direction is obtained by balancing the linkage about the joint tracing the straight line with only two counter-masses. All solutions are also statically balanced.

16.1 Introduction

Straight-line linkages have been fascinating for centuries, first the simple planar linkages generating approximate straight line motion followed by the simple planar linkages generating exact straight-line motion [2]. Also shaking force balancing is a topic that has fascinated scholars for well over a century. Whenever mechanisms move at high speeds, shaking force balance is important to keep base vibrations low [3, 7]. For shaking force balance, a mechanism is designed such that the common center of mass (CoM) of all elements is in a stationary point in the base for all motions. This means that a shaking force balanced mechanism is also statically gravity-balanced, which is advantageous for reducing actuation power and for safety since the mechanism keeps its pose without brakes or actuation.

In this paper the inherent shaking force balance of the Peaucellier-Lipkin straight-line linkage is investigated. Since this linkage incorporates a parallelogram, it is

V. van der Wijk (✉)

Faculty of Mechanical, Maritime, and Materials Engineering, Department of Precision and Microsystems Engineering, Mechatronic System Design, Delft University of Technology, Delft, The Netherlands

e-mail: v.vanderwijk@tudelft.nl

expected to show excellent balance properties. This is since the motions of parallel moving links are linearly related for which, in general, advantageous balance solutions can be found requiring fewer balance constraints or counter-masses.

After introducing the Peaucellier-Lipkin linkage, first the balance solutions for the common force balance approach are shown, subsequently the balance solutions when considering the parallelogram a balanced pantograph are presented followed by the balance solutions when considering the parallelogram a mass equivalent linkage. At the end it is shown how the parallelogram can be balanced about the joint tracing the straight line with which force balance in a single direction is obtained.

16.2 The Peaucellier-Lipkin Straight-Line Linkage

Figure 16.1 shows the Peaucellier-Lipkin straight-line linkage [1, 2]. It consists of seven moving links of which three have a fixed pivot with the base link in A_0 and A_1. The moving links have a length l_i and a mass m_i with i the number of the link. The CoM of each link is located at a distance e_i from the link joint as illustrated. The linkage has one degree of freedom, indicated with angle θ. When in motion, joint B_1 traces a straight line which is orthogonal with respect to the line through the fixed joints A_0 and A_1. The geometric conditions for which B_1 traces a straight line are: (1) linkage $B_0B_1B_2B_3$ is a parallelogram with equal link lengths ($l_1 = l_2 = l_3 = l_4$); (2) $l_5 = l_6$; and (3) the length of link 7 equals the radius of the circle through A_0 and B_3 of which A_1 is the origin. This means that the size of the parallelogram can be chosen independently from the links connecting the base l_5, l_6, and l_7. The size of the parallelogram and of links 5 and 6 determine the distance of the traced straight line with respect to the base joints.

The linkage without link 7 is known as the Peaucellier-Lipkin inversor cell [2]. With link 7 the inversor cell is constrained such that the circle through A_0 and B_3 is inverted into the straight line through B_1.

Fig. 16.1 Peaucellier-Lipkin straight-line linkage with seven moving links with lengths l_i and mass m_i of which the CoM is located at a distance e_i from a pivot as illustrated. A_0 and A_1 are the fixed pivots and joint B_1 traces a straight line
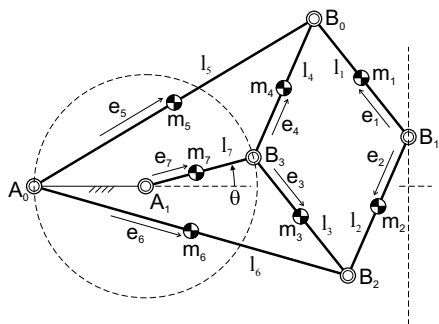
16.3   Shaking Force Balance Solutions with Three Approaches

First the common approach for shaking force balancing a linkage is investigated of which Fig. 16.2a shows the solution and Fig. 16.2b shows the explanation. The masses of link 3 and link 4 are modeled with equivalent masses $m_3^a = m_3(1 - e_3/l_3)$, $m_3^b = m_3 e_3/l_3$, $m_4^a = m_4(1 - e_4/l_4)$, and $m_4^b = m_4 e_4/l_4$ of which m_3^a and m_4^a are located in joint B_3, m_3^b is located in B_2, and m_4^b is located in B_0. For a symmetric balance solution it is required that the CoM of link 1 is located in B_0 ($e_1 = l_1$) and that the CoM of link 2 is located in B_2 ($e_2 = l_2$). Subsequently the parallelogram linkage is balanced with respect to the base by masses m_5, m_6, and m_7. In fact each of the three links 5, 6, and 7 is balanced individually by having the CoM of each model in the fixed pivot for which the force balance conditions are written as

$$m_5 e_5 + (m_1 + m_4^b)l_5 = 0 \tag{16.1}$$

$$m_6 e_6 + (m_2 + m_3^b)l_6 = 0 \tag{16.2}$$

$$m_7 e_7 + (m_3^a + m_4^a)l_7 = 0 \tag{16.3}$$

In practice the balance solution in Fig. 16.2a requires five countermasses, three at the base pivots and two to have the CoMs of link 1 and link 2 be in their respective joint.

Because of the parallelogram, the Peaucellier-Lipkin linkage contains specific kinematic conditions that lead to advantageous force balance solutions. Figure 16.3a shows the balance solution for the second approach where the parallelogram is
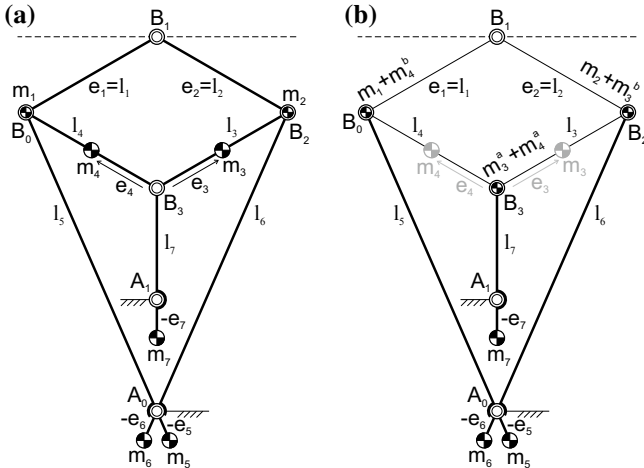
Fig. 16.2 Peaucellier-Lipkin linkage balanced with the common approach for shaking force balancing. Links 3 and 4 are modeled with equivalent masses, m_1 is in B_0, m_2 is in B_2, and m_5, m_6, and m_7 act as countermasses about the base pivots
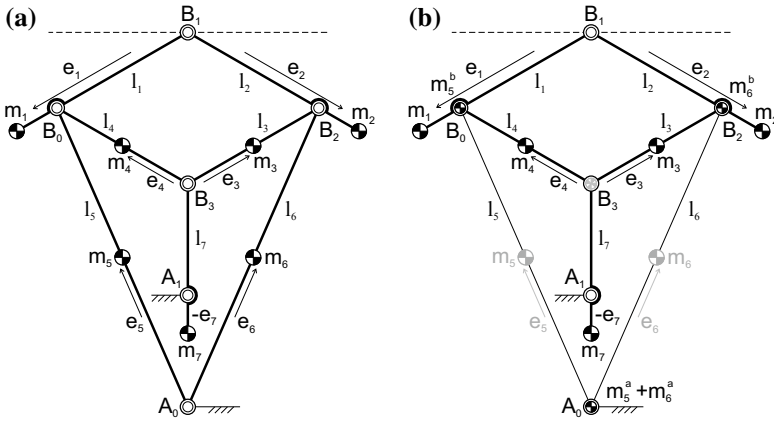
Fig. 16.3 Peaucellier-Lipkin linkage with the force balance solution when the parallelogram is considered a balanced pantograph linkage. Links 5 and 6 are modeled with equivalent masses and the pantograph CoM in B_3 is balanced with respect to A_1 by m_7

considered a balanced pantograph linkage. The approach for balancing is illustrated in Fig. 16.3b. Here links 5 and 6 are modeled with equivalent masses $m_5^a = m_5(1 - e_5/l_5)$, $m_5^b = m_5 e_5/l_5$, $m_6^a = m_6(1 - e_6/l_6)$, and $m_6^b = m_6 e_6/l_6$ of which m_5^a and m_6^a are located in A_0, m_5^b is located in B_0, and m_6^b is located in B_2. Hence m_5^b and m_6^b are included in the pantograph linkage $B_0 B_1 B_2 B_3$ which is balanced with the common CoM of $m_1 + m_2 + m_3 + m_4 + m_5^b + m_6^b$ located in B_3 for the balance conditions [3]

$$m_3 e_3 + m_1(l_1 - e_1) + m_2 l_1 + m_6^b l_1 = 0 \qquad (16.4)$$

$$m_4 e_4 + m_2(l_2 - e_2) + m_1 l_2 + m_5^b l_2 = 0 \qquad (16.5)$$

Subsequently the mass of $m_1 + m_2 + m_3 + m_4 + m_5^b + m_6^b$ in B_3 is balanced by m_7 to have the common CoM in fixed pivot A_1 for which the balance condition writes

$$m_7 e_7 + (m_1 + m_2 + m_3 + m_4 + m_5^b + m_6^b)l_7 = 0 \qquad (16.6)$$

In practice this solution requires three countermasses, two for the pantograph links 1 and 2 and one about base pivot A_1. This saves two countermasses with respect to the balance solution in Fig. 16.2a.

The balanced pantograph can also be designed as shown in Fig. 16.4a. Then m_3 and m_4 are used as countermasses to have the common CoM of the pantograph in B_3. For this solution the force balance conditions are written as [3]
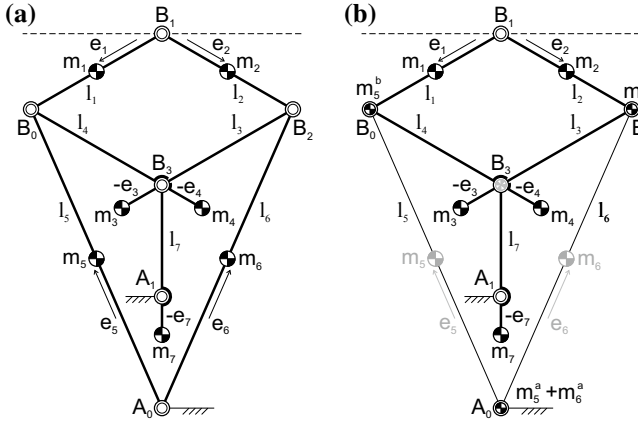
Fig. 16.4 Alternative form of the balanced pantograph as compared to Fig. 16.3. Here m_3 and m_4 are used as countermasses to have the common CoM of the pantograph in B_3

$$m_3e_3 + m_1(l_1 - e_1) + m_2l_3 + m_6^bl_3 = 0 \qquad (16.7)$$

$$m_4e_4 + m_2(l_2 - e_2) + m_1l_4 + m_5^bl_4 = 0 \qquad (16.8)$$

$$m_7e_7 + (m_1 + m_2 + m_3 + m_4 + m_5^b + m_6^b)l_7 = 0 \qquad (16.9)$$

which, since $l_1 = l_2 = l_3 = l_4$, turn out to be equal as for the solution in Fig. 16.3. In practice also here three countermasses are required, two about joint B_3 and one about base pivot A_1.

The third approach is shown in Fig. 16.5 where the parallelogram is considered a mass-equivalent linkage. A mass-equivalent linkage is a linkage that can be modeled with a set of equivalent masses projected in the joints of the other links, equal to modeling a single link as shown for instance for link 5 in Fig. 16.4b [4–6]. In this case the parallelogram together with m_7^b in B_3 (link 7 is modeled mass equivalently with $m_7^b = m_7e_7/l_7$) is modeled with solely the two equivalent masses m_{eq}^a and m_{eq}^b in B_0 and B_2, respectively. This is illustrated in Fig. 16.5b. The common CoM of links 1, 2, 3, and 4 together with m_7^b in B_3 then must be located on the line through B_0 and B_2 at a distance d_a from B_0 and at a distance d_b from B_2. The values of d_a and d_b change when the linkage moves, however for mass equivalence the ratio $\lambda = d_a/d_b$ remains constant for all motions. The conditions for mass equivalence of a pantograph have been derived in [5, 6] from which the balance conditions can be obtained as

$$m_{eq}^a l_1 = m_1e_1 + m_3(l_3 - e_3) + (m_4 + m_7^b)l_1 \qquad (16.10)$$

$$m_{eq}^b l_2 = m_2e_2 + m_4(l_4 - e_4) + (m_3 + m_7^b)l_2 \qquad (16.11)$$

$$m_5e_5 + m_{eq}^a l_5 = 0 \qquad (16.12)$$

$$m_6e_6 + m_{eq}^b l_6 = 0 \qquad (16.13)$$
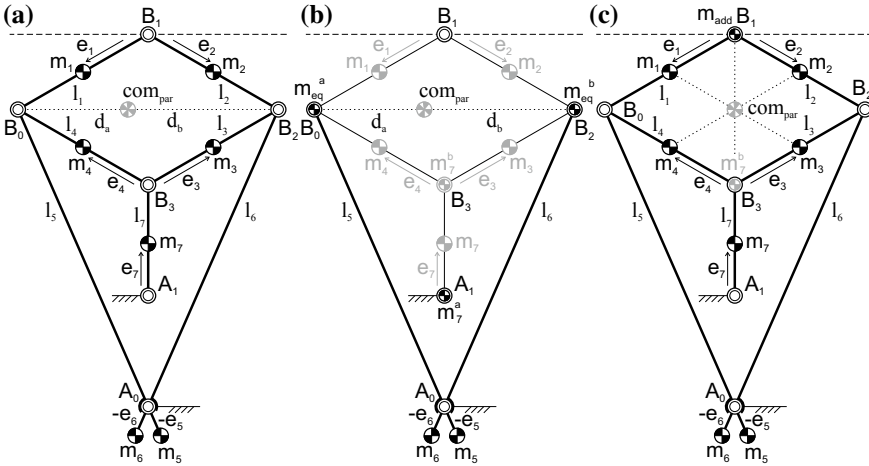
Fig. 16.5 **a–b** Force balance solution with solely two countermasses where the parallelogram is considered a mass-equivalent linkage, modeled with the two equivalent masses m_{eq}^a and m_{eq}^b in joints B_0 and B_2, respectively; **c** Symmetric balance solution with equal links 1, 2, 3, and 4 and with an additional real mass in B_1 to compensate equivalent mass m_7^b in B_3

with $m_{eq}^a = m_{eq}(1 - \lambda)$, $m_{eq}^b = m_{eq}\lambda$, and $m_{eq} = m_1 + m_2 + m_3 + m_4 + m_7^b$. For this solution only two countermasses are required, which are included in the masses of link 5 and link 6.

Figure 16.5c shows a slight variation of the balance solution of Fig. 16.5a. When in practice the four links 1, 2, 3, and 4 are all equal with equal mass properties—which is a likely scenario—then the common CoM of m_1, m_2, m_3, and m_4 will be exactly in the center of the parallelogram. However the equivalent mass m_7^b in B_3 then is not yet included. To include m_7^b can be done by slightly increasing masses m_1 and m_2 with respect to masses m_3 and m_4 according to Eqs. (16.10)–(16.11) such that the CoM still remains on the line through B_0 and B_2. Another solution is to add a real mass $m_{add} = m_7^b$ in joint B_1. Then the common CoM of m_7^b in B_3 and m_{add} in B_1 is also in the center of the parallelogram. In this case the equivalent masses m_{eq}^a in B_0 and m_{eq}^b in B_2 are each half of the total mass of the four links with m_7^b and m_{add} together. In practice mass m_{add} could be the mass of an end-effector such as a grasper. It is also possible to include the mass of an end-effector in the solution of Fig. 16.5a.

With the second approach of considering the parallelogram a balanced pantograph it is also possible to balance the parallelogram with respect to joint B_1, the joint tracing the straight line. The solutions then are only shaking force balanced and statically balanced in the direction perpendicular to the straight line, since the common CoM then also moves along a straight line parallel to the straight line trajectory of B_1. Two such balance solutions are shown in Fig. 16.6. In Fig. 16.6a it is shown how m_3 and m_4 act as balancing masses. The mass of link 5 and link 6 are modeled mass equivalently as in Fig. 16.4b with $m_5^b = m_5 e_5 / l_5$ in B_0 and $m_6^b = m_6 e_6 / l_6$ in B_2.
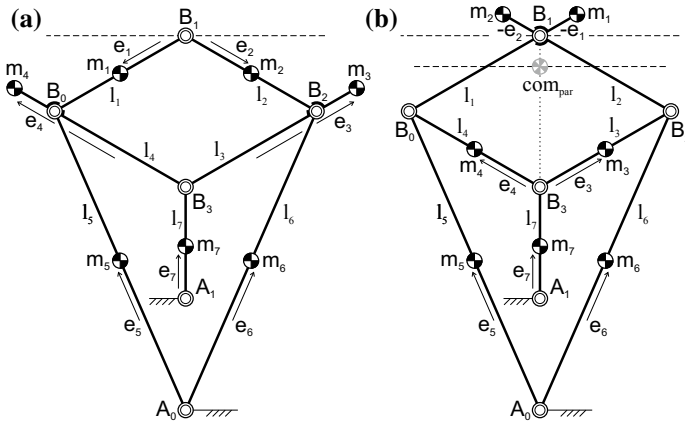
Fig. 16.6 Solutions with the parallelogram as a pantograph balanced about B_1: **a** where m_3 and m_4 are used as balancing masses and **b** where m_1 and m_2 are used as balancing masses. Since B_1 moves along a straight line and hence the common CoM moves along a straight line parallel to it, the linkage is shaking force balanced and statically balanced in the direction perpendicular to the straight line

Also link 7 is modeled mass equivalently as in Fig. 16.5b with $m_7^b = m_7 e_7 / l_7$ in B_3. With these three equivalent masses and the masses of the four parallelogram links the force balance conditions for which B_1 is the common CoM can be derived as [3]

$$m_1 e_1 + m_3 (l_3 - e_3) + (m_4 + m_5^b + m_7^b) l_3 = 0 \tag{16.14}$$

$$m_2 e_2 + m_4 (l_4 - e_4) + (m_3 + m_6^b + m_7^b) l_4 = 0 \tag{16.15}$$

Since equivalent masses $m_5^a = m_5 (1 - e_5 / l_5)$ and $m_6^a = m_6 (1 - e_6 / l_6)$ in A_0 and $m_7^a = m_7 (1 - e_7 / l_7)$ in A_1 are not part of the balanced pantograph, the common CoM of the complete linkage is not in B_1, but moves along a straight line parallel to the straight line of B_1, which is illustrated in Fig. 16.6b.

For the solution shown in Fig. 16.6b masses m_1 and m_2 act as balancing masses. Also here links 5, 6, and 7 are modeled mass equivalently with $m_5^b = m_5 e_5 / l_5$ in B_0, $m_6^b = m_6 e_6 / l_6$ in B_2, and $m_7^b = m_7 e_7 / l_7$ in B_3. The balance conditions of the pantograph including these three equivalent masses then can be derived as [3]

$$m_1 e_1 + m_3 (l_3 - e_3) + (m_4 + m_5^b + m_7^b) l_1 = 0 \tag{16.16}$$

$$m_2 e_2 + m_4 (l_4 - e_4) + (m_3 + m_6^b + m_7^b) l_2 = 0 \tag{16.17}$$

Since the length of all the parallelogram links is equal, the force balance conditions turn out to be equal for both solutions in Fig. 16.6. Of the two solutions in Fig. 16.6, the solution shown in Fig. 16.6b may be most practical since m_1 and m_2 are located close to B_1 while in Fig. 16.6a m_3 and m_4 are located at a large distance from their joints, beyond the straight line (Fig. 16.6a is not drawn to scale).

16.4 Conclusions

In this paper the shaking force balance of the Peaucellier-Lipkin straight-line linkage was investigated with three approaches. It was shown that with the common approach of balancing a linkage a balance solution was found requiring five countermasses. Since the linkage consists of a parallelogram, advantageous balance solutions could be found. When, as the second approach, the parallelogram was considered a balanced pantograph, force balance solutions were obtained requiring three countermasses in total. The most advantageous force balance solutions were obtained by a third approach considering the parallelogram a mass-equivalent linkage. The results then require only two countermasses.

It was also shown how with the second approach of considering the parallelogram a balanced pantograph, the Peaucellier-Lipkin straight-line linkage can be force balanced with respect to the joint tracing the straight line with only two countermasses. These solutions then are shaking force balanced in a single direction only, which is in the direction perpendicular to the traced straight line. When the traced straight line is oriented horizontally, then the results are perfectly statically gravity-balanced Peaucellier-Lipkin straight-line linkages as well.

References

1. Artobolevskii, I.I.: Mechanisms for the Generation of Plane Curves. Pergamon Press (1964)
2. Dijksman, E.A.: Motion Geometry of Mechanisms. Cambridge University Press (1979)
3. Van der Wijk, V.: Methodology for analysis and synthesis of inherently force and moment-balanced mechanisms - theory and applications (dissertation). University of Twente (free download: http://dx.doi.org/10.3990/1.9789036536301) (2014)
4. Van der Wijk, V.: Force balance conditions of complex parallel mechanisms with mass equivalent modeling. In: Husty, M., Hofbaur, M. (eds.) New Trends in Medical and Service Robots: MMS 48, pp. 275–287. Springer International Publishing, Cham (2016)
5. Van der Wijk, V.: Mass equivalent pantographs for synthesis of balanced focal mechanisms. In: Lenarčič, J., Merlet, J.-P. (eds.) Advances in Robot Kinematics 2016, vol. 4, pp. 1–10. Springer International Publishing, Cham (2018)
6. Van der Wijk, V., Herder, J.L.: On the addition of degrees of freedom to force-balanced linkages. In: Proceedings of the 19th CISM-IFToMM Symposium on Robot Design, Dynamics, and Control, pp. 2012–025 (2012)
7. Van der Wijk, V., Krut, S., Pierrot, F., Herder, J.L.: Design and experimental evaluation of a dynamically balanced redundant planar 4-RRR parallel manipulator. Int. J. Robot. Res. **32**(6), 744–759 (2013)

Chapter 17
The Potential of the 7R-R Closed Loop Mechanism to Transfer Motion Between Two Shafts with Varying Angular Position

Luca Luzi, Nicola Sancisi and Vincenzo Parenti-Castelli

Abstract Transmission of the motion between two shafts can be obtained by a Double Cardan Joint (DCJ), which, under particular geometrical conditions, can be homokinetic. A DCJ can be regarded as a 7R closed loop mechanism, which highly reduces the technical/manufacturing complexity when compliant joints are used to replace the R revolute joints. The case of intersecting shaft axes with varying relative orientation is of particular interest in many applications and can be efficiently modeled by a symmetric 7R-R closed loop mechanism to get a homokinetic transmission. This paper deals with the analysis of a type of symmetric 7R-R mechanism, for the homokinetic motion transmission between two incident shafts. Specialized closure equations are written to obtain a closed-form solution of the position analysis. The analysis of both the radial envelope (which affects the mechanism size) and the mechanism singularities are conducted. In particular, a direct relation between the maximum value of the radial envelope and the angle between the shafts is presented. Moreover, the geometrical parameters that determine singularity conditions of the mechanism are found. The singularity configurations are also geometrically analyzed, which disclose the feature of the mechanism to evolve into two different configurations, namely a spherical 4R and a symmetric 7R mechanism. These results can be used for the mechanism dimensioning.

17.1 Introduction

The Double Cardan Joint (DCJ) is often used to transfer motion with a high efficiency between two shafts with incident or skew axes, with a constant and unitary transmission ratio (homokinetic joint). In particular, the DCJ can be represented as

L. Luzi (✉) · N. Sancisi · V. Parenti-Castelli (✉)
Department of Industrial Engineering, University of Bologna, Bologna, Italy
e-mail: luca.luzi3@unibo.it

V. Parenti-Castelli
e-mail: vincenzo.parenti@unibo.it

N. Sancisi
e-mail: nicola.sancisi@unibo.it
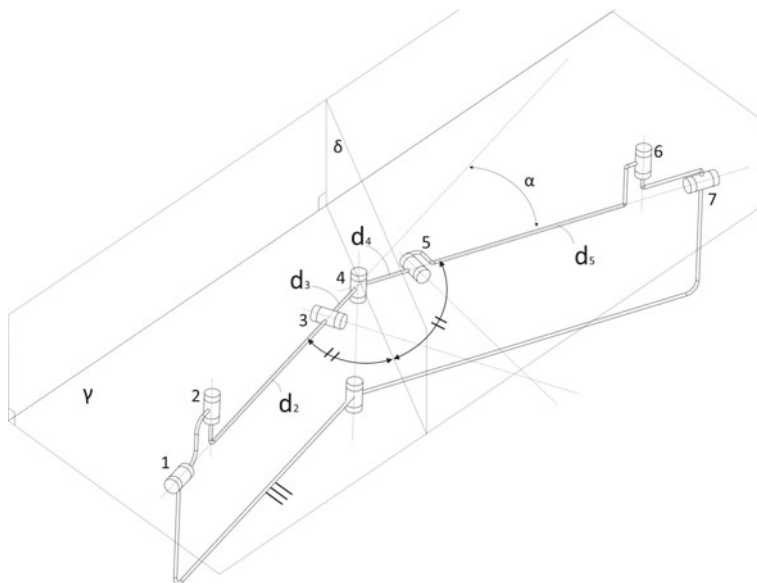
Fig. 17.1 7R mechanism, parameter description

a special 7R or 3RP3R mechanism, or also as an overconstrained 6R mechanism, where R and P stand for revolute and prismatic joints respectively.

The 7R representation can be useful, for instance, when compliant joints are used instead of the standard R joints. In the DCJ, indeed, two groups of three R joints have intersecting axes: this can be easily achieved with standard R joints, but the use of compliant joints is more challenging and the solutions proposed in the literature are complicated and bulky for some applications [2]. However, homokinetic joints for motion transmission between incident input and output shafts can be obtained using 7R mechanisms with intermediate R joints with non-intersecting axes [3, 4], that look similar to the DCJ but greatly simplify the application of compliant joints.

In addition, some practical applications require a varying angle α between input and output shaft during motion. Examples are automobile transmission systems, where the angle α between the input shaft (i.e., on the axle) and the output shaft (i.e., on the wheels) changes due to the suspension system; motion transmissions for machine tools; laparoscopic tools, where the output shaft that brings the surgery tool can change orientation with respect to the input shaft driven by the surgeon. A varying α angle can be obtained by adding an R joint on the frame, centred at the intersection point between the input and output axes and orthogonal to both axes (Fig. 17.1). The angle α is thus defined by rotating the two segments of the frame about this additional R joint. The 7R-R mechanism so obtained can be used as an alternative to the DCJ to transmit motion with a constant velocity ratio between incident axes with compliant joints and varying orientation α.
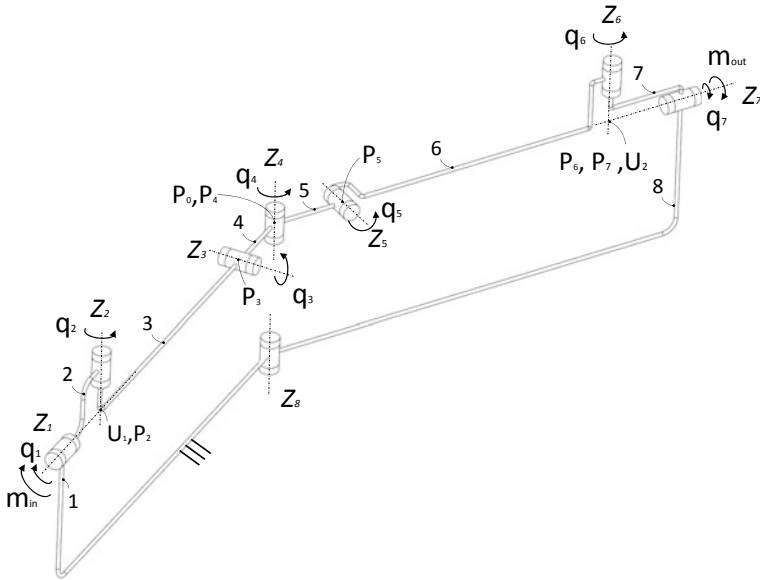
Fig. 17.2 7R-R mechanism, parameter description

This paper presents the mechanical characterization of this homokinetic 7R-R mechanism. In particular, it is interesting to analyse the behaviour of the mechanism when the distances d_2 and d_5 (Fig. 17.1) between the skew R joints (and so the difference with the DCJ) increases. Moreover, although it is possible to define homokinetic 7R mechanisms with skew non-orthogonal axes [4], the 7R geometry where the first three and the last three R joints have skew orthogonal axes is particularly interesting, both for its greater practical interest and for its closer analogy to the standard DCJ. Specialised closure equations are defined for this geometry of the 7R-R mechanism and both a kinematic and a static characterization is performed. In particular, the kinematic analysis is focused also on the radial envelope of the intermediate members during motion. Indeed, in the standard DCJ the central member rotates about a fixed axis, so its radial envelope is zero (practically the volume of the intermediate shaft); when the central R (with axis Z_4 in Fig. 17.2) is added to obtain the 7R-R mechanism, the radial envelope increases and this affects the overall volume occupied by the mechanism. This aspect could be important in some applications like in laparoscopic surgery where the mechanism dimensions are particularly critical.

17.2 Methods

17.2.1 Considered 7R Geometry and Loading Scenario

Each rotation axis Z_i, $i = 1,..,7$, (Fig. 17.2) is orthogonal to the next axis. $\mathbf{z}_i$ and q_i ($i = 1,..,7$), are the unit vectors of and the rotation angle about the Z_i axis respectively. Z_1 and Z_7 lie on the same plane γ; α and P_0 are the angle and the intersection point between them respectively (Fig. 17.1). Axes Z_1 and Z_2 intersect at point U_1, while axes Z_6 and Z_7 intersect at point U_2 (Fig. 17.2); d_0 and d, are the distances between them for $\alpha = 0$ and for a generic α. The overall geometry is symmetric with respect to a plane δ, namely the bisecting plane [4] (Fig. 17.1), and this property is maintained during motion. Thus, always $q_1 = q_7$ (i.e., the mechanism is homokinetic), $q_2 = q_6$ and $q_3 = q_5$. The distance between the Z_{i-1} and Z_i axes is d_i ($i = 2,..,7$); for the symmetry $d_3 = d_6$ and $d_4 = d_5$, whereas $d_2 = d_7 = 0$. P_i ($i = 2,..,7$) is the closest point to Z_{i-1} on Z_i (Fig. 17.2) that is, $P_{i-1}P_i$ is the shortest distance between Z_{i-1} and Z_i axes. The unit vector normal to δ is $\mathbf{u}$, and has the same direction of the line r passing through U_1 and U_2. When $\alpha = 0$, the mechanism is distended so that all the points P_i lie on the line r. In particular, when Z_2 is perpendicular to γ, at this configuration all $q_i = 0$; moreover, it is clear that $d_3 + d_4 + d_5 + d_6 = d_0$, and for the symmetry, $d_3 + d_4 = d_5 + d_6 = d_0/2$. A Cartesian coordinate system S_f, fixed with respect to the frame, is chosen with origin at point U_1 and Z axis coincident with Z_1, X axis orthogonal to the Z axis and lying on γ, Y axis is chosen according to the right-hand rule. Hereinafter, all vectors are represented in S_f; in particular, $\mathbf{p}_i$ ($i = 2,..,7$) are the position vectors of points P_i with respect to S_f. As for the loads, the mechanism is subjected only to an input and output couples (m_{in} and m_{out}, Fig. 17.2) and to the resulting constraint reactions. Friction in kinematic pairs and link weights are ignored.

17.2.2 Direct Position Analysis

For a given α, the 7R-R mechanism becomes a 7R mechanism. The direct position analysis (DPA) problem of the 7R mechanism is to find the joint variables q_i ($i = 2,..,7$) as a function of the input variable q_1 for a given α value. Position analysis of the general 7R mechanism was already solved in the literature [1, 6]. A different approach is used in this case, to take advantage of the considered specific 7R geometry. In particular, the symmetry with respect to the bisecting plane δ makes it possible to write the closure equations of the DPA only for the first half of the 7R mechanism. Thus, the DPA can be reduced to a system of two equations in two unknowns (namely, rotations q_2 and q_3). In particular, Z_4 and P_4 lie on the bisecting plane, and Z_4 is normal to the r line. These two conditions define the closure equations:

$$\mathbf{z}_4 \cdot \mathbf{u} = 0 \qquad\qquad (17.1)$$

$$\mathbf{p}_4 \cdot \mathbf{u} = \frac{d}{2} \tag{17.2}$$

In Eqs. (1) and (2), vector $\mathbf{u}$ depends on α, whereas $\mathbf{z}_4$ and $\mathbf{p}_4$ can be expressed as functions of q_1, q_2, q_3:

$$\mathbf{z}_4' = \begin{bmatrix} \mathbf{z}_4 \\ 0 \end{bmatrix} = \mathbf{A}_1\mathbf{A}_2\mathbf{A}_3[0010]^T \tag{17.3}$$

$$\mathbf{p}_4' = \begin{bmatrix} \mathbf{p}_4 \\ 1 \end{bmatrix} = \mathbf{A}_1\mathbf{A}_2\mathbf{A}_3[0001]^T \tag{17.4}$$

where $\mathbf{A}_i$ is the Denavit-Hartenberg transformation matrix related to the i-th link. These equations make it possible to find the closed-form solution of q_2 and q_3 (and q_5, q_6) as functions of q_1. Finally, q_4 is obtained as:

$$q_4 = 2arccos\left(\frac{(\mathbf{p}_4 - \mathbf{p}_3)'\mathbf{u}}{||(\mathbf{p}_4 - \mathbf{p}_3)||\,||\mathbf{u}||} \right) \tag{17.5}$$

where $\mathbf{p}_3$ is:

$$\mathbf{p}_3' = \begin{bmatrix} \mathbf{p}_3 \\ 1 \end{bmatrix} = \mathbf{A}_1\mathbf{A}_2[0001]^T \tag{17.6}$$

In order to evaluate the radial envelope of the intermediate members about the line r during motion, the trajectory of the point P_4 on δ is determined as a function of q_1, d_2/d_0 and α. It can be shown that the maximum distance $d_{4,r}$ of the point P_4 from r normalized to d_0 (namely, $d_{4,r}/d_0$) depends only on α. Indeed, when Z_2 is perpendicular to r ($q_1 = 0$ and $q_1 = \pi$), since Z_4 is always perpendicular to r, Z_2 and Z_4 are parallel because of the constraint given by Z_3. Since in this condition the links 3 and 4 are collinear, points P_2 (i.e., U_1) and P_4 are at their maximum distance $d_0/2$ and thus P_4 is at the maximum distance from r:

$$\frac{d_{4,r}}{d_0} = \left| \frac{\sin\beta}{2} \right| \tag{17.7}$$

where $\beta = \alpha/2$ is the angle between Z_1 and r. Equation (7) shows clearly that the radial envelope increases with α (for $0 < \alpha < \pi/2$) and it is independent on d_2/d_0.

17.2.3 Velocity Analysis

The velocity analysis of the 7R mechanisms could be performed by deriving Eqs. (1) and (2) with respect to time. However, a reduced equation system could prevent some

singularities to be detected. Thus, for the singularity analysis, a full equation system including all joint velocities ω_i ($i = 1,..,7$) is used instead, where ω_i is the relative angular velocity of link $i + 1$ with respect to link i. This system can be written in the standard form [7]:

$$\mathbf{J}\boldsymbol{\omega} = \begin{bmatrix} \mathbf{v}_1 \\ \boldsymbol{\omega}_1 \end{bmatrix} \tag{17.8}$$

where

$$J = \begin{bmatrix} \mathbf{z}_2 \times \mathbf{p}_2 & \cdots & \mathbf{z}_7 \times \mathbf{p}_7 \\ \mathbf{z}_2 & \cdots & \mathbf{z}_7 \end{bmatrix}; \tag{17.9}$$

and

$$\boldsymbol{\omega} = [\omega_2\omega_3\omega_4\omega_5\omega_6\omega_7]^{\mathrm{T}} \tag{17.10}$$

where for the case studied

$$\begin{bmatrix} \mathbf{v}_1 \\ \boldsymbol{\omega}_1 \end{bmatrix} = \begin{bmatrix} 0 \\ 0 \\ 0 \\ 0 \\ 0 \\ 1 \end{bmatrix} \tag{17.11}$$

Hence

$$\mathbf{J}\boldsymbol{\omega} = \begin{bmatrix} 0 \\ 0 \\ 0 \\ 0 \\ 0 \\ 1 \end{bmatrix} \omega_1 \tag{17.12}$$

where $\mathbf{v}_1$ is the vector velocity of point U_1, and $\boldsymbol{\omega}_1$ is the relative angular velocity vector of link 2 with respect to link 1. Joint velocities are obtained by solving the linear system (12), thus by inverting matrix $\mathbf{J}$. Singular configurations are those in which the determinant of $\mathbf{J}$ equals zero.

17.2.4 Static Analysis

The static analysis is performed by obtaining the constraint reactions of the frame on link 2 (Fig. 17.2). These are equivalent to a force $\mathbf{f}$ and a moment $\mathbf{m}$ and can be represented in S_f by their components f_x, f_y, f_z, and m_x, m_y, m_z, respectively as:

$$\mathbf{f} = \begin{bmatrix} f_x \\ f_y \\ f_z \end{bmatrix} ; \mathbf{m} = \begin{bmatrix} m_x \\ m_y \\ m_{in} \end{bmatrix} \tag{17.13}$$

Given the moment m_{out} acting on link 7, the six unknowns components that appear on (13) can be found from:

$$\mathbf{J}^T \mathbf{w} = \begin{bmatrix} 0 \\ 0 \\ 0 \\ 0 \\ 0 \\ m_{out} \end{bmatrix}. \tag{17.14}$$

where

$$\mathbf{J}^T = \begin{bmatrix} (\mathbf{z}_2 \times \mathbf{p}_2)^T & \mathbf{z}_2^T \\ \vdots & \vdots \\ (\mathbf{z}_7 \times \mathbf{p}_7)^T & \mathbf{z}_7^T \end{bmatrix} \tag{17.15}$$

and

$$\mathbf{w} = \begin{bmatrix} \mathbf{f} \\ \mathbf{m} \end{bmatrix} \tag{17.16}$$

17.3 Results and Numerical Example

Figure 17.3 shows the trajectory of P_4 on δ (normalized to d_0), as a function of α and d_2/d_0. As determined through Eq. (7), the trajectory depends on both parameters, but the maximum normalized distance $d_{4,r}/d_0$ (obtained for $q_1 = 0$ and $q_1 = \pi$) depends only on α.

Equations (8) and (14) show that when the determinant of $\mathbf{J}$ is zero, the system is in a singular configuration. The determinant of $\mathbf{J}$ is a function of q_1, d_2/d_0 and α, and its zeroes are represented in (Fig. 17.4a) by the orange and the yellow sur-
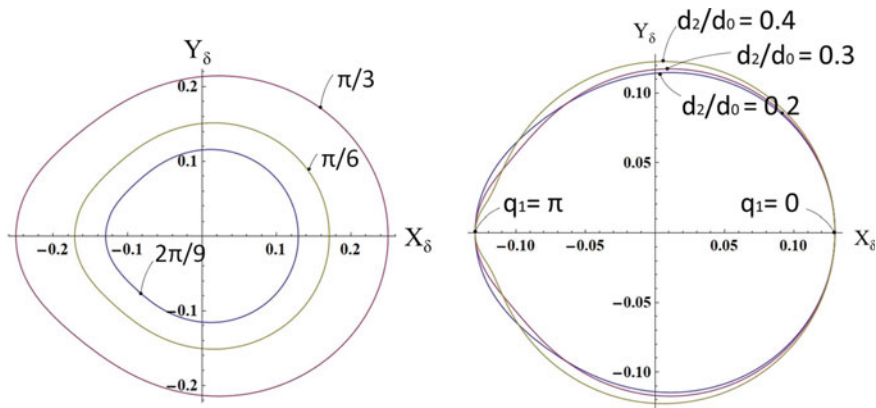
Fig. 17.3 Trajectory of point P_4, $d_{4,r}/d_0$, on δ plane for different values of α with $d_2/d_0 = 0.5$ (left), and trajectory of point P_4, $d_{4,r}/d_0$, for different values of d_2/d_0, with $\alpha = \pi/6$ (right). Cartesian axes X_δ and Y_δ belong to the plane δ, are respectively parallel and perpendicular to γ and with origin at the middle point of the segment $U_1 U_2$
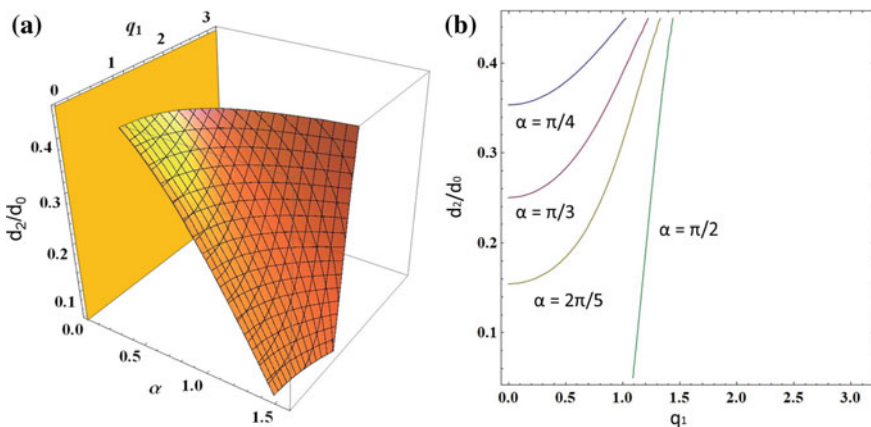
Fig. 17.4 **a** Singularity surface; **b** Singularity curves for several values of α

faces. The singularity conditions are geometrically characterized. In particular, for the considered 7R geometry, axes Z_2, Z_4, Z_6 always meet at a point B during motion.

Moreover, Z_3 and Z_5 always meet at a point C, while Z_1 and Z_7 always meet at point P_0 (Fig. 17.5a). In the singular condition represented by the orange surface in Fig. 17.4a, the points C and P_0 coincide, thus Z_1, Z_3, Z_5, Z_7 all meet at P_0. From this configuration, the mechanism can evolve into two different one degree-of-freedom mechanisms: the first one is the symmetric 7R here analyzed, that keeps axes Z_2, Z_4, Z_6 meeting at the point B (Fig. 17.5a); the second one is a spherical four-bar linkage, that keeps axes Z_1, Z_3, Z_5, Z_7 intersecting at the point P_0 (Fig. 17.5b). Under the second functioning condition, q_2, q_4, q_6 are constant during motion, i.e., the pairs
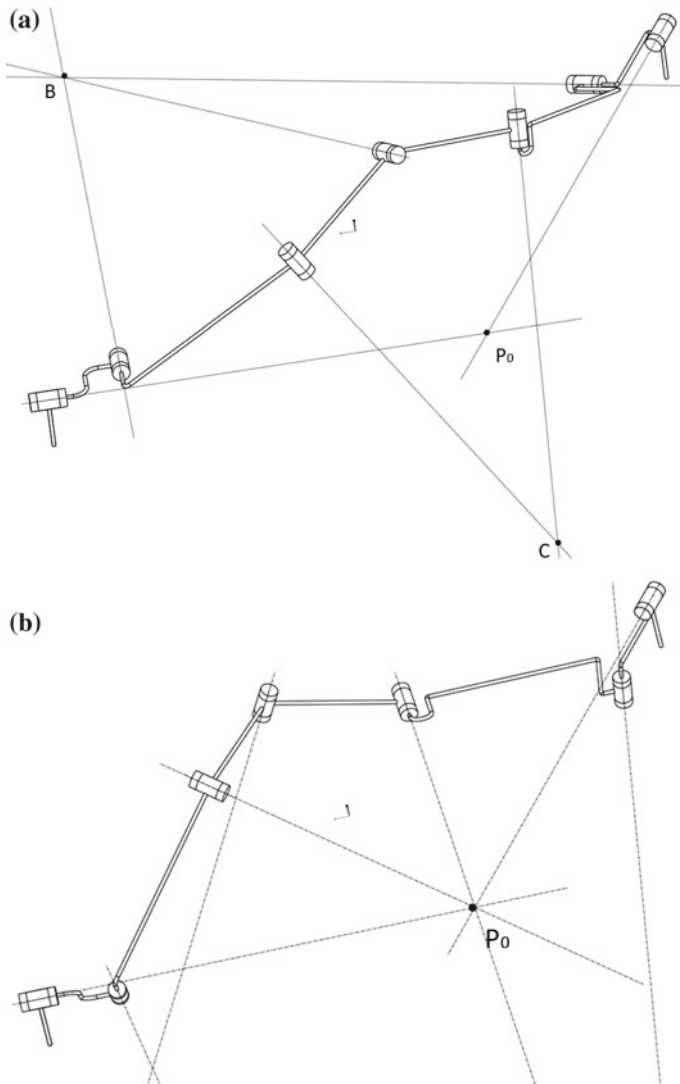
Fig. 17.5 Functioning conditions of the mechanism

of links 1 and 2, 3 and 4, 5 and 6 behave as single rigid links. Moreover, under this condition, the mechanism shows also the singularity configuration of the spherical four-bar linkage. The singular condition represented by the yellow plane in Fig. 17.4a (the plane for $\alpha = 0$), occurs when the axes Z_2, Z_4 and Z_6 are coplanar (this situation corresponds to a configuration in which the mechanism is fully extended). It is worth noting, that Eqs. (1) and (2) can be used only to solve the DPA of the mechanism in the 7R functioning condition. To solve the DPA for the other functioning conditions,

the closure equations for the general geometry 7R [1, 6] or for the spherical four-bar linkage [5] should be used.

As far as the mechanism remains in the 7R functioning condition, the joint velocities do not show discontinuities, remain finite and different from zero when crossing the singular configuration. In particular, the transmission ratio between input and output axes remain always unitary. However, joint velocities have different values at the singularity when the mechanism is in the 7R or four-bar functioning conditions. The frame reactions, instead, tend to infinity at singularity, while keeping $m_{in} = m_{out}$ always.

From Fig. 17.4b it is possible to determine the maximum value of the ratio d_2/d_0 to avoid singularity for each value of the angle α. For instance, when $\alpha = \pi/3$, d_2/d_0 must be minor than 0.25.

17.4 Conclusion

The homokinetic 7R-R closed-loop mechanism can be useful for those applications in which the transmission of the motion by a Double Cardan Joint (DCJ) with intersecting axes of varying orientation is not suitable. In this study, an efficient geometry of the 7R-R mechanism, which can be used instead of the DCJ, is characterized from a kinematic and static point of view. In particular, the analyses of the mechanism radial envelope and the mechanism singularities, together with the simplified closure equations are reported, which can be used for the dimensioning of the mechanism. The radial envelope of the mechanism shows a direct dependency of its maximum value from the parameter α. Moreover, a singularity condition was found when the axes Z_1, Z_3, Z_5 and Z_7 meet at the same point P_0. This result can be used to choose the mechanism parameters to avoid singularities. When this singularity occurs, it is revealed that the mechanism can evolve into a spherical 4R or a 7R mechanism respectively. Furthermore, the determinant of $\mathbf{J}$ can be used as a performance index: the farther from zero the determinant of $\mathbf{J}$ is, the better, in general, the performance of the mechanism.

References

1. Duffy, J., Crane, C.: A displacement analysis of the general spatial 7-link, 7R mechanism. Mech. Mach. Theory **15**, 153–169 (1980)
2. Farhadi Machekposhti, D., Tolou, N., Herder, J.L.: A review on compliant joints and rigid-body constant velocity universal joints toward the design of compliant homokinetic couplings. J. Mech. Des. **137** (2015)
3. Gilmartin, M.J., Duffy, J.: Displacement analysis of spatial 7R mechanisms suitable for constant-velocity transmission between parallel shafts. J. Mech. Des. **101**, 604–613 (1979)
4. Hunt, K.H.: Constant-velocity shaft couplings: a general theory. J. Eng. Ind. **95**, 455–464 (1973)
5. Hunt, K.H.: Kinematic Geometry of Mechanism. Clarendon Press, Oxford (1978)

6. Lee, H.-Y., Liang, C.-G.: Displacement analysis of the general spatial 7-link 7R mechanism. Mech. Mach. Theory **23**, 219–226 (1988)
7. Tsai, L.W.: Robot analysis: the mechanics of serial and parallel manipulators. A Wiley-Interscience Publication (1999)

Chapter 18
Auxetic Regions in Large Deformations of Periodic Frameworks

Ciprian S. Borcea and Ileana Streinu

Abstract In materials science, auxetic behavior refers to lateral widening upon stretching. We investigate the problem of finding domains of auxeticity in global deformation spaces of periodic frameworks. Case studies include planar periodic mechanisms constructed from quadrilaterals with diagonals as periods and other frameworks with two vertex orbits. We relate several geometric and kinematic descriptions.

18.1 Introduction

Periodic frameworks are mathematical abstractions which model atom-and-bond structures in crystalline materials or man-made trusses and repetitive articulated systems [2, 22]. Recent advances in additive manufacturing have brought about new possibilities for producing complex structures at microscales, giving new impetus to rational design of metamaterials, particularly those based on a periodic organization [1, 4, 13, 19].

Auxetic behavior is a rather counter-intuitive mechanical response of certain materials and structures which involves lateral widening under stretching and, in reverse, lateral shrinking under compression. This type of response is desirable for various applications, ranging from medical implements to shock-absorbing curtains and has been investigated with increased interest over the last three decades [14–16, 20]. Even so, most studies have addressed only small deformations of a confined repertory of structural designs and the problem of large deformations has been barely considered [24]. Auxetic growth implies, in particular, volume increase [8] and is therefore limited by certain structural bounds. Thus, for large deformations, auxetic behavior can be expected only over restricted regions. The main purpose of the

C. S. Borcea (✉)
Department of Mathematics, Rider University, Lawrenceville, NJ 08648, USA
e-mail: borcea@rider.edu

I. Streinu (✉)
Department of Computer Science, Smith College, Northampton, MA 01063, USA
e-mail: istreinu@smith.edu; ileana.streinu@gmail.com

present contribution is to offer an introduction to this type of kinematic inquiry, based on our geometric theory of auxetic deformations and recent fundamental results on the structure and design of auxetic periodic frameworks [8, 11, 12].

We review in Sect. 18.2 some key notions on periodic frameworks and auxetics. We proceed in Sect. 18.3 with a fairly intuitive scenario in dimension two, by associating a periodic framework to a given quadrilateral, which is repeatedly translated by its diagonal vectors, as shown below in Fig. 18.1. As a planar linkage, a quadrilateral is a four-bar mechanism and our opening discussion is just an interpretation of the classical kinematics of this mechanism in the periodic setting. Yet, even this elementary situation proves the value of a strictly geometric approach to auxetics and suggests useful algebraic parametrizations based on spectrahedra. This point of view is pursued in subsequent sections and leads to a unified perspective for identifying auxetic regions in global deformations of periodic frameworks with two vertex orbits.

18.2 Prerequisites

We begin with a concise review of notions which are necessary for a mathematical formulation of our problem.

Periodic Frameworks and Deformation Spaces. The principal reference is [2].

Definition 18.1 A *d-periodic graph* is a pair (G, Γ), where $G = (V, E)$ is a simple infinite graph with vertices V, edges E and finite degree at every vertex, and $\Gamma \subset Aut(G)$ is a free Abelian group of automorphisms which has rank d, acts without fixed points and has a finite number of vertex (and hence, also edge) orbits.

We assume G to be connected. The group Γ is isomorphic to Z^d and is called the *periodicity group* of the periodic graph G. Vertices which are equivalent under Γ form a vertex orbit and similarly for edges.

Definition 18.2 A (periodic) *placement* of a d-periodic graph (G, Γ) in R^d is defined by two functions: $p : V \to R^d$ and $\pi : \Gamma \hookrightarrow \mathcal{T}(R^d)$, where p assigns points in R^d to the vertices V of G and π is a faithful representation of the periodicity group Γ, that is, an injective homomorphism of Γ into the group $\mathcal{T}(R^d)$ of translations in the Euclidean space R^d, with $\pi(\Gamma)$ being a lattice of rank d. These two functions must satisfy the natural compatibility condition $p(\gamma v) = \pi(\gamma)(p(v))$. The translation group $\mathcal{T}(R^d)$ can be identified with the additive group of vectors in R^d.

In a framework, edges are seen as segments between the corresponding vertices. Mechanical interpretations consider edges as rigid bars and vertices as (spherical) joints, hence the name bar-and-joint framework.

Definition 18.3 Given a d-periodic framework $\mathcal{F} = (G, \Gamma, p, \pi)$, the collection of all periodic placements of (G, Γ) in R^d which maintain the lengths of all edges is

called the *realization space* of the framework. After factoring out equivalence under Euclidean isometries, we obtain the *configuration space* of the framework (with the quotient topology). The *deformation space* is the connected component of the configuration space which contains the initial framework.

It is important to notice that the representation of the periodicity group Γ by a lattice of translations may well vary when the framework deforms.

Auxetic Deformations. The motivations for the following definition of auxetic paths are detailed in [8]. Let $(G, \Gamma, p_\tau, \pi_\tau)$, $\tau \in (-\varepsilon, \varepsilon)$ be a one-parameter deformation of the periodic framework (G, Γ, p, π), where $p = p_0$ and $\pi = \pi_0$. Suppose we have chosen an independent set of generators γ_i, $i = 1, \ldots, d$ for the periodicity group Γ. Then, we have at every moment τ a lattice basis $\pi_\tau(\gamma_i)$, which we write as a $d \times d$ matrix (with column vectors) Λ_τ. The Gram matrix of the lattice basis is therefore $\omega_\tau = \Lambda_\tau^t \Lambda_\tau$.

Definition 18.4 A one-parameter deformation $(G, \Gamma, p_\tau, \pi_\tau)$, $\tau \in (-\varepsilon, \varepsilon)$ is called an *auxetic path*, or simply *auxetic*, when the curve of Gram matrices ω_τ has all its velocity vectors in the cone of positive semidefinite symmetric $d \times d$ matrices. When all velocity vectors are in the positive definite cone, the deformation is called *strictly auxetic*.

In short, for periodic frameworks, auxetic behavior is expressed through the evolution of the Gram matrix of periodicity generators. A number of recent results derived from this geometric approach to auxetics can be found in [11, 12]. The present inquiry will be oriented towards questions involving large deformations, that go beyond a small neighborhood of a given initial configuration.

18.3 Four-Bar Mechanisms and Associated Periodic Frameworks

We open our investigation with a simple type of planar periodic framework which offers an intuitive setting for the abstract concepts reviewed above. We start with a quadrilateral $ABCD$ and construct an associated periodic framework by adopting the two diagonal vectors $\overrightarrow{AC}$ and $\overrightarrow{BD}$ as periodicity generators. Repeated translations of the quadrilateral by these vectors will articulate into a periodic framework when shared vertices are identified as single joints. The process is illustrated in Fig. 18.1, where the two diagonal vectors are shown as red arrows. The formal construction is described in a more general setting in [11]. When the quadrilateral is imagined as a four-bar mechanism (and as long as the two diagonal vectors remain independent), this association converts a one-degree-of-freedom linkage into a one-degree-of-freedom periodic framework.

The deformation space of a four-bar mechanism is well studied in classical kinematics and our task in the periodic setting is reduced to recognizing which intervals correspond to auxetic (or reversed-auxetic) behavior.
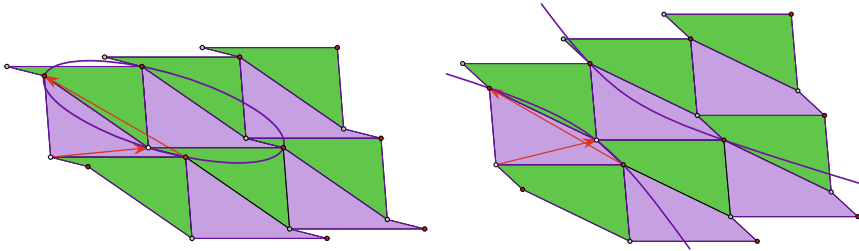
Fig. 18.1 (Left) A periodic framework can be associated to a quadrilateral by adopting the two diagonals as generators of the periodicity lattice. A four bar mechanism is converted into a planar periodic framework with one degree of freedom. When the quadrilateral is in a pseudotriangle configuration, the result is a periodic pseudotriangulation. The local deformation is expansive, hence auxetic, and this property is confirmed by the ellipse running through a vertex and the endpoints of the four bars emanating from it. (Right) Auxetic behavior ends when the generating quadrilateral becomes convex or self-intersecting. This is reflected in the fact that the conic through a vertex and the endpoints of the four bars emanating from it becomes a hyperbola

We assume a generic quadrilateral. By Grashof's rule, the oriented configuration space is topologically either (i) a single loop, if the longest edge plus the shortest edge are more than the other two edges together, or (ii) two loops, if the longest edge plus the shortest edge are less than the rest. Parallel diagonals occur only in the former case. Equivalence under reflections identifies the two loops in one case and gives an involution without fixed points of the single loop in the other case (with matching of the two configurations with parallel diagonals). Thus, in both cases, the deformation space of the linkage (considered up to planar isometries) is topologically a single loop (i.e. a circle). For the deformation space of the associated periodic framework, case (i) requires the exclusion of one point for the case when the diagonals become parallel.

For brevity, we expand here on case (ii), which is illustrated in Fig. 18.1. As mentioned in the introduction, an auxetic deformation will increase the area of a unit cell (fundamental domain under periodicity) and auxetic intervals in our deformation loop cannot contain relative minima or maxima of the area function. A precise determination of these intervals can be obtained by direct computation, but we present a more advanced point of view, based on pseudotriangulations [6, 7, 21].

A pseudotriangle is a simple planar polygon with exactly three interior angles less than π. In a quadrilateral linkage, the lengths of the two diagonals vary in the same way (i.e. both increase or both decrease) if and only if the quadrilateral is in a pseudotriangle configuration [21]. Periodic pseudotriangulations are introduced and treated at large in [7] and their role in understanding expansive planar periodic deformations is described in [6]. Expansive deformations require all distances between pairs of vertices to increase or stay the same [9]. Periodic pseudotriangulations deform expansively and expansive implies auxetic [7, 8]. Assembling these facts, we obtain the following geometric characterization.
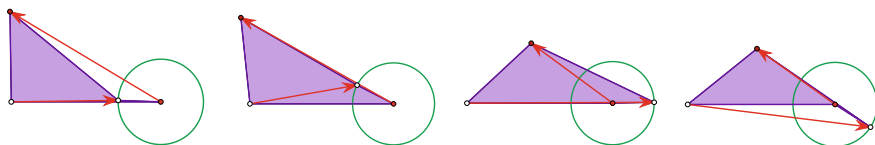
Fig. 18.2 Auxetic-to-non-auxetic transition configurations: as the second edge rotates clockwise around the fixed first edge, there is an auxetic interval between the two configurations on the left and another one (in reverse) between the two configurations on the right

Theorem 18.1 *The periodic framework associated to a quadrilateral has a local auxetic deformation if and only if the quadrilateral is in a pseudotriangle configuration.*

If we use a general structural result established in [12], we can state an equivalent characterization.

Theorem 18.2 *The periodic framework associated to a quadrilateral has a local auxetic deformation if and only if the conic passing through a chosen vertex and the endpoints of the four bars emanating from it is an ellipse.*

The two theorems are illustrated in Fig. 18.1. The four transition configurations (from auxetic to non-auxetic behavior) of the quadrilateral are shown in Fig. 18.2.

18.4   The Elliptope and Other Spectrahedra

When aiming at more general results, an immediate problem is that of an adequate description of the configuration space of a given periodic framework. For a couple of instances where global configuration spaces have been determined, we refer to [2, 3, 10]. In the present context, as we focus on periodic frameworks with two vertex orbits, we rely on a procedure initiated in [10].

   In arbitrary dimension d, a connected periodic framework with two vertex orbits and all edges with endpoints in different orbits is completely determined by a vertex and the edge vectors emanating from it. The endings of these vectors are all in the opposite orbit and the periodicity lattice is generated by vectors between pairs of such endings. We fix the first vertex at the origin and denote the edge vectors emanating from it by $v_i, i = 0, 1, \ldots, m - 1$. In dimension d, connectedness requires $m \geq d + 1$. We may and shall assume that the labeling is such that the period vectors $\mu_j = v_j - v_0$ form a basis of R^d for $j = 1, \ldots, d$. Then, period vectors $\mu_k = v_{k+1} - v_1, k > d$ have unique expressions with rational coefficients a_{ki}:

$$\mu_k = \sum_{i=1}^{d} a_{ki}\mu_i, \quad k > d \tag{18.1}$$

These relations must be preserved in any periodic deformation of the framework and together with the first $d + 1$ vectors v_i will determine the framework.

Up to isometry, the configuration of vectors $v_i \in R^d, i = 0, 1, \ldots, d$ is determined by their Gram matrix $G = V^t V$, where V is the $d \times (d + 1)$ matrix with column vectors v_i. This $(d + 1) \times (d + 1)$ symmetric matrix is positive semidefinite of rank d. If we take into account the prescribed squared lengths of the edges, say:

$$\langle v_i, v_i \rangle = s_i > 0 \tag{18.2}$$

we see that, as the framework deforms, the corresponding matrix $G = (g_{ij})$ belongs to the affine section of the positive semidefinite cone defined by $g_{ii} = s_i, i = 0, 1, \ldots, d$. This is a *spectrahedron* linearly equivalent whith the spectrahedron of *correlation matrices*, also known as the *elliptope*, which corresponds to all diagonal entries equal to one [17, 18, 23]. More precisely, G belongs to the boundary of this spectrahedron, which is part of the algebraic hypersurface of degree $d + 1$ given by the vanishing of the determinant. Now, we use the fact that relations (18.1) and (18.2) for $k > d$ amount to affine sections of the spectrahedron and obtain:

Theorem 18.3 *The configuration space of a connected periodic framework in R^d with two vertex orbits has a natural compactification as the boundary of a spectrahedron, which is itself linearly equivalent with an affine section of an elliptope. Topologically, this compactification is a sphere.*

This generalizes the result in Sect. 18.3, where the configuration space was a circle or a circle without a point.

18.5 Equations in Lattice Coordinates

Lattice coordinates are linear coordinates relative to a basis made of independent generators for the periodicity lattice [5, 12]. In crystallography they are called *fractional coordinates*. Suppose, as in Definition 18.4, that the chosen periodicity generators form the $d \times d$ matrix Λ, with associated Gram matrix $\omega = \Lambda^t \Lambda$. Metric relations in lattice coordinates are expressed via ω. For periodic frameworks with two vertex orbits, one orbit will be represented in lattice coordinates by the integer lattice Z^d and the other one by $q + Z^d$, for some $q \in R^d$. We have $(q, \omega) \in R^d \times R^{d(d+1)/2}$.

Relating to notations used in the previous sections, the period vectors μ_i become vectors $n_i \in Z^d$ and the vertex used there as origin has now lattice coordinates q. Thus, the edge vectors emanating from this vertex are $n_i - q, i = 0, 1, \ldots, m - 1$. The system of equations expressing the constancy of the squared length of the edges becomes:

$$\langle \omega(n_i - q), n_i - q \rangle = s_i \tag{18.3}$$

This gives:

$$\langle \omega n_i, n_i \rangle - 2\langle \omega q, n_i \rangle + \langle \omega q, q \rangle = s_i \tag{18.4}$$

and leads to the equivalent system:

$$\langle \omega q, q \rangle = s_0$$

$$2\langle \omega q, n_i \rangle = s_0 - s_i + \langle \omega n_i, n_i \rangle, \quad i = 1, \ldots, d \tag{18.5}$$

$$2\langle \omega q, n_j \rangle = s_0 - s_j + \langle \omega n_j, n_j \rangle, \quad j > d.$$

Expressing n_j, $j > d$, as linear combinations (with rational coefficients) of n_i, $i = 1, \ldots, d$ via (18.1), Eq. (18.5) can be used to eliminate ωq from the subsequent equations which become linear constraints just for ω.

Moreover, the system (18.5) can be used to write all coordinates of ωq as degree one expressions in the coordinates of ω. Substituting in the first equation and rewriting (18.5) as:

$$2\langle q, \omega n_i \rangle = s_0 - s_i + \langle \omega n_i, n_i \rangle, \quad i = 1, \ldots, d \tag{18.6}$$

we obtain a system of $d + 1$ equations in (q, ω), where ω is already restricted to the affine subspace described above. The equations have degree one in q as well as in ω.

If we return to the case $d = 2$, $m = 4$ of Sect. 18.3, we have a curve defined by three equations in $(q, \omega) \in R^2 \times R^2$. Projection on $q \in R^2$ gives a planar cubic curve and allows a graphical recognition of the auxetic intervals based on Theorem 18.2.

18.6 Conclusion

In this paper we studied the problem of finding auxetic regions in the global deformation space of a periodic framework. Points in such regions allow local auxetic one-parameter deformations. We focused on periodic frameworks with two vertex orbits in arbitrary dimension d, for which the case of planar frameworks associated to four-bar mechanisms served as an intuitive example. We described algebraic techniques and geometric perspectives for addressing the problem.

References

1. Bertoldi, K., Vitelli, V., Christensen, J., van Hecke, M.: Flexible mechanical metamaterials. Nat. Rev. Mater. **2**, 17066 (2017)
2. Borcea, C.S., Streinu, I.: Periodic frameworks and flexibility. Proc. Royal Soc. A **466**, 2633–2649 (2010)

3. Borcea, C.S., Streinu, I.: Flexible crystal frameworks. In: Proceedings Canadian Conference on Computational Geometry (CCCG 2012), Charlottetown, Prince Edward Island, Canada, Aug 2012. http://2012.cccg.ca/e-proceedings.pdf

4. Borcea, C.S., Streinu, I.: Minimally rigid periodic graphs. Bull. LMS **43**, 1093–1103 (2011). https://doi.org/10.1112/blms/bdr044

5. Borcea, C.S., Streinu, I.: Frameworks with crystallographic symmetry. Philos. Trans. Royal Soc. A **372**, 20120143 (2014). https://doi.org/10.1098/rsta.2012.0143

6. Borcea, C.S., Streinu, I. Kinematics of expansive planar periodic mechanisms. In: Advances in Robot Kinematics, $J. Lenar\check{c}i\check{c}$ and $O. Khatib$ editors, pp. 395–407. Springer (2014)

7. Borcea, C.S., Streinu, I.: Liftings and stresses for planar periodic frameworks. Discret. Comput. Geom. **53**, 747–782 (2015)

8. Borcea, C.S., Streinu, I.: Geometric auxetics. Proc. Royal Soc. A **471**, 20150033 (2015). https://doi.org/10.1098/rspa.2015.0033

9. Borcea, C.S., Streinu, I.: Expansive periodic mechanisms. In: IMA Conference on Mathematics of Robotics, 2015; preprint arXiv:1507.03132

10. Borcea, C.S., Streinu, I.: Deforming diamond. IMA J. Appl. Math. **82**(2), 371–383 (2017). https://doi.org/10.1093/imamat/hxw055

11. Borcea, C.S., Streinu, I.: New principles for auxetic periodic design. SIAM J. Appl. Algebra Geom. **1**(1), 442–458 (2017). https://doi.org/10.1137/16M1088259

12. Borcea, C.S., Streinu, I.: Periodic auxetics: structure and design. Q. J. Mech. Appl. Math. **71**(2), 125–138 (2018). https://doi.org/10.1093/qjmam/hbx028

13. Christensen, J., Kadic, M., Kraft, O., Wegener, M.: Vibrant times for mechanical metamaterials. MRS Commun. **5**, 453–462 (2015)

14. Greaves, G.N., Greer, A.L., Lakes, R., Rouxel, T.: Poisson's ratio and modern materials. Nat. Mater. **10**, 823–837 (2011)

15. Kolken, H.M.A., Zadpoor, A.A.: Auxetic mechanical metamaterials. RSC Adv. **7**, 5111–5129 (2017)

16. Lakes, R.S.: Negative-Poisson's-Ratio materials: auxetic solids. Annu. Rev. Mater. Res. **47**, 51–61 (2017)

17. Laurent, M., Poljak, S.: On the structure of the set of correlation matrices. SIAM J. Matrix Anal. Appl. **17**, 530–547 (1996)

18. Ottem, J-C., Ranestad, K., Sturmfels, B., Vinzant, C.: Quartic spectrahedra. Math. Programm. Ser. B, **151** (2):585–612 (2015)

19. Reis, P.M., Jaeger, H.M., van Hecke, M.: Designer matter: a perspective. Extreme Mech. Lett. **5**, 25–29 (2015)

20. Saxena, K.K., Das, R., Calius, E.P.: Three decades of auxetics research: Materials with negative Poisson's ratio: a review. Adv. Eng. Mater. **18**(11), 1847–1870 (2016)

21. Streinu, I.: Pseudo-triangulations, rigidity and motion planning. Discret. Comput. Geom. **34**, 587–635 (2005)

22. Sunada, T.: Topological Crystallography. Springer, Japan (2013)

23. Vinzant, C.: What is ... a spectrahedron? Notices AMS **61**, 492–494 (2014)

24. Zang, J., Lu, G., Wang, Z., Ruan, D., Alomarah, A., Durandet, Y.: Large deformation of an auxetic structure in tension: experiments and finite element analysis. Compos. Struct. **184**, 92–101 (2017)

Chapter 19
Singularity Analysis of a Spherical Robot Used in Upper Limb Rehabilitation

I. Birlescu, C. Vaida, A. Pisla, G. Carbone and D. Pisla

Abstract The paper presents the singularity analysis of a spherical robot with parallel architecture. This robot has been designed for the upper limb rehabilitation. Thus, singularity analysis is carried out for validating the robotic structure to the motion needs of the rehabilitation exercises. Singularities are derived from the forward kinematics using the Study parameters of SE(3) and the near singularity poses are evaluated in order to determine the motion capabilities in the whole robot workspace. A simulated motion is presented near the robot singular configuration.

19.1 Introduction

The progress of medical treatments has significantly reduced the lethality rate of many diseases such as stroke. At same time the number of patients that need post incident rehabilitation continues to increase. This is also due to the aging of population where the main target group for strokes including people aged 65 and older is forecast to achieve a 30% increase in Europe by 2060 [1]. Medical specialists and facilities focusing on post-stroke rehabilitation will be overwhelmed by the sheer number of patients coming in. Dealing with this boom of patients requires to increase the efficiency and effectiveness of rehabilitation also by means of robotic rehabilitation

I. Birlescu · C. Vaida · A. Pisla · D. Pisla (✉)
Technical University Cluj-Napoca, Cluj-Napoca, Romania
e-mail: doina.pisla@mep.utcluj.ro

I. Birlescu
e-mail: iosif.birlescu@mep.utcluj.ro

C. Vaida
e-mail: calin.vaida@mep.utcluj.ro

A. Pisla
e-mail: adrian.pisla@muri.utcluj.ro

G. Carbone
University of Calabria, Rende, Italy
e-mail: carbone@unical.it

[2–4]. These devices not only can cope with the shortage of physiotherapists but they can also provide longer and more frequent therapy sessions per patient while also allowing the therapist to remotely supervise the training of more than one patient at a time as discussed in [3–6]. However, these robotic devices require a very careful design where proper operation and safety are key issues.

A specific problem for safe operation of robotic devices is the identification and avoidance of singularities. Singularity analysis can be achieved mathematically with different methods, such as vector methods or algebraic methods, both used previously in kinematics and singularity study of medical robots such as in [7, 8]. An interesting method to solve the forward kinematics and singularities is based on the Study parameters of SE(3) [9]. This algebraic method based on quaternions, proved to be very efficient in describing the singularities of parallel robots, and may suggests more singularities (although some of them are theoretical as not physically reachable) which are not identifiable by classical vector methods, such as in [7]. By using the Study parameters of SE(3) there is more confidence in finding the singular poses and investigate their influence in the robot functionality.

This paper describes the singularity analysis of the ASPIRE parallel robot used in upper limb rehabilitation, by means of the forward kinematics and the Study parameters of SE(3), and it presents an evaluation of the near singularity poses, with a focus at the motion capabilities of the robot correlated with the rehabilitation exercises. The paper is structured as follows: Sect. 19.2 presents the ASPIRE robotic system based on the motion requirements, the robot kinematic scheme, and derives the forward kinematics based on Study parameters. Section 19.3 derives the singularity conditions and presents near singularity behavior analysis with a motion simulation near the edge of the workspace where the moving platform may be considered near a singular configuration. Section 19.4 presents the conclusions of this study.

19.2 ASPIRE, a Spherical Robot for Upper Limb Rehabilitation

In order to define the preliminary design requirements for the robotic structures used in the upper limb rehabilitation, the rehabilitation exercises motions are discussed. The most common motions around the shoulder are the up and down arm movement in plane parallel with the *sagittal* or the *frontal* plane of the human body, and the left and right movement in plane parallel with the *transversal* plane of the human body [4, 10].

The ASPIRE robot used for upper limb rehabilitation (patent pending [11]) is a spherical robot with a parallel structure with 2 degrees of freedom (DOF) for each required motion along sagittal, frontal, and transversal planes. The kinematic scheme of the robot is presented in Fig. 19.1a. By fixing a coordinate system OXYZ into the rotation center of the shoulder (with OX axis pointing in front of the patient, the OZ axis above the patient), the base coordinate system is defined. A second
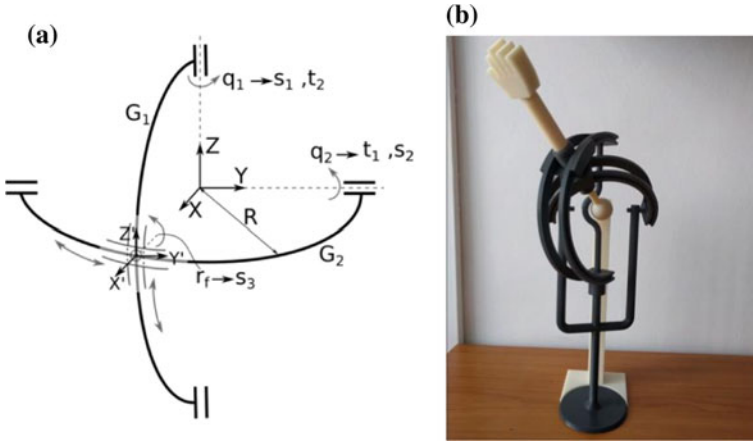
Fig. 19.1 ASPIRE robotic system [6]; **a** Kinematic scheme; **b** 3D printed design

coordinate system is introduced for the mobile platform denoted O'X'Y'Z' as shown in Fig. 19.1a. The mobile platform serves as the anchor point for the forearm thus allowing the motion of the arm when the robot is actuated. The 2 DOF are as follows: q_1 is a rotation around OZ axis, and q_2 is a rotation around OX axis. It can be seen in Fig. 19.1a that the moving platform position is based on the intersection of two geodesics which describe geometrically the two kinematic chains. An initial design of the ASPIRE robot is presented in Fig. 19.1b [6] (not to scale) with the geodesics being circular rails and the moving platform composed of 2 linked sledges.

The geodesics can rotate only around one axis of the sphere defining the mechanism (G_1 around OZ, and G_2 around OY according to Fig. 19.1). Consequently the angle between the two geodesics (β) which may be defined as the angle between the normal vectors ($\vec{v}_1$ and $\vec{v}_2$) of the planes containing the geodesics (Eq. 19.1) is variable as shown by Eq. 19.2. The denominator of Eq. 19.2 will always be 1 and for example if $q_1 = q_2 = \pi/4$, $\beta = 60°$, while for the initial conditions ($q_1 = q_2 = 0$) $\beta = 90°$.

$$\vec{v}_1 = \sin(q_1)\hat{x} + \cos(q_1)\hat{y}$$
$$\vec{v}_2 = \sin(q_2)\hat{x} - \cos(q_2)\hat{z} \qquad (19.1)$$

$$\beta = \arccos\left(\frac{\vec{v}_1 . \vec{v}_2}{\|v_1\| \cdot \|v_2\|}\right) \qquad (19.2)$$

For the reason stated above, it is necessary that the robot design allows one free DOF at the intersection of the two kinematic chains (i.e. a free rotation around O'X'). In order to solve the forward kinematic problem and compute the singularities the Study parameters of SO(3) are used. Simpler methods were used to solve the forward kinematics, such as using the spherical coordinates based on the active joints, as in [4],

however these methods did not provide enough information about the singularities, as the velocity Jacobians in that computation were the identity matrix suggesting no singularities. Accordingly, an alternative method was used based on algebraic geometry (the Study method).

For the Study model of forward kinematics, two kinematic chains are defined. The first kinematic chain is geometrically described by the G_1 curve, and it has 3 DOF (one active defined by q_1, and two passive ones defined by q_2 and r_f), while the second kinematic chain is defined by G_2 and has 2 DOF (q_2 active and q_1 passive). Since one rotation for both kinematic chains will be around an arbitrary axis (e.g. after rotating G_1 around OZ the next rotation should be around OY and not O'Y') the generalized rotation matrix (Eg. 3) is used. Note that for the computation, homogenous matrices were used in the form described in Eq. 19.4, where t is column vector and R is a proper orthogonal matrix.

$$ROT = \begin{bmatrix} x_0^2 + (y_0^2 + z_0^2)c(\alpha) & x_0y_0(1 - c(\alpha)) - z_0s(\alpha) & x_0z_0(1 - c(\alpha)) + ys(\alpha) \\ x_0y_0(1 - c(\alpha)) + z_0s(\alpha) & y_0^2 + (x_0^2 + z_0^2)c(\alpha) & y_0z_0(1 - c(\alpha)) - x_0s(\alpha) \\ x_0z_0(1 - c(\alpha)) - ys(\alpha) & y_0z_0(1 - c(\alpha)) + x_0s(\alpha) & z_0^2 + (x_0^2 + y_0^2)c(\alpha) \end{bmatrix}$$
(19.3)

$$Mat = \begin{bmatrix} 1 & 0 \\ t & R \end{bmatrix}$$
(19.4)

The vector $v(x_0, y_0, z_0)$ in Eq. (19.3) is the unit vector defining the rotation axis and α is the angle of rotation in radians. The constraints for the both kinematic chains are defined in 4×4 homogeneous matrices as follows:

$$K_1 = R_{OZ}(q_1) \cdot ROT_{OY}(q_2) \cdot T_X(R) \cdot R_{O'X'}(r_f)$$
(19.5)

$$K_2 = R_{OY}(q_2) \cdot ROT_{OZ}(q_1) \cdot T_X(R)$$
(19.6)

where K_1 are the constraints of the first kinematic chain, K_2 are the constraints of the second kinematic chain, $R_{OZ}(q_1)$ and R_{OY} the rotation matrices around OZ and OY axes with an angle defined by q_1 and q_2. $ROT_{OY}(q_2)$ is the matrix ROT evaluated with $\{\alpha = q_1, x_0 = \sin(q_2), y_0 = \cos(q_2), z_0 = 0\}$, $ROT_{OZ}(q_1)$ is the matrix ROT evaluated with $\{\alpha = q_2, x_0 = -\sin(q_1), y_0 = 0, z_0 = \cos(q_1)\}$, and finally R is the radius of the sphere and r_f is a free rotation around O'X'.

The Study parameters of SO(3) are extracted from Eqs. (19.5) and (19.6) after substituting the trigonometric functions with the tangent of half angle formulae: $cos(q_{1,2}) = (1 - s_{1,2}^2)/(1 + s_{1,2}^2)$, $sin(q_{1,2}) = 2s_{1,2}^2/(1 + s_{1,2}^2)$, $cos(r_f) = (1 - s_3^2)/(1 + s_3^2)$, $sin(r_f) = 2 s_3^2/(1 + s_3^2,)$ for the first kinematic chain, and $cos(q_{1,2}) = (1 - t_{2,1}^2)/(1 + t_{2,1}^2)$, $sin(q_{1,2}) = 2t_{2,1}^2/(1 + t_{2,1}^2)$, for the second kinematic chain. The methods of extracting the Study parameters from a homogenous transformation matrix are described in [9] (Eqs. (19.6) and (19.7)), the result for K_1 and K_2 being presented below (note that the $x_0:x_1:x_2:x_3$ describe a rotation and $y_0:y_1:y_2:y_3$ describe a displacement):

$$
\begin{bmatrix} x_0 \\ x_1 \\ x_2 \\ x_3 \\ y_0 \\ y_1 \\ y_2 \\ y_3 \end{bmatrix} = \begin{bmatrix} 2 \cdot s_1 \cdot s_2 \cdot s_3 - 2 \\ -2 \cdot s_1 \cdot s_2 - 2 \cdot s_3 \\ -2 \cdot s_1 \cdot s_3 - 2 \cdot s_2 \\ -2 \cdot s_1 + 2 \cdot s_3 \cdot s_2 \\ -(s_1 \cdot s_2 + s_3) \cdot R \\ -(s_1 \cdot s_2 \cdot s_3 - 1) \cdot R \\ (s_1 - s_2 \cdot s_3) \cdot R \\ -(s_1 \cdot s_3 + s_2) \cdot R \end{bmatrix}
\tag{19.7}
$$

$$
\begin{bmatrix} x_0' \\ x_1' \\ x_2' \\ x_3' \\ y_0' \\ y_1' \\ y_2' \\ y_3' \end{bmatrix} = \begin{bmatrix} 2 \\ -2 \cdot t_1 \cdot t_2 \\ 2 \cdot t_1 \\ 2 \cdot t_2 \\ -t_1 \cdot t_2 \cdot R \\ -R \\ -t_2 \cdot R \\ t_1 \cdot R \end{bmatrix}
\tag{19.8}
$$

Equation (19.7) describes the Study parameters for the first kinematic chain, while Eq. (19.8) for the second kinematic chain. The known parameters will be t_1, s_1, and R as they describe the active joints parameters (q_1 and q_2) and the sphere radius. Two ideals of varieties are generated over the Study parameters, I for Eq. (19.7) and I' for Eq. (19.8), and two lexdeg Gröbner bases are computed eliminating the unknown parameters and obtaining the implicit equations of the two kinematic chains (B for I and B' for I'):

$$
\begin{aligned}
B = [& Rx_3 + 2y_2; \; -2y_3 + x_2 R; \; Rx_1 - 2y_0; \; x_0 R + 2y_1; \\
& (-s_1^2 - 1)y_3 y_0 + s_1 y_0^2 + (-s_1^2 - 1)y_2 y_1 + s_1 y_2 + s_1 y_3]
\end{aligned}
\tag{19.9}
$$

$$
\begin{aligned}
B' = [& y_3 + y_1 t_1; \; -t_1 y_2 + y_0; \; Rx_3 + 2y_2; \; -2y_3 + Rx_2; \\
& - 2t_1 y_2 + Rx_1; \; Rt_1 x_0 - 2y_3]
\end{aligned}
\tag{19.10}
$$

The two bases of the ideals have the Study parameters as variables, and to solve the forward kinematic problems, the "intersection" between the varieties described by the bases should be computed. The base B' can be linearly solved (first 3 equations and the last one) for y_i yielding a set of solutions:

$$
\left\{ y_0 = -\frac{1}{2} Rt_1 x_3; \; y_1 = -\frac{1}{2} Rx_0; \; y2 = -\frac{1}{2} Rx_3; \; y_3 = \frac{1}{2} Rt_1 x_0 \right\}
\tag{19.11}
$$

The solution from Eq. (19.11) can be substituted into Eq. (19.9) and a pure lexicographic Gröbner basis (B^*) is computed. Although not presented in this paper due to its length, the final basis represents the constraints of the mechanism as a whole. One

can solve B^* for x_i after inserting numerical values for the active joint parameters (t_1 and s_1) and by back-substituting Eq. (19.11) into the results the numerical values for Study parameters are reviled (and solving thus the forward kinematics). Two unique solutions for the Study parameters are obtained (there are a total of 4 solutions but 2 of them are the other 2 multiplied by -1) suggesting two working modes, which are expected as the defined geodesics may be viewed as whole circles which intersect in two points on the sphere. However only one working mode is possible on the ASPIRE robot as it is mechanically constrained to function only on one side of the sphere since the moving platform cannot pass through a rotation joint of the robot (see Fig. 19.1). The final basis B^* will be used further in analyzing the singularities in Sect. 19.3.

19.3   Singularity Analysis

In this section the singularity equations are derived, and the behavior of near singularity positions is discussed. For a parallel robot when a singularity occurs, the robot may lose its control instantaneously by gaining or losing one or more DOF. Mathematically, one way to derive the singularities is by investigating the cases were two or more solutions to the forward kinematics coincide. The basis B^* contains a univariate polynomial in x_3. In order to obtain the singularities the discriminant of the univariate polynomial is computed (when the discriminant vanishes one or more solutions coincide) by taking the resultant of the univariate polynomial with its first derivative in x_3. The computed resultant was returned by Maple software as a product of 5 factors which are presented as the singularity conditions in the form

$$s_1^2 - 1 = 0 \tag{19.12}$$

$$t_1 - 1 = 0 \tag{19.13}$$

$$t_1 + 1 = 0 \tag{19.14}$$

$$s_1^2 + 1 = 0 \tag{19.15}$$

$$-t_1^6 - t_1^6 s_1^4 + 2t_1^6 s_1^2 + t_1^4 s_1^4 + t_1^4 + 14t_1^4 s_1^2 + t_1^2 + t_1^2 s_1^4 + 2s_1^2 - s_1^4 - 1 = 0 \tag{19.16}$$

Equations (19.12)–(19.14) imply the robot is in singular pose when the active joints q_1 or q_2 are actuated at $\pm 90°$ (similar to a gimbal lock). In that configuration the moving platform loses one DOF. Equation 19.15 does not have real solutions and it's not of interest. Solving Eq. 19.16 for s_1 and evaluating the solutions for $s_1 = 0$ leads to $t_1 = \pm 1$ which is analog to Eqs. (19.12)–(19.14). When both q_1 and q_2
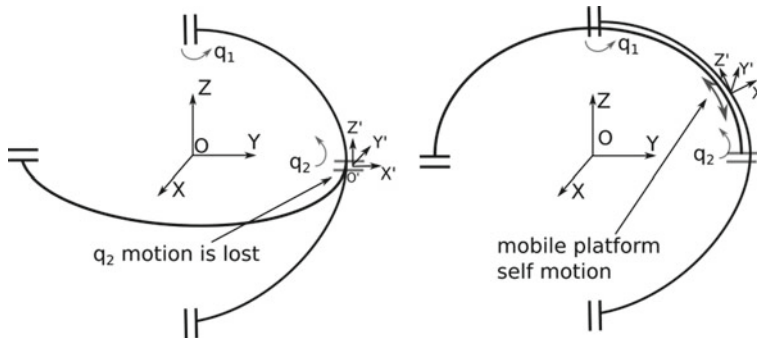
Fig. 19.2 Singularity poses for the ASPIRE robot

Fig. 19.3 Near singularity behavior. t_1 behavior as s_1 approaches a singularity
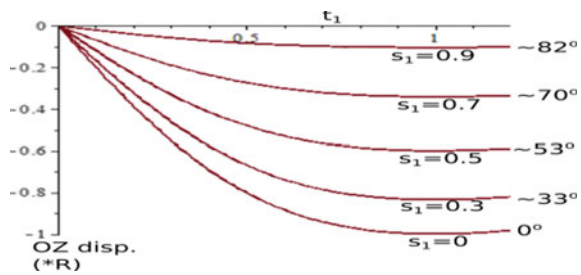
are actuated at $\pm 90°$ (the two geodesics are in the same plane) the moving platform acquires self-motion. These configurations are illustrated in Fig. 19.2.

The singularity poses presented in Fig. 19.2 are avoided in the ASPIRE robotic system by constraining the mechanism so that the moving platform never reaches those configurations. Even if no mechanical constraint was used, the singularities may be avoided by imposing stroke limits for the active joints in the control system. Further, the behavior of near singularity is investigated and correlated with the motion imposed by the rehabilitation exercises.

To evaluate how the mechanism behaves near singularities and the consequences to the rehabilitation exercises, the relative OZ displacement of the moving platform (relative to the fixed coordinate frame) was chosen, and five scenarios were evaluated, with different s_1 parameter values (as s_1 approached singularity).

The results are plotted in Fig. 19.3, where it is pointed how t_1 parameter flattens and the OZ displacement is lost as s_1 goes to 1. The angles in degrees shown in Fig. 19.3 represent the values of the active joint q_1 from the starting position.

For the common rehabilitation exercises the mechanism should be viable as the required motion for the rehabilitation exercises are not passing through singularities. From the starting position (arm pointing in front of the patient) the robot performs the left/right motion and up/down with ease until it reaches the boundary of its workspace. One particular motion exercise is where the arm is placed near the patient body on a vertical position, and it is moved up and down remaining in the frontal plane of the
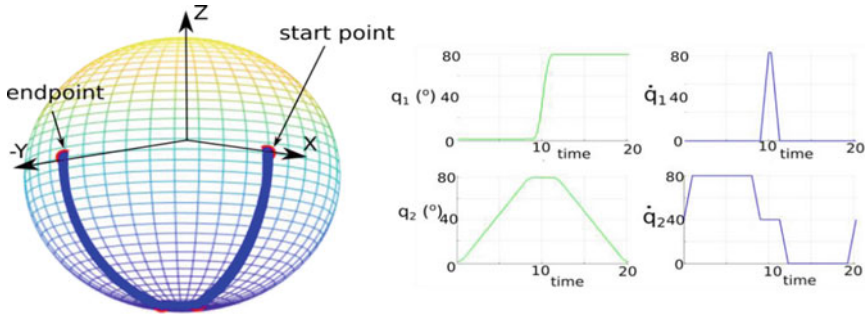
Fig. 19.4 MATLAB simulation of a trajectory near the edge of the workspace

patient. It is easy to observe that for the kinematic scheme in Fig. 19.1 this motion has to start from a singular pose as the active joint q_2 has to be actuated until 90°. By imposing limits in the mechanical components or in the active joint values in the robot control (e.g. $-0.9 < s_1, t_1 < 0.9$) a version of the discussed rehabilitation motion (near the edge of the workspace) is possible. Figure 19.4 illustrates this motion and the displacement function of the active joints during the motion. It is visible that for q_1, there still is a bad behavior at time $= 10$ (the velocity spikes).

19.4 Conclusions

This paper reports the singularity analysis of ASPIRE robot, which is a spherical robot with parallel architecture for upper limb rehabilitation. Singularity conditions are derived by using Study parameters. A near singularity analysis is performed to evaluate the motion capabilities of the robot at the edge of the workspace. Due to its mechanical constraints the ASPIRE robot cannot reach any singular pose. However, a limitation on the motion range of active joints (e.g. until near $\pm 80°$) can allow the robot to perform reliably most of the common exercises in upper limb rehabilitation.

References

1. Robotics 2020 Multi-Annual Roadmap, Call 2 ICT24 (2015) – Horizon 2020 (2015)
2. Stein, J.: Robotics in rehabilitation: technology as destiny. Am. J. Phys. Med. Rehab. **91**(11) (Supplement 3), S199–S203 (2012)
3. Reinkensmeyer, D.J., Boninger, M.L.: Technologies and combination therapies for enhancing movement training for people with a disability. J. Neuroeng. Rehab. (2011)
4. Plitea, N., Vaida, C., Carbone, G., Pisla, A., Ulinici, I., Pisla, D.: On the kinematics of an innovative spherical parallel robot for shoulder rehabilitation. In: Carvalho, J., Martins, D., Simoni, R., Simas, H. (eds.), Multibody Mechatronic Systems. MuSMe 2017. Mechanisms and Machine Science, vol. 54. Springer, Cham (2017)
5. Vaida, C., Carbone, G., Maior, K., Maior, Z., Plitea, N., Pisla, D.: On human robot interaction modalities in the upper limb rehabilitation after stroke. ACTA TECHNICA NAPOCENSIS, Appl. Math. Mech. Eng. **60**(I) (2017)
6. Vaida, C., Carbone, G., Plitea, N., Pisla, D.: Preliminary design for a spherical parallel robot for shoulder rehabilitation. In: The 12th IFToMM International Symposium on Science of Mechanisms and Machines—SYROM 2017. Iaşi, România, 02–03 November, 2017
7. Vaida, C., Pisla, D., Schadlbauer, J., Husty, M., Plitea, N.: Kinematic analysis of an innovative medical parallel robot using Study parameters. In: New Trends in Medical and Service Robots. Mechanisms and Machine Science, vol. 39, pp. 85–99. Springer (2016)
8. Birlescu, I., Tucan, P., Gherman, B., Vaida, C., Crisan, N., Radu, C., Plitea, N., Pisla, D.: Kinematic analysis for a prostate biopsy parallel robot using Study parameters. In: Computational Kinematics. Mechanisms and Machine Science, vol 50. Springer, Cham (2018)
9. Husty, M., Pfurner, M., Schroecker, H.-P., Brunnthaler, K.: Algebraic methods in mechanism analysis and synthesis. Robotica **25**(6), 661–675 (2007)
10. Drake, R., et al.: Gray's Anatomy for students. 2 edn Churchill Livingstone, Elsevier. pp. 910–912. eBook ISBN: 9781437720556 (2009)
11. Vaida, C., Plitea, N., Pisla, D., Carbone, G., Gherman, B., Ulinici, I.: Spherical robot for the medical rehabilitation of the proximal area of the upper limb. OSIM patent pending: A00374/14.06.2017 (2017)

Chapter 20
Higher-Order Kinematics of Rigid Bodies. A Tensors Algebra Approach

Daniel Condurache

Abstract The problem of determining the tensors and the vector invariants that describe the vector field of the nth order accelerations is generally avoided in rigid body kinematics. This paper extends the discussion from velocities and accelerations to nth order accelerations. Using the tensor calculus and the dual numbers algebra, a computing method for studying the nth order acceleration field properties is proposed for the case of the general motion of the rigid body. This approach uses the isomorphism between the Lie group of the rigid displacements $S\mathbb{E}_3$ and the Lie group of the orthogonal dual tensors $\underline{S\mathbb{O}}_3$.

20.1 Velocity and Acceleration Fields in Rigid Body Motion

The general framework of this paper is a rigid body that moves with respect to a fixed reference frame $\{\Re^0\}$. Consider another reference frame $\{\Re\}$ originated at a point Q that moves together with the rigid body. Let $\boldsymbol{\rho}_Q$ denote the position vector of point Q with respect to the frame $\{\Re^0\}$, $\mathbf{v}_Q$ its absolute velocity and $\mathbf{a}_Q$ its absolute acceleration.

The vector parametric equation of motion is:

$$\boldsymbol{\rho} = \boldsymbol{\rho}_Q + \mathbf{R}\mathbf{r}, \tag{20.1}$$

where $\boldsymbol{\rho}$ represents the absolute position of a generic point P of the rigid body with respect to $\{\Re^0\}$ and $\mathbf{R} = \mathbf{R}(t)$ is an orthogonal proper tensorial function in $\mathbf{SO}_3^{\mathbb{R}}$ [2, 5]. Vector $\mathbf{r}$ is constant and it represents the relative position vector of the arbitrary point P with respect to $\{\Re\}$.

The results of this section succinctly present the velocity and acceleration vector field in rigid body motion. These results lead to the generalization presented in the next section.

D. Condurache (✉)
Technical University of Iasi, D. Mangeron Street no. 59, 700050 Iasi, Romania
e-mail: daniel.condurache@tuiasi.ro; daniel.condurache@gmail.com

With the notations that were introduced, the vector fields of velocities and accelerations are described by:

$$\begin{cases} \mathbf{v} - \mathbf{v}_Q = \dot{\mathbf{R}}\mathbf{R}^T (\boldsymbol{\rho} - \boldsymbol{\rho}_Q) \\ \qquad \text{and} \\ \mathbf{a} - \mathbf{a}_Q = \ddot{\mathbf{R}}\mathbf{R}^T (\boldsymbol{\rho} - \boldsymbol{\rho}_Q) \end{cases} \tag{20.2}$$

respectively.

The tensors:

$$\begin{cases} \boldsymbol{\Phi}_1 = \dot{\mathbf{R}}\mathbf{R}^T \\ \boldsymbol{\Phi}_2 = \ddot{\mathbf{R}}\mathbf{R}^T \end{cases} \tag{20.3}$$

represent the **velocity tensor** and the **acceleration tensor**, respectively [2, 5]. The tensor $\boldsymbol{\Phi}_1 = \tilde{\boldsymbol{\omega}} \in \mathbf{so}_3^{\mathbb{R}}$ is the skew-symmetric tensor associated to the instantaneous angular velocity $\boldsymbol{\omega} \in \mathbf{V}_3^{\mathbb{R}}$. The tensor $\boldsymbol{\Phi}_2 = \tilde{\boldsymbol{\omega}}^2 + \tilde{\boldsymbol{\varepsilon}}$, where $\boldsymbol{\varepsilon} = \dot{\boldsymbol{\omega}}$ is the instantaneous angular acceleration of the rigid body. One may remark that the vectors:

$$\begin{cases} \mathbf{a}_1 = \mathbf{v} - \boldsymbol{\Phi}_1 \boldsymbol{\rho} = \mathbf{v}_Q - \boldsymbol{\Phi}_1 \boldsymbol{\rho}_Q \\ \mathbf{a}_2 = \mathbf{a} - \boldsymbol{\Phi}_2 \boldsymbol{\rho} = \mathbf{a}_Q - \boldsymbol{\Phi}_2 \boldsymbol{\rho}_Q \end{cases} \tag{20.4}$$

do not depend on the choice of point P of the rigid body. They are called the **velocity invariant** respectively the **acceleration invariant** (at a given moment of time) [5].

The velocity field in rigid body motion is described by:

$$\mathbf{v} - \mathbf{v}_Q = \boldsymbol{\Phi}_1 (\boldsymbol{\rho} - \boldsymbol{\rho}_Q). \tag{20.5}$$

The instantaneous angular velocity $\boldsymbol{\omega}$ of the rigid body may be determined as $\boldsymbol{\omega} = \text{vect}\,\boldsymbol{\Phi}_1$. The major property that may be highlighted from Eq. (20.4) is that the velocity of a given point of the rigid body may be computed when the velocity tensor $\boldsymbol{\Phi}_1$ and the velocity invariant $\mathbf{a}_1$ are known:

$$\mathbf{v} = \mathbf{a}_1 + \boldsymbol{\Phi}_1 \boldsymbol{\rho}. \tag{20.6}$$

The acceleration field in rigid body motion is described by

$$\mathbf{a} - \mathbf{a}_Q = \boldsymbol{\Phi}_2 (\boldsymbol{\rho} - \boldsymbol{\rho}_Q). \tag{20.7}$$

The absolute acceleration of a given point of the rigid body may be computed when the acceleration tensor $\boldsymbol{\Phi}_2$ and the acceleration invariant $\mathbf{a}_2$ are known:

$$\mathbf{a} = \mathbf{a}_2 + \boldsymbol{\Phi}_2 \boldsymbol{\rho}. \tag{20.8}$$

20.2   The Vector Field of the nth Order Accelerations

This section extends some of the previous considerations to the case of the nth order accelerations, $n \in \mathbb{N}^*$. We define the nth order acceleration of a point as:

$$\mathbf{a}_{\boldsymbol{\rho}}^{[n]} \underset{=}{\mathrm{def}} \frac{d^n}{dt^n} \boldsymbol{\rho}, \, n \geq 1. \tag{20.9}$$

For $n = 1$ it represents the velocity and for $n = 2$ the acceleration. By taking successive time derivatives in Eq. (20.2), it follows that:

$$\mathbf{a}_{\boldsymbol{\rho}}^{[n]} - \mathbf{a}_Q^{[n]} = \mathbf{R}^{(n)} \mathbf{R}^T (\boldsymbol{\rho} - \boldsymbol{\rho}_Q), \text{ where } \mathbf{R}^{(n)} \underset{=}{\mathrm{def}} \frac{d^n}{dt^n} \mathbf{R}. \tag{20.10}$$

We denote as:

$$\boldsymbol{\Phi}_n = \mathbf{R}^{(n)} \mathbf{R}^T \tag{20.11}$$

the **nth order acceleration tensor** in rigid body motion. With this notation, a vector invariant can be emphasized in Eq. (20.10). Thus, the vector:

$$\mathbf{a}_n = \mathbf{a}_{\boldsymbol{\rho}}^{[n]} - \boldsymbol{\Phi}_n \boldsymbol{\rho} = \mathbf{a}_Q^{[n]} - \boldsymbol{\Phi}_n \boldsymbol{\rho}_Q \tag{20.12}$$

does not depend on the choice of the point of the rigid body for which the acceleration $\mathbf{a}^{[n]}$ is computed. The vector $\mathbf{a}_n$ is named the **invariant vector** of the **nth order accelerations**. Then Eq. (20.7) may be generalized as follows:

$$\mathbf{a}_{\boldsymbol{\rho}}^{[n]} - \mathbf{a}_Q^{[n]} = \boldsymbol{\Phi}_n (\boldsymbol{\rho} - \boldsymbol{\rho}_Q). \tag{20.13}$$

The next Theorem gives the fundamental properties of the vector fields of the nth order accelerations.

Theorem 20.1 *In the rigid body motion, at a moment of time t, there exist a tensor* $\boldsymbol{\Phi}_n$ *defined by* Eq. (20.11) *and a vector* $\mathbf{a}_n$, *such that:*

$$\mathbf{a}_{\boldsymbol{\rho}}^{[n]} - \mathbf{a}_Q^{[n]} = \boldsymbol{\Phi}_n (\boldsymbol{\rho} - \boldsymbol{\rho}_Q)$$
$$\mathbf{a}_n = \mathbf{a}_{\boldsymbol{\rho}}^{[n]} - \boldsymbol{\Phi}_n \boldsymbol{\rho} = \mathbf{a}_Q^{[n]} - \boldsymbol{\Phi}_n \boldsymbol{\rho}_Q$$

for any point P of the rigid body with the absolute position defined by the vector $\boldsymbol{\rho}$.

Remark 20.1 Given the absolute position of a point of the rigid body and knowing $\boldsymbol{\Phi}_n$ *and* $\mathbf{a}_n$, its nth order acceleration can be calculated as:

$$\mathbf{a}_{\boldsymbol{\rho}}^{[n]} = \mathbf{a}_n + \boldsymbol{\Phi}_n \boldsymbol{\rho}.$$

Remark 20.2 The tensor $\mathbf{\Phi}_n$ and the vector $\mathbf{a}_n$ generalize the notions of velocity/acceleration tensor and velocity / acceleration invariant, respectively. They are fundamental in the study of the vector field of the nth order accelerations. The recursive formulas for computing $\mathbf{\Phi}_n$ and $\mathbf{a}_n$ are:

$$\begin{cases} \mathbf{\Phi}_{n+1} = \dot{\mathbf{\Phi}}_n + \mathbf{\Phi}_n \mathbf{\Phi}_1 \\ \mathbf{a}_{n+1} = \dot{\mathbf{a}}_n + \mathbf{\Phi}_n \mathbf{a}_1 \end{cases}, n \geq 1, where \; \mathbf{\Phi}_1 = \tilde{\mathbf{\omega}}, \mathbf{a}_1 = \mathbf{v}_Q - \mathbf{\Phi}_1 \mathbf{\rho}_Q \underline{\underline{def}} \mathbf{v}. \quad (20.14)$$

Remark 20.3 One may remark that from Eq. (20.14) it follows by direct computation:

$$\begin{cases} \mathbf{\Phi}_n = \mathbf{\Phi}_{n-1}\mathbf{\Phi}_1 + \left(\frac{d^{n-1}}{dt^{n-1}}\mathbf{\Phi}_1\right) + \sum_{k=1}^{n-2}\left[\frac{d^k}{dt^k}(\mathbf{\Phi}_{n-k-1}\mathbf{\Phi}_1)\right] \\ \mathbf{a}_n = \mathbf{\Phi}_{n-1}\mathbf{a}_1 + \left(\frac{d^{n-1}}{dt^{n-1}}\mathbf{a}_1\right) + \sum_{k=1}^{n-2}\left[\frac{d^k}{dt^k}(\mathbf{\Phi}_{n-k-1}\mathbf{a}_1)\right] \end{cases}, n \geq 3. \quad (20.15)$$

20.2.1 Homogenous Matrix Approach to the Field of nth Order Accelerations

The set of affine maps $g : \mathbf{V}_3 \to \mathbf{V}_3$, $g(\mathbf{u}) = \mathbf{R}\mathbf{u} + \mathbf{w}$, where $\mathbf{R}$ is an orthogonal proper tensor and $\mathbf{w}$ a vector in $\mathbf{V}_3$ is a group under composition of maps and it is called *the Lie group of rigid displacement* and is denoted with $S\mathbb{E}_3$. Such a map may describe any rigid finite motion. The tensor $\mathbf{R}$ models the rotation of the considered rigid body and the vector $\mathbf{w}$ its translation. An affine map from $S\mathbb{E}_3$ may be represented as a 4×4 square matrix [2]:

$$g = \begin{bmatrix} \mathbf{R} & \mathbf{w} \\ \mathbf{0} & 1 \end{bmatrix}. \quad (20.16)$$

One may remark that the following relations hold true:

$$\begin{cases} \begin{bmatrix} \mathbf{R}_1 & \mathbf{w}_1 \\ \mathbf{0} & 1 \end{bmatrix}\begin{bmatrix} \mathbf{R}_2 & \mathbf{w}_2 \\ \mathbf{0} & 1 \end{bmatrix} = \begin{bmatrix} \mathbf{R}_1\mathbf{R}_2 & \mathbf{R}_1\mathbf{w}_2 + \mathbf{w}_1 \\ \mathbf{0} & 1 \end{bmatrix} \\ \begin{bmatrix} \mathbf{R} & \mathbf{w} \\ \mathbf{0} & 1 \end{bmatrix}^{-1} = \begin{bmatrix} \mathbf{R}^T & -\mathbf{R}^T\mathbf{w} \\ \mathbf{0} & 1 \end{bmatrix} \end{cases}. \quad (20.17)$$

We may extend now $S\mathbb{E}_3$ to $S\mathbb{E}_3^{\mathbb{R}}$, the set of the functions with the domain $\mathbb{R}$ and the codomain $S\mathbb{E}_3$. The parametric vector equation of the rigid body motion (20.1) may be rewritten with the help of a homogenous matrix function in $S\mathbb{E}_3^{\mathbb{R}}$:

$$\begin{bmatrix} \mathbf{\rho} \\ 1 \end{bmatrix} = \begin{bmatrix} \mathbf{R} & \mathbf{\rho}_Q \\ \mathbf{0} & 1 \end{bmatrix}\begin{bmatrix} \mathbf{r} \\ 1 \end{bmatrix}. \quad (20.18)$$

From Eq. (20.18) it results that:

$$\begin{bmatrix} \dot{\boldsymbol{\rho}} \\ 0 \end{bmatrix} = \begin{bmatrix} \dot{\mathbf{R}} & \dot{\boldsymbol{\rho}}_Q \\ \mathbf{0} & 0 \end{bmatrix} \begin{bmatrix} \mathbf{r} \\ 1 \end{bmatrix} = \begin{bmatrix} \dot{\mathbf{R}} & \dot{\boldsymbol{\rho}}_Q \\ \mathbf{0} & 0 \end{bmatrix} \begin{bmatrix} \mathbf{R}^T & -\mathbf{R}^T \boldsymbol{\rho}_Q \\ \mathbf{0} & 1 \end{bmatrix} \begin{bmatrix} \boldsymbol{\rho} \\ 1 \end{bmatrix} \quad (20.19)$$

and by making the computations and taking into account Eqs. (20.3) and (20.4) it follows that:

$$\begin{bmatrix} \dot{\boldsymbol{\rho}} \\ 0 \end{bmatrix} = \begin{bmatrix} \boldsymbol{\Phi}_1 & \mathbf{a}_1 \\ \mathbf{0} & 0 \end{bmatrix} \begin{bmatrix} \boldsymbol{\rho} \\ 1 \end{bmatrix}. \quad (20.20)$$

Taking into account the previous considerations Eq. (20.18) may be extended like:

$$\begin{bmatrix} \mathbf{a}^{[n]} \\ \mathbf{0} \end{bmatrix} = \begin{bmatrix} \boldsymbol{\Phi}_n & \mathbf{a}_n \\ \mathbf{0} & 0 \end{bmatrix} \begin{bmatrix} \boldsymbol{\rho} \\ 1 \end{bmatrix}. \quad (20.21)$$

Equation (20.21) represents a unified form of describing the vector field of the nth order accelerations in rigid body motion. The matrix:

$$\boldsymbol{\Psi}_n = \begin{bmatrix} \boldsymbol{\Phi}_n & \mathbf{a}_n \\ \mathbf{0} & 0 \end{bmatrix} \quad (20.22)$$

contains both the nth order acceleration tensor $\boldsymbol{\Phi}_n$ and the vector invariant $\mathbf{a}_n$. Equation (20.14) may be put in a compact form:

$$\boldsymbol{\Psi}_{n+1} = \dot{\boldsymbol{\Psi}}_n + \boldsymbol{\Psi}_n \boldsymbol{\Psi}_1, n \geq 1$$
$$\boldsymbol{\Psi}_1 = \begin{bmatrix} \tilde{\boldsymbol{\omega}} & \mathbf{v} \\ \mathbf{0} & 0 \end{bmatrix}. \quad (20.23)$$

The pair of vectors $(\boldsymbol{\omega}, \mathbf{v})$ is also known as *the spatial twist of rigid body*.

If follows that $\boldsymbol{\Psi}_n$ may be written as:

$$\boldsymbol{\Psi}_n = \boldsymbol{\Psi}_{n-1} \boldsymbol{\Psi}_1 + \left(\frac{d^{n-1}}{dt^{n-1}} \boldsymbol{\Psi}_1 \right) + \sum_{k=1}^{n-2} \left[\frac{d^k}{dt^k} (\boldsymbol{\Psi}_{n-k-1} \boldsymbol{\Psi}_1) \right], n \geq 3. \quad (20.24)$$

20.3 Symbolic Calculus of Higher-Order Kinematics Invariants

We shall present a method for the symbolic calculation of higher-order kinematics invariants for rigid motion.

Let $\mathcal{A}$ be the ring of matrices

$$\mathcal{A} = \left\{ \mathbf{A} \in \mathcal{M}_{4 \times 4}(\mathbb{R}) \middle| \mathbf{A} = \begin{bmatrix} \mathbf{\Phi} & \mathbf{a} \\ \mathbf{0} & 0 \end{bmatrix}; \mathbf{\Phi} \in \mathrm{L}(\mathbf{V}_3, \mathbf{V}_3), \mathbf{a} \in \mathbf{V}_3 \right\} \qquad (20.25)$$

and $\mathcal{A}[X]$ the set of polynomials with coefficients in the non-commutative ring $\mathcal{A}$. A generic element of $\mathcal{A}[X]$ has the form

$$\mathbf{P}(X) = \mathbf{A}_0 X^m + \mathbf{A}_1 X^{m-1} + \ldots + \mathbf{A}_{m-1} X + \mathbf{A}_m, \mathbf{A}_k \in \mathcal{A}, k = \overline{0, m}. \qquad (20.26)$$

Theorem 20.2 *There exists a unique polynomial* $\mathbf{P}_n \in \mathcal{A}[X]$ *such that* $\mathbf{\Psi}_n$ *can be written as*

$$\mathbf{\Psi}_n = \mathbf{P}_n(\mathbf{D})\mathbf{\Psi}_1, n \in \mathbb{N}^*, \qquad (20.27)$$

where $\mathbf{D} = \frac{d}{dt}$ *is the operator of time derivative.*

Proof Taking into account the Eqs. (20.23) and (20.27), we will obtain the following relationship of recurrence for $\mathbf{P}_n(\mathbf{D})$:

$$\begin{cases} \mathbf{P}_{n+1} = \mathbf{D}\mathbf{P}_n + \mathbf{P}_n(\mathbf{\Psi}_1) \\ \mathbf{P}_1 = \mathbf{I} \end{cases}. \qquad (20.28)$$

Since $\mathbf{\Psi}_1 = \begin{bmatrix} \tilde{\boldsymbol{\omega}} & \mathbf{v} \\ 0 & 0 \end{bmatrix}$ it follows the next outcome.

Theorem 20.3 *There exists a unique polynomial with the coefficients in the non-commutative ring of Euclidean tensors* $\mathrm{L}(\mathbf{V}_3, \mathbf{V}_3)$ *such that the vectors and the tensor invariants of the nth order accelerations can respectively be written as*

$$\begin{matrix} \mathbf{a}_n = \mathbf{P}_n \mathbf{v} \\ \mathbf{\Phi}_n = \mathbf{P}_n \tilde{\boldsymbol{\omega}} \end{matrix}, n \in \mathbb{N}^*, \qquad (20.29)$$

where $\mathbf{P}_n$ *fulfills the relationship of recurrence*

$$\begin{cases} \mathbf{P}_{n+1} = \mathbf{D}\mathbf{P}_n + \mathbf{P}_n(\tilde{\boldsymbol{\omega}}), n \in \mathbb{N}^* \\ \mathbf{P}_1 = \mathbf{I} \end{cases}. \qquad (20.30)$$

It follows

$$\mathbf{P}_2 = \mathbf{D} + \tilde{\boldsymbol{\omega}}$$
$$\mathbf{P}_3 = \mathbf{D}^2 + \tilde{\boldsymbol{\omega}}\mathbf{D} + 2\dot{\tilde{\boldsymbol{\omega}}} + \tilde{\boldsymbol{\omega}}^2 \qquad (20.31)$$
$$\mathbf{P}_4 = \mathbf{D}^3 + \tilde{\boldsymbol{\omega}}\mathbf{D}^2 + \left(3\dot{\tilde{\boldsymbol{\omega}}} + \tilde{\boldsymbol{\omega}}^2 \right)\mathbf{D} + 3\ddot{\tilde{\boldsymbol{\omega}}} + 3\dot{\tilde{\boldsymbol{\omega}}}\tilde{\boldsymbol{\omega}} + 2\tilde{\boldsymbol{\omega}}\dot{\tilde{\boldsymbol{\omega}}} + \tilde{\boldsymbol{\omega}}^3.$$

Using (20.29), (20.30) and (20.31), it follows:

– The *velocity field invariants*

$$\begin{cases} \mathbf{a}_1 = \mathbf{v} \\ \mathbf{\Phi}_1 = \tilde{\boldsymbol{\omega}} \end{cases} ; \tag{20.32}$$

– The *acceleration field invariants*

$$\begin{cases} \mathbf{a}_2 = \dot{\mathbf{v}} + \tilde{\boldsymbol{\omega}}\mathbf{v} \\ \mathbf{\Phi}_2 = \dot{\tilde{\boldsymbol{\omega}}} + \tilde{\boldsymbol{\omega}}^2 \end{cases} ; \tag{20.33}$$

– The *jerk field invariants*

$$\begin{cases} \mathbf{a}_3 = \ddot{\mathbf{v}} + \tilde{\boldsymbol{\omega}}\dot{\mathbf{v}} + 2\dot{\tilde{\boldsymbol{\omega}}}\,\mathbf{v} + \tilde{\boldsymbol{\omega}}^2\mathbf{v} \\ \mathbf{\Phi}_3 = \ddot{\tilde{\boldsymbol{\omega}}} + \tilde{\boldsymbol{\omega}}\,\dot{\tilde{\boldsymbol{\omega}}} + 2\dot{\tilde{\boldsymbol{\omega}}}\,\tilde{\boldsymbol{\omega}} + \tilde{\boldsymbol{\omega}}^3 \end{cases} ; \tag{20.34}$$

– The *hyper-jerk field invariants*

$$\begin{cases} \mathbf{a}_4 = \dddot{\mathbf{v}} + \tilde{\boldsymbol{\omega}}\ddot{\mathbf{v}} + \left(3\dot{\tilde{\boldsymbol{\omega}}} + \tilde{\boldsymbol{\omega}}^2\right)\dot{\mathbf{v}} + 3\ddot{\tilde{\boldsymbol{\omega}}}\,\mathbf{v} + 3\dot{\tilde{\boldsymbol{\omega}}}\,\tilde{\boldsymbol{\omega}}\mathbf{v} + 2\tilde{\boldsymbol{\omega}}\,\dot{\tilde{\boldsymbol{\omega}}}\,\mathbf{v} + \tilde{\boldsymbol{\omega}}^3\mathbf{v} \\ \mathbf{\Phi}_4 = \dddot{\tilde{\boldsymbol{\omega}}} + \tilde{\boldsymbol{\omega}}\,\ddot{\tilde{\boldsymbol{\omega}}} + \left(3\dot{\tilde{\boldsymbol{\omega}}} + \tilde{\boldsymbol{\omega}}^2\right)\dot{\tilde{\boldsymbol{\omega}}} + 3\ddot{\tilde{\boldsymbol{\omega}}}\,\tilde{\boldsymbol{\omega}} + 3\dot{\tilde{\boldsymbol{\omega}}}\,\tilde{\boldsymbol{\omega}}^2 + 2\tilde{\boldsymbol{\omega}}\,\dot{\tilde{\boldsymbol{\omega}}}\,\tilde{\boldsymbol{\omega}} + \tilde{\boldsymbol{\omega}}^4 \end{cases} . \tag{20.35}$$

Remark 20.4 The higher order time derivatives of spatial twist completely solve the problem of determining the field of the *n*th order acceleration of rigid motion.

20.4 Higher-Order Kinematics and Dual Numbers Algebra

Let the rigid body motion be given by the following parametric equation with respect to a given reference frame:

$$\begin{cases} \boldsymbol{\rho} = \boldsymbol{\rho}(t) \in V_3 \\ \mathbf{R} = \mathbf{R}(t) \in S\mathbb{O}_3 \end{cases} \tag{20.36}$$

where $t \in \mathbf{I} \subseteq \mathbb{R}$ is time variable.

The dual orthogonal tensor that describes the rigid body motion is [1, 3, 4]:

$$\underline{\mathbf{R}} = (\mathbf{I} + \varepsilon\tilde{\boldsymbol{\rho}})\mathbf{R}. \tag{20.37}$$

In the relation (20.37), the skew symmetric tensor associated to the vector $\boldsymbol{\rho}$ is denoted by $\tilde{\boldsymbol{\rho}}$, and ε is a dual quantity, $\varepsilon^2 = 0$, $\varepsilon \neq 0$ [3, 4, 6].

It can easily be demonstrated that:

$$\underline{\mathbf{R}}\underline{\mathbf{R}}^{\mathrm{T}} = \underline{\mathbf{I}}; \det \underline{\mathbf{R}} = 1$$
$$\underline{\mathbf{a}} \cdot \underline{\mathbf{b}} = (\underline{\mathbf{R}}\underline{\mathbf{a}}) \cdot (\underline{\mathbf{R}}\underline{\mathbf{b}}), \forall \underline{\mathbf{a}}, \underline{\mathbf{b}} \in \underline{\mathbf{V}}_3 \qquad (20.38)$$
$$\underline{\mathbf{R}}(\underline{\mathbf{a}} \times \underline{\mathbf{b}}) = \underline{\mathbf{R}}(\underline{\mathbf{a}}) \times \underline{\mathbf{R}}(\underline{\mathbf{b}}), \forall \underline{\mathbf{a}}, \underline{\mathbf{b}} \in \underline{\mathbf{V}}_3.$$

The tensor $\underline{\mathbf{R}}$ transports the dual vectors from the body frame in the space frame with the conservation of the dual angles and the relative orientation of lines that corresponds to the dual vectors $\underline{\mathbf{a}}$ and $\underline{\mathbf{b}}$.

The tensors from Eq. (20.37) form a Lie group denoted by $\underline{S\mathbb{O}_3}$. The Lie group $\underline{S\mathbb{O}_3}$ is isomorphic with the Lie group $S\mathbb{E}_3$ [4].

The dual angular velocity for the rigid body motion (20.36) is given by (20.37):

$$\underline{\boldsymbol{\omega}} = \mathrm{vect}\, \underline{\dot{\mathbf{R}}}\underline{\mathbf{R}}^{\mathrm{T}}. \qquad (20.39)$$

It can be demonstrated that [3]:

$$\underline{\boldsymbol{\omega}} = \boldsymbol{\omega} + \varepsilon \mathbf{v}, \qquad (20.40)$$

where

$$\boldsymbol{\omega} = \mathrm{vect}\, \dot{\mathbf{R}}\mathbf{R}^{\mathrm{T}} \qquad (20.41)$$

is the instantaneous angular velocity of the rigid body and

$$\mathbf{v} = \dot{\boldsymbol{\rho}} - \boldsymbol{\omega} \times \boldsymbol{\rho} \qquad (20.42)$$

is the linear velocity of a point of the rigid body that coincides with the origin of the reference frame at the moment when the velocity is calculated.

The dual angular velocity $\underline{\boldsymbol{\omega}}$ completely characterizes the distribution of the velocity field of the rigid body.

Let be the following equation:

$$\underline{\mathbf{V}}_{\boldsymbol{\rho}} = \boldsymbol{\omega} + \varepsilon \mathbf{v}_{\boldsymbol{\rho}} \qquad (20.43)$$

the dual velocity for a point localized with respect to the reference frame by the position vector $\boldsymbol{\rho}$.

In (20.43), $\boldsymbol{\omega}$ is the instantaneous angular velocity of the rigid body and $\mathbf{v}_{\boldsymbol{\rho}}$ is the linear velocity of the point. Using the equation [3]:

$$e^{\varepsilon \tilde{\boldsymbol{\rho}}} = \mathbf{I} + \varepsilon \tilde{\boldsymbol{\rho}} \qquad (20.44)$$

from (20.40), (20.42), (20.43) and (20.44), it results:

$$e^{\varepsilon \tilde{\boldsymbol{\rho}}}\underline{\mathbf{V}}_{\boldsymbol{\rho}} = \underline{\boldsymbol{\omega}}. \qquad (20.45)$$

Consequently, $e^{\varepsilon\tilde{\rho}}\underline{\mathbf{V}}_{\rho}$ is an invariant having the same value for any ρ .

Writing this invariant in two different points of the rigid body (denoted by P and Q), it results that:

$$e^{\varepsilon\tilde{\rho}_P}\underline{\mathbf{V}}_P = e^{\varepsilon\tilde{\rho}_Q}\underline{\mathbf{V}}_Q. \tag{20.46}$$

From (20.46), it follows:

$$\underline{\mathbf{V}}_P = e^{\varepsilon\widetilde{PQ}}\underline{\mathbf{V}}_Q \tag{20.47}$$

with $PQ = \rho_Q - \rho_P$.

The relation (20.47) is true for any P and Q.

Similar with the Eq. (20.45), the following equation also defines an invariant:

$$e^{\varepsilon\tilde{\rho}}\underline{\mathbf{A}}_{\rho} = \dot{\underline{\omega}}, \forall \rho \in V_3, \tag{20.48}$$

where we denoted

$$\underline{\mathbf{A}}_{\rho} = \dot{\omega} + \varepsilon\mathbf{A}_{\rho} \tag{20.49}$$

$\mathbf{A}_{\rho}$ being the reduced acceleration in a point given by the position vector ρ:

$$\mathbf{A}_{\rho} = \mathbf{a}_{\rho} - \omega \times \mathbf{v}_{\rho}. \tag{20.50}$$

Similar with the Eq. (20.47) one may also write:

$$\underline{\mathbf{A}}_P = e^{\varepsilon\widetilde{PQ}}\underline{\mathbf{A}}_Q. \tag{20.51}$$

All properties are extended for higher-order accelerations. The vector $\underline{\omega}^{(n-1)} = \frac{d^{n-1}\underline{\omega}}{dt^{n-1}}, n \in \mathbb{N}^*$ describes completely the helicoidal field of the nth order reduced accelerations, for $n \in \mathbb{N}^*$:

$$e^{\varepsilon\tilde{\rho}}\underline{\mathbf{A}}_{\rho}^{[n]} = \underline{\omega}^{(n-1)}. \tag{20.52}$$

In Eq. (20.52), $\underline{\mathbf{A}}_{\rho}^{[n]} = \omega^{(n-1)} + \varepsilon\mathbf{A}_{\rho}^{[n]}$ denotes the nth order the dual reduced acceleration of a given point by the position vector ρ.

It follows that the dual part of the nth order differentiation of $\underline{\omega}^{(n-1)}$,

$$\underline{\omega}^{(n-1)} = \omega^{(n-1)} + \varepsilon\mathbf{v}^{(n-1)} \tag{20.53}$$

is the nth order reduced acceleration of that point of the rigid body that at the given time passes through the origin of the reference frame.

From equation

$$\mathbf{v} = \dot{\boldsymbol{\rho}} - \boldsymbol{\omega} \times \boldsymbol{\rho} \tag{20.54}$$

it follows that

$$\mathbf{v}^{(n-1)} = \boldsymbol{\rho}^{(n)} - \sum_{k=0}^{n-1} C_{n-1}^k \boldsymbol{\omega}^{(n-k-1)} \times \boldsymbol{\rho}^{(k)}, n \in \mathbb{N}^*. \tag{20.55}$$

The following notations will be used

$$\mathbf{a}_{\boldsymbol{\rho}}^{[n]} \triangleq \boldsymbol{\rho}^{(n)}, n \in \mathbb{N}^* \tag{20.56}$$

for the nth order accelerations of the point given by the position vector $\boldsymbol{\rho}$ and

$$\mathbf{A}_{\boldsymbol{\rho}}^{[n]} \triangleq \mathbf{a}_{\boldsymbol{\rho}}^{[n]} - \sum_{k=1}^{n-1} C_{n-1}^k \tilde{\boldsymbol{\omega}}^{(n-k-1)} \mathbf{a}_{\boldsymbol{\rho}}^{[k]} \tag{20.57}$$

for the nth order reduced acceleration of the same point. From (20.55) and (20.57) it results:

$$\mathbf{A}_{\boldsymbol{\rho}}^{[n]} = \mathbf{v}^{(n-1)} + \boldsymbol{\omega}^{(n-1)} \times \boldsymbol{\rho} \tag{20.58}$$

which proves that the field of the nth order reduced accelerations is helicoidal.

For $\boldsymbol{\rho} = 0$, from Eqs. (20.57) and (20.58), the relation between the nth order reduced acceleration and the nth order acceleration of a point of the rigid body which passes through the origin of the reference frame at a given moment of time, is:

$$\mathbf{v}^{(n-1)} = \mathbf{a}_n - \sum_{k=1}^{n-1} C_{n-1}^k \tilde{\boldsymbol{\omega}}^{(n-k-1)} \mathbf{a}_k, n \in \mathbb{N}^*. \tag{20.59}$$

In Eq. (20.59), $\mathbf{a}_k$ are the vector invariants of the kth order acceleration, with $k = \overline{1, n}$.

Using (20.29), the inverse of the previous equation is:

$$\mathbf{a}_n = \mathbf{P}_n \mathbf{v}, n \in \mathbb{N}^*, \tag{20.60}$$

where $\mathbf{P}_n$ is a polynomial with the coefficients in the ring of the second order Euclidean tensors. The polynomials $\mathbf{P}_n(\mathbf{D})$ follow the recurrence relation given by Eq. (20.30). The polynomials $\mathbf{P}_1, \mathbf{P}_2, \mathbf{P}_3, \mathbf{P}_4$ are given by the Eqs. (20.30) and (20.31).

For the case of the velocities, accelerations, jerks and hyper-jerks from Eqs. (20.59) and (20.60), we will obtain the concise symbolic form:

$$
\begin{bmatrix} \mathbf{v} \\ \dot{\mathbf{v}} \\ \ddot{\mathbf{v}} \\ \dddot{\mathbf{v}} \end{bmatrix} = \begin{bmatrix} \mathbf{I} & \mathbf{0} & \mathbf{0} & \mathbf{0} \\ -\tilde{\boldsymbol{\omega}} & \mathbf{I} & \mathbf{0} & \mathbf{0} \\ -2\dot{\tilde{\boldsymbol{\omega}}} & -\tilde{\boldsymbol{\omega}} & \mathbf{I} & \mathbf{0} \\ -3\ddot{\tilde{\boldsymbol{\omega}}} & -3\dot{\tilde{\boldsymbol{\omega}}} & -\tilde{\boldsymbol{\omega}} & \mathbf{I} \end{bmatrix} \begin{bmatrix} \mathbf{a}_1 \\ \mathbf{a}_2 \\ \mathbf{a}_3 \\ \mathbf{a}_4 \end{bmatrix} ;
\tag{20.61}
$$

$$
\begin{bmatrix} \mathbf{a}_1 \\ \mathbf{a}_2 \\ \mathbf{a}_3 \\ \mathbf{a}_4 \end{bmatrix} = \begin{bmatrix} \mathbf{I} & \mathbf{0} & \mathbf{0} & \mathbf{0} \\ \tilde{\boldsymbol{\omega}} & \mathbf{I} & \mathbf{0} & \mathbf{0} \\ 2\dot{\tilde{\boldsymbol{\omega}}}+\tilde{\boldsymbol{\omega}}^2 & \tilde{\boldsymbol{\omega}} & \mathbf{I} & \mathbf{0} \\ 3\ddot{\tilde{\boldsymbol{\omega}}}+2\tilde{\boldsymbol{\omega}}\dot{\tilde{\boldsymbol{\omega}}}+3\dot{\tilde{\boldsymbol{\omega}}}\tilde{\boldsymbol{\omega}}+\tilde{\boldsymbol{\omega}}^3 & 3\dot{\tilde{\boldsymbol{\omega}}}+\tilde{\boldsymbol{\omega}}^2 & \tilde{\boldsymbol{\omega}} & \mathbf{I} \end{bmatrix} \begin{bmatrix} \mathbf{v} \\ \dot{\mathbf{v}} \\ \ddot{\mathbf{v}} \\ \dddot{\mathbf{v}} \end{bmatrix} .
\tag{20.62}
$$

Theorem 20.4 *The field of the nth order accelerations of a rigid body in a general motion is uniquely determined by the kth order time derivative of a dual twist $\underline{\boldsymbol{\omega}}$, with $k = \overline{1, n-1}$.*

20.5   Conclusions

The higher-order kinematics properties of rigid body in general motion have been deeply studied. Using the tensor calculus and the isomorphism between the Lie group of the rigid displacements $S\mathbb{E}_3$ and the Lie group of the orthogonal dual tensors $\underline{S\mathbb{O}}_3$, a general method for the study of the field of arbitrary higher-order accelerations is described. It is proved that all information regarding the properties of the distribution of nth-order accelerations are contained in the kth order derivatives of the dual twist of the rigid body, $k = \overline{0, n-1}$. These derivatives belong to the Lie algebra associated to the Lie group $\underline{S\mathbb{O}}_3$.

The obtained results interest the theoretical kinematics, jerk with hyper-jerk analysis in the case of parallel manipulators, control theory and multibody kinematics.

References

1. Angeles, J.: The application of dual algebra to kinematic analysis. In: Computational Methods in Mechanical Systems, vol. 161, pp. 3–32 (1998)
2. Angeles, J.: Fundamentals of Robotic Mechanical Systems. Springer (2014)
3. Condurache, D., Burlacu, A.: Dual tensors based solutions for rigid body motion parameterization. Mech. Mach. Theory **74**, 390–412 (2014)
4. Condurache, D., Burlacu, A.: Orthogonal dual tensor method for solving the AX = XB sensor calibration problem. Mech. Mach. Theory **104**, 382–404 (2016)
5. Condurache, D., Matcovschi, M.H.: Computation of angular velocity and acceleration tensors by direct measurements. Acta Mech. **153**(3–4), 147–167 (2002)
6. Pennestri, E., Valentini, P.: Linear dual algebra algorithms and their application to kinematics. In: Multibody Dynamics: Computational Methods and Applications, vol. 12, pp. 207–229 (2009)

Chapter 21
Design of a Solar Powered Mobile Illumination Tower with a Solar Tracker Mechanism for Increased Efficiency

D. Lavayen, E. Pujada, D. Olivera, A. Maguina, M. Choque and W. Bullon

Abstract Electrical Grid Connection is still a problem in Peru since there are plenty of remote areas across the Peruvian land, even industries as mining have this problem due to the fact that their operations are located mainly in these remotes areas, and they require artificial light 24/7 to work. This need is currently covered mainly by diesel powered towers, however they produce noise, pollution and have high logistic and operation costs. The proposed alternative consists of a solar powered illumination tower with a pre-programmed solar tracker mechanism to increase its efficiency and electric energy output, reduce battery loading times and increase capacity. Two prototypes have been developed: the first prototype has fixed-position photovoltaic panels, as most of the commercially available solar powered illumination towers; the second prototype possesses a modified slider-crank mechanism driven by a linear actuator which is used to reposition the panels to an optimal position for better energy collection. Field tests show a notable increase in electric energy output when using a solar tracker mechanism which leads to reduced required area for solar panels, reduced number of batteries, reduced weight, and increased efficiency with higher luminosity and power output.

21.1 Introduction

Non-renewable energy sources, such as gas, oil, coal have a strong impact on the environment, which can already be seen in the high percentage of CO_2 in the atmosphere, global warming and green house effect [1]. There has also been a huge increase in the energy consumption and needs of mankind, which leads to an inevitable search

D. Lavayen (✉) · M. Choque · W. Bullon
Section of Mechanical Engineering, Pontifical Catholic University of Peru,
Ave. Universitaria 1801, Lima, Peru
e-mail: dlavayen@pucp.pe

E. Pujada · D. Olivera · A. Maguina
DINAMO Tecnologias S.A.C. (ex - Qumir Tecnologias S.A.C.),
Ave. Del Parque Norte 1174, Lima, Peru
e-mail: epujadag@gmail.com

for alternative sources of energy [2–5]. One of the most widely-used alternatives is solar energy. The solar energy that reaches earth can easily cover most of the energy needs of mankind; however, this needs large surfaces dedicated only to capture and transform solar radiation into usable electricity [6]. This has lead to efforts and research in order to increase the efficiency of photovoltaic panels and cells. Such efforts include increasing the conversion efficiency of the cell itself and also mechanisms that track and follow the sun, so that the solar panel always faces the sun directly and orthogonally [7, 8].

On the other hand, mobile illumination towers are a common solution for artificial illumination in places away from the electrical grid. In Peru, they are common at mining operations and places that require only temporal illumination. Most of these towers are diesel or gas powered, which produce noise and air pollution. Lately, solar powered mobile illumination towers have been introduced to the Peruvian national market; however due to their high initial cost and low luminosity (both compared to their diesel and gas powered counterparts), they have not been highly accepted into the market yet.

The issues mentioned above can be solved by introducing a mechanism to track the sun or solar-tracking mechanism to a mobile illumination tower, so that the panels always face the sun. By doing so, the amount of energy captured is highly increased and the size of the solar panels can be reduced. This procedure has already been widely adopted only in non-mobile solar panels; however they are designed for certain locations.

21.2   Solar Tracking Rotations in Photovoltaic Panels

Solar tracking takes into consideration two main angles as shown in Fig. 21.1, these angles can describe the exact position of the sun during the day. The first movement corresponds to the elevation or tilt angle with respect to the latitude angle from south to north, which slightly changes during the different seasons of the year. The lattitude angle can be generally fixed, and is typically set to 15° for the locations of the main mining operations in southern parts of Peru [9]. The second movement angle corresponds to the azimuth rotation or the movement from east to west that the sun describes during the daylight hours (Fig. 21.1). Most solar tracking panels only possess the azimuth rotation, and are typically referred to as single axis solar tracking devices.

Field tests show that single axis solar tracking mechanism have a large impact on the efficiency of the solar panel, increasing it up to 35–60% depending on the location [10–12]. When a solar tracking mechanism possess both of the movements described above, it is referred to as a double axis solar tracking mechanism. Double axis solar tracker mechanisms show an even larger increase in the electric power output (up to an extra 10%), but the mechanisms needed are far more complex and require more detailed maintenance procedures. Due to this complexity and the fact that the panels of a mobile solar powered mobile illumination tower needs to be
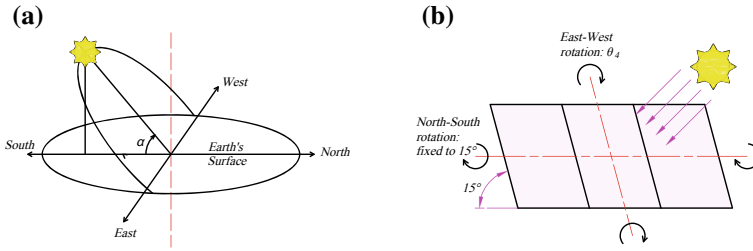
Fig. 21.1 a Description of the angles used to describe the movement of the sun. **b** Desired degrees of freedom for each photovoltaic panel

folded and unfolded for transportation; a single axis solar tracking mechanism is chosen for development for the mobile tower of this article, with an expected rise in efficiency, collected energy, and luminosity output.

21.3 Description of the Developed Prototypes

Two prototypes of solar powered mobile illumination towers have been developed. For mobility, the panels of both prototypes can be folded and unfolded for transport. Only the second prototype includes a solar tracking mechanism, and addresses some issues found in the first prototype.

21.3.1 First Prototype with Fixed Photovoltaic Panels

The first prototype (Fig. 21.2) of the mobile illumination tower consists of fixed solar panels attached to a trailer, so the tower can be transported where needed. The solar panels can be manually folded and unfolded for transportation. Although it is practical and has a high luminosity output, it possessed some issues, especially related to bulkiness and weight of 1300 kg. It also required a large area covered by solar panels (specifically 9.75 m^2) to obtain enough energy to power the illumination lights for the night (around 500 W).

21.3.2 Second Prototype with Solar Tracker Mechanism

An improved prototype was later developed to address the issues of the first one. As mentioned before, the main improvement is the introduction of a solar tracking mechanism (see Fig. 21.3), which allowed a noticeable reduction in the covered area

Fig. 21.2 First prototype of the mobile illumination tower

Fig. 21.3 Second and improved prototype, showing its solar tracking mechanism in different positions at 8 am (left) and 4 pm (right) during a field test in the Peruvian highlands

by the solar panels (down to 8 m^2), leading to a decrease in overall weight down to 900 kg. Other improvements consist of flexible solar panels, lighter structure to support them and batteries with larger capacities. The second prototype must also be manually folded into a more compact form for transportation.

The mechanism that provides the solar tracking consists of a modified slider crank mechanism, as shown in Fig. 21.4. Each photovoltaic panels arrange is driven by an identical mechanism and all are inclined 15°, making a total of four mechanisms. All of them are also driven at the same by a linear actuator S_2, located at the center of the tower, so each mechanism behaves as a modified slider-crank. Even though there are other actuation options, such as a spring loaded mechanism or compressed gas, an electric actuator was chosen due to its reprogramming capabilities on the on-board PLC.

Fig. 21.4 Detail of the solar tracker mechanism, which consists of a modified slider crank mechanism: The bottom black bar is the slider and the triangular plate is the crank, connected to the solar panel
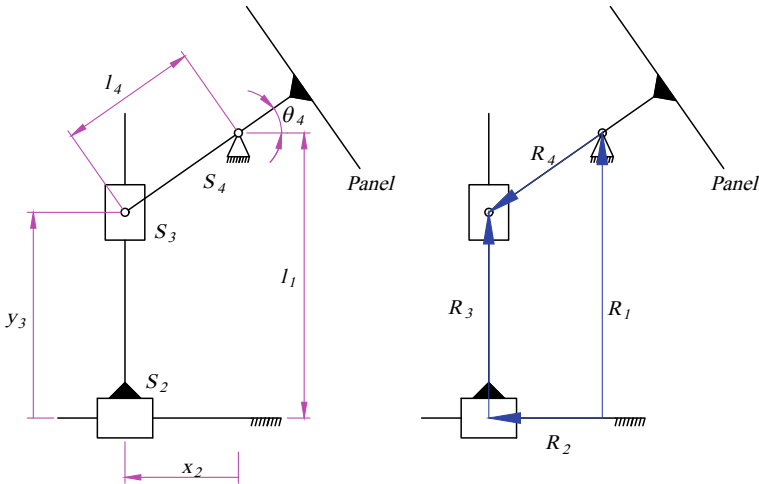

Fig. 21.5 Parameters used for the solar tracker mechanism and vectors used to define each body: R_1

Since the tower needs to be mobile, the panels must be folded for transportation. The solution for this requirement is conceived as a second slider S_3. When the panels are deployed, the panel S_4 clutches into S_3, thus the modified slider crank mechanism is obtained, as seen in Fig. 21.5. For this mechanism, the input or driver parameter is x_2 (and a constant velocity v_2), the main output is θ_4 (and the angular velocity ω_4), which is the angle of the panels and is used to track the sun.

From Fig. 21.5, the kinematic equations can be deduced as follows:

$$\mathbf{R_2} + \mathbf{R_3} = \mathbf{R_1} + \mathbf{R_4} \tag{21.1}$$

$$\begin{Bmatrix} -x_2 \\ y_3 \end{Bmatrix} = \begin{Bmatrix} -l_4 \cos \theta_4 \\ l_1 - l_4 \sin \theta_4 \end{Bmatrix} \tag{21.2}$$

By time-differentiating Eq. 21.2, the velocities (angular and linear) of the mechanism can be determined as follows:

$$\begin{Bmatrix} v_2 \\ v_3 \end{Bmatrix} = \begin{Bmatrix} -l_4 \omega_4 \sin \theta_4 \\ -l_4 \omega \cos \theta_4 \end{Bmatrix} \tag{21.3}$$

From Eq. 21.2, the output parameters y_3 and θ_4 are determined. The latter must sweep and follow the movement of the sun from East to West (recall Fig. 21.1). The dimensions of the mechanism and the linear actuator must guarantee this movement. Thus, the dimensions shown in Table 21.1 are defined.

Setting the system to move continuously showed a high energy consumption. The solution for this problem is to power the actuator each 15 min. A reference that the sun moves 15° each hour was used to set up the movement, based on the curves in Figs. 21.6 and 21.7.

Table 21.1 Parameters used for the solar tracker mechanism

Parameter	Type	Values	Units
l_1	Length	350	mm
l_4	Length	220	mm
x_2	Input (actuator)	$[-220; 220]$	mm
v_2	Input (actuator)	8	mm/s

Fig. 21.6 Solar tracking angle θ_4 as a function of the displacement of the linear actuator. The mechanism is designed to obtain an almost linear relationship between the position of the linear actuator and the θ_4 angle
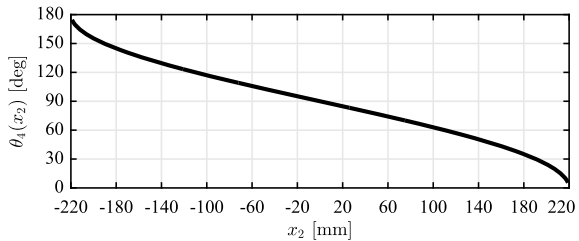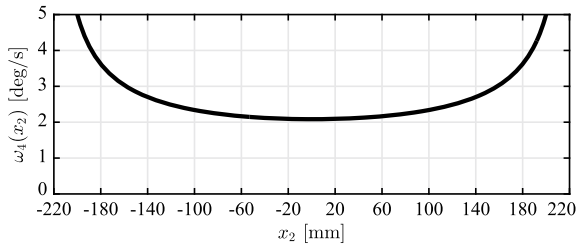

Fig. 21.7 Angular velocity ω_4 of the photovoltaic panels as a function of the position of the linear actuator

21.4 Performance Comparison in Solar Energy Recollection

Using a PLC installed on-board in the prototypes, power measurements could be taken to compare the performance of the first (without tracking mechanism) and second (with tracking mechanism) prototypes. The measurements shown in Table 21.2 took place during field test in July 2017 (see Fig. 21.3) in a mine in the Peruvian south highlands from 9 am to 12 pm - more measurements could not be taken due to outside factors (mainly permissions from the mining operator). Voltage and current measurements were used to obtain the power received by the tower. Measurements were taken each 10 min to observe the tendency in the increase of efficiency and power generated.

According to design calculations, after 12 h of continuous illumination with 500 W LED lamps, the batteries should have a remaining 49% capacity. After the field test, it was found that the batteries had 45% capacity left, meaning that approximately 4% of the total energy stored by the batteries was used to power the linear actuator.

Table 21.2 Power measurement comparison between the first (fixed angle) and second (with solar tracking mechanism)

	Without Tracker (fixed θ_4)	With Tracker (variable θ_4)	Difference
Daytime	Power (W)	Power (W)	Power increase (%)
09:00	201.40	286.84	42.42
09:10	197.28	281.16	42.52
09:20	198.10	266.02	34.29
09:30	203.76	302.10	48.26
09:40	217.91	291.49	33.77
09:50	224.36	266.96	18.99
10:00	220.76	308.47	39.73
10:10	226.40	303.88	34.22
10:20	232.06	297.15	28.05
10:30	237.72	313.50	31.88
10:40	255.60	299.98	17.36
10:50	254.70	307.80	20.85
11:00	266.96	303.88	13.83
11:10	268.85	308.47	14.74
11:20	276.36	309.56	12.01
11:30	280.17	304.95	8.84
11:40	289.43	298.20	3.03
11:50	299.25	299.98	0.24
12:00	308.47	315.24	2.19

21.5 Conclusions and Future Work

The current investigations show that there is notable increase in the electric energy output in the tower when using a solar tracker mechanism by an average of 20%. The increase in power is more noticeable in the early mornings reaching a 40% increase. The increase is less noticeable near noon (when the sun is in the zenith point), due to the fact that both prototypes have almost the same θ_4 angles at this hour.

This fact translates into more luminosity at night, longer battery lifespan, and more energy to power other devices. This increase makes the second prototype even comparable in luminosity to diesel and gas powered illumination towers, which currently dominate the market.

More field tests are still required during the whole year to determine the average increase in generated power in each season. The results obtained can also be used to develop an optimized algorithm to control the movements of the mechanism and increase even more the electric energy output. The authors are also currently working on a third, totally automatized prototype, with a dual axis solar tracker mechanism. It is worth noting that the second prototype has a pending utility patent in INDECOPI Peru (2/IN/2016/002798), property of DINAMO Tecnologias S.A.C. (ex Qumir Tecnologias S.A.C.).

Note: During the time between the conference and the publication of this article, Qumir Tecnologias S.A.C. has been acquired by a third-party and renamed DINAMO Tecnologias. The patent and intellectual property remain with the authors of this work.

References

1. Rosenberg, N.J., Easterling, W.E., Crosson, P.R., Darmstadter, J.: Greenhouse Warming: Abatement and Adaptation. Taylor & Francis. ISBN: 9781317332510 (2016)
2. Zhang, Q.-X., Yu, H.-Y., Zhang, Q.-Y., Zhang, Z.-Y., Shao, C.-H., Yang, D.: A solar automatic tracking system that generates power for lighting greenhouses. Energies (2015). https://doi.org/10.3390/en8077367
3. Chao, R.M., Ko, S.H., Pai, F.S., Lin, I.H., Chang, C.C.: Evaluation of a photovoltaic energy mechatronics system with a built-in quadratic maximum power point tracking algorithm. Energy, Sol (2009). https://doi.org/10.1016/j.solener.2009.08.011
4. Riyad A M, Salah A, Iyad M M (2011) Design, construction and operation of spherical solar cooker with automatic sun tracking system. Energy Convers. Manag. https://doi.org/10.1016/j.enconman.2010.07.037
5. Crockett, R.G., Newborough, M., Highgate, D.J.: Electrolyser-based energy management: a means for optimising the exploitation of variable renewable-energy resources in stand-alone applications. Energy Sol (1997). https://doi.org/10.1016/S0038-092X(97)00078-9

6. Visa, I., Comsit, M.: Tracking systems for solar energy conversion devices. In: Proceedings of the 14th ISES International Conference EUROSUN 2004, pp. 783–788 (2004)
7. Algifri, A.H., Al-Towaie, H.A.: Efficient orientation impacts of box-type solar cooker on the cooker performance. Solar Energ. (2001). https://doi.org/10.1016/S0038-092X(00)00136-5
8. Bairi, A.: Method of quick determination of the angle of slope and the orientation of solar collectors without a sun tracking system. Solar Wind Technol. (1990). https://doi.org/10.1016/0741-983X(90)90104-A
9. SENAMHI-Peru: Atlas de Energia Solar en Peru (2003). http://www.senamhi.gob.pe/pdf/Atlas%20_de_Radiacion_Solar.pdf. Cited 15 Nov 2017
10. Deepthi, S., Ponni, A., Ranjitha, R., Dhanabal, R.: Comparison of efficiencies of Single-Axis tracking system and Dual-Axis tracking system with fixed mount. Int. J. Eng. Sci. Innov. Technol. **2**(2), 425–430 (2013)
11. Dhanabal, R., Bharathi, V., Ranjitha, R., Ponni, A., Deepthi, S., Mageshkannan, P.: Comparison of efficiencies of solar tracker systems with static panel Single Axis Tracking System and Dual-Axis tracking system with fixed mount. Int. J. Eng. Technol. **2**(5), 1925–1933 (2013)
12. Singh, S.P., Srikant, K., Jairaj, K.S.: Performance comparison and cost analysis of single axis tracking and fixed Tilt PV systems. In: Proceedings of International Conference on Current Trends in Engineering, Science and Technology, 2nd edn, Grenze Scientific Society (2017)

Chapter 22
Computational Tool for the Intelligent Design of Gearboxes of Cylindrical Gears and Welded Housing

Rosendo Franco, Michael A. Blas, Luis H. Inafuku, Angel A. C. Peinado, Jean C. Soto, Alberto E. Solano, Daniel H. Fernández, Alexander R. López, José F. Montalván, Herbert Yépez and Quino Valverde

Abstract The present work reports the development of intelligent software that permits to design gearboxes of cylindrical gears and welded housing with a high degree of automation. At the time there is a large amount of CAD software with options to design machine elements, but there is not any that focuses on the complete design of gearboxes. This is because a gearbox is a product of high complexity, in which many variables are involved and, at the same time, there are innumerable solutions for the same need. To overcome these difficulties, the authors have used the Artificial Intelligence technique known as Case Based Reasoning (CBR). The developed software has the characteristic modules of a case-based system: a base of resolved cases, a retrieve module and an adaptation module. The main advantage of this type of systems is that they manage to acquire the experience (knowledge) of the specialists and store it through the resolved cases. This experience is reused in the solution of new problems. During the research process it was necessary to define the main characteristics that describe a gearbox, i.e., its similarity attributes, as well as to establish the similarity function and implement a parametric adaptation technique. Additionally, the software has modules for calculating and selecting the components of a gearbox, to tune the design to meet the requirements established by technical standards or by a user. The implementation was done in Visual Basic language in the form of an add-in, which is automatically loaded into the Autodesk Inventor® environment. From the input data, the developed program, called *aiGearboxDesigner*, is capable of generating a complete design, 3D models and the corresponding assembly planes and manufacturing drawings.

Keywords Mechanical design · Gearbox · Case based reasoning

R. Franco (✉) · M. A. Blas · L. H. Inafuku · A. A. C. Peinado · J. C. Soto · A. E. Solano · D. H. Fernández · A. R. López · J. F. Montalván · H. Yépez · Q. Valverde
INACOM Group/Aula PUCP-CIMNE, Mechanical Engineering Section Engineering Department, Pontificia Universidad Catolica del Peru, Lima 32, Peru
e-mail: rofranco@pucp.pe

237

22.1   Introduction

The design of gearboxes is a task of high demand of time. Currently there are many aids in the design process of some mechanical components, such as gears, shafts, bearings and fasteners. However, no specific tool for some components has been found, for example, to design housings, which is a gearbox's fundamental component. Therefore, no software has been found that permits to design a gearbox completely in an automated way. Among the most well-known software related to the design of gearboxes, are MASTA [14], RomaxDESIGNER [13] and KISSsoft [7]. For the proper use of these programs the user requires a lot of experience and knowledge in design of the machine elements that are part of a gearbox, since the level of user's interaction is very high. In this regard, software that permits the automated design of gearboxes would be very useful.

Precisely, Case Based Reasoning (CBR) is an artificial intelligence technique that is based on taking advantage of experience and knowledge about a past resolved problem to solve a new one [1, 9]. This technique is used in different topics of science and technology, including engineering. There are evidences that CBR has been used in mechanical design and, specifically, in gear design [5, 10]. In addition, it has been developed a CBR application to design two-step gearboxes, however, modifications, after the adaptation phase, are user's responsibility [6], which limits the degree of automation of the program.

The *aiGearboxDesigner* developed by the authors realize the integral design of gearboxes of two and three steps with horizontal parallel shafts, cylindrical gears, and welded housing with a high degree of automation. It has the characteristic modules of a CBR system and an additional module to tune up the design. The designer is able to introduce modifications or to provide criteria based on their own experience both after adapting the retrieved case and after the tune-up module.

22.2   CBR's Application

A CBR system is composed of three essential elements: a case base, a retrieve module and an adaptation module. Figure 22.1 shows a general diagram of the developed system, in which the three specific components are distinguished. There is also the tuning-the-design module, previous to the final design.

The cases are characterized by their fundamental parameters, the minimum necessary to carry-out the design of a gearbox. These are: power (P), input speed (n_i), output speed (n_s), gear life (L_h) and alignment of the output shaft with respect to the input shaft (Al). These parameters are the attributes of the gearbox, which are stored in the case base with a file that contains all the details of the design. The
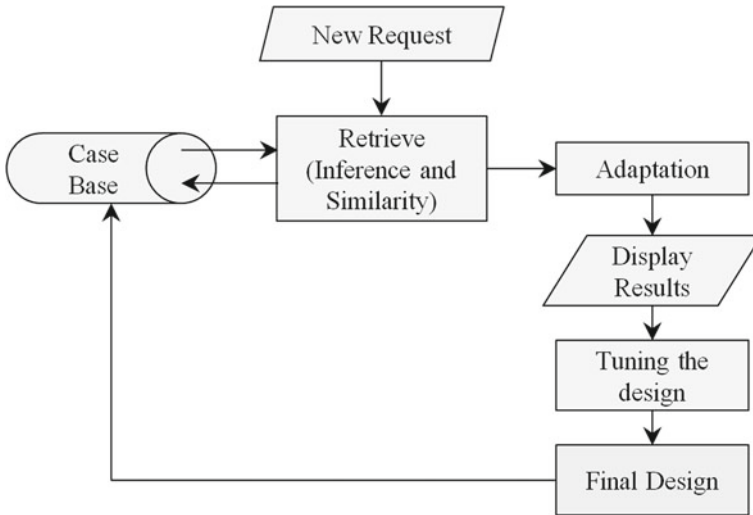
Fig. 22.1 General diagram of *aiGearboxDesigner*

retrieve module aims to retrieve the case of higher similarity, using the attributes of the new design, for which the similarity function is used. Then, the adaptation module is responsible for modifying the retrieved design so that it approximates the specifications of the new request. For this, adaptive rules are used, which are based in empirical recommendations for the design of mechanical components.

22.2.1 Case Base

Case base is a database that contains the resolved cases. The data of a case consist of its attributes and an XML file which contains the detailed information of each component and the assembly. The database was developed in SQL language, using free SQLite software, through its System.Data.SQLite library for .NET.

22.2.2 Retrieve

This phase aims to retrieve, from the case base, the most similar case to the new request. For this, the similarity function

$$S(u, v) = \frac{\sum \omega_i \cdot \delta_i(u, v)}{\sum \omega_i} \tag{22.1}$$

Table 22.1 Similarity attributes and weights

Similarity attribute	Weight (ω)
Transmission ratio (i)	1
Power (P)	0.5
Gear life (L_h)	0.5
Alignment of the output shaft (Al)	0.75

is used, where ω_i is the weight of the attribute i, δ_i is the comparison criterion of the attribute i, u is the attribute of the stored case and v is the attribute of the new request. Table 22.1 shows the similarity attributes and weights used in the present application. The attribute has greater weight if it impacts more on the design of the gearbox.

The comparison criterion of the attribute between the stored case and the new request depends on the type of data with which the attribute is represented: numerical or logical [9]. For the case of the numerically represented attribute (transmission ratio, power and gear life), the distance between attributes is used, defined by

$$\delta(u, v) = 1 - \frac{|u - v|}{u_{max} - u_{min}} \tag{22.2}$$

where u_{max} and u_{min} represent the maximum and minimum values of the attribute analyzed, in the domain of the case base. The logical data is used to compare the attribute related to the alignment of the output shaft, which can take two possible values: "Same side" or "Opposite side". This criterion is defined as

$$\delta(u, v) = \begin{cases} 1, & u = v \\ 0, & u \neq v \end{cases} \tag{22.3}$$

The developed application will show the cases with the greatest similarity according to Eq. (22.1), and permit to select (retrieve) the case that will be adapted.

22.2.3 Adaptation

In general, the retrieved case does not fully satisfy the requirements of the new request, and may even be pretty far from it. In the adaptation phase, a first approximation of the design is obtained, close to the requested, but which is not yet the final design. The adaptation is done based on recommendations for the "quick calculation" of some components of the gearbox, as well as geometric relationships that must be satisfied among all the components.

First, the total transmission ratio

Table 22.2 Steps and partial transmission ratios

Total ratio	Steps	Partial ratio
$i < 45$ (max. 60)	2	$i_1 \approx 1.25 \cdot \sqrt{i}$
$i < 200$ (max. 300)	3	$i_1 \approx 1.25 \cdot \sqrt{i}$ $i_2 \approx 1.25 \cdot \sqrt{i/i_1}$

$$i = \frac{n_i}{n_s} \tag{20.4}$$

is calculated, and then the number of steps and the partial transmission ratios are defined using the recommendations detailed in Table 22.2 [11, 15].

The calculation of the quantity of steps is done before the retrieve, so that the cases are filtered by the quantity of steps. In this setting, the number of steps is not considered an attribute, since it would be very difficult to adapt a two-step gearbox to obtain a three-step gearbox and vice versa. Consequently, the simplest case base must contain at least one two-step and one three-step gearbox.

The components that present key parameters to be adapted are the gears and the shafts. For example, we can estimate the diameter of shafts under torsion and bending using

$$d_{design} \approx d_{case} \cdot \sqrt[3]{\frac{T_{design}}{T_{case}}}, \tag{20.5}$$

since according to [8] the diameter can be written as a function of $T^{1/3}$, where T is the torque, and "design" and "case" subscripts refer to values of the new request and the retrieved case, respectively.

The value of the normal module m_n of the gears is also adapted as a function of the equivalent torque, which considers the "application factor" of the gearbox [15]. Thus, the number of teeth of the gear is adapted according to the partial transmission ratios, holding the values of helical angle, number of teeth in the pinions and material properties according to those of the retrieved case. It is taken into account that gear modules are standardized according to DIN 780 and shaft diameters take preferred values, according to manufacturing criteria.

By modifying the key parameters mentioned before (number of teeth of the gear, modules and shaft diameters), the rest of the parameters are adapted according to the established geometric relationships. The adaptation process involves the resizing of several components and a new selection of standardized elements. To achieve this goal it is necessary that the geometric model of the gearbox is well-structured and -parameterized. For this reason, object-oriented programming was used through the Visual Basic .NET language, and the necessary classes to represent adequately a gearbox reducer were defined. The main class is called "Gearbox", which has as Properties the classes "Sub-Assembly Shaft" and "Sub-Assembly Housing". These two classes in turn are broken down into other classes that represent their components.
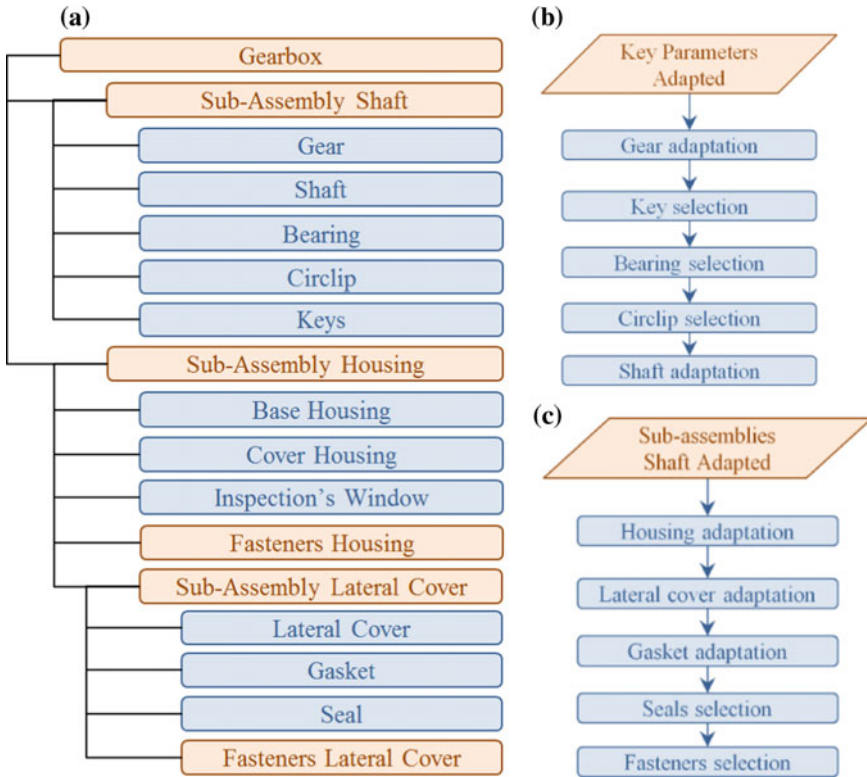
Fig. 22.2 **a** Object structure of *aiGearboxDesigner,* **b** Adaptation sequence for "Sub-assembly Shaft", **c** Adaptation sequence for "Sub-assembly Housing"

Figure 22.2a shows the object structure used for the developed application. The adaptation sequence of the "Sub-assembly Shaft" and the "Sub-assembly Housing" are shown in Fig. 22.2b, c.

22.3   Tuning Up the Design

The adaptation permits to obtain a preliminary design according to the new request, which fulfills all the geometric relationships between the different components and whose parameters have a better approximation than the retrieved case. However, an additional phase is needed to tune up the design to fulfill all the design requirements, like the safety factors and the transmission life among others.

Before proceeding, the user is able to modify some parameters depending on his needs and experience. This is relevant because it is possible for the user to have certain restrictions for the fabrication of the new design, for example, not to have
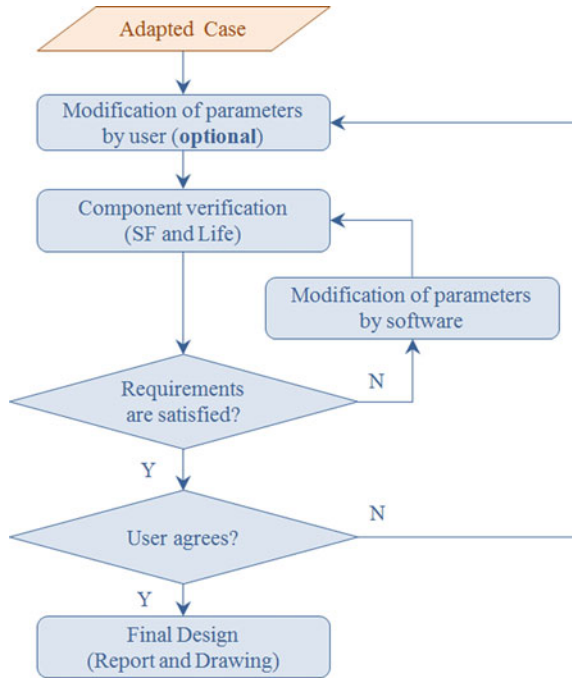
the same materials used in the retrieved case. Also, if the user has experience in the design of this reducer, he could suggest some modifications to improve the design. Figure 22.3 shows the tuning-the-design diagram, where the iterative component verification process and the user intervention are detailed.

22.3.1   Component Verification

The iterative verification process includes the calculation of the reference criteria, ergo, the safety factor or the life calculation, depending on the case. If the design does not fulfill all of the requirements, the software will automatically modify some parameters until all these requirements are fulfilled.

The verification of some components is based on standards. For instance, ISO Standards 6336-1, 6336-2 and 6336-3 are used to verify the gears. These standards stablish the design guidelines, including recommendations for the gearing factor and the contact and bending safety factors. At the time, the most-used bearings, keys, fasteners, among other components in gearbox reducer applications, have been considered according to DIN Standards. Fundamentals of Machine elements design

[3, 4, 12] are used to verify the shafts and other not normalized elements. For example, a procedure that uses both analytical and numerical simulation methods was developed to calculate stresses in the lateral walls of the welded housing [2]. Some elements are simply selected based on the dimensions of other components: this is the case of the circlips and the seals.

22.3.2 User Intervention and Final Design

The user is able to make modifications at two different phases of the design process: first, after adapting the retrieved case and second, after the verification of the components and tune up of the design. If the user makes changes after the tuning-the-design phase, the software will repeat the verification of all the components and the tune-up of the design. When the user accepts the design, the next phase is the generation of the manufacturing and assembly drawings. Also the user can generate a report of the obtained results and visualize the design in 3D. Finally, the design can be added to the case base, which can be utilized in future designs.

22.4 Software Implementation

The software is an Add-In that works on the Autodesk Inventor Professional 2017 platform or upper. This platform was chosen for the facilities offered for the generation and parameterization of 3D models, and the libraries of standard elements contained in the gearboxes.

When starting a new design, a window will be shown, where the workpath and the name of the project will be entered. Then the window shown in Fig. 22.4a will be opened, allowing entering the required data for the new design. By pressing the "Search a case" button, the program will execute the retrieve module and will show the retrieved cases in the right part of the window, where the calculated similarity value and the parameters of each case will be indicated. The most similar case will be selected by default, but the user will be able to select another case and continue with the adaptation through the "Adapt selected case" button. Using the "Take a Look at 3D Model" button, the 3D model of the assembly with the case already adapted will be opened in the working window. This can be seen in Fig. 22.4b. At this point, the user can make some changes using the "Make Design Changes" button if desired, or proceed to the final design tuning up, with the "Tuning the Design" button. Figure 22.4c shows the form that opens when the "Make Design Changes" button is pressed, where parameters that can be modified in the gears, shafts, bearings and housing can be seen.
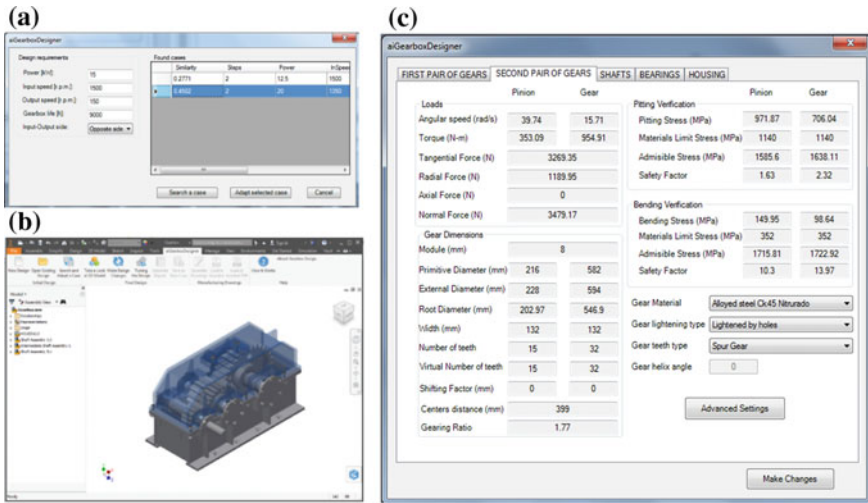
Fig. 22.4 **a** Data entry and retrieved cases, **b** 3D model of the adapted case, **c** Form to make changes in the design

The user can make also other modifications and repeat the tuning-the-design process. The same window has also a button to access to advanced settings of components.

The options for saving the design in the case base, generating the design report and the manufacturing drawings, are enabled at the end of the tuning-the-design process. *aiGearboxDesigner* automatically generates all the drawings of the gearbox, including the assembly drawings and manufacturing drawings of the components with non-standardized geometry on the same Autodesk Inventor platform or in PDF format. Figure 22.5 shows a drawing generated in PDF format of a gearbox.

22.5   Conclusions

aiGearboxDesigner developed by the authors is a software to completely design gearboxes of two and three steps with horizontal parallel shafts, cylindrical gears, and welded housing for medium and high power. The high degree of automation of the software does not prevent the user of the possibility of intervening in the design and making modifications, according to his needs and experience. The facilities offered by the system include the complete generation of the gearbox drawings. Artificial Intelligence, through the Case Based Reasoning technique, proves to be very useful in the task of machine design. The experience of this work permits to suggest its use in the design of other equipment and machines.
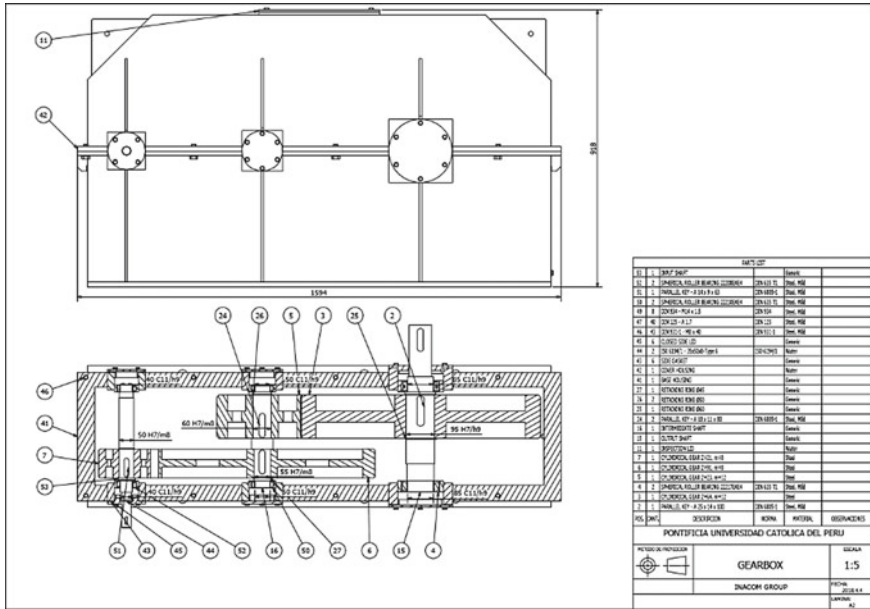
Fig. 22.5 Assembly drawing of a gearbox

References

1. Avramenko, Y., Kraslawski, A.: Case Based Design: Applications in Process Engineering. Springer (2008)
2. Blas, M.: Desarrollo de un algoritmo para el diseño de carcasas soldadas para cajas reductoras de engranajes cilíndricos, PUCP (2016)
3. Decker, K.: Elementos de máquinas, Urmo (1980)
4. Dobrovolsky, V.: Elementos de Máquinas, Editorial MIR (1976)
5. Hu, C., Zhao, D., Chen, X.: Knowledge base system of spiral bevel gear based on design tree. Adv. Mater. Res. **472**, 1739–1743 (2012)
6. Ji, A., Huang, Z., Xu, H., Chen, Z.: Design system of the two-step gear reducer on case-based reasoning. Chin. J. Mech. Eng. **22**(5), 671–679 (2009)
7. KISSsoft AG: KISSsoft. www.kisssoft.ch
8. Klebanov, B., Barlam, D., Nystrom, F.: Machine Elements: Life and Design. CRC Press (2007)
9. Lenz, M., Bartsch-Spörl, B., Burkhard, H., Wess, S.: Case-Based Reasoning Technology: From Foundations to Applications. Springer (1998)

10. Moya-Rodríguez, J., Becerra-Ferreiro, A., Chagoyén-Méndez, C.: Utilización de Sistemas Basados en Reglas y en Casos para diseñar transmisiones por tornillo sinfín. Ingeniería Mecánica **15**(1), 01–09 (2012)
11. Niemann, G.: Tratado teórico-práctico de elementos de máquinas: cálculo, diseño y construcción, Editorial Labor (1973)
12. Orlov, P.: Ingeniería de Diseño, Editorial MIR (1985)
13. Romax Technology: RomaxDESIGNER. www.romaxtech.com/software/romaxdesigner
14. Smart Manufacturing Technology: MASTA, www.smartmt.com/cae-software/masta/
15. Wittel, H., Muhs, D., Jannasch, D.: Roloff/Matek Maschinenelemente: Normung, Berechnung, Gestaltung-Lehrbuch und Tabellenbuch. Springer (2011)

Chapter 23
Compliant Mechanisms for Ultra-Precise Applications

**René Theska, Lena Zentner, Thomas Fröhlich, Christian Weber,
Eberhard Manske, Sebastian Linß, Philipp Gräser, Felix Harfensteller,
Maximilian Darnieder and Michael Kühnel**

Abstract This paper reports about enhanced compliant mechanisms with flexure hinge based on new analytic and/or FEM models that have been manufactured by state of the art wire EDM technology. Experimental proofs at test benches, equipped with ultra-precise interferometer based length and angular measurement systems, show first time the residual deviation to the intended path of motion with a resolution of nanometers/arc seconds. Theoretically determined and measured data are in good

R. Theska (✉) · P. Gräser · M. Darnieder
Precision Engineering Group, Department of Mechanical Engineering, Institute of Design and Precision Engineering, Technische Universität Ilmenau, Ilmenau, Germany
e-mail: rene.theska@tu-ilmenau.de

P. Gräser
e-mail: philipp.graeser@tu-ilmenau.de

M. Darnieder
e-mail: maximilian.darnieder@tu-ilmenau.de

L. Zentner · S. Linß
Compliant Systems Group, Department of Mechanical Engineering, Technische Universität Ilmenau, Ilmenau, Germany
e-mail: lena.zentner@tu-ilmenau.de

S. Linß
e-mail: sebastian.linss@tu-ilmenau.de

T. Fröhlich · M. Kühnel
Process Measurement Group, Department of Mechanical Engineering, Institute of Process Measurement and Sensor Technology, Technische Universität Ilmenau, Ilmenau, Germany
e-mail: thomas.froelich@tu-ilmenau.de

M. Kühnel
e-mail: michael.kuehnel@tu-ilmenau.de

C. Weber · F. Harfensteller
Engineering Design Group, Department of Mechanical Engineering, Institute of Design and Precision Engineering, Technische Universität Ilmenau, Ilmenau, Germany
e-mail: christian.weber@tu-ilmenau.de

F. Harfensteller
e-mail: felix.harfensteller@tu-ilmenau.de

correlation. Repeatability limitations are rather more given by the residual noise of the overall test arrangement and mainly not by the mechanism itself.

Keywords Compliant mechanism · Ultra-precise applications · Flexure hinge · Nanopositioning · Nanomeasurement · Precision engineering

23.1 Introduction

Compliant mechanisms with flexure hinges are widely used in precision engineering, precision metrology and precision positioning since they are free of friction and backlash. They do not need lubrication and they do not show wear, thus being the perfect choice for clean room, vacuum or even space applications. Drawbacks are given by limited motion ranges and deviations to the ideal trajectory. Existing theories are describing the kinematic behavior not with adequate precision as required for ultra-precise devices and machines. Advanced manufacturing technologies are opening more design freedom for the flexure hinge and the overall mechanism geometry. Non-conventional shaped hinges with minimized wall thicknesses are allowing functional improvements. A systematic synthesis of compliant mechanisms, taking geometries that are more complex in consideration, which is supporting goal-oriented solutions and optimization in the design process, is missing. This paper presents investigations at the department of mechanical engineering of the TU Ilmenau, ongoing at the research groups of compliant systems, process metrology, production and precision measurement technology, precision engineering and design methodology that are conjointly directed to gain a better understanding of compliant mechanisms and to develop advanced synthesis strategies. These activities are driven by demands out of actual research field's at the Faculty of Mechanical Engineering, namely compliant systems [18], nanopositioning, nanomeasurement [14], nanofabrication, ultra-precise force, torque and tilt measurement and ultra-precise weighing technology [2, 3]. The whole development circle from simulation over design and manufacturing of prototypes, testing and measurement and back to simulation will be addressed.

23.2 Basic Elements of Compliant Mechanisms

Flexure hinges are material coherent pairings with the function of pivot joints in compliant mechanisms. The elasto-kinematic behavior is influenced by their geometrical form and their integration in the compliant mechanism [13]. Based on

E. Manske
Production and Precision Measurement, Department of Mechanical Engineering, Institute of Process Measurement and Sensor Technology, Technische Universität Ilmenau, Ilmenau, Germany
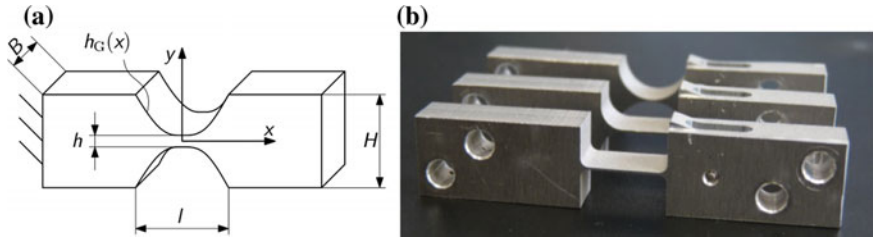e-mail: eberhard.manske@tu-ilmenau.de

Fig. 23.1 Geometrical parameters of a flexure hinge (**a**) and flexure hinges with different notch contours (**b**)
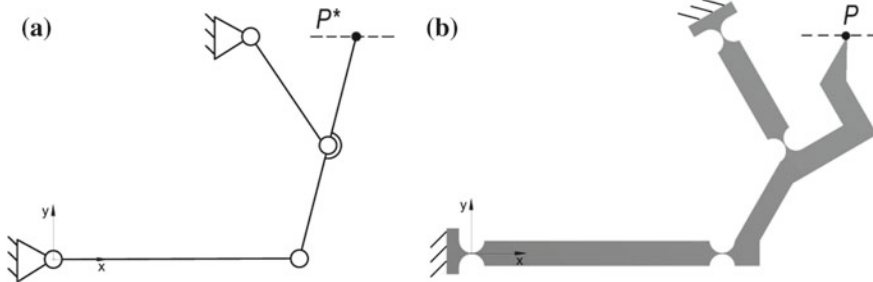

Fig. 23.2 Four-bar mechanism as example for the replacing method in synthesis process of a compliant mechanism: rigid-body model (**a**) and a compliant mechanism (**b**) with four revolute joints and four links

conventional machining, flexure hinges are commonly shaped to semi-circular or corner-filleted geometries see Fig. 23.1. These contours are causing limited angles of rotation and considerable shifts of the center of rotation [10, 16]. To overcome this, flexure hinges with optimized polynomial contours are investigated and integrated in compliant mechanisms [11]. All mechanisms presented in this paper are based on flexure hinges with concentrated compliance, rectangular cross-section and a symmetric polynomial contour.

There are different approaches for the synthesis of compliant mechanisms. A widely accepted one, also chosen for this research, is the rigid-body replacement approach [7]. Based on the requirement on the kinematic behavior of the mechanism, a rigid-body model with a predetermined path of motion is chosen or designed. Alternatively, classical methods of structural mechanism synthesis can be applied as well, which is not the focus of this work. To transform the rigid-body model into a compliant mechanism, flexure hinges substitute the idealized pivot joints; while the rotation axes are kept in the same position, see Fig. 23.2. The hinges are connected by links with vastly higher stiffness.

Thereby resulting deviations to the ideal path of motion are depending on several influences. The shift of the rotation axis of the hinges and the residual deformations of the interlinking elements are of capital importance. Refined analytical models

Table 23.1 Comparison of the values of the FEM simulation and the measurement of manufactured prototype a parallel four-bar mechanism and a planar stage with a maximum travel range of ± 10 mm

	Parallel crank mechanism		Planar stage			
	Calculation	Measurement	Calculation		Measurement	
Travel direction	x	x	x	y	x	y
$|d_x|$ in m	–	–	–	$2 \cdot 10^{-6}$	–	$2.8 \cdot 10^{-6}$
$|d_y|$ in m	$614 \cdot 10^{-6}$	$665 \cdot 10^{-6}$	$1.2 \cdot 10^{-6}$	–	$1.2 \cdot 10^{-6}$	–
δ in"	0.29	6.9	5	5.9	5	6

and/or FEM simulations of flexure hinges and links are implemented to calculate the path of motion of compliant mechanisms more precisely.

23.3 Compliant Mechanisms

In high-precision measurement and positioning frequently a straight line respectively, an approximated straight-line motion with best possible reproducibility is required [1]. In comparison to rigid-body models with exact straight-line motion, compliant mechanisms show always deviations. The developed synthesis algorithm allows it, to simulate the kinematic behavior before manufacturing. The magnitude of deviation can be minimized by the variation of parameters of the hinges, as well as by dedicated combination and orientation of the hinges.

Figure 23.3 shows first a common parallel crank mechanism with approximated straight-line motion (Fig. 23.3a). The second one is a planar stage based on an in-house created mechanism with exact straight-line motion, based on two parallel crank mechanisms and an additional crank in both directions (Fig. 23.3b). Flexure hinges with optimized polynomial contours (6th-order for parallel crank; 4th-order for planar stage) are replacing the idealized joints. For the simulation and the investigation of the kinematic behavior, FEM models are created (Fig. 23.3c, d).

For the evaluation of the FEM simulations measurements are done at manufactured prototypes by use of test benches designed specifically for this purpose (Fig. 23.4a, b).

23.4 Experimental Verification

The optimized models are verified by measurements taken at prototypes made from different materials (hard aluminum alloys AW 2024, AW 7075) [4, 5, 9]. Output parameters like lateral (d_x, d_y) and angular (δ) deviations to the straight line are measured by use of appropriate especially designed test benches (Table 23.1, Fig. 23.4).
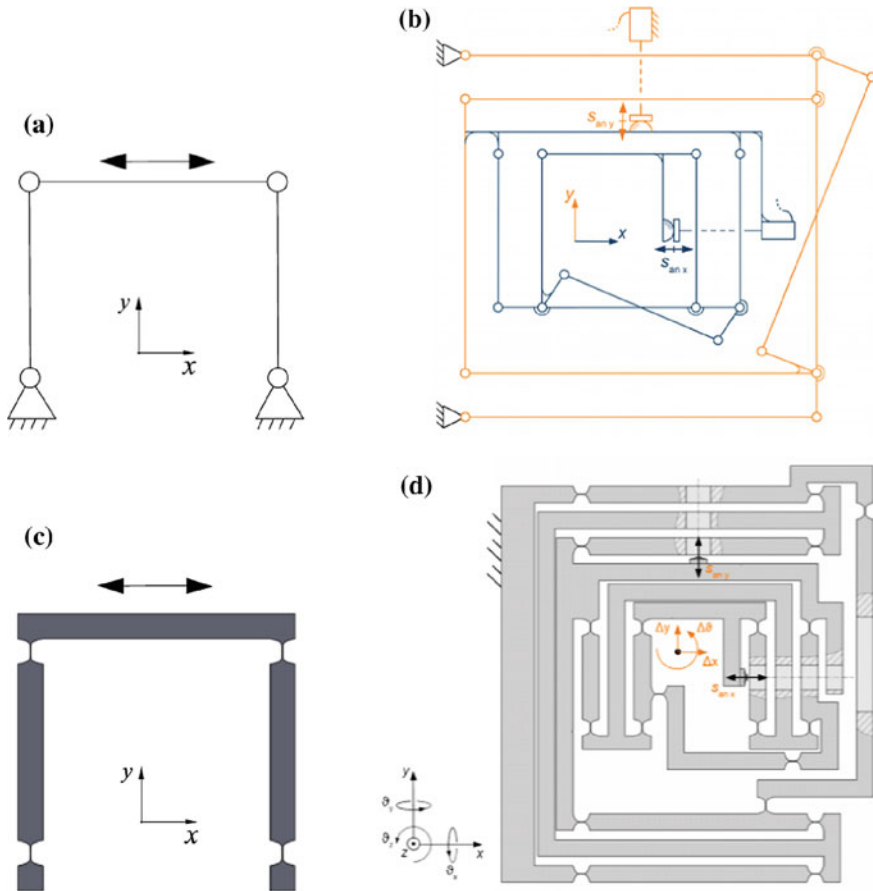
Fig. 23.3 Rigid-body models of parallel crank mechanism and planar stage based on two orthogonal 10-hinge mechanisms (**a**) and (**b**); designed compliant mechanisms with polynomial flexure hinge design (**c**) and (**d**)

Beside the absolute deviations to the path of motion, excellent reproducibility of the motion behavior is of severe interest, since systematic deviations can be corrected or compensated. First taken measurements at the parallel crank mechanism (Fig. 23.3e) are showing reproducibility below 300 nm for the motion in x- and y-direction. For the planar stage mechanism (Fig. 23.3f) the measured values in x-direction are under 140 nm and in y-direction under 20 nm. While the results for the planar stage is in accordance to the expectations, the comparably weak result for the simpler geometry of the parallel crank mechanism leads to the conclusion, that there is the need of improvement of the test set up.
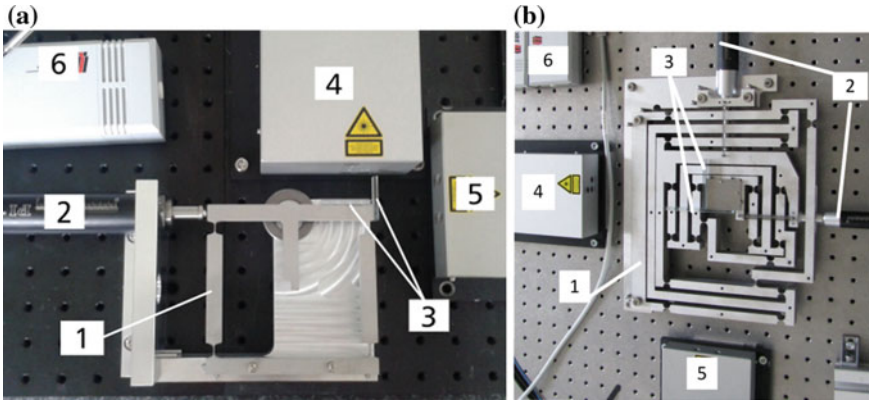
Fig. 23.4 Measurement of manufactured prototypes on special designed test benches with 1—compliant mechanism, 2—linear actuators, 3—plane mirrors, 4—Double Beam Interferometer, 5—Single Beam Interferometer and 6—environmental sensors
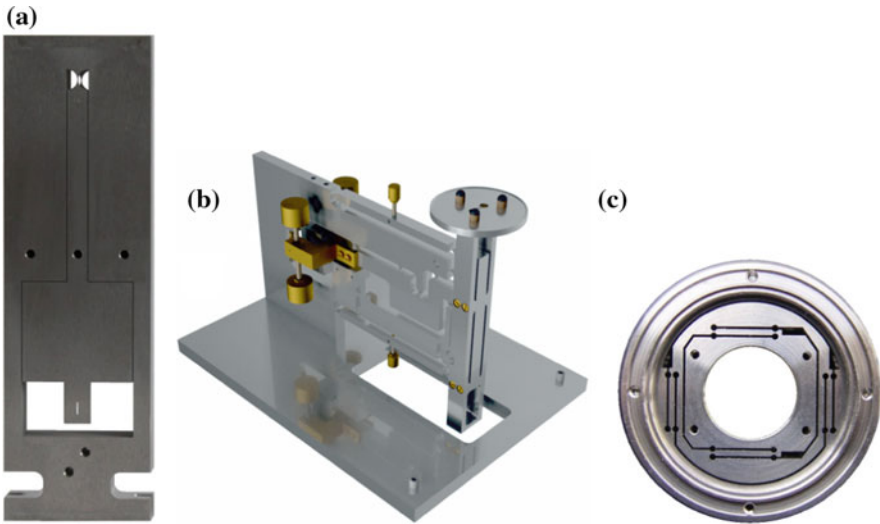

Fig. 23.5 Applications for compliant mechanisms in ultra-precise measurement systems: **a** monolithic pendulum of a tilt-meter, **b** monolithic load cell **c** adjustable lens mount

23.5 Applications

Compliant mechanisms are used in a growing number of actual research fields at TU Ilmenau like nanopositioning, nanomeasurement [4–6, 9–12, 14, 15, 17], nanofabrication, ultra-precise force, torque and tilt measurement [8] and ultra-precise weighing technology [2, 3]. Figure 23.5 shows three examples.

23.6 Summary

Compliant mechanisms show many advantages in precision engineering. In combination of advanced synthesis strategies and manufacturing technologies there is further potential of optimization of the kinematic behavior, e.g. deviations to the path of motion and/or the maximum travel range. Measurements taken at manufactured prototypes show a good correlation to the theoretical results. Ongoing research work will concentrate on further enhancements by use of different flexure hinge contours and different hinge orientations in mechanisms. The measurement set up will be further improved.

References

1. Brouwer, D.M., Meijaard, J.P., Jonker, J.B.: Large deflection stiffness analysis of parallel prismatic leaf-spring flexures. Precis. Eng. **37**, 505–521 (2012). https://doi.org/10.1016/j.precisioneng.2012.11.008
2. Darnieder, M., Marangoni, R.R., Theska, R., Fröhlich, T., Rahneberg, I.: Contribution to the mechanical enhancement of load cells in precision weighing technology by means of advanced adjustment strategies. In: Proceedings of the 17th International Conference of the European Society for Precision Engineering and Nanotechnology, pp. 411–412 (2017)
3. Darnieder, M., Torres, M., Linß, S., Theska, R.: On precise modelling of very thin flexure hinges. In: Proceedings of the 18th International Conference of the European Society for Precision Engineering and Nanotechnology, pp. 87–88, ISBN: 978-0-9957751-2-1 (2018)
4. Gräser, P., Linß, S., Zentner, L., Theska, R.: Design and experimental characterization of a flexure hinge-based parallel four-bar mechanism for precision guides, In: Zentner, L., Corves, B., Jensen, B., Lovasz, E.-C. (Eds.), Microactuators and Micromechanisms, Vol. 45 of Mechanisms and Machine Science, Springer International Publishing, Cham, pp. 139–152. https://doi.org/10.1007/978-3-319-45387-3_13 (2017)
5. Gräser, P., Linß, S., Zentner, L., Theska, R.: Increasing the stroke of an ultra-precise compliant mechanism with optimised flexure hinge contours. In: Proceedings of the 16th International Conference of the European Society for Precision Engineering and Nanotechnology, pp. 487–488. ISBN: 978-0-9566790-8-6 (2016)
6. Gräser, P., Linß, S., Räder, T., Zentner, L., Theska, R.: Investigations of the geometrical scaling in the systematic in the systematic synthesis of compliant mechanisms. In: Proceedings of the 18th International Conference of the European Society for Precision Engineering and Nanotechnology, pp. 67–88. ISBN: 978-0-9957751-2-1 (2018)
7. Howell, L.L., Magleby, S.P., Olsen, B.M.: Handbook of Compliant Mechanisms. Wiley, Chichester (2013)
8. Kuehnel, M., Fern, F., Fröhlich, T.: Novel monolithic pendulum tiltmeter with nanorad resolution. In: Technisches Messen: tm: Sensoren, Geräte, Systeme—Berlin: De Gruyter. https://doi.org/10.1515/teme-2017-0097 (2017)
9. Kuehnel, M., Hilbrunner, F., Büchner, H., Jäger, G., Manske, E., Fröhlich, T.: Traceable determination of mechanical parameters of binocular shaped force transducers according to EN ISO 376. In: Proceedings of XX IMEKO World Congress. Busan, Republic of Korea (2012)

10. Linß, S., Erbe, T., Theska, R., Zentner, L.: The influence of asymmetric flexure hinges on the axis of rotation. In: 56th International Scientific Colloquium, Ilmenau, Germany, urn:nbn:de:gbv:ilm1-2011iwk-006:6 (2011)
11. Linß, S., Milojevic, A., Pavlovic, N.D., Zentner, L.: Synthesis of compliant mechanisms based on goal-oriented design guidelines for prismatic flexure hinges with polynomial contours. In: 14th World Congress in Mechanism and Machine Science, Taipei, Taiwan. https://doi.org/10.6567/iftomm.14th.wc.ps10.008 (2015)
12. Linß, S., Gräser, P., Räder, T., Henning, S., Theska, R., Zentner, L.: Influence of geometric scaling on the elasto-kinematic properties of flexure hinges and compliant mechanisms. Mech. Mach. Theor. **125C**, 220–239 (2018). https://doi.org/10.1016/j.mechmachtheory.2018.03.008
13. Lobontiu, N.: Compliant Mechanisms: Design of Flexure Hinges, CRC Press, Boca Raton, Fla. (2003)
14. Manske, E., Füssl, R., Mastylo, R., et al.: Ongoing trends in precision metrology, particularly in nanopositioning and nanomeasuring technology. In: TM-Technisches Messen 82 (2015) 7–8 pp. 359–366 (2015)
15. Marangoni, R.R., Rahneberg, I., Hilbrunner, F., Theska, R., Fröhlich, T.: Analysis of weighing cells based on the principle of electromagnetic force compensation. In: Measurement Science and Technology (2017)
16. Paros, J.M., Weisbord, L.: How to design flexure hinges. Mach. Des. **25**, 151–156 (1965)
17. Sondermann, M.: Mechanische Verbindungen zum Aufbau optischer Hochleistungssysteme, PhD Thesis, Institut für Maschinen- und Gerätekonstruktion, TU Ilmenau, Ilmenau, XVI, 162 (2011)
18. Zentner, L.: Nachgiebige Mechanismen. De Gruyter Oldenbourg, München (2014)

Chapter 24
Tilt Sensitivity Modeling of a Monolithic Weighing Cell Structure

Maximilian Darnieder, Thomas Fröhlich and René Theska

Abstract Weighing cells used in mass comparators are among the most sensitive force measurement devices existing, while being subject to high loads of e.g. 1 kg. The mechanical system needs to be extremely sensitive in measurement direction while being insensitive in all other directions. A disturbing factor is the tilt of the compliant mechanism relative to the gravity vector. In a small scale this tilt is time dependent and requires either an additional compensation mechanism or an insensitive configuration of the weighing cell itself. The present study focuses on the latter. A planar structure of a weighing cell is modeled by the use of a three dimensional finite element model. The gravity vector is represented in spherical coordinates, allowing the modeling of tilt about two axes. The resulting tilt reactions for the two axes are evaluated and compared.

24.1 Introduction

Over a wide range of applications in technology quasistatic ground tilt can be neglected completely. For sensitive measurement equipment, leveling of the device is critical for precise results. This holds true for precision weighing technology. Vacuum mass comparators reach measurement uncertainties down to fractions of a micro-gramm. At this level of sensitivity, time dependent ground tilt, due to natural events, represents a relevant contribution to the measurement uncertainty. Two possible solutions are available to reduce the impact on the measurand [8]:

M. Darnieder (✉) · R. Theska
Precision Engineering Group, Institute for Design and Precision Engineering, Department of Mechanical Engineering, Technische Universität Ilmenau, Ilmenau, Germany
e-mail: maximilian.darnieder@tu-ilmenau.de

R. Theska
e-mail: rene.theska@tu-ilmenau.de

T. Fröhlich
Process Measurement Group, Institute for Process Measurement and Sensor Technology, Department of Mechanical Engineering, Technische Universität Ilmenau, Ilmenau, Germany
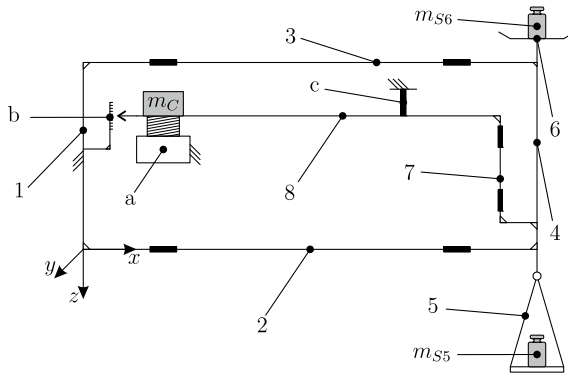e-mail: thomas.froehlich@tu-ilmenau.de

Fig. 24.1 Basic weighing cell structure with 1-base, 2-lower lever, 3-upper lever, 4-load carrier, 5-lower weighing pan, 6-upper weighing pan, 7-coupling element, 8-transmission lever. Further components attached to the monolithic structure are: m_{S5}, m_{S6}- sample weights, m_C- counter weight, a- voice coil actuator, b- position sensor, c- flexure hinges

- compensation by closed loop control of base tilt
- insensitive adjustment of the weighing cell (*autostatic state*)

The latter is dealt with in the following theoretical study on the tilt sensitivity of a monolithic weighing cell structure. For equal arm beam balances the term *autostatic state* was coined by Conrady already in 1922 [1] and was taken up and extended in [6, 8]. In this special state, the balance is insensitive to tilt of its base about the y-axis (Θ). The theory was initially derived for knife edge balances and was then applied to beam balances with flexure strips.

Electro-mechanically force compensated balances (EMFC-balance) have an extended mechanism, consisting of a transmission lever in combination with a parallelogram guide, see Fig. 24.1. Similar to the beam balances it was shown for EMFC weighing cells that the tilt sensitivity of the structure can be significantly reduced [2–4]. A possibility represents the mounting of adjustment masses to certain part of the weighing cell in order to adjust the respective centers of gravity within the weighing cell.

The present consideration is restricted to the planar weighing cell structure shown in Fig. 24.2. It stands to reason that this structure differs in their tilt sensitivity for tilts in different directions. Previous research on the tilt sensitivity of weighing cells focused on the tilt about the z-axis in the notation of this paper. The tilt about the x-axis, though is of the same relevance and has not been considered so far.

24.2 Modeling

The outset for the investigation is a three dimensional finite element model, developed in ANSYS® parametric design language. Geometrical nonlinearities are considered. It was shown in theory that the tilt sensitivity can be adjusted to very small values.
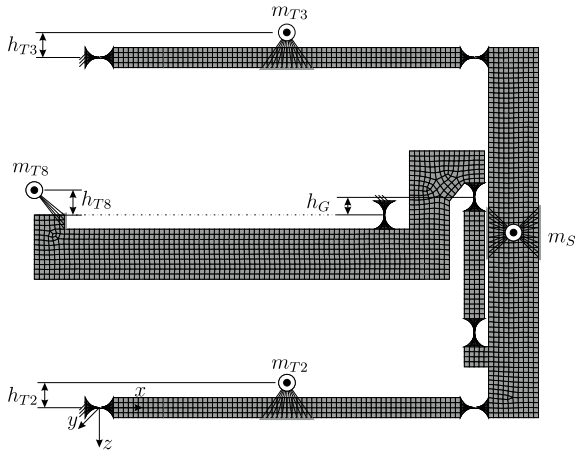
Fig. 24.2 Three-dimensional finite element model of the structure with adjustable point masses connected to the respective parts. The geometrical properties are: structure depth $10\,\mathrm{mm}$; ratio of the transmission lever $i = 18/70$; $h_{\mathrm{G}} = h_{\mathrm{T2}} = h_{\mathrm{T3}} = h_{\mathrm{T8}} = 0\,\mathrm{m}$; $m_{\mathrm{S}} = 1.0\,\mathrm{kg}$; $m_{\mathrm{T8}} = 0.272\,\mathrm{kg}$; $m_{\mathrm{T2}} = m_{\mathrm{T3}} = 0.05\,\mathrm{kg}$; $g = 9.81\,\mathrm{m\,s^{-2}}$; $E = 71000\,\mathrm{N\,mm^{-2}}$; $\nu = 0.33$; $\rho_{\mathrm{Al}} = 2770\,\mathrm{kg\,m^{-3}}$

Especially in this adjusted case, the tilt sensitivity for $\varPhi$ may represent a major limiting factor. Besides the two tilt axis x and y, the consideration distinguishes between *precision balances* with significant electrical weighing ranges and *mass comparators* with a very limited weighing range. Even though these devices are generally operated under well controlled environmental conditions, temperature, air pressure and many more factors have to be taken into account. The present modeling approach neglects these effects and focuses on the tilt reaction of the structure.

The tilt sensitivity of the weighing cell is defined as the difference of the measurand versus the tilt angle of the base of the weighing cell relative to the gravity vector **g**. For a balance, this would suggest a value in kilogram versus degrees. However, the present consideration is limited to force differences since the focus is the mechanical system itself. The closed loop control of the electromagnetic force compensation exerts a Lorentz force to the free end of the transmission lever to keep the weighing cell in static equilibrium. If this force changes with the tilt of the weighing cell with respect to the gravity vector, the weighing cell is tilt sensitive. The mechanical part of the tilt sensitivity is exactly this force difference at the transmission lever without considering the voice coil actuator and the position sensor. The tilt sensitivity can be expressed by the difference quotients $dF/d\varTheta$ and $dF/d\varPhi$. The results from the calculations are obtained in the form $F^* = F - F_0$, where F_0 is the reaction force for a perfectly aligned weighing cell ($\varTheta = \varPhi = 0°$). The slope of the presented plots of F^* equals the tilt sensitivity at the respective point. Modeling assumptions are:

- the weighing pan (5) is connected to the load carrier (4) at its geometrical center through a perfect gimbal mount with zero stiffness, realized by a fixed point mass

- each weighing cell structure is modeled in *precision balance* and *mass comparator* configuration, referring to the initial force the electromagnetic actuator exerts on the transmission lever:

  – *precision balance*: electromagnetic actuator force equivalent to 0.1 kg
  – *mass comparator*: electromagnetic actuator force equivalent to 0.001 kg

24.2.1 Tilt

The tilt is modeled kinematically reversed. Instead of the base of the weighing cell, the gravity vector **g** is tilted with respect to the fixed base of the weighing cell. To consider tilt about two axes, the gravity vector **g** is described in spherical coordinates to determine its components in the spatial directions g_x, g_y, g_z, see Fig. 24.3. The following equations describe the components of the gravity vector:

$$g_x = g \, \cos(\varphi) \, \sin(\theta)$$
$$g_y = g \, \sin(\varphi) \, \sin(\theta)$$
$$g_z = g \, \cos(\theta)$$

Fig. 24.3 Spherical coordinates (g, θ, φ) to represent the gravity vector **g** in the three-dimensional space. The main symmetry plane of the weighing cell coincides with the xz-plane in this figure. The azimut angle θ is the tilt angle of the weighing cell. The polar angle is: $\varphi \in [0° \ 360°]$
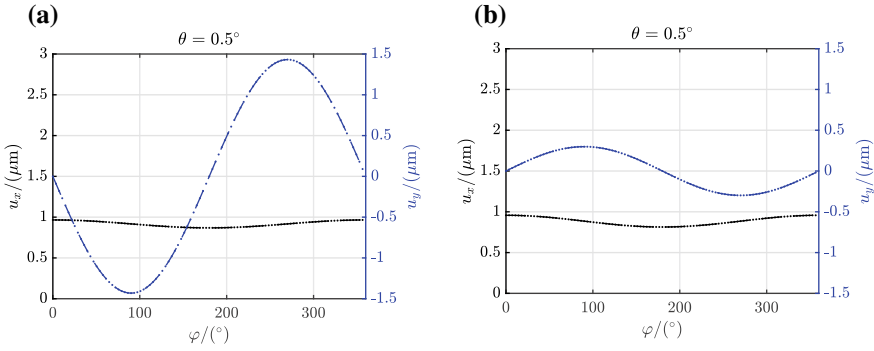
(a)

(b)
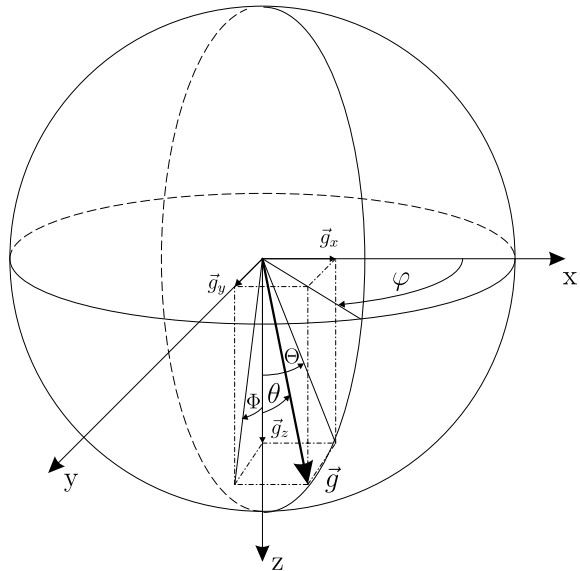
Fig. 24.4 Tilt induced deformation at the free end of the transmission lever of the weighing cell. Voice coil actuator and position sensor are directly affected by the displacements **a** Deformations of the precision weighing cell configuration **b** Parasitic deformations of the *mass comparator* configuration

24.2.2 Interaction with Other Components

The determination of a mass value in kilogram involves additional components like the position sensor and the voice coil actuator. These are simplified as ideal components in the pure mechanical simulations. Parasitic deformations of the weighing cell due to tilt affects the sensitivity of these components and will result in additional changes to the measured value in kilogram. The consideration of the mentioned effects is limited to a deflection based linear determination of the change in sensitivity of the components that is known by preceding research activities. For the voice coil actuator the deviations of the actuator constant in force over current has been determined experimentally in [7]. They state that the actuator constant varies quadratically for the radial displacement of the coil relative to the fixed pot magnet. The prefactor was determined to about $40 \cdot 10^3 \, \text{NA}^{-1}\text{m}^{-2}$. With a nominal value of $4.6 \, \text{NA}^{-1}$, a relative displacement of 0.1 mm changes the actuator constant by about 87 ppm [7].

The position sensor is based on a differential measurement that is insensitive to parasitic deflections in the z-direction if the components are perfectly aligned. The sensitivity of the sensor changes for the mentioned deflections as shown in [5], but this can be neglected, since it is solely utilized to reference the zero position of the transmission lever. Without experimental investigation it is not possible to derive a statement about the error contribution of the position sensor which is assumed to be negligible at this point ($\Delta F_{\text{ps}} \approx 0$).

24.3 Results

The deformation of the structure of the weighing cell is especially relevant at the location of the components of the electromagnetic force compensation. In the pre-
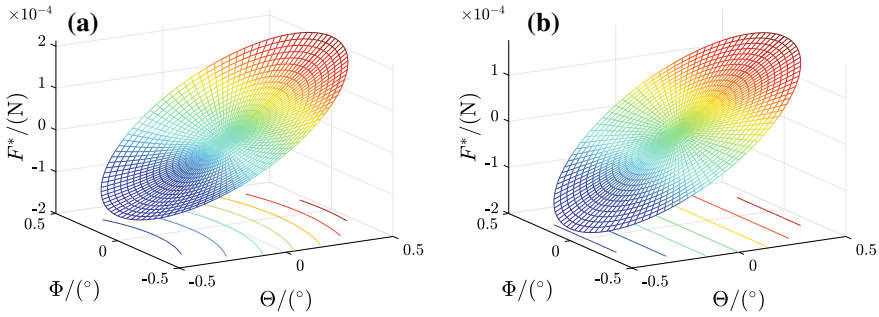
Fig. 24.5 Two axis tilt reaction at the location of the voice coil **a** Precision balance (weighing range ± 0.1 kg) **b** Mass comparator (weighing range ± 0.001 kg)

sented configuration, this point is located at the free end of the transmission lever. In Fig. 24.4a and b, the calculated deflection is presented. Even for a pronounced tilt angle of $\theta = 0.5°$, the deflection at the free end of the transmission lever is restricted to a few micrometers. Based on the previous information about the voice coil, the impact on the measurand is in the range of $0.1\,\mu g$ for a mass comparator. It becomes relevant for extremely precise measurements with vacuum mass comparators.

The tilt induced changes of the reaction force at the transmission lever are presented in the two main directions as surface plot, showing a full rotation of the **g**-vector with a constant tilt angle up to $0.5°$. This results in a characteristic form for the configurations of the weighing cell presented in Fig. 24.5a and b. A general observation for the unadjusted weighing cell with $h_G = h_{T2} = h_{T3} = h_{T8} = 0$ is that the tilt sensitivity for Θ is larger than for Φ. The Fig. 24.5a and b show an inclined disk. The tilt reaction for Θ is almost equal for the two configurations, but for Φ the *precision balance* configuration is more sensitive. This can be seen by the slightly indented disk in Fig. 24.5a.

In Figs. 24.6 and 24.7, the tilt behavior is presented for each direction separately. The *mass comparator* configuration (Fig. 24.6b) shows a linear behavior, whereas the *precision balance* (Fig. 24.6a) is additionally overlaid by a nonlinear function. The origin of this nonlinear function can be be explained when considering the tilt Φ. Here, the behavior is nonlinear and may be expressed by a trigonometric function. The comparison of Fig. 24.7a with Fig. 24.7b reveals that the values F^* differ by two orders of magnitude. The force carried by the electromagnetic actuator equally differs by two orders of magnitude. This suggests that this imbalance of masses is responsible for this part of the tilt sensitivity. As the Fig. 24.7a and b show, Eq. 24.1 describes the tilt reaction for Φ appropriately:

$$m_S\, g\, i\, \cos(\theta) = m_C\, g\, \cos(\theta) + F(\theta)$$
$$F^* = F(\theta = 0) - F(\theta) = (m_S\, i - m_C)\, g\, (1 - \cos(\theta)) \qquad (24.1)$$

Presumably, the origin of the nonlinear part for Θ is also caused by this imbalance.

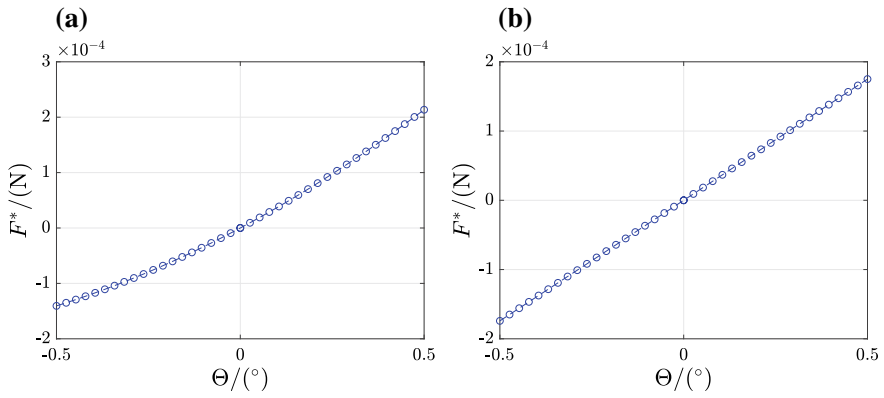**(a)**   **(b)**

Fig. 24.6 Two axis tilt reaction at the location of the voice coil for tilts about the z-axis **a** Precision weighing cell **b** Mass comparator

(a)   **(b)**
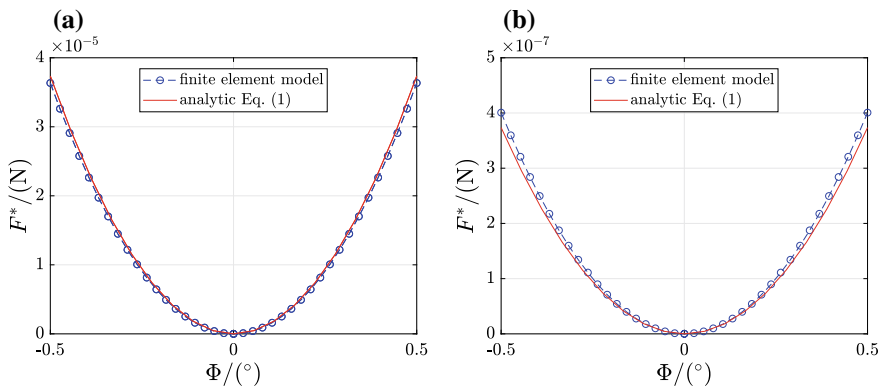

Fig. 24.7 Symmetric tilt effect about the x-axis. Finite element solution and analytic Eq. 24.1 **a** Precision weighing cell **b** Mass comparator

24.3.1   Summary

In a practical use of precision weighing cells, the tilt of their base is not restricted to one direction. A first theoretical approach for modeling the tilt reaction of the monolithic structure in two axis has been conducted with the following results:

- for a monolithic weighing cell with $h_G = h_2 = h_3 = h_8 = 0$ the tilt reaction is larger for Θ-tilt compared to Φ-tilt
- the tilt reaction for $\Phi \neq 0$ gains importance for an adjusted weighing cell
- for neither configuration the parasitic deflections of the free end of the transmission lever reach problematic values—even for large tilt angles of 0.5°, these values are limited to a few micrometers

- the additional tilt induced effects of the electro-magnetic force compensation system are comparably small
- the tilt reaction for Φ is predominantly influenced by the mass equivalent of the force F_0 that needs to be exerted by the electromagnetic actuator

References

1. Conrady, A.E.: A study of the balance. Proc. R. Soc. London Ser. A, Containing Papers of a Mathematical and Physical Character **101**(710), 211–224 (1922)
2. Darnieder, M., Marangoni, R.R., Theska, R., Fröhlich, T., Rahneberg, I.: Contribution to the mechanical enhancement of load cells in precision weighing technology by means of advanced adjustment strategies. In: Billington, D., Phillips, D. (eds.) Proceedings of the 17th International Conference of the European Society for Precision Engineering and Nanotechnology, pp. 411–412 (2017)
3. Darnieder, M., Theska, R., Fröhlich, T., Pabst, M., Wenig, R., Hilbrunner, F.: Design of high-precision weighing cells based on static analysis. In: Scharff, P., Weber, C., Schneider, A. (eds.) Engineering for a Changing World (2017)
4. Marangoni, R.R., Rahneberg, I., Hilbrunner, F., Theska, R., Fröhlich, T.: Analysis of weighing cells based on the principle of electromagnetic force compensation. Meas. Sci. Technol. (2017)
5. Marangoni, R.R., Schleichert, J., Rahneberg, I., Hilbrunner, F., Fröhlich, T.: A self-calibrating multicomponent force/torque measuring system. In: Engineering for a Changing World: Proceedings of 59th IWK, Ilmenau Scientific Colloquium, Technische Universität Ilmenau (2017)
6. Quinn, T.J.: The beam balance as an instrument for very precise weighing. Meas. Sci. Technol. **3**(2), 141 (1992)
7. Schleichert, J., Carlstedt, M., Marangoni, R.R., Rahneberg, I., Fröhlich, T.: Dynamische Charakterisierung eines Dreikomponenten Kraftsensors mit Hilfe eines Lorentzkraft-Lastwechslers. tm - Technisches Messen 83(7–8) (2016)
8. Speake, C.C.: Fundamental limits to mass comparison by means of a beam balance. Proc. R. Soc. A: Math. Phys. Eng. Sci. **414**(1847), 333–358 (1987)

Chapter 25
Optimization of Compliant Mechanisms by Use of Different Polynomial Flexure Hinge Contours

P. Gräser, S. Linß, L. Zentner and R. Theska

Abstract This paper presents the application of different polynomial flexure hinge contours in one compliant mechanism in order to increase both simultaneously the precision and the stroke of the output motion of compliant mechanisms. The contours of the flexure hinges are optimized in dependency of the required elasto-kinematic properties of the mechanism. This new approach for optimization is described in comparison to the use of identical common hinge contours. Based on previously optimized single polynomial flexure hinges, the validity of proposed guidelines is analyzed for a combination of several flexure hinges in two compliant mechanisms for linear point guidance. The rigid-body models of both mechanisms realize an approximated straight line as output motion. The compliant mechanisms are designed through the rigid-body replacement method and with different polynomial flexure hinges with orders varying from 2 to 16. The multi-criteria optimization is performed by use of non-linear FEM simulations. The derived values for the kinematic output parameters are compared for the ideal model and the optimized compliant mechanism. The results are discussed and conclusions for ongoing research work are drawn.

Keywords Compliant mechanism · Flexure hinge · Different polynomial contours · Optimization

P. Gräser (✉) · R. Theska (✉)
Precision Engineering Group, Department of Mechanical Engineering, Technische Universität Ilmenau, Ilmenau, Germany
e-mail: philipp.graeser@tu-ilmenau.de

R. Theska
e-mail: rene.theska@tu-ilmenau.de

S. Linß · L. Zentner
Compliant Systems Group, Department of Mechanical Engineering, Technische Universität Ilmenau, Ilmenau, Germany
e-mail: sebastian.linss@tu-ilmenau.de

L. Zentner
e-mail: lena.zentner@tu-ilmenau.de

25.1 Introduction

Systematic investigations on compliant mechanisms with flexure hinges have become necessary with increasing requirements for the resolution and reproducibility of high-precision applications in positioning and measurement technology.

As state of the art, different approaches for the design and synthesis of compliant mechanisms are available [3]. In dependency of the application of the compliant mechanism, the appropriate synthesis method is chosen. In the presented research, first a rigid-body model is selected and synthetized for the required path of motion. To transfer the rigid-body model into a compliant mechanism, the idealized revolute joints are replaced by flexure hinges with the same position of the rotation axes [2]. The hinges are connected by links with a significantly higher moment of inertia and thus stiffness. This approach of the synthesis is exemplarily shown in Fig. 25.1.

25.2 Design and Model of the Flexure Hinges

A flexure hinge is a material-coherent pairing with the function of a revolute joint due to the reduction of the stiffness in one section through notches [7]. The usual shape of the flexure hinge is a prismatic body with symmetrical notch contours [8]. Only in the non-deflected state, the ideal rotation axis is situated in the hinge center. In all other states, a shift of the rotational axis occurs [6].

The design of a flexure hinge includes different geometrical parameters with influence on the kinematic behavior of the single hinge and subsequently on the whole mechanism. Frequently used contours for the notch design are the:

- semi-circular contour (Fig. 25.2a),
- corner-filleted contour (Fig. 25.2b),
- elliptical contour (Fig. 25.2c).

To optimize the elasto-kinematic behavior of a flexure hinge—in order to minimize the rotational axis shift and to maximize the deflection angle by reducing the resulting
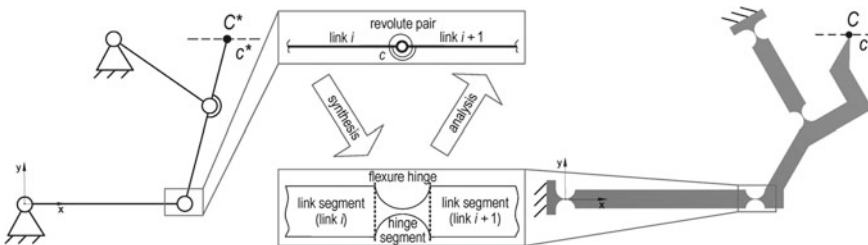

Fig. 25.1 Rigid-body replacement approach exemplified on a four-bar compliant mechanism for the guidance of the coupler point C along the approximated linear path c
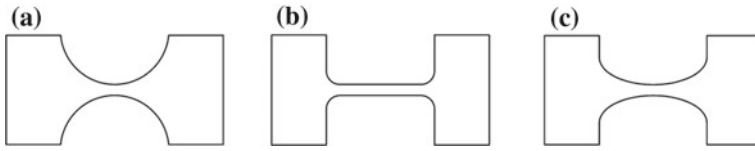
Fig. 25.2 Flexure hinges with varying notch design: **a** semi-circular contour, **b** corner-filleted contour, **c** elliptical contour
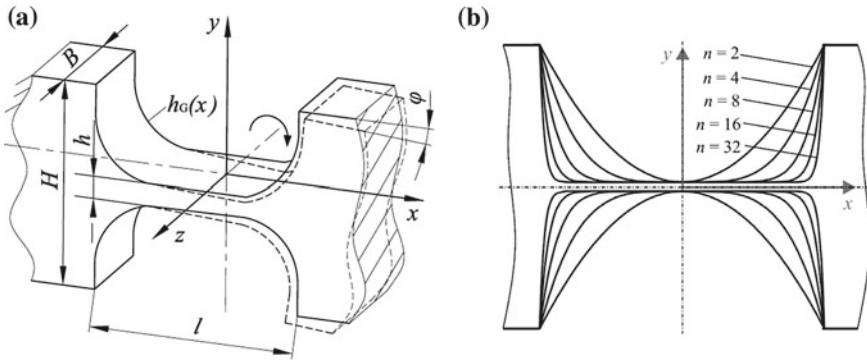

Fig. 25.3 Investigated notch flexure hinge as part of a compliant mechanism: **a** geometric parameters with deflected state, **b** adjustable polynomial hinge contour $h_G(x)$ according to Eq. (25.2) in dependence of the order n (drawn for hinge dimension ratios $\beta_l = 1$ and $\beta_h = 0.03$)

stress resp. strain—usually the notch contour is varied compared to standard contours. In the presented investigations, polynomial functions with different higher orders are used, which have been introduced in [4]. Depending on the polynomial order and the coefficients, arbitrary complex curves can be realized. Furthermore, nearly any elementary geometry can be approximated.

With the novel approach it is possible to optimize each hinge in dependence of the rotation angle in the rigid-body model. This allows simultaneously the minimization of the resulting strain and of path deviations [1]. The geometric parameters of a flexure hinge with a polynomial contour are shown in Fig. 25.3a. Most important are the hinge length ratio β_l, height ratio β_h and width ratio β_B, see Eq. 25.1.

$$\beta_l = \frac{l}{H}, \quad \beta_h = \frac{h}{H}, \text{ and } \beta_B = \frac{B}{H} \tag{25.1}$$

In the case of a polynomial contour, the order n of the contour height $h_G(x)$, see Eq. 25.2, is a further parameter to optimize the elasto-kinematic behavior. To illustrate this, some examples of polynomial contours with different orders are shown in Fig. 25.3b.

$$h_G(x) = h + \frac{(H - h)}{\left(\frac{l}{2}\right)^n} |x|^n; \text{ with } n \in \mathbb{N}, n \geq 2 \tag{25.2}$$
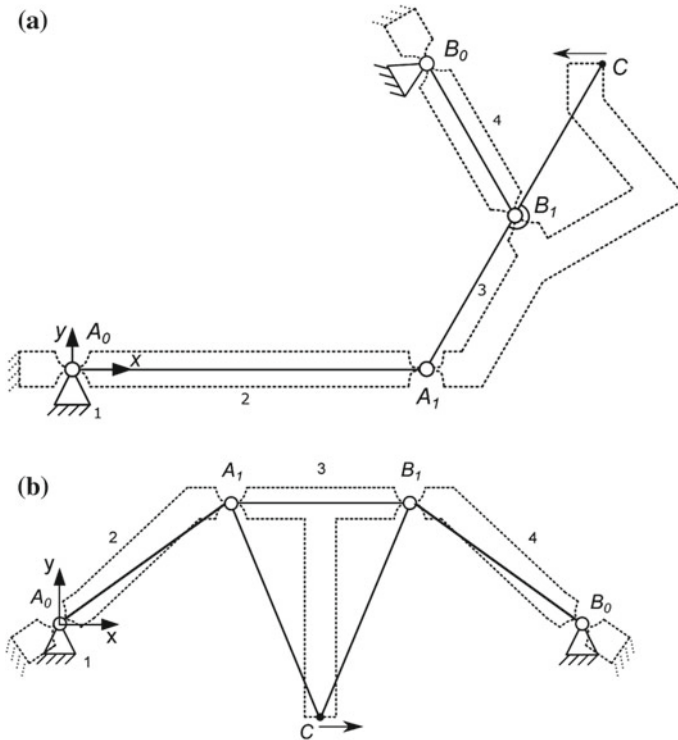
Fig. 25.4 Design of compliant point guidance mechanisms with polynomial flexure hinge design by replacing the rigid-body model: **a** EVANS mechanism, **b** ROBERTS mechanism

25.3 Angle-Based Synthesis of Compliant Mechanisms with Different Hinge Contours

The presented approach for the synthesis of a compliant mechanism with different polynomial flexure hinge contours is applied for linear guidance of the coupler point C. Two rigid-body models are chosen and synthesized for an approximated linear path of motion in x-direction up to $u_x = \pm 10$ mm. The first rigid-body model is a non-symmetric EVANS mechanism, see Figs. 25.4a and 25.5a, with the suitable link lengths $\overline{A_0 A} = \overline{AC} = 100$ mm, $\overline{AB} = \overline{BC} = 50$ mm, $\overline{A_0 B_0} = 132.3$ mm. The second rigid-body model is a symmetric ROBERTS mechanism, see Figs. 25.4b and 25.5b, with the suitable link lengths $\overline{A_0 A} = \overline{B_0 B} = 66.6$ mm, $\overline{AB} = 56.6$ mm, $\overline{A_0 B_0} = 165.7$ mm, $\overline{AC} = \overline{BC} = 73.6$ mm.

For the optimization of the compliant mechanism the relative rotation angles for each hinge are calculated based on the rigid-body models. The results for these angles for the displacement $|u_x| = 10$ mm are $\varphi_{A0} = 2.9°$, $\varphi_{A1} = 9.2°$, $\varphi_{B1} = 12.8°$, $\varphi_{B0} = 6.5°$ for the EVANS mechanism and $\varphi_{A0} = 3.8°$, $\varphi_{A1} = 10.4°$,
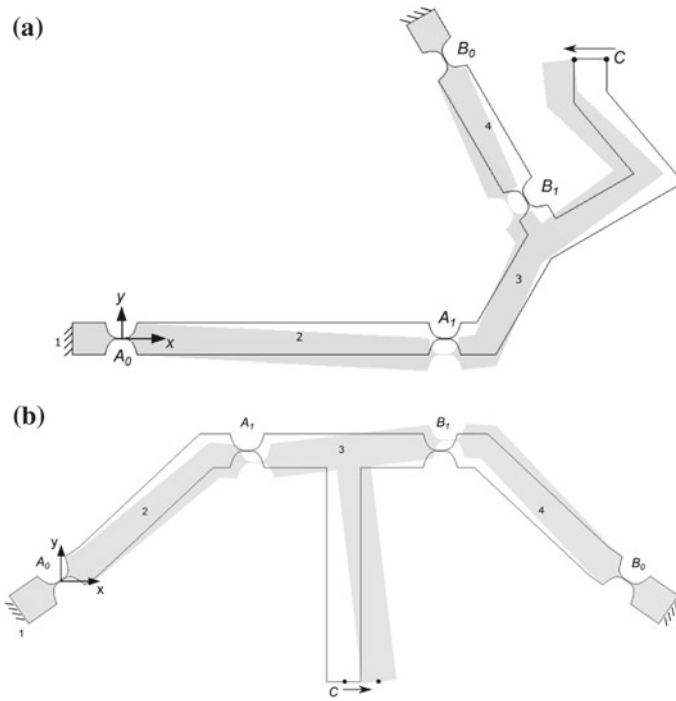
Fig. 25.5 Initial and deflected state of the compliant guidance mechanisms with the same direction of the crank rotation (FEM simulation results for $|u_x| = 10$ mm of point C; $\beta_l = 1$ and $\beta_h = 0.03$): **a** EVANS mechanism, **b** ROBERTS mechanism

Fig. 25.6 Simulation results for the motion paths c^* of the investigated mechanisms: straight-line deviation of the rigid-body model for both mechanisms
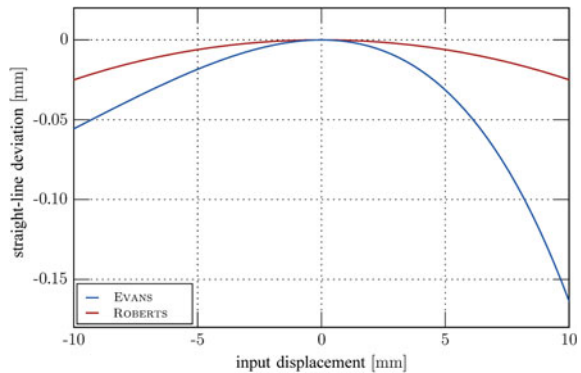
$\varphi_{B1} = 9.5°$, $\varphi_{B0} = 3.0°$ for the ROBERTS mechanism. These values are the basis of the presented approach for the multi-criterial optimization with different polynomial hinges. The motion paths of the rigid-body models already show a straight-line deviation in the hundred micrometer range, see Fig. 25.6.

25.4   Optimization and Results

In previous investigations, the order n of the polynomial function of each hinge contour was determined by a simplified, angle-based synthesis method based on design charts [5]. Accordingly, the presented investigations are intended to verify these results by a FEM-based full-factorial optimization. Therefore, the order n of each hinge is varied independently with each of the following values: 2, 3, 4, 5, 6, 8, 12, and 16. All 4096 possible combinations are simulated and evaluated for:

- straight-line deviation d_S (deviation of point C to the ideal straight line),
- path deviation d_P (deviation of C to the path of C^* in the rigid-body model),
- maximum strain ε_{max} in the whole mechanism (which limits the stroke),
- input force F_{in} at the coupler point to realize the deformed state.

For the presented mechanisms, the path of motion is calculated by means of non-linear FEM simulations for all designs. With regard to an accurate FEM model elaborate mesh studies are done. The mesh structure is varying for the link and hinge sections of the mechanism, while the hinges are meshed very fine. All simulations are done with large deflections. In Fig. 25.7 a set of curves of the motion path of all 4096 calculated designs is exemplarily shown for the EVANS mechanism.

Because of several optimization criteria and thus different cases, which can be regarded, there are different elasto-kinematic results for the optimal compliant mechanisms. The novel approach is, to use different polynomial flexure hinges in one mechanism. In contrast to this, the use of the same order for each hinge is especially suitable for mechanisms in which all hinge angles are comparable, like a parallel four-bar linkage [1]. The optimal results for the cases of identical hinges and different hinges in dependence of the objectives are shown in Table 25.1 for the EVANS mechanism and in Table 25.2 for the ROBERTS mechanism.

From both tables it is obvious that the polynomial order n of each flexure hinge influences the regarded elasto-kinematic properties. It depends on the application which optimization criterion is more important resp. weighted. In the case of the opti-

Fig. 25.7 Simulation results for the motion paths c of the investigated mechanisms: straight-line deviation of all 4096 calculated designs of the compliant EVANS mechanism with different polynomial flexure hinges ($\beta_l = 1$, $\beta_h = 0.03$)
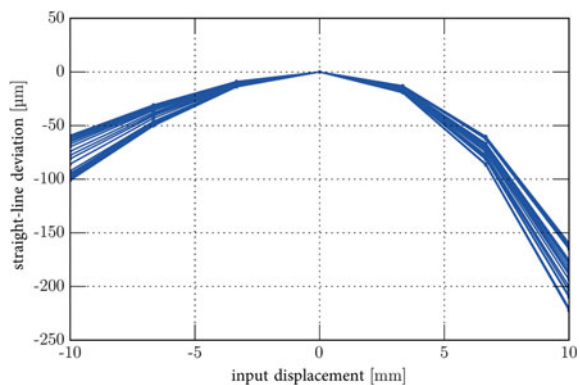
Table 25.1 Optimal results for the properties of compliant EVANS mechanisms ($u_x = -10$ mm, $\beta_l = 1$, $\beta_h = 0.03$, $\beta_B = 0.6$)

Minimization criterion		Polynomial orders				FEM results			
		n_{A0}	n_A	n_B	n_{B0}	d_s (μm)	d_p (μm)	ε_{max} (%)	F_{in} (N)
Identical hinges	Straight-line deviation d_s	2	2	2	2	−65.1	−9.5	3.29	8.7
	Path deviation d_p	2	2	2	2	−65.1	−9.5	3.29	8.7
	Maximum strain ε_{max}	16	16	16	16	−96.3	−40.7	0.54	1.2
	Straight-line deviation and strain equally weighted	16	16	16	16	−96.3	−40.7	0.54	1.2
Different hinges	Straight-line deviation d_s	16	16	2	2	−59.3	−3.6	3.29	6.4
	Path deviation d_p	16	16	2	2	−59.3	−3.6	3.29	6.4
	Maximum strain ε_{max}	16	16	16	16	−96.3	−40.7	0.54	1.2
	Straight-line deviation and strain equally weighted	3	8	16	5	−94.3	−38.7	0.54	1.6

Table 25.2 Optimal results for the properties of compliant ROBERTS mechanisms ($u_x = 10$ mm, $\beta_l = 1$, $\beta_h = 0.03$, $\beta_B = 0.6$)

| Minimization criterion		Polynomial orders				FEM results			
		n_{A0}	n_A	n_B	n_{B0}	d_s (μm)	d_p (μm)	ε_{max} (%)	F_{in} (N)
Identical hinges	Straight-line deviation d_s	8	8	8	8	0.1	25.1	0.57	1.2
	Path deviation d_p	2	2	2	2	−14.9	10.1	2.66	6.7
	Maximum strain ε_{max}	16	16	16	16	8.1	33.1	0.42	0.9
	Straight-line deviation and strain equally weighted	8	8	8	8	0.1	25.1	0.57	1.2
Different hinges	Straight-line deviation d_s	2	6	8	3	0	25.0	0.96	1.8
	Path deviation d_p	2	16	2	2	−24.6	0.4	2.43	3.8
	Maximum strain ε_{max}	16	16	16	16	8.1	33.1	0.42	0.9
	Straight-line deviation and strain equally weighted	2	6	8	3	0	25.0	0.96	1.8
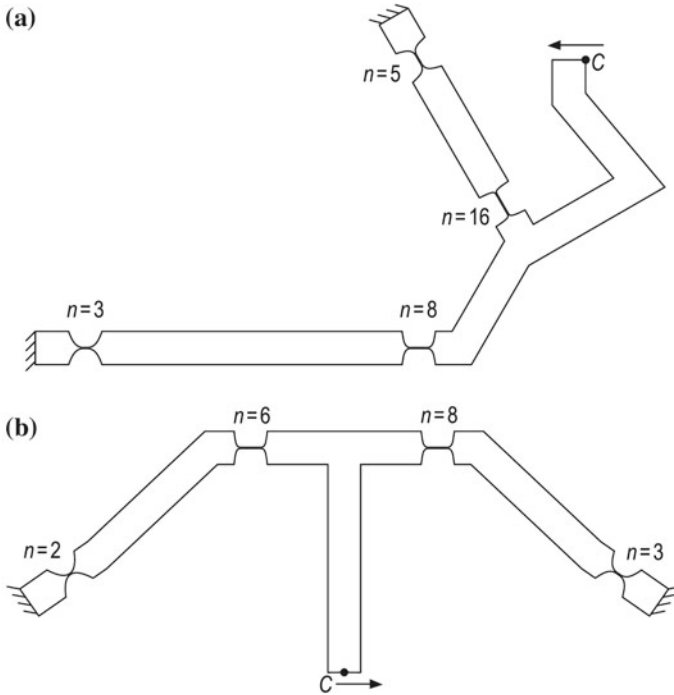
Fig. 25.8 Optimal compliant guidance mechanisms with different polynomial flexure hinges for a minimal straight-line deviation and large motion stroke (CAD model, $\beta_l = 1$, $\beta_h = 0.03$): **a** EVANS mechanism, **b** ROBERTS mechanism

mal compliant mechanism, the straight-line deviation can be even less than resulting for the rigid-body model. The path deviation compared to the rigid-body model can be nearly compensated in some cases.

A multi-criterial optimization with regard to a minimal straight-line deviation and, equally weighted, a minimal strain leads to an optimal design for each compliant mechanism with different polynomial flexure hinges (last rows of Tables 25.1 and 25.2), as shown in Fig. 25.8. Thus, these optimal compliant straight-line guidance mechanisms show a large motion range and precision simultaneously. Additionally, the input force can be adapted to requirements with this design approach.

25.5 Conclusion

For the investigations presented in this paper the application of different polynomial flexure hinge contours is introduced in order to increase simultaneously both, the precision and the stroke of the output motion of compliant mechanisms. Advantages of notch contour shapes, following polynomial functions of different orders for the

flexure hinges in one mechanism are shown. Numerous geometrically non-linear FEM studies generally confirm the results of previous analytic calculations and suggested design charts. Hence, the benefit of the novel angle-based synthesis method is verified. The utilization in the design and synthesis process is shown for two example mechanisms, the EVANS and the ROBERTS mechanism.

In further investigations the analytic and numeric calculations for the path of motion of exemplary compliant mechanism will be verified by measurements that will be taken at manufactured prototypes. This enables a qualitative and quantitative evaluation of the results for the synthesis process. Simultaneously it allows the formulation of guidelines and recommendations for the design of compliant mechanisms for highly precise motions in enlarged working areas as requested in numerous applications.

References

1. Gräser, P., Linß, S., Zentner, L., Theska, R.: Design and experimental characterization of a flexure hinge-based parallel four-bar mechanism for precision guides. In: Zentner, L., Corves, B., Jensen, B., Lovasz, E.-C. (Eds.), Microactuators and Micromechanisms, Vol. 45 of Mechanisms and Machine Science, pp. 139–152. Springer International Publishing, Cham. https://doi.org/10.1007/978-3-319-45387-3_13, 2017

2. Howell, L.L., Midha, A.: A method for the design of compliant mechanisms with small-length flexural pivots. J. Mech. Des. **116**, 280–290 (1994). https://doi.org/10.1115/1.2919359

3. Howell, L.L., Magleby, S.P., Olsen, B.M.: Handbook of Compliant Mechanisms. Wiley, Chichester (2013)

4. Linß, S., Erbe, T., Zentner, L.: On polynomial flexure hinges for increased deflection and an approach for simplified manufacturing. In: 13th World Congress in Mechanism and Machine Science, Guanajuato, Mexico, p. A11_512 (2011)

5. Linß, S., Milojevic, A., Pavlovic, N.D., Zentner, L.: Synthesis of compliant mechanisms based on goal-oriented design guidelines for prismatic flexure hinges with polynomial contours. In: 14th World Congress in Mechanism and Machine Science, Taipei, Taiwan. https://doi.org/10.6567/iftomm.14th.wc.ps10.008 (2015)

6. Linß, S.: Ein Beitrag zur geometrischen Gestaltung und Optimierung prismatischer Festkörpergelenke in nachgiebigen Koppelmechanismen, doctoral thesis, TU Ilmenau, Ilmenau, urn:nbn:de:gbv:ilm1-2015000283 (2015)

7. Lobontiu, N.: Compliant Mechanisms: Design of Flexure Hinges. CRC Press, Boca Raton, Fla. (2003)

8. Tseytlin, Y.M.: Notch flexure hinges: An effective theory. Rev. Sci. Instrum. **73**, 3363–3368 (2002). https://doi.org/10.1063/1.1499761